NOTE TO USERS

Ultrasonic Imaging of Pore Fluid Pressure and Scaling to Field Measurement

by

Paul Kobina Frempong

Submitted in partial fulfillment of the requirements for the degree of

DOCTOR OF PHILOSOPHY

Major Subject: Mining Engineering

at

DALHOUSIE UNIVERSITY

Halifax, Nova Scotia, Canada August, 2005

Your file Votre référence
ISBN: 0-494-13049-0
Our file Notre référence
ISBN: 0-494-13049-0

DALHOUSIE UNIVERSITY

To comply with the Canadian Privacy Act the National Library of Canada has requested that the following pages be removed from this copy of the thesis:

Preliminary Pages
- Examiners Signature Page
- Dalhousie Library Copyright Agreement

Appendices
- Copyright Releases (if applicable)

Dedication

To my dear wife, Augustina, and two beautiful children, Kofi and Asantewaah, for their love, support and understanding

TABLE OF CONTENTS

APPENDECES:

LIST OF FIGURES

LIST OF TABLES

LIST OF ABBREVIATIONS AND SYMBOLS

P_e	Effective stress
P_d	Differential pressure
P_c	Confining pressure
P_p	Pore pressure
n	Effective stress coefficient (Coefficient of deformation)
V	Compressional wave velocity
Q	Attenuation quality factor
c_b	Bulk compressibility of the rock
c_r	Compressibility of the rock matrix
α	Biot coefficient
K	Effective Bulk moduli
K_0	Grain Bulk moduli
ϕ	Porosity
A	Physical quantity of the rock
ε_{ij}	Elements of the strain tensor,
σ_{ij}	Element of the stress tensor
ε_{aa}	Volumetric strain summed over repeated index,
δ_{ij}	Kroenecker's delta
λ	Lame constant
K	Bulk modulus
σ_o	Hydrostatic stress
σ_{aa}	Mean stress times 3 sum over repeated index
μ	Shear modulus
E	Young Modulus
σ_{zz}	Extensional stress
ε_{zz}	Extensional strain
ε_{ij}^{Pp}	Strain due to pore pressure
H	Biot effective modulus due to pore pressure
θ	Total volumetric strain with pore pressure effect
TAE	Time average equation
VIS	Virtual infinite stiffness
ROM	Read Only Memmery
ASTM	American Association of Testing Material
A	Physical property
UCS	Uniaxial Compressive Strength
Q	Quality factor
NSERC	Natural Science and Engineering Research Council of Canada
PRAC	Petroleum Research Atlantic Canada
D	Darcies

ACKNOWLEDGEMENTS

Acknowledgements go to my supervisor, Dr Steve D. Butt, my co-supervisor, Dr Rafiqul Islam and the committee members, Dr Maria Rockwell and Dr. Lei Liu for their invaluable technical discussions and suggestions. I am pleased for the large number of people who contributed in diverse ways to this thesis, especially those with whom I shared my time in all the field trips and the experimental work. Mr. Donald Adam, in particular, provided invaluable assistance in the design of the laboratory equipment and the experimental techniques. I thank all the technicians especially Mr. Brian Liekens and and Mr. Darrell Adams for always being there to cut the metals, bend the plates and provide technical assistance.

I would also like to thank the members of staff, students and lecturers in the mining engineering department for their support and continuous tenure in giving me the opportunity to study at the department. Many financial sponsoring groups have contributed to my study. They include: Natural Science and Engineering Research Council (NSERC) of Canada, Atlantic Investment Fund (AIF) and Petroleum Research Atlantic Canada (PRAC). I express appreciation to all these sponsoring groups. Thanks to the oil and gas research group of Dalhousie University for the useful discussions and guidelines.

Appreciation also goes to my dear wife, Augustina, and my two beautiful children, Kofi and Asantewaah, for their unprecedented understanding and love and for allowing me to spend all the cold season in the office in Canada instead of spending summer quality time with them in Australia. The sacrifices are great and unprecedented. I appreciate all the love and care they have provided.

Last and the greatest appreciation is to the only SUPREME ALMIGHTY GOD for being the overall mastermind of this research in particular and sustaining my life in general. What has been accomplished in the three years of this research is just by HIS grace and mercies.

ABSTRACT

The thesis deals with the development of scaling models for acoustic imaging of pore pressure in reservoir. This topic has gained interest in the last decade mainly because of the appealing possibilities given by non invasive methods of imaging, which are very flexible and cost effective. P and S wave velocities and attenuation characteristics are used to retrieve information from the earth through non-destructive techniques. However, there are some problems on how to resolve the discrepancies between, laboratory/core velocity that uses high frequency waves and field velocity that uses low frequency waves. This velocity discrepancy, discussed intensively in scientific literature, is referred to as scaling problem, and has caught the attention of many practitioners. Extensive literature review indicates that, to date, Backus averaging is the only practical method that provides a finely foliated velocity model in an attempt to solve the scaling problems. However, Backus averaging has two major shortcomings and limitations: (i) there is no source of intrinsic energy dissipation such as friction or viscosity (attenuation) catered for in the model, (ii) the model also applicable to layered formation and requires that layer thickness of the media must be larger than the seismic wavelength: how greater is still a question of disagreement among scientist. The author believes that, the way to reconcile the various velocity differences is to develop a numerical model that would scale the velocities depending on the type of waves used at a given frequencies and wavelength.

The research therefore provides the opportunity to examine the dispersion of elastic wave velocity over a wide frequency range. The thesis has three main objectives: (i) To answer the question of what factors contribute to velocity differences in acoustic imaging across the various frequency bands (ii) to develop practical scaling models and methodology that take into account intrinsic energy dissipation and (iii) to find ways to image pore pressure at high overburden pressure (deep depth of reservoirs).

The methodology used was based on laboratory experimental methods and numerical modeling. The laboratory experiments coupled elastic, petrophysical and geomechanical measurements under insitu conditions, over a broad frequency band, on texturally well-characterized artificial and natural sandstones. Equipments and experimental methods were designed and developed for measuring the velocity and attenuation of compressional and shear waves over a frequency range from 240 kHz to 1.5 MHz in reservoir rock samples under simulated insitu pressure conditions. A variety of representative sandstone samples, ranging in strength, stiffness, porosity and permeability, were used for the experiments. Bench-top geomechanical and petrophysical testing were done to evaluate the individual rock characteristics. The pore-permeability, mineralogical and pore-structures of the samples were fully characterized using a scan microscopy. This suite of experiments resulted in a database of petrophysical, geomechanical and acoustic properties of the rock. The experimental results were used to validate the numerical model.

The numerical methods investigated the fundamental science underlying seismic wave propagation in reservoir rocks. Ideas and techniques were developed which were applicable and relevant to the current practicing methods of reservoir engineering and pore pressure predictions at deep depth. The specific numerical methods were based on both the finite difference models (for velocity profile) and numerical spectral discretization (for attenuation profile). These methods were used to develop wave propagation in a visco-elastic medium that unifies the dispersion theory, under Klein Gorden (KG) wave propagation model, and uses frequency dependant velocity approaches to velocity predictions at all frequencies and wavelengths.

It was found that different dispersion and attenuation mechanisms in the rocks caused by intrinsic anelasticity, scattering, and diffraction are responsible for the velocity differences across the different frequency waves along the spectrum. The accuracy of measuring velocity across the frequency spectrum therefore depends on the dispersion characteristics of the waves and the nature of the rocks that disperse the waves. High frequency waves tend to travel faster than low frequency waves. Weak, loose, inhomogeneous and incompetent rocks present more inaccuracies in velocity measurements than competent homogenous and strong rocks, because the latter tends to disperse waves more than the former. Spectral discretization technique adopted in this research is able to decompose the waves in frequency domain so that different frequency components could be analyzed and accurate velocity differences and errors quantified for a particular frequency. The model that was developed for the multi-frequency velocity analysis scales the velocities across the various frequency band. This velocity-frequency relationship works for sandstones of similar attenuation characteristics. For different rocks, the attenuation values are needed as inputs into the developed spectral discretization model, in order to predict changes in velocity with frequency.

On ultrasonic imaging at deep depth, it was found that at high pressures, velocity data does not provide the resolution needed for identifying slight changes in the physical state of rock over varying insitu conditions. Attenuation quality factor is far more sensitive than velocity to changes in pore pressure and therefore attenuation offers the best opportunity for imaging at high depth. The small changes in velocities can however be incorporated into reservoir monitoring using attenuation instead of velocity, if accurate insitu attenuation measurements techniques are developed.

The whole thesis has been detailed in a series of technical papers and conference proceedings that have been published, accepted or under consideration in reputable international journals and conferences. The thesis also includes introductory, discussion and conclusion sections that link with the technical papers to form a common theme. Highlights of the results, scientific achievements and the value of this whole work, in terms of its practicality and its contribution to scientific knowledge are given in the conclusion. New research areas have also been identified and recommended for further studies.

CHAPTER ONE

INTRODUCTION

1.0 Overview

This chapter gives the background and motivation of the thesis and specifically defines the problems that lead to the research. It presents the specific problems that are to be solved. It also outlines the aims and objectives of the thesis and explains the experimental and numerical methods used to achieve the objectives. The scientific value of the thesis, applications and its contribution to knowledge are also given. The style, outline, organization and the scope of the dissertation are also discussed.

1.1 Background and motivation

This research was motivated by the need to develop and implement techniques that link laboratory seismic imaging to field seismic imaging of petrophysical and geomechanical properties of reservoir rocks. Interpretation of laboratory, field seismic and borehole data requires knowledge of rock and elastic properties at different scale along the seismic frequency band. Laboratory scale ultrasonic velocity measurements can be useful for log calibration and data interpretation in field measurements. However, a number of

complications arise due to the use of high frequency waves in the laboratory measurements. This is partly due to the scale of measurements. Laboratory, sonic and seismic measurements investigates different volume of rocks because of their geometry and source frequency (Taltham and McCounick, 1999). Experimental techniques and data interpretation models are needed to help characterize the competing mechanisms controlling velocity dispersion and attenuation in rocks. Velocity dispersion and attenuation have been singled out as the main reasons for velocity disparities between the laboratory and the field measurements (Parra et al., 1999). This research develops scaled models of multi-frequency data so that different seismic properties derived from different wave characteristics could be integrated in seismic imaging techniques.

Seismic imaging is a broad topic that encompasses non-destructive estimation and quantification of the physical properties and characteristics of material (for example rocks) using seismic waves. It is a non-invasive or non-destructive technique (NDT), based on the principle of elastic wave propagation through rocks, without physically destroying the rocks. Traditionally, rock properties have been derived by, what is known as non destructive technique. The rocks are physically destroyed by drilling, blasting and crushing before their properties could be retrieved. The non-destructive technique is very appealing and has gained a lot of interest. This is because of its flexibility and cost-effectiveness. In today's world where projects are driven mainly by economics, it is not surprising that more attention is being shifted to non-destructive imaging techniques. Multi million dollars are spent by oil companies, on oil exploration wells, in order to get

a few centimeter drill core sample to represent a reservoir image of 100 kilometer area. This practice presents a typical example of serious economic implications involved in destructive imaging techniques. However, the non destructive technique using seismic waves is cost effective and economically appealing. By analyzing the travel times, velocities, attenuation, reflections, refractions, impedances and other seismic properties, one is able to relate the seismic properties to the actual physical, mechanical and petrophysical properties of the reservoir rock. This analysis is done through a catalogue of both empirical and non empirical relationships, under the banner of rock physics (Table 1.1). Each small portion of the formation, fundamentally called a cell, could then be quantified and given a unique characteristic physical and petrophysical property (permeability, porosity, saturation, pore pressure, density, type of fluid, rock or fluid composition etc.), based on their seismic properties. The sizes of the cells depend on many factors including: (i) properties of the wave used (frequency, wavelength, velocity), (ii) properties of the rock formation, (iii) data input, as for example how sparse or dense is the input velocity data collected. Table 1.1 (after Wang, 2001) shows the physical properties of materials that have been derived through seismic techniques and applying empirical and non-empirical relationships.

Table 1.1: Some properties of materials that have been derived through seismic techniques using empirical and non-empirical relationships (Wang, 2001)

Some properties that have been derived directly from seismics	Some properties that have been derived indirectly from seismic
Density	Permeability
Modulus	Lithology
Poisson Ratio	Clay content
Porosity	Fracture
Saturation	Pore shape
Quality factor	Gas-oil / Gas-water ratio
Pore fluid	

Seismic imaging is either specific or general and can take many forms. For example, one could decide to use, velocity to relate to porosity and thus give a porosity image of the rock formation. Similarly, seismic velocity can be related to permeability to give a permeability image. In fact seismic properties can now be related to compressive strength, sand production, viscosity, saturation, pore pressure (Wang, 2001). Imaging has unlimited application in the petroleum industry and elsewhere.

Despite all the appealing possibilities and economic gains, seismic imaging does present challenges. Among them are:

(i) The unresolved issue of scaling, i.e. problems relating to the scale dependence of the seismic wave velocity (Marion et al., 1994; Mukerji et al., 1995; Imhof, 2003)

(ii) Difficulties in imaging of high pore pressures and stress conditions (Landro and Kvam, 2002).

The main purpose of this research is to find solutions to some of the challenges in the petroleum industry. Generally, scaling is a common problem in many scientific researches, where results from laboratory experiments or in a pilot plant are to be transferred into the field/large scale operations for practical use. This research is therefore, in part, focused on the so-called seismic scaling problem. It investigates how results of seismic images produced in the laboratory on rock cores, under different pore pressure and stress conditions, could be scaled to field images. It finds the interrelationship between laboratory and field models and vice versa. In other words the research aims at developing practical methodology useful for pore pressure imaging. It explores laboratory-field scaling methodologies for reservoir application. It involves laboratory experimental and numerical modeling to find accurate scaling law that governs the communication between various scales of seismic models.

Literature review (Chapter 2) indicates that, despite the detailed research on scaling, none has been focused on inverse and forward scaling methodology that is applied to seismic imaging. Most of the scaling methods in the literature focus on flow, heat/mass transfers and chemical processes (Ziolkowski and Bokhorst, 1993; Islam, 1996; Islam, 2001). The review did not identify many literatures that focus on scaling in seismic imaging. In this research, the author has identified and developed various scaling methodologies that are considered to be important in ultrasonic imaging techniques that are appropriate to scale multi-frequency data from the laboratory to the field and vice versa.

Another challenge in petroleum exploration involves difficulties in performing seismic imaging of extreme effective stress conditions (Prasad and Manghnani, 1997). Low overburden depth, high permeability (>100 mD), high porosity (>20 %) and intermediate to low strength (15 to 55 MPa UCS) reservoir rocks have traditionally been the focus of petroleum exploration and subsequent research in the area of laboratory ultrasonic testing (Hottman and Johnson, 1965; Eaton, 1975; Bowers, 1995; Sayers et al., 2000). However, as the reservoir depth are becoming deeper, more drilling and exploration are now focusing on deep depth in highly stressed reservoir rocks with vastly different characteristics than those described above. Consequently, engineers and scientists are trying to apply these traditional velocity models to deep reservoirs at highly stressed levels, with difficulty (Briers, 2004). The relationships between the petrophysical characteristics and effective stresses within these types of rocks have little variation on velocity measurements. As a result, new methods for pore pressure imaging at high effective stress conditions are required to provide more reservoir information. Highlighting these key relationships for these reservoir rocks in the laboratory is essential before investigating direct field measurements of velocities and attenuation quality factor.

1.2 Statement of the problem

1.2.1 Detailed description and analysis of the first problem

The first part of the research is directly related to the response of seismic imaging under different pore pressure, confining pressure, differential stress and effective stress

conditions. Hydrocarbon reservoirs are generally under pressure. This situation can, in principle, be characterized by seismic waves. The dependence of the P-wave and S-wave velocities on effective stress can be used to predict abnormal pore pressures in advance of drilling (Miranda et al., 1996). An integrated study of the state of stress, pore pressure and physical properties of reservoirs provides a context within which to understand the interactions between geological conditions and engineering and production practices. The primary parameters controlling these interactions are the state of in-situ stress, rock strength, bedding orientation and pore pressure distribution. Unlike the past, where most reservoirs are near surface, depletion of oil reserves has resulted in digging very deep wells in the search for new deposits. Reservoirs at large depth, for example, wells in the Gulf of Mexico, are under very high overburden pressure and stress. However, the effectiveness of seismic waves to image over-pressured reservoirs present many challenges (Carcione and Hellev, 2002; Dvorkin and Walls, 2000). This stress state has an impart on the seismic imaging, since velocity, attenuation and most of the seismic properties are affected by the stress and pore pressure conditions. Traditionally, seismic velocity have been studied as a function of the variation of both external hydrostatic pressure and internal pore pressure in the range of 0 to 2500 psi and has been found to be a function of stress or overburden pressure (Carcione and Hellev, 2002). However, at certain stress level, (currently 180MPa, about 10km deep) the relationship between stress and seismic velocity becomes weaker. The stress becomes insensitive to velocity, as the overburden pressure increases. The first part of this research is based on imaging pore pressure in extreme stress conditions in order to analyze and find the stress levels, at

which stress-velocity relationship becomes insensitive. It predicts the relationship between the seismic properties and the overburden pressure at deep depth and find alternate way to image at high overburden pressure.

The physics of geo-pressure is complicated, especially taking all fracture systems and orientation into consideration, and resolving all forces to find the magnitude and direction of the stress. However, the main concept can be presented in simpler terms as shown in Figure 1 (from Carcione and Hellev, 2002). The pore pressure, also known as formation pressure, is the *insitu* pressure of the fluids in the pores. This pressure can vary depending on porosity, pore structure, shapes and sizes and the type of fluid (brine, water, oil) that filled the pore spaces. The pore pressure is equal to the hydrostatic pressure when the pore fluids only support the weight of the overlying pore fluids (mainly brine). Typically, this occurs at a reservoir depth of about 3-4km. The lithostatic pressure is the same as confining pressure and it is due to the weight of overlying sediments, including the pore fluids. In the absence of any state of stress in the rock, the pore pressure attains lithostatic pressure and the fluids support all the weight. However, fractures perpendicular to the minimum compressive stress direction appear for a given pore pressure, typically 70-90% of the confining pressure (Carcione and Hellev, 2002). In this case, the fluid

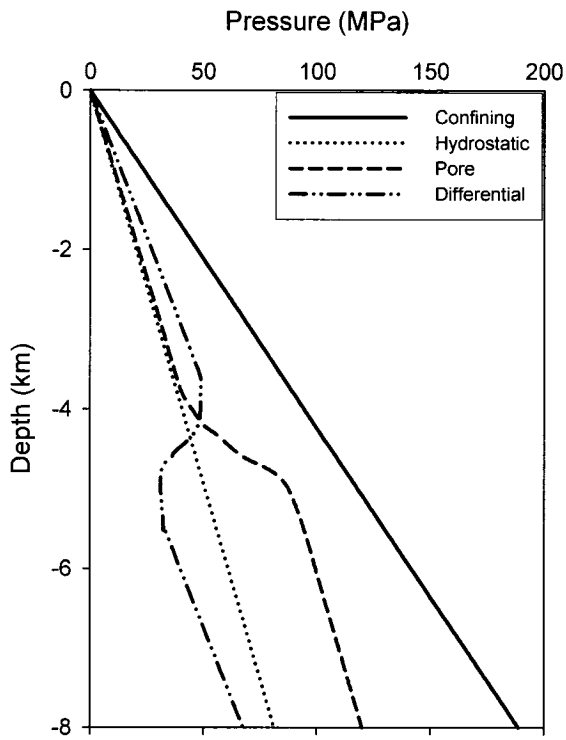

Figure 1.1: Typical pressure-depth plot where the different pressure definitions are illustrated (after Carcione and Hellev, 2002).

escapes from the pores and pore pressure decreases pressure (Carcione and Hellev, 2002). A rock is said to be over-pressured when its pore pressure is significantly greater than hydrostatic pressure. Most deep oil exploration drillings are in this zone of overburden formation and it is at deep depth where seismic imaging presents challenges. The relationships between the petrophysical characteristics and effective stresses within these types of rocks at high stress have little variation on velocity measurements. New methods of seismic imaging are required to provide more information about in-situ stress conditions. Highlighting the key relationships between seismic velocities and effective stresses for reservoir rocks in the laboratory is essential before investigating direct field

measurements. Seismic properties of rocks generally depend on effective pressure, a combination of pore and confining pressures, taking effective stress coefficient into consideration.

1.2.2 Detailed description and analysis of the second problem

The second and the main part of the problem that this thesis seeks to address is how to scale data derived from multi-frequency seismic velocities used across the various frequency bands. This has been a major issue in seismic imaging. Different dispersion mechanisms based on differences in wave frequency, wavelength, and reservoir flow units and thicknesses cause differences in seismic velocity. For example the laboratory velocity (core scale) is greater than the seismic velocity (log scale) and in turn greater than vertical seismic profiling velocity (seismic scale). One of the reasons is because the frequencies of the waves used in estimation of these velocities are different (Carcione and Tinivella, 2001; Dvorkin, and Walls, 2000). Figure 1.2 (from Winkler, 1986) shows relationship between frequency and velocity for a typical sandstone rock. As indicated, the velocity in dry rock is assumed to be independent of frequency and the velocity in liquid-saturated rock increases with frequency. Total velocity dispersion is the fractional increase of the high-frequency velocity in the saturated rock relative to the low-frequency velocity.

The wave frequencies exhibit different dispersion characteristics that results in differences in the arrival times of the waves and thus differences in velocities. Table 1.2

shows the frequency, wavelength and corresponding velocities at various scales in seismic imaging. If the data from these frequency ranges (Lab/log/seismic) are to be integrated there is the need for the velocities to be scaled by developing appropriate scaling models and methodologies.

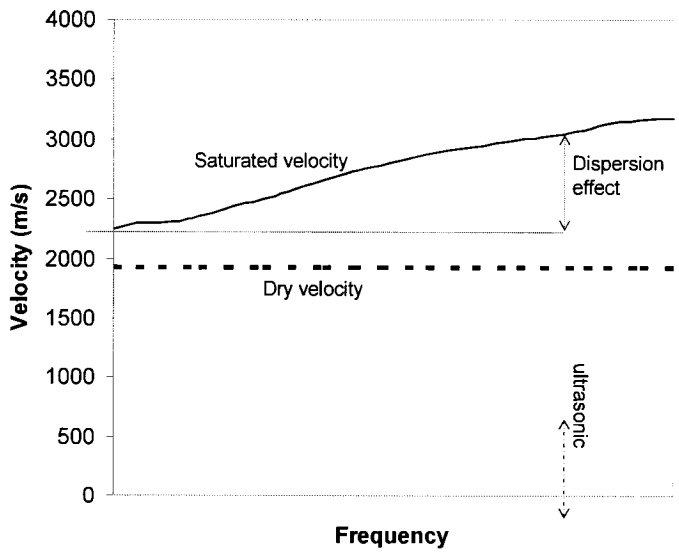

Figure 1.2: Schematic of compressional wave velocity as a function of frequency for a typical sandstone. (after Winkler 1986)

Table 1.2: Various seismic measurements across varying frequency-wavelength band.

Measurements	Thickness	Frequency	Wavelength
Laboratory Measurements (Core scale)	Millimeters to Centimeters	100KHz to 1MHz	0.008 Meters
Field Measurements (Log scale)	Centimeters to Meters	100Hz to 15KHz	0.027 Meters
Field Measurements (Seismic scale)	Meters to Killometers	1Hz to 100Hz	20 Meters

To date, there are no practical scaling laws between laboratory imaging based on core logs and seismic imaging based on well logs and vertical seismic profiling and other seismic technique. Velocities in materials have been assumed constant irrespective of the frequency of waves. This proposition is valid in isotropic and homogenous materials, where wave dispersion is considered minimum or negligible. However, for rock materials that are considered heterogeneous under the visco-elastic model, the proposition is invalid. This has resulted in the variation of velocities between the laboratory and the field seismic imaging. There is therefore the need to scale the velocities from the laboratory to the field and vice versa.

1.3 Aims and objectives

1.3.1 General objectives

There are four main objectives for this research:

(i) To produce seismic images under varying pore pressure and stress conditions in the laboratory.

(ii) To find how the various seismic properties used in seismic imaging relate with pore pressure and *insitu* stress conditions at the laboratory scale.

(iii) To answer the question of what factors contribute to velocity differences in seismic imaging across the various frequency bands.

(iv) To develop practical forward and inverse laboratory-field scaling methodologies for seismic imaging and reservoir rock characterization.

In order to accomplish these general objectives, they were first broken down into specific sub objectives as explained in the next section (section 1.3.2).

1.3.2 Specific sub objectives

(i) To do a detailed literature review of the current laboratory-field scaling methodologies used in seismic imaging, bringing out their limitations and shortcomings. This includes detailed review of wave propagation mechanisms in visco-elastic medium that takes into account intrinsic energy loss and scattering. The aim of the literature review was to identify the current practices of scaling methods and techniques and to identify the

shortcomings and limitations. It also helped to accumulate knowledge and study the fundamental science underlying seismic propagation in reservoir rocks. Thus, ideas and techniques were developed which were applicable and relevant to the current practicing methods of reservoir imaging.

(ii) To perform suites of petrophysics, geomechanics and seismic laboratory experiments on natural and artificial sandstone. In the experiments, measurements of porosity, permeability, saturations, P and S elastic wave velocities, seismic emission, attenuation and quality factor were made, under both hydrostatic and deviatoric stresses. The aims of these experiments are to (a) develop experimental techniques for ultrasonic wave measurements on core samples under in-situ stress and pore pressure conditions in the laboratory, (b) perform simulated depletion tests on various representative reservoir rock samples under the uniaxial strain condition and (c) build a large seismic imaging database consisting of mechanical, petrophysical and dynamic rock properties.

(iii) To use finite difference modeling (for velocity profile) and numerical spectral discretization (for attenuation profile) to develop wave propagation in a visco-elastic medium (a low-permeability, low-porosity, reservoir rock referred to as quartz sandstone) that unifies the dispersion theory, under Klien Gorden wave propagation model. The model uses frequency dependant velocity approaches to velocity predictions at all frequencies and wavelengths.

(iv) To use the above model to scale velocities at all frequencies, wavelength and flow thickness combination, that would be useful and practical for field application.

(v) To evaluate and validate the model, i.e. by testing the validity of the scaling model using actual field and or experimental data verses numerical modeled results.

1.4 Methodology

1.4.1 General

The above research objectives were achieved by a combination of (i) field work involving sample collection; (ii) laboratory experimental studies; and (iii) numerical analysis, that led to widely applicable predictive scaling models. The research strategy investigated the fundamental science underlying seismic propagation in reservoir rocks and developed ideas and techniques which were applicable and relevant to the current practicing methods of reservoir engineering. The specific methodologies are given in the next sections.

1.4.2 Field work, data collection and preparation of natural sandstone

The field work involves the collection of natural sandstone sample and detailed field geological studies of the rock sample spanning over six months. This was done in

conjunction with the Nova Scotia Department of Natural Resource. The quartz sandstone came from upper member of the Horton Bluff formation found in the Minas and Cumberland Basin of Nova Scotia, Canada. This sandstone is a reservoir rock that contains mainly natural gas under high pressure. It was collected at approximately 100 km to the north-east, in the province of New Brunswick. This unit exists at a depth of approximately 2500 m where it is known for its high accumulation of natural gas (over-pressured gas reservoir (Ryan, 1998)). The outcrop rock sample was originally under pressure from overburden stresses when it was under in-situ conditions. Details information of the sample (geology, mineralogy and physical properties are given in Appendix 2. The samples were drilled perpendicular to the bedding plane using the diamond drill machine at the mining engineering rock mechanics laboratory. It was prepared into cores of dimensions 108mm long by 54mm in diameter. The surfaces were ground smooth with the surface perpendicular to the core axis according to the American Standard of Testing Materials (ASTM, 2003). The samples have Uniaxial Compressive Strength (UCS) of approximately 100MPa, porosity of 15%, and permeability of 3.9mD (Table 1.3). The initial bench top measurements of the water-saturated properties of the sandstone at 2MPa initial pressure and all the detailed geological and mineralogical characteristics are shown in the Appendix 2.

1.4.3 Manufacturing of synthetic sandstone

The natural sandstone from the field (quartz sandstone described earlier) was supplemented with synthetic sandstone. This is to get weakly consolidated sandstones which are difficult to get from the field because of coring problems. It can also be used to validate the results from the natural rocks. The synthetic sandstone consists of sand, Portland cement, and water. The material composition contained a weight ratio of approximately 0.8, .0.09 and 0.10 for sand, cement and water respectively. Details of the grain size distributions of the silica sand grains and other material characterization are given in the Appendix 3.

1.4.4 Performing suites of laboratory experiments

The laboratory experiments coupled seismic, petrophysical and geomechanical measurements under in situ conditions, over a broad frequency band, on the texturally well-characterized artificial and natural sandstones described above. The equipment design was done to adapt to a triaxial compression cell to simultaneously measure geomechanical, petrophysical and seismic properties of the sandstone rocks. The design was made to accommodate axially mounted ultrasonic P-wave transducers (Appendix 4). The experimental measurement techniques were developed to accurately determine the velocity and attenuation quality factor for rock the samples within the cell. Simulated production experiments were performed using the triaxial cell on different rock samples.

The seismic measurements were done for the velocity and attenuation of compressional - and shear-waves over a frequency range from 200 kHz to 1.5 MHz in the reservoir rock samples under simulated *insitu* pressure conditions. The measurements were undertaken on 54mm diameter/108mm length core samples using propagating compressional - and shear-waves. The samples were measured under dry, fully- and partially-saturated conditions with water as the pore fluids. The pore-permeability, mineralogical and pore-structures of the samples were fully characterized using a scan microscopy (Appendix 2). In the data processing, computer algorithms were developed for seismic processing that give accurate determination of the arrival time, velocities and attenuation of compressional- and shear-waves from full-waveform ultrasonic data. Other programs were developed in house with MATLB to handle the processing and regimes like diffraction and scattering. Appendix 11 gives all the MATLAB programs that were developed in this research. These algorithms were used in conjunction with standard processing routines for investigating the seismic properties of reservoir rocks in the KHz to MHz frequency range for well-characterized rocks. Techniques for interpretation of rock properties from seismic data were developed. The following properties were of particular interest and were measured during the experiments:

(a) Seismic properties:

Measurement of S and P wave velocity.

Measurement of S wave polarization for anisotropic determination.

Measurement attenuation characteristics and quality factor.

Measurement of dynamic modulus (shear, bulk and Young modulus).

(b) Geomechanical properties:

Uniaxial compressive strength (UCS).

Shear strength.

Static Modulus (shear, bulk and Young modulus).

Density.

(c) Petrophysical properties:

Permeability

Porosity

Saturation

The flow chart in Figure 1.3 shows the summary of the suites of experiments that were conducted.

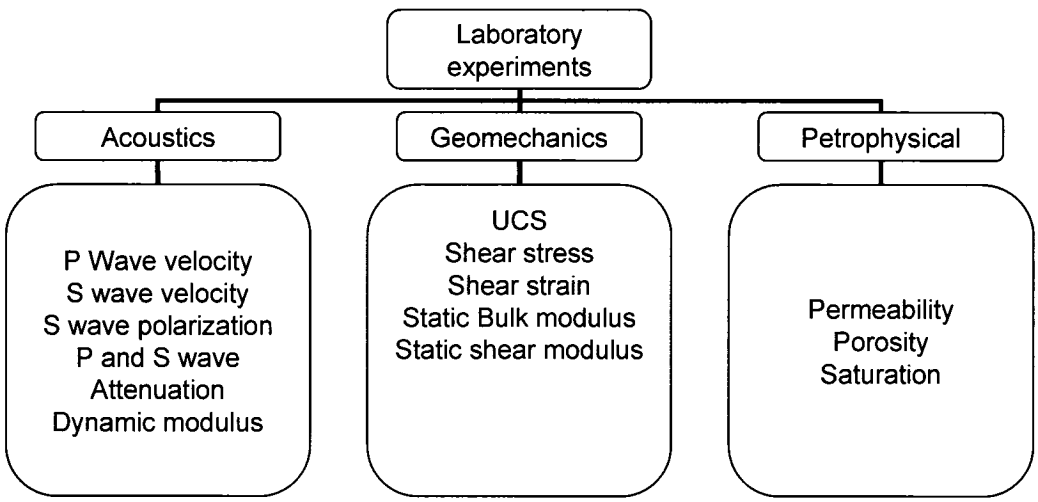

Figure 1.3: The summary of the experimental work.

1.4.5 Numerical modeling

The numerical modeling methodology was based on both finite difference models (for velocity profile) and numerical spectral discretization (for attenuation profile). These methods were used to develop wave propagation in a visco-elastic medium, (a low-permeability, low-porosity, reservoir rock referred to as quartz sandstone) that unifies the dispersion theory, under Klien Gorden wave propagation model, and uses frequency dependant velocity approaches to velocity predictions at all frequencies and wavelengths. The finite difference method includes analysis of fundamental wave equation, analysis of governing partial differential equation and the boundary conditions. The spectral decomposition (SD) broke the waves down into various frequency components. The wave was then discretized in a spectral domain and back transformed into real domain. The aim was to develop a discretization technique that treats wave velocity, 'c' as a function of the wave number, 'k'. These two methodologies provided the opportunity to examine the dispersion of elastic wave velocity over a wide frequency range – the main cause of differences in velocities.

1.5 Significance of the thesis

The next five sections explains the main ways that this research has contributed to science.

1.5.1 Equipment design and experimental techniques

New equipment components were designed and manufactured. The components were used to modify an existing triaxial cell, thus adapting it to simultaneously measure seismic, petrophysical and geomechanical properties of a core sample. This technique simultaneously performs ultrasonic wave measurements on core samples under changing *insitu* stress and pore pressure conditions in the laboratory. The equipment designed and developed in this research is able to measure the geomechanical, petrophysical and seismic properties of materials. The methods and the techniques have been verified by other researchers and the results published in reputable international journal (Donald et al., 2004). Details of the equipment design are found in the Appendix 4.

1.5.2 Population and quantification of a geo-scientific database

The research resulted in a database consisting of mechanical, petrophysical and dynamic rock properties. The database is particularly useful for geophysics and engineering work, to study the structure, composition and physical state of reservoir rocks. The values that were acquired under very high pressure (600MPa) would particularly be useful for earthquake studies. The low pressure seismic values are also useful for sub-surface imaging analysis and for petroleum applications. The laboratory and actual formation velocities could be used to estimate formation porosity and other petrophysical properties. Other applications include the prediction of seismic reflectivity at lithologic

boundaries in the crust and estimation of the engineering properties of rocks. The geo-scientific database would generally, provide a quantitative basis for many engineering applications. The database has been organized into a usable format useful for further research and teaching at the Dalhousie University, specifically at the mining engineering and the geology departments.

1.5.3 Technical publications

Another way of assessing the value of a research is its contribution to scientific literature through technical publications. Many technical publications, which add to the pool of scientific knowledge and literature, resulted from this research. Most of the papers are in various stages of publication in reputable international scientific journals and conferences. Some of the papers, which were direct result of the research, have been included in the thesis. Those that are not directly related to the thesis were not included but a list of all the publications is found in Appendix 12

1.5.4 Development of scaling model

As spelt out in the objectives (Section 1.3), the development of a scaling model, that takes into account intrinsic energy dissipation, is the heart of this research. This is the main value of the research. A model was developed that works by quantifying the expected change in velocity, based on the frequency of the wave used. The model has

been validated with experimental data within the range of frequency that was considered and it was in agreement.

1.5.5 Applications of the scaling model

The scaling model gives the relationship between velocity from different frequency waves and could be applied in imaging by applying the scaling model factor to the velocity images, based on the frequency of the wave used (laboratory, log and seismic velocities). This application would help to remove errors associated with using different frequency waves to image pore pressure. Another application of the model is estimation of *insitu* quality factor. The potential for high-resolution attenuation imaging is evident in the laboratory under a controlled environment. However, there are many difficulties for direct measurements of attenuation in the field. One of the challenges is the frequency independence assumption when using the spectral ratios techniques. The *insitu* method of spectral ratio in estimating Q is based on the spectral ratio of signals recorded at two different stations of the same event. This ignores dispersion effect between the two stations. The above developed model can be used to estimate Q by quantifying the attenuation effect due to dispersion, between these two stations, before the spectral ratio method is applied.

1.5.6 Development of computer programs and codes

The value of the research can also be assessed by the development of computer codes and executables. Many computer programs were developed and written for the various tasks accomplished in this research. The programs were developed in MATLAB programming language. This would make it easier for both engineers and those with limited programming ability to use, either directly or make some changes to suit a particular interest and need. The programs include:

(i) Diffraction correction program (MATLAB)

(ii) Dispersion programs using numerical Fourier discretization (MATLAB)

(iii) Finite difference program for velocity profile (MATLAB)

(iv) Excel spreadsheet program and macros for seismic data processing and estimation of quality factor (EXCEL MACRO)

(v) Stacking program for 50 digitized seismic data (MATLAB)

All the above programs are found in Appendix 11 and they are also available at the mining engineering server as public domain software. The application of these programs ranges from seismic data processing, through finite element modeling to spectral discretization techniques.

1.6 Style, structure and scope of the thesis

1.6.1 Thesis style and format

The style of this thesis is the technical paper format that includes six journal publications and two conference proceedings. These technical papers and conference proceedings have been published, accepted or under consideration in reputable international journals and conferences. The status of each publication is given before each chapter as a preface. The author is the main writer of most of the publications. Where the author is not the sole, primary, or main contributor and writer of the paper, but a co-author, the specific contribution made is clearly outlined within the preface of the paper. In addition there are appropriate introductory and concluding chapters and appendices that link all these papers into a common theme.

1.6.2 Structure and organization

The general structure and organization of the thesis is in five sections of 9 chapters: Section one is made up of chapter 1, which is the introductory chapter. This introductory chapter outlines the background and motivation of the research and defines specifically the problem statement that led to the research. It highlights the aims, objectives and the methods used to achieve the objectives. The value of the research as well as the plan, structure and organization of the thesis are also presented.

After chapter 1, the main body of the thesis is divided into four parts (Part I to Part IV). Part I is made up of one chapter (Chapter 2), of one publication based on literature review of acousto-mechanical models, scaling and wave propagation mechanisms.

Part II is made up of 4 chapters (Chapter 3 to Chapter 6) of four technical publications each forming a chapter. All the papers are based on laboratory investigations ranging from, data preparation through equipment design to experimental methodology and data processing. Specifically the papers investigate the effect of injection and depletion cycles on ultrasonic velocity and quality factor in glass sandstone. It investigates and characterizes volumetric failure in weak sandstone reservoirs using P-wave quality factor, velocity and seismic emissions. It also highlights non destructive techniques to determine the effective stress coefficient of porous sandstone and characterizes the permeability and seismic properties of an outburst-prone sandstone.

Part III is made up of two chapters (Chapter 7 and Chapter 8) of two technical publications, one in each chapter, and they are all based on numerical modeling and scaling development. The first paper studies the modeling of the effect of diffraction on velocity and attenuation measurements in rock materials and the second paper is based on numerical Fourier discretization to scale multi-frequency velocity data.

Part IV is made up of chapter 9 and the appendices. This chapter discusses all the work done in the thesis and gives detailed analysis of the results and findings of the research. It explains how the introduction and the preceding technical publications link together with the conclusions and the appendices to form a common theme. The discussion takes into account how the results from the research achieved the objectives outlined in the introductory chapter. Practical application and the value of the thesis have been explained. Pertinent areas have been highlighted and recommendation given with regard to further research that needs to be done. New research areas have also been identified and could be considered for further studies. This chapter therefore links together all the proceeding chapters and technical papers and the whole project into a common theme.

The appendices contain some literature reviews, computer programs and codes, mathematical derivations, formulas, equipment and experimental designs, pictures and photos during field work, list of other publications, references, measurements information and tables.

1.6.3 Scope and extent of thesis

The thesis was initially limited to a particular aspect of seismic imaging – the so called scaling problem - and to find solutions. However, due to the complexity of the scaling problem, it became pertinent to broaden the scope to explore and investigate other areas which were not directly related to scaling. These areas includes, pore pressure prediction,

estimation of effective stress coefficients, analysis of diffraction loss, population of database and *insitu* measurement of Q. The results from these new areas that were studied complemented the original scaling results. This helped to give better meaning and understanding involved in scaling multi-frequencies data. Results and findings from these new areas are included in the thesis.

PART I

REVIEW OF ACOUSTO-MECHANICAL MODELS

I: Overview

This chapter gives a detailed review of the current acousto-mechanical models used in seismic imaging, bringing out their limitations and shortcomings. In addition, there is a detailed review of wave propagation mechanisms in visco-elastic medium that takes into account intrinsic energy loss, scattering and diffraction. The aim of the literature review was to identify current reservoir imaging practices and the shortcomings of the existing scaling models to assist with applying laboratory results to field. Thus, ideas and techniques were reviewed which were applicable and relevant to the current practicing methods of reservoir imaging. The paper identifies some of the problems and shortcomings which led to the research presented in the thesis.

Chapter 2: Linking acoustic and mechanical properties of materials with particular reference to reservoir rocks: a critical literature review

2.1 Summary

The P-wave velocity in an infinite medium is proportional to the square root of the ratio of the effective elastic constant to the effective density. Ever since this relationship was established by Christoffel (1877), elastic techniques have been used to determine the elastic properties of materials, whether solids, liquids, gases or mixtures of these.

The intent of this paper is to examine the general and the limited use of acoustic velocity to derive the elastic, mechanical, petrophysical and hydrological properties of geological materials. General concepts as well as details of mechanical behavior of different materials subjected to wave propagation are included. Areas that could be subjected to abuse and misuse have been highlighted. Specific useful applications of the theories with regard to characterizing reservoir rocks, some limitations and the adherence to the homogeneity and isotropic assumptions have been explained.

2.2 Introduction

Ever since it was established that the P-wave velocity is proportional to the square root of the ratio of the effective elastic constant to the effective density, seismic techniques have

been used to determine the elastic properties of material whether solids, liquids, gasses or a mixture of these (Nur, 1991; Best et al., 1991; Kuntz et al., 1997). Once the elastic constants are obtained, other relevant mechanical properties and parameters of the materials such as Young's modulus, Poison ratio and Bulk modulus may be determined. Table 2.1 shows the list of some properties of materials that have been derived directly or indirectly by seismic means.

The large variation in the material properties values derived from non destructive technique as compared to the ones derived from conventional methods raise questions whether these empirical relations and hypotheses apply to all materials in nature. There is also a concern as to what laboratory and field conditions, temperature and pressure ranges are these theories applicable without fully stretching the assumptions and limitations behind the theories. The elastic constants in real materials may be complex, with the real component primarily related to the P-wave velocity under very strict assumptions and limitations as shown in the original Christoffel equation (Christoffel, 1877). When these assumptions are not adhered to, erroneous results are generated. Telford et al., (1990) have reported differences of error of 20 to 25 % in the elastic property values derived from using different frequency waves (laboratory MHz frequencies, sonic frequencies and log frequencies)

Table 2.1: Properties of materials that could be derived through acoustic techniques

Properties that have been derived directly from acoustics	Properties that have been derived indirectly from acoustics
Density	Permeability
Modulus	Lithology
Poisson Ratio	Clay content
Porosity	Fracture
Saturation	Pore shape
Quality factor	Gas-oil / Gas-water ratio
Pore fluid	

However when this same theory is applied to some materials appropriately, under the assumptions given, it does provide very good and accurate results. In most cases accurate values of elastic constants are obtained from a measurement of P-wave velocity (Levy et al., 2001).

While many potential theories have been proposed in the literature, they have also created much confusion due to conflicting findings, narrow focus, and lack of interdisciplinary approach. Many of these theories are fragmented and site specific and difficult to fit a general acousto-mechanical model. A comprehensive review of the latest research development in this field of study can dispel some of the misconceptions that have dominated this important area of study. One of the objectives of this literature review therefore is to critically look into the general and limited use of elastic wave velocity used to derive the elastic, mechanical and hydrological properties of geological material through these empirical relationships.

2.3 The theory and assumptions

Combining Hooke's law with Newton's second law of motion, and including the description of a propagating planar wave, Christoffel derived an equation showing the connection between coefficient of stiffness (Young modulus, shear modulus and Lame constants) wave velocity and density. The Christoffel equation basically states that the elasticity tensor of a material is related to the propagation velocity of a planar mechanical wave by:

$$(C_{ijkm} n_j n_m - \rho c^2{}_{sound} . \delta_{ik}) U_k = 0 \qquad (2.1)$$

where C_{ijkm} is the adiabatic tensor of elasticity, n is the unit vector of direction of propagation, ρ is the density of material, c_{sound} is the sound wave velocity, δ_{ik} is the Kronecker symbol and U_k is the vector of particle displacement in the medium. Using the isotropic conditions and introducing the Lame constants the two types of bulk waves can be propagated through the material - longitudinal (P-waves) and transverse (S-waves). Introducing bulk and shear modulus the velocities of P-waves and S-waves can be deduced as:

$$V_P = \sqrt{\frac{K + \frac{4}{3}\mu}{\rho}} \qquad (2.2)$$

$$V_S = \sqrt{\frac{\mu}{\rho}} \qquad (2.3)$$

where, V_p is the P-wave velocity and V_s is the S-wave velocity. ρ is the density, K is the bulk modulus and μ is the shear modulus. Several useful direct and indirect relationships can be deduced from these basic equations (equation 2.2 and 2.3) involving the wave velocities and Poisson's ratio, Lamé constants, porosity, saturation, density and lithology (Mavko et al., 1998). It should be noted that the above relationship were derived under compressible, elastic, homogenous and isotropic conditions (Mavko et al., 1998; Christoffel, 1877) which do not exist in a lot of practical situations especially in a geologic environment. Such relationships should therefore be applied cautiously.

2.4 Relationship between density and velocity

Simple atomic model theories predict that the bulk modulus (K) is proportional to the density (ρ) and the mean atomic mass m by the relation $K= (\rho/m)^{4/3}$. For example, for Mg_2SiO_4, m = (2 x 24.3+28.3+4x16)/7 =20.13. Thus, from equation 2.1 and 2.2, one expects correlation between density and velocities. Based on the correlation of density and velocity measurements, Birch (1961) suggested a linear relationship known as Birch's Law given by:

$$V_p = a\,(m) + b\rho \qquad (2.4)$$

Where, a (m) is a constant related to the mean atomic mass, ($20 \leq m \geq 22$) and b is a constant. For example, at shallow depth, it is found that $V_p \approx 0.33 + 2.2\rho$ and $V_s \approx 0.48 +$

1.13ρ where ρ is given in g/cc and velocities are in km/s. Christensen and Salisbury (1975) disagreed with Birch and instead proposed a nonlinear relationship given by:

$$V_{p,s} = a_v(m) + b_v\rho^c \quad (2.5)$$

Where, a_v, b_v and c are different constants for P and S waves. In general, the relationship between velocity and density are parameterized by *m*, thus distinct relations exist for different rocks and formation (i.e. anhydrite, sandstone, carbonates, salt). The equations are also limited in the sense that even for sedimentary rocks it is applicable under normal fluid pressure and no extensive micro-fracturing. For crystalline rocks, it is applicable when no positive geothermal anomalies are present since partial melt, chemical alterations and the generation of micro cracks by cooling will result in a stronger decrease of V_p and V_s values than in ρ values. In fact, there is no general acceptable single relationship between velocity and density in the literature.

2.5. Can lithology be inferred from velocity?

Generally some reservoir rocks have higher velocity than others. For example, dolomite and limestone have higher velocities than sandstone and shale. However, Hearst, et al., (2001) iterated that P and S wave velocity is not a very strong function of lithology. Unless the porosity and the exact composition of a rock is known, one cannot distinguish, for instance, carbonates from sandstone/shale, based on velocity alone. Tatham and McCormack (1991) concluded that the inverse problem of relating an observed change in V_p, V_s and V_p/V_s to a variation to a particular rock property is difficult. For example a

decrease in V_P/V_S in a clastic formation could be produced by a decrease in shaliness, a change in fluid saturant from brine to gas or a decrease in bulk porosity. Tatham and McCormack (1991) further concluded that the key to resolving this ambiguity is to seek additional information that is independent of multicompnemt seismic measurements. In fact, mineralogy is only one of the factors that determine the velocities of a rock. Porosity, microstructure, presence of secondary minerals, fluids type, fluid saturation, temperature, pressure, and even age of the rock also affects the wave velocities in rocks. Nevertheless, there have been attempts to infer lithology (mineralogy and fluid present) from velocity (Engelmark 2001). Table 2.2 shows and ranks the factors affecting seismic properties of sedimentary rocks.

Table 2.2: Factors affecting seismic properties of rocks (Wang, 2001)

Decreasing significance ↓

Rock Properties	**Fluid Properties**	**Environment**
Compaction	Viscosity	Frequency
Consolidation	Density	Stress History
History	Wettability	Depositional environment
Age	Fluid compositin	Temperature
Cementation	Phase	Reservoir process
Texture	Fluid type gas/oil gas/water ratio	Production history
Bulk Density	Saturation	Layer geometry
Clay content		Net reservoir pressure
Anisotropy		
Fractures		
Porosity		
Lithology		
Pore shape		

2.6 Relationship between porosity and velocity

Traditionally porosity has been measured in the laboratory on cores by measuring any two of the bulk volume (V_b), the matrix volume (V_m) or the pore volume (V_p). Measuring porosity directly in situ is not feasible however, the well established Time Averaged Equation (TAE) which correlates acoustic wave velocities (P and S wave) and porosity could be used to estimate porosity both in the laboratory and in-situ. Wyllie (1956) proposed the TAE (Equation 2.5) which is the relationship between the velocity of a fluid saturated porous rock (V_{pr}), velocity of the fluid (V_f), velocity of the mineral grain (V_m) and inter-granular porosity ϕ .

$$\frac{1}{V_{pr}} = \frac{1-\phi}{V_m} + \frac{\phi}{V_f} \tag{2.6}$$

Using time instead of velocities, and making porosity the subject, the TAE becomes:

$$\phi = \frac{\Delta t_{\log} - \Delta t_m}{\Delta t_f - \Delta t_m} \tag{2.7}$$

Where, Δt_{log} is the transit time through the fluid saturated rock, Δt_f is the transit time through the fluid and Δt_m is the transit time through the solid mineral grain. The TAE equation has been used successfully in sonic logs (Hearst et al., 2001; Dvorkin and Nur, 1998). Despite its wide acceptance, it should be noted that the equation is purely an empirical result based on the effective properties of rocks. It is applicable to fluid-saturated porous sedimentary rocks, that have no significant fracturing and whose pore fluid pressure is normal (Ransom, 1995). In addition, rocks like sandstone must be slightly cemented; carbonates must have inter-granular porosity and no vugs or fractures.

There are so many conditions that the TAE is less accurate for oil saturation than water saturation and it is also not applicable to gas saturation and material with shale.

Over the years there have been modifications in Wyllie's TAE taking into account compaction, porosity, differential pressure, fluid type, fluid saturation, clay content and so on. In an attempt to include clay content (C) and differential pressure (P_d) into the TAE, Eberhart-Phillips et al. (1989) found that for water-saturated sandstones:

$$V_p \text{ (km/s)} = 5.77 - 6.94\phi - 1.73\sqrt{C} + 0.446 (Pd - e^{-16.7\, Pd}) \quad (2.8)$$

$$V_s \text{ (km/s)} = 3.70 - 4.94\phi - 1.57\sqrt{C} + 0.361(Pd - e^{-16.7\, Pd}). \quad (2.9)$$

In these equations ϕ and C tend to decrease velocity, but P_d will increase velocity. This is due to the closing of cracks and pores. Rafavich et al. (1984) also found that at constant P_d, velocity for water-saturated carbonates also depends on bulk density ρ_b and quartz content Cq. Thus:

$$V = a_0 + a_1 \rho_b - a_2\phi - a_3 Cq \quad (2.10)$$

Different materials behave differently when subjected to seismic wave propagation and therefore these estimated values can only be described as inferred porosity. Trying to make a quantitative value out of these individual relationships leaves a big margin of error. Despite the disagreements, many writers have attempted to estimate porosity from P and S wave velocities. For example, several attempts have been made in estimating the amount of hydrate from seismic velocities and amplitudes. Most studies (Korenaga et al., 1997; Sholl and Hart, 1993; Wood et al., 1994) determined the desired saturation using a weighted mean of the Wyllie equation (Wyllie, 1958; Dillon et al., 1993) together with

Wood's equation (Wood, 1941). After intensive study on velocity and porosity, Khaksar (1999) recognized that both petrography information and rock properties including porosity, permeability and capillary pressure curves were necessary to interpret his experimental results. He concluded that there was no significant correlation between porosity, clay content and stress sensitivity of P and S wave velocities at high pressures for the studied samples and explained that this insignificant correlation is primarily related to the textural characteristic and the type of clay distribution within the studied samples. Moos et al. (1997) iterated that because these relationships are not based on physics, they often fail in the region within which they have not been calibrated, leading to the abandonment of certain logging technologies in some regions.

As shown above, Wyllie's TAE was obtained empirically for consolidated reservoir rocks and cannot be used for high-porosity unconsolidated sediments. In order to apply this equation to high-porosity marine sediments, calibration is required based on extensive core measurements or well-log data. It is likely that such equations can indeed link velocity to porosity and gas hydrate content if they have been derived from an extensive experimental database. However, such equations cannot be used for diagnosing sediments, i.e., inferring their internal structure from seismic. Figures 2.1 and 2.2 show the laboratory-measured effect and Gassmann-calculated effect of fluid displacement on compressional wave velocities. There is hardly any correlation between the theory and the laboratory measurement.

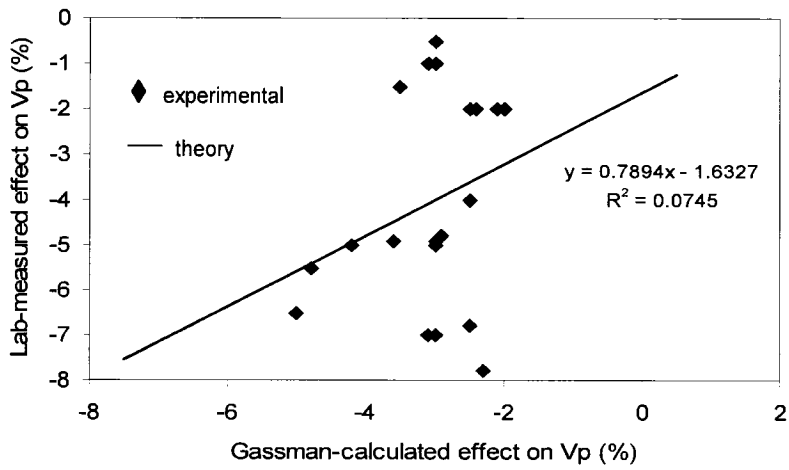

Figure 2.1: Gassmann-calculated and laboratory-measured effect of fluid displacement on compressional waves from a CO_2 flood (Data from Wang, 2001)

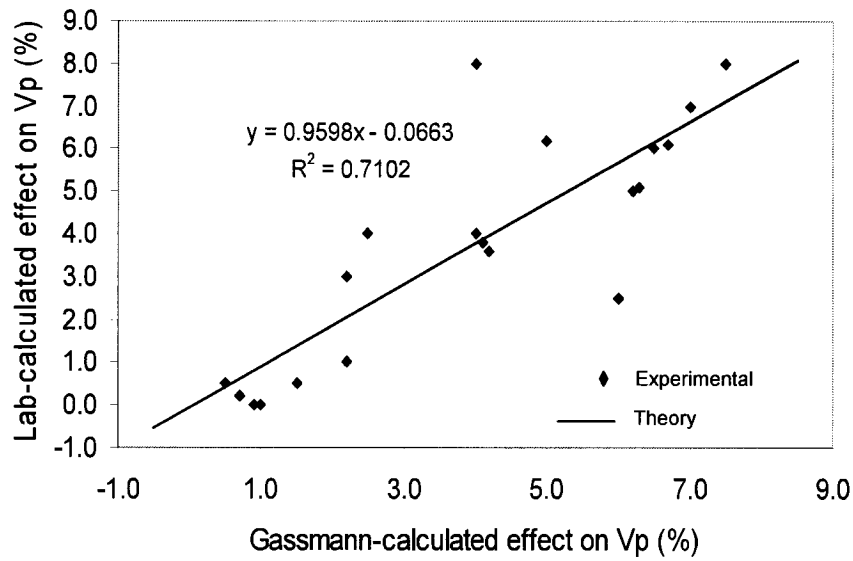

Figure 2.2: Gassmann-calculated and laboratory-measured effect of fluid displacement on compressional waves from H_2O flood (Data from Wang, 2001)

2.7 Estimation of elastic moduli and Poisson's ratio

Probably the most extensively used mechanical property that has been derived from wave velocity are the elastic modulus (Young's and Bulk Modulus, Lame constants and Poisson ratio). This may, in part, be due to the direct relationship between velocity and the modulus as presented in equation 2.2 and 2.3. It may also be due to the highly important application of the elastic moduli in a wide range of engineering fields. Traditionally, the elastic moduli have been determined through measuring the stress and the strain in the laboratory and taking the ratio between them. A quick and inexpensive way to estimate elastic moduli both in laboratory and in-situ is to use the acoustic velocity through the theory in equation 2.2 and 2.3 (Geyer and Myung, 1970; King, 1983).

Yearsley and Crowder (1990) used P wave technique in three-inch diameter boreholes to produce a full sonic log of velocity and amplitude information in the boreholes with the aim of calculating the engineering properties of a granite rock mass. The author recognized some inconsistencies in the application of the theory and criticized the negative nature of Poisson's ratio when V_p / V_s ratio was less than 1.42. Dodd et al. (2001) used ultrasonic P wave to study ceramic aluminum nitride to estimate the modulus of elasticity and related mechanical properties (shear stiffness, adiabatic Young modulus, and Poison ratio). They expressed their concern about the wide error margin and the inconsistencies in the literature of estimating these moduli values from P and S wave

velocities. The results presented by Dodd et al. (2001) were in agreement with the results of recent high pressure X-ray diffraction measurements and theoretical calculations. Table 2.3 shows the ultrasonic P and S wave velocity, adiabatic elastic stiffness, moduli and other properties of the ceramic at 295 K in comparison with data taken from other literature.

Table 2.3: Comparison of results of some mechanical and elastic properties derived from acoustic techniques for ceramic aluminum nitride (Dodd et al., 2001)

Description	Dodd et al. .(2001)	Gerlich et al. .(1986)	Resenburg et al. .(1991)	Subhash & Ravichandra (1998)
Density ρ (kgm^{-3})	3260±10	3270	3226	3250
Longitudinal wave velocity V_L (ms^{-1})	10700±10	10127	10720	10700
Shear wave velocity V_S (ms^{-1})	6307±10	6333	6370	6300
Longitudinal Stiffness C_l (Gpa)	373±2	3343	Not available	Not available
Shear Stiffness μ (Gpa)	130±1	130.8	127	129
Bulk Modulus B (Gpa)	200±2	159.9	201	203
Young Modulus E (Gpa)	320±3	308.3	314	320
Poisson Ratio σ	0.234±0.002	0.179	0.238	0.237

2.8 Estimation of permeability from velocity

Traditionally, permeability has been estimated based on Darcy's equation. However, many attempts have been made to estimate permeability from acoustic velocity (Durrast et al., 2002; Lu and McMechan, 2002). However special conditions occur when, say, an ionic solution comes into contact with clay or other rock samples resulting in deviations from Darcy's equation. Yamamoto et al. (1995) used P wave tomography to image permeability in limestone and detected that different velocity values were created in the

permeable layers but no difference in velocity in the impermeable layer. They concluded that the permeability values of the cavity filled limestone layer inferred from the theory was 200 D, whereas permeability measured from pumping test was 331 D, a difference of 30%.

Durrast et al. (2002) performed a laboratory experiment to study rock fabric element and petro-physical properties on several sandstone samples. They iterated that permeability values are generally higher in the plane of the nearly horizontal sedimentary layering. Using a geological-petrophysical model, Durrast et al. (2002) said that the complex symmetry of the V_p distributions could only be explained by the rock fabric element. Petrophysics (mineralogy, grain size, size distribution, shape, pores size, pore pressure...) plays a very important role in the estimation of porosity. There is neither any direct nor indirect generally accepted relationship between permeability and velocity in the literature. However, Pride et al., (2003) iterated that there is likelihood that seismic amplitudes do contain some type of permeability information and suggested an inversion strategy that could, in principle, extract such permeability information from full-waveform three-component data. They recommended that in the short term, further laboratory experiments at the scale of meters research be done controlled materials with known mesoscopic and macroscopic properties be done to test the inversion strategy. This is further addressed in the next section

2.9 Seismic wave attenuation and dispersion mechanism

When a seismic wave moves through a body of rock, the waveform amplitudes are reduced. The primary mechanisms of the amplitude reduction are spherical divergence, scattering, and intrinsic attenuation. Spherical divergence is independent of frequency and a correction is commonly applied to seismic data. This has been addressed in detail in the paper of diffraction loss in chapter three. Scattering and intrinsic attenuation can also result in waveform dispersion. Each mechanism can dominate under certain experimental conditions of frequency, saturation and strain amplitude. Under typical conditions in the earth's crust, in homogeneous rocks, attenuation and dispersion are dominated by viscous fluid/solid interactions. In heterogeneous rocks, scattering can cause significant dispersion and loss of energy for the primary waves. Attenuation and dispersion are physically related, one implying the other. For most mechanisms, attenuation varies with frequency. Frequencies having high attenuation also have the greatest dispersion. Scattering results from multiples that lag the primary seismic energy and tend to cause some cancellation of primary energy. This scattering loss is frequency dependent and is often difficult to separate from intrinsic attenuation. However, as iterated by Winkler and Murphy (1995), the intrinsic attenuation appears to more dominant than scattering attenuation.

Intrinsic attenuation is energy loss due to friction and occurs by several mechanisms. Grain to grain friction in sedimentary rocks causes some attenuation. However the major

source of intrinsic attenuation in porous rocks such as sand, shale or carbonate occurs when motion of the rock and the fluid in the pores becomes uncoupled. The rock becomes anelastic as energy is lost due to fluid friction. The fluid motion is caused by pressure equilibration as the seismic wave passes through the rock (Pride et al., 2003). Knowledge of attenuation can be very useful in seismic data processing, as its removal increases resolution. But perhaps its greatest potential lies as a direct hydrocarbon indicator. Attenuation depends on fluid mobility (Batzle et al., 2003, Kumar et al., 2003) which in tern depends on the viscosity and bulk modulus of the pore fluid, and the permeability of the rock. If the pore space is completely filled with fluid, the fluid has less mobility than if there is partial gas saturation and it has been shown that attenuation is highest in a partially fluid saturated rock (Kumar et al 2003, Winkler and Nur (1982). Pride et al., (2003) give a good overview of attenuation mechanisms and discuss the possibility of extracting information about the permeability of the rock. Pride and Berryman (2003) give a more detailed theoretical description of attenuation mechanisms.

The amplitude loss due to attenuation and dispersion can be measured using various techniques. The simplest relation of the amplitude is represented by the following relation;

$$A = A_0 \exp(-\alpha x) \tag{2.11}$$

Where, α is the attenuation coefficient. The attenuation coefficient is intend related to the quality factor by Tokzos and Johnston, (1981) as:

$$\frac{1}{Q} = \frac{\alpha v}{\pi f} \tag{2.12}$$

Where v is the velocity of a wave and f is the frequency. Thw Q factor has components of scattering loss and intrinsic attenuation.

Measurements of the loss Q are often made at a well using Vertical Seismic Profiles (VSP). Receivers record the seismic wavelet at many depths in the well. Q can be derived for the interval between two depths by using the spectral ratio of the amplitude spectra at the two depths. Quan and Harris (1997) used the decrease in average frequency as a seismic wave is attenuated to calculate Q. Much of our knowledge of attenuation comes from laboratory measurements (Kumar et al 2003). Attempts to extract attenuation from seismic data recorded at the surface have met with little success. A major stumbling block is that the amplitude spectrum of the seismic record contains the imprint of the amplitude spectrum of the earth's reflectivity as well as the amplitude spectrum of the seismic wavelet. Separation of the two spectra is difficult. Dilay et al (1995) observed changes in the amplitude spectra below a sand that was undergoing steam flood for enhanced oil recovery. Mitchell et al (1996) fit an exponential function to the amplitude spectra of several short time windows of the seismic data and compared the rate of decay of the spectra to measure attenuation in a gas filled sand. Dasgupta and Clark (1998) compared the rate of amplitude decay at 2 levels on pre-stack gathers to estimate Q. Hedlin et al (2001) observed an increase in attenuation (an anomalous decrease in average frequency) below an oil sand undergoing steam flood. The ability to extract accurate values of attenuation or changes in attenuation using relatively short windows of seismic data could be very helpful in exploration for gas reservoirs.

The following are detailed sections dealing with intrinsic, attenuation, scattering attenuation and attenuation due to macroscopic fluid-flow.

2.9.1 Friction

For many years, frictional sliding between grains was considered the dominant mechanism of attenuation in rocks. In addition to its intuitive simplicity, friction predicts attenuation independent of frequency (constant Q) and no velocity dispersion. This was consistent with some early experimental data on dry rocks, and with data on saturated rocks over limited frequency bands. It was also consistent with the cusped nature of stress-strain loops measured in low-frequency experiments, implying a non-linear mechanism. More recent work, however, has shown that attenuation can have significant frequency dependence, with corresponding velocity dispersion (Avseth, 2005: Pride et al., 2003; Hearst et al., 2001; Mavko et al., 1998; Sato and Fehler 1998; Ransom, 1995). The frictional mechanism is now associated with amplitude dependent velocity and attenuation that is only important at large strain amplitudes (Avseth, 2005; Mavko et al., 1998). At atmospheric pressures, strains > 10^{-6} are generally required to observe amplitude dependence. At larger effective stresses, even larger strains are needed. The frictional mechanism probably is most important in the near field of seismic sources such as explosions and earthquakes.

2.9.2 Scattering

Wave scattering occurs whenever velocity or density heterogeneities occur on the same length scale as the wavelength (Sato and Fehler, 1998). Although the scattered energy is not absorbed by the rock as heat, it does result in energy loss to the primary pulse. Pride et al., (2003) iterated that there are certain situations where intrinsic attenuation is simply not operative so that all attenuation is due to scattering. Scattering also reduces the velocity of the primary pulse, causing velocity to decrease as frequency increases (Sato and Fehler, 1998). Most scattering models are designed for systems of weak scatterers, and so have not been successful in quantitatively predicting scattering in rocks. Sayers (1981) presented a model predicting attenuation (α) increasing with the fourth power of frequency and velocity decreasing with the second power of frequency. Winkler (1983) also presented experimental results showing scattering effects in sandstones at ultrasonic frequencies, where the scatterers are the grains and pores of the rock. He concluded that in dry rock, attenuation is well-fit by a fourth-power frequency dependence, and velocity decreases with increasing frequency, both in agreement with theory. Winkler (1983) said that in water-saturated rock, these effects are not so clearly observed because of the addition of fluid-flow effects. This is discussed below in section 2.9.3. However, at high effective stresses, fluid-flow effects are minimized and the data approach the trends expected for a scattering mechanism.

2.9.3 Macroscopic Flow (Biot)

Biot (1956a, 1956b) developed a theory of wave propagation in fluid saturated porous media that focuses on macroscopic fluid-flow. Various applications of Biot theory to porous media have been discussed (Avseth et al., 2005; Mavko, et al, 1998 and Ransom, 1995). Biot theory shows that elastic waves create relative motion between the fluid and the solid frame due to inertial effects (Biot, 1956a; 1956b). As the matrix is accelerated, the fluid lags behind, resulting in viscous dissipation of wave energy. At low frequencies, the viscous skin depth is much larger than the pore size and fluid and solid are virtually locked together, moving in phase. This indicates minimum velocity and little attenuation. At high frequencies, the viscous skin depth is very small and the fluid and solid are essentially decoupled. Velocity is a maximum, and attenuation is low. For water-saturated rocks, the critical frequency in the Biot theory where attenuation and dispersion are maximum, is often on the order of 100 kHz. Increasing viscosity pushes the critical frequency even higher. Therefore seismic waves and sonic logging are almost always in the low-frequency range of Biot theory. The low-frequency limit of Biot theory gives Gassmann's equations. An interesting prediction of Biot theory is the existence of a second compressional wave dominated by the properties of the pore fluid (often called the Biot slow wave). At low frequencies this wave is diffusive and at high frequencies it is propagatory. The propagating wave is very difficult to observe in rocks, though it has been seen in synthetic materials.

2.9.4 Local-Flow

The Biot theory as discussed above, is concerned with macroscopic fluid-flow controlled by the permeability of the rock. Another fluid-flow absorption/dispersion mechanism which often called 'local-flow' is based upon microscopic fluid motion which is not coherent over macroscopic length scales. The pore space of a rock is generally very heterogeneous, some regions being very compliant while others are very stiff. This can result in fluid being squeezed out of grain contacts into nearby pores, or squeezed between adjacent cracks having different orientations with respect to a passing stress wave. This model has been addressed theoretically by many authors (e.g. Mavko and Nur 1979: Murphy et al., 1986). While most of these models can be fit to experimental data, none of them yet have the predictive power of the Biot theory. This is because they are all highly dependent on details of the microstructure that cannot yet be adequately quantified. Nevertheless, many experimental results have been interpreted in terms of the local-flow mechanism (Winkler, 1985: Winkler, 1986: Winkler et al., 1989). These experiments have addressed effects of saturation, stress, temperature, viscosity and frequency. Winkler and Nur (1982) showed that shear wave attenuation increases monotonically with saturation, while compressional wave attenuation is greater in partially saturated rock than in fully saturated rock. More detailed data are shown by Murphy (1982). These effects, along with the overall magnitude of attenuation, are consistent with theoretical predictions. At low pressures, the attenuation is approximately an order of magnitude greater than that predicted by Biot theory. The local flow

mechanism predicts that absorption and dispersion will scale with the product of frequency and viscosity (cm). By varying viscosity as well as frequency, experimentalists have been able to effectively broaden the frequency range available to any particular experimental technique.

Many experimental results now exist showing attenuation varying with 077, with associated velocity dispersion (Dunn, 1986: Jones and Nur, 1983). Some of these observations may have been affected by fluid-flow to the boundaries of the sample, and therefore are not truly representative of a local-flow mechanism. However, some measurements are not affected by boundary flow. When pore fluid viscosity varies strongly with temperature, velocities can be significantly affected. At low temperature the viscosity is high and fluid cannot flow easily, so the measurement is on the high-frequency, high-velocity, unrelaxed side of the local-flow mechanism. As temperature increases, viscosity decreases, fluid flows more easily and velocity decreases as we move to the relaxed side of the absorption/dispersion mechanism. This effect is especially strong when the rock is saturated with viscous hydrocarbons (Wang and Nur, 1990). The concept of relaxed verses unrelaxed velocities was explored in some detail by Murphy (1985). Murphy showed that seismic measurements made near 1 kHz could be well described using Gassmann's equations, but ultrasonic data were better described using a model with unrelaxed pore fluid (O'Connell and Budianski, 1977). Winkler used ultrasonic velocity measurements on dry rock as input to Gassmann's equations to calculate the low-frequency velocity limit for saturated rock. He then noted that ultra

sonic velocity measurements on saturated rock always exceeded this low-frequency limit in a manner consistent with dispersion caused by the local-flow mechanism. This showed that ultrasonic lab measurements were being affected by mechanisms operating at lower frequencies, and so were not entirely representative of velocities at seismic or sonic frequencies.

The above literature review has provided opportunity to examine the dispersion of elastic wave velocity over a wide frequency range. This would involve answering the question of what factors contribute to velocity differences in imaging across the various frequency bands. This would lead to developing a practical scaling models and methodology that take into account intrinsic energy dissipation.

2.10 References

Avseth, P., Mukerji, T. and Mavko, G., (2005), Quantitative Seismic Interpretation : Applying Rock Physics Tools to Reduce Interpretation Risk, Cambridge University Press, pages 360p

Batzle, M., Han, D. and Hofmann, R., (2003), Macroflow and velocity dispersion, 73rd Ann. Internat. Mtg.: Soc. of Expl. Geophys., 1691-1694.

Best, A.I., Sothcott, J. and McCann, C., (1991), Seismic attenuation and permeability in clay rich sandstone European Assoc. of Explor. geophy, 53 rd. meeting and techn. Exhib., Italy, 1: 252-253.

Biot, M. A., (1956a), Theory of propagation of elastic wave in a fluid saturated porous solid. I Low Frequency range. J. Acoust.Soc. Am Vol. 28, p168

Biot, M. A., (1956b), Theory of propagation of elastic wave in a fluid saturated porous solid. II High Frequency range. J. Acoust.Soc. Am Vol. 28, p179

Birch, F., (1961), The velocity of Compressional Waves in Rocks to 10 kilobars, Part 2. Journal of Geophysical Research, 66: 2199-2224.

Christensen, N.I. and Salisbury, M.H., (1975), Structure and constitution of the lower oceanic crust, Rev. Geophys. Space Phys., 13:57-86.

Christoffel, E. W., (1877), Annali di matematica pura, ed. Applicata Ser II 8: 193.

Dasgupta, R. and Clark, R. A., (1998), Estimation of Q from surface seismic reflection data: Geophysics, Soc. of Expl. Geophys., 63, 2120-2128.

Dilay, A. and Eastwood, J., (1995), Spectral analysis applied to seismic monitoring of thermal recovery: The Leading Edge, Vol. 14, no. 11, 1117-1122.

Dillon, W. P., Lee, M. W., Fehlhaber, K. and Coleman, D. F., (1993), Gas hydrates on the Atlantic continental margin of the United States - controls on concentration: The Future of Energy Gases, U.S. Geo. Surv., Prof. Paper 1570.

Dodd, S. P., Saunders G. A., Cankurtaran M. and James B., (2001), Ultrasonic study of the elastic and nonlinear acoustic properties of ceramic aluminum nitride, J. of Mater. Sci., 36: 723 - 729.

Dunn, K.J., (1986), (1986), Acoustic attenuation in fluid-saturated porous cylinders at low frequencies, J. Acoust. So of. Am., 79, 1709.

Durrast, H., Rasolofosaon, P. N. J. and Siegesmund S., (2002), P-wave velocity and permeability distribution of sandstones from a fractured tight gas reservoir, Geophysics, 67: 341-253.

Dvorkin, J. and Nur A., (1998), Time-average equation revisited, Geophysics, 63: 1-5.

Eberhart-Phillips, D., Han, D.H. and Zoback, M. D. (1989) Empirical relationships among seismic velocity, effective pressure, porosity, and clay content in sandstone, Geophysics, 54: 82-89.

Engelmark, F., (2001), Using 4-C to characterize lithologies and fluids in clastic reservoirs, The Leading Edge, 9, 20: 1053-1061.

Gerlich, D., Dole S.L. and Slack G. A., (1986), Elastic Properties of Aluminum Nitride, Journal of Physics and Chemistry of Solids 47: 437- 450.

Geyer, R.L, and Myung, J. I., (1970), The 3-D velocity log; a tool for in-situ determination of the elastic moduli of rocks, Twelfth Annual Symp. on Rock Mech, Univer. of Missouri-Rolla, USA, 36-40.

Hearst, J. R., Nelson, P. H. and Paillet, F., (2001), Well Logging for Physical Properties: A Handbook for Geophysicists, Geologgists and Engineers, Second Edition, John Wiley & Sons Ltd, UK, p483 (pages 256 to 285)

Hedlin, K., Mewhort, L. and Margrave, G., 2001, Delineation of steam flood using seismic attenuation, 71st Ann. Internat. Mtg: Soc. of Expl. Geophys., 1572-1575.

Jones, T. and Nur, A., (1983), Velocity and attenuation in sandstone at elevated temperatures and pressures, Geophys. Res. Lett., 10,140.

Khaksar, A., (1999), A petrophysical study of the influence of effective stress and fluid saturation on acoustic velocities in sandstone, PhD thesis, University of Adelaide, Australia.

King, M. S., (1983), Static and dynamic elastic properties of rocks from the Canadian shield, Int. J. of Rock Mech. Min. Sci. & Geomech. Abstr. 20: 237-241.

Korenaga, J., Holbrook, W. S., Singh, S. C. and Minshull, T. A., (1997), Natural gas hydrates on the southeast U.S. margin: Constraints from full-waveform and travel time inversions of wide-angle seismic data, J. Geophys. Res., 102: 15345-15365.

Kumar, G., Batzle, M. and Hofmann, R., (2003), Effect of fluids on attenuation of elastic waves, 73rd Ann. Internat. Mtg.: Soc. of Expl. Geophys., 1592-1595.

Küntz, M., Lavallée, P. and Mareschal J. C., (1997), Determination of elastic properties of very heterogeneous media with cellular automata, J. Geophys. Res. 102: 7647-7659.

Levy, M., Bass H. E. and Stern, R., (2001), Modern technique for the measurement of mechanical properties Vol. 39, Experimental methods in physical sciences, ed., Acad. Press, CA, USA.

Lu, S. and McMechan, G.A., (2002), Estimation of gas hydrate and free gas saturation, concentration, and distribution from seismic data, J. Geopysics, 67: 582-593.

Mavko, G., Mukerji, T. and Dvorkin, J., (1998), The rock Physics Handbook-Tools for Seismic Analysis in porous media, Cambridge University Press, New York, 329p.

Mavko, G.M. and Nur, A., (1997), Wave attenuation in partially saturated rocks, Geophysics, Vol. 44, p161.

Mitchell, J. T., Derzhi, N., Lichman, E. and Lanning, E. N., 1996, Energy absorption analysis: A case study, 66th Ann. Internat. Mtg: Soc. of Expl. Geophys., 1785-1788.

Moos, D., Dvorkin J. and Hooks, A. J., (1997), Application of theoretically derived rock physics relationships for clastic rocks to log data from the Wilmington Field, California, Geophysics. Res. Lett. 24 : 329-340.

Murphy, W.F., (1982), Water saturation on attenuation in Massilon sandstone and Vycor porous glass, J. Acoust. Sot. Am., 71, 1458.

Murphy, W., F., (1985), Sonic and ultrasonic velocities: Theory versus experiment, Geophys. Res. Lett., 12, 85.

Murphy, W.F., Winkler, K. W. and Kleinberg, R. L., (1986), Acoustic relaxation in sedimentary rocks: Dependence on grain contacts and fluid saturation, Geophysics, 51, 757.

Nur, A., (1991), Critical Porosity, elastic bound and seismic velocity in Rocks, European Assoc. of Explo. Geophy., 53 rd. meeting and technical exhibition, Italy, 248-249.

O'Connell R.J and Budianski, B., (1977), Viscoelastic properties of fluid-saturated cracked solids, J. Geophys. Res.. 82,5719.

Peselnick, L and Outerbridge, W. F. (1961) Internal Friction in shear and shear modulus of Solenhofen Limestone over Frequency range of 10^7 cycles per second, J. Geoph Res., 66, 581.

Pride, S. R and Berryman, J. G., (2003), Linear dynamics of double-porosity dual-permeability materials I. Governing equations and acoustic attenuation, Physical Review, E, 68, 036603.

Pride, S. R and Berryman, J. G., (2003), Linear dynamics of double-porosity dual-permeability materials II. Fluid transport equations, Physical Review, E, 68, 036604.

Pride, S. R., Harris, J., Johnson, D. L., Mateeva, A., Nihei, K., Nowack, R. L., Rector, J., Spetzler, H., Wu, R., Yamomoto, T., Berryman, J. and Fehler, M., (2003), Permeability dependence of seismic amplitudes: The Leading Edge, Vol. 22, no. 6, 518-525.

Quan, Y. and Harris, J. M., 1997, Seismic attenuation tomography using the frequency shift method: Geophysics, Soc. of Expl. Geophys., Vol. 62, p 895-905.

Ransom, R. C., (1995), Practical Formation Evaluation, John Wiley & Sons, Inc, 490 pages.

Rafavich, F., Kendall, C. H. ST. C. and Todd, T. P., (1984), The relationship between acoutic properties and the petrophisical character of carbonate rocks, J. Geophysics, 49 :1922-1636.

Rosenburg, Z., Brar, N. S. and Bless, S.J., (1991), Dynamic high-pressure properties of AlN ceramic as determined by flyer plate impact, J. Applied Physics, 1. 70 :167-171.

Sayers, C. M., (1981) Ultrasonic velocity dispersion in porous materials, J. Phys. D Vol. 14, P 413

Sato, H. and Fehler M., (1998), Seismic Wave Propagation and Scattering in the Heterogeneous Earth, Springer-Verlag and American Institute of Physics Press, 308p

Sholl, D. W. and Hart, P. E., (1993), Velocity and amplitude structure on seismic-reflection profiles- possible massive gas-hydrate deposits and underlying gas accumulations in the Bering Sea: The Future of Energy Gases, U.S. Geo. Surv. Prof. paper 1570

Subhash, G. and Ravichandran, G., (1998), Mechanical Behavior of Hot Pressed Aluminum Nitride Under Uniaxial Compression, Journal of Materials Science 33:1933-1939.

Telford, W.M., Geldart L. P. and Sheriff R. E., (1990), Applied Geophysics, Second edition, Cambridge University Press, Cambridge, London .

Tatham R. H., and McCormack M. D., (1991), Multicomponent Seismology in Petroleum Exploration, Edited by E. B. Neitzel and D. F. Winterstein, Society of Exploration Geophysicists, Tulsa, 248 p.

Toksoz, M. N and Jonston, D. H. (1981), Seismic wave attenuation, S.E.G., Geophysics Reprint Series, No. 2,

Wang, Z., (2001), Fundamental of seismic rock physics, Geophysics, 66: 398-412.

Winkler, K., and Nur, A., 1982, Seismic attenuation: effects of pore fluids and frictional sliding: Geophysics, Vol. 47, no. 1, p1-15.

Winkler K. W. (1983), Frequency dependent ultrasonic properties of high porosity sandstone, J Geophs. Res. Vol 88, p 9493

Wang, Z. and Nur, A., (1990), Wave velocities in hydrocarbon-saturated rocks: Experimental results, Geophysics, 55,723, 1990. .

Winkler, K.W. and Nur, A. (1982), Seismic attenuation: Effects of pore fluids and frictional sliding, Geophysics, 47, 1.

Winkler, K.W., (1985), Dispersion analysis of velocity and attenuation in Berea sandstone, J. Geophys. Res., 90, 183,

Winkler, K.W., (1986), Estimates of velocity dispersion between seismic and ultrasonic frequencies, Geophysics, 51,6793.

Winkler, K.W., Liu, H. and D. L. Johnson, D. L., (1989), Permeability and borehole Stoneley waves: Comparison between experiment and theory, Geophysics, 54, 66.

Winkler K. W. and Murphy W. F., (1995), Rock Physics and Phase Relations: A Handbook of Physical Constants, AGLJ Reference Shelf 3, American Geophysical Union.

Wood, A. B., (1941), A text book of sound, MacMillan publ., New York, USA..

Wood, W. T., Stoffa, P. L. and Shipley, T. H., (1994), Quantitative detection of methane hydrate through high-resolution seismic velocity analysis, J. Geophys. Res., 99: 9681-9695.

Wyllie, M. R. J., Gregory, A. R. and Gardner, G. H. F., (1958), An experimental investigation of factors affecting elastic wave velocities in porous media, Geophysics, 23: 459-493.

Yearsley, E. N. and Crowder, R. E., (1990), Acoustic spectrum analyses of borehole sonic logs for engineering properties and fracture characterization, Proc. of the 1990 Annual Symp. Eng. Geol. and Geotech. Eng., Idaho State University, Idaho, USA, 25.1 - 25.14.

PART II

LABORATORY INVESTIGATION

II: Overview

Part 2 is made up of 4 chapters (Chapter 3 to Chapter 6), and contains four technical publications. The papers are in various stages of publication in reputable journals and conferences. All the papers are based on laboratory investigations. Specifically, the papers investigate the effect of injection and depletion cycles on ultrasonic velocity and quality factor in glass sandstone. It investigates and characterizes volumetric failure in weak sandstone reservoirs using P-wave quality factor, velocity and acoustic emissions. It also highlights non destructive techniques to determine the effective stress coefficient of porous sandstone and characterizes the permeability and acoustic properties of an outburst-prone sandstone.

Chapter 3: The effect of injection and depletion cycles on ultrasonic velocity and quality factor in glass sandstone

This paper was submitted to the journal of Geophysics and is currently under review. It has passed through first review, been corrected and sent for second review. The main author is Mr. Paul K. Frempong, co-authored by Mr. J. Adam Donald and Dr. Stephen D. Butt. The figure numbers and reference formats have been altered to match the formatting guidelines set out by Dalhousie University compared with the submitted manuscript to Geophysics. Sample names in the figure and table captions have been changed to be consistent with the rest of the thesis content.

3.1 Abstract

The fluctuating stresses in rocks caused by passing of seismic waves induce pore pressure gradient that affects velocity and attenuation characteristics in the rocks. Compressional ultrasonic wave velocities (V_P) and quality factors (Q_P) in a quartz sandstone were measured under varying degrees of pore pressure, and uniaxial strain conditions during a laboratory simulated injection and depletion process. The main objective was to study the effect of hysteresis as well as the loading and unloading history on the acoustic characteristics and some geomechanical behavior of the reservoirs. V_P and Q_P were confirmed to increase with effective stress. It was also found that, V_P and Q_P increase

with increasing pore pressure, at constant effective stress. The effective stress coefficient, n, was found to be less than 1 and dependent on the pore pressure, confining stress and load. At low pore pressures, n approached 1 and reduced non-linearly at high pore pressures. V_P variation with pore pressure was small at high pore pressures. This was also true for Q_P. Whilst V_P variation with pore pressure follows a three parameter exponential rise to a maximum limit, that of Q_P has no clear limit and follows a two parameter exponential growth. The pore pressure depletion and injection cycles caused pores opening and closure, viscoelastic relaxation, creep and strain weakening in the rock which resulted in an increased effect on the V_P and Q_P with increasing cyclic loading. Q_P was found to be more sensitive in responding to the loading cycle and changes in pore pressures than V_P. Thus Q_P may be a better indicator for time-lapse reservoir monitoring than V_P. However there was lack of stability and the repeatability of Q_P at low effective stress.

3.2 Introduction

Much of the variation of seismic velocities and attenuation characteristics in reservoir rocks is plausibly attributed to lithology, porosity, permeability, pore fluids and effective stress (Berryman, 1992; Stoll, 1989; Prasad, 1998). Some researchers have investigated the effect of hysteresis as well as the loading and unloading history and have shown that, the fluctuating stresses in rocks caused by the passing of seismic wave induces a pore pressure gradient that affect velocity and attenuation characteristics in rocks (Dvorkin and Nur, 1993; Dvorkin et al., 1994; Dvorkin et al., 1995). This pressure gradient,

according to Dvorkin et al., (1994), impacts on the viscoelstic behaviour of the rock. Other writers have also shown that high-pressure viscoelastic relaxation, creep in the rock fabrics, closure of micro cracks and pores by the loading and unloading history affect compressional waves velocity (V_P) and attenuation quality factor (Q_P) in reservoir rocks (Doverkin and Nur, 1993; Williams and Ravji, 1999; Sabinin et al., 2003). The viscoelastic relaxation and the strain weakening are brought about by a number of mechanisms including passing of seismic waves (Dvorkin et al., 1995), the varying loading regime, mainly changes in the pore pressure and the confining stress. For example, in a cyclic loading process, unequal rate of loading and unloading, and time and history of loading and unloading may all affect the acoustic behavior of rocks. Whilst the effect of cyclic loading on acoustic properties have not been studied extensively, the effects of pore pressure and confining stress on the ultrasonic velocities in rocks have been studied in detail (Nur and Simmons, 1969; Nur and Byrelee, 1971; Christensen and Wang, 1985; Green and Wang, 1986; Khaksar et al., 1999). The different influence of the pore pressure and confining stress on acoustic velocities and attenuations led to the concept of effective stress. Christensen and Wang (1985) define effective stress as:

$$P_e = P_c - nP_p \tag{3.1}$$

Where P_e is the effective stress, P_c is the confining stress, P_P is the pore pressure and n is the effective stress coefficient or coefficient of internal deformation. The effective stress coefficient n, is unknown and often assumed to be close to 1. It could however be determined empirically or derived (Todd and Simmons, 1972) using Biot's theory (Biot, 1956a; Biot, 1956b). For convenience and possibly because of the difficulty in estimating

n, it is normally assumed to be equal to 1. In this case, effective stress is then equal to the differential stress (i.e., the arithmetic difference between the pore pressure and the confining stress ($P_d = P_c - P_p$). Some researchers (Nur and Byrelee, 1971; Berryman, 1992) argue that, although the effective stress relationship is valid for n = 1 in some rocks, different rock types could exhibit different effective stress coefficients and in some cases, n must be very small. Also n is different for different properties of the rock. Experiments conducted by Prasad and Manghnani (1997) show that the n value might be as low as 0.6, especially under very low effective stress conditions. In this case the interpretation of pore pressure-velocity curves in reservoirs can be in error. Other studies have also related V_P and Q_P to the effective stress, fluid permeability and saturation (Berryman, 1992; Stoll, 1989). Although the effects of pore pressure and confining stress on V_P and Q_P have been studied extensively on different rock types, research including that of Dvorkin and Nur (1993), Williams and Ravji (1999) and Sabinin et al. (2003), have been done on the effect of pore pressure cyclic loading of injection and depletion on V_P and Q_P. The cyclic loading by Plona and Cook (1995) investigates the effects of the compressive stress cycles on static and dynamic moduli. It is believed that injection would result in the opening of pores and microcracks (Dvorkin and Nur, 1993), originally developed by the sudden release of pressure on the rock when it was removed from the field in its in-situ state. On the other hand depletion would result in the closure of the same pores and microcracks. As pointed out by Dvorkin and Nur (1993), this cyclic process would induce viscoelastic relaxation and strain weakening in the rocks. Thus, the un-relaxed state of the rock would cause high velocity and low attenuation whilst the relaxed state

would cause low velocity and high attenuation as in the unified Biot squirt flow (BISQ) model introduced by Dvorkin and Nur (1993) and Dvorkin et al. (1994). This paper therefore assesses the combined effect of pore pressure, confining pressure, axial stress, and viscoelastic relaxation phenomenon, on V_P and Q_P during cyclic loading of injection and depletion. The purpose of this study is to (1) study the behavior of V_P and Q_P in the quartz sandstone under simulated cyclic injection and depletion of pore fluid, (2) determine the effective stress coefficient n, for the quartz sandstone, (3) determine what effect the increasing pore pressure, at constant effective stress, may have on the behavior of V_P and Q_P, (4) confirm the increasing velocity and attenuation quality factor with increasing effective stress and (5) determine both the sensitivity and stability of V_P and Q_P in the simulated injection and depletion cycles. The results would also indicate, which of the two acoustic properties (V_p and Q_p) is more sensitive to changes in depletion and injection and such information would help increase the reliability of reservoir property predictions from seismic measurements (Landro and Kvam, 2002).

In this investigation, a suite of ultrasonic laboratory experiments were conducted on quartz sandstone. The main experiment involves simulating an injection and depletion process under uniaxial strain conditions. This was done to simulate petroleum production far from the well bore where lateral displacement is considered negligible (Goulty, 2003). The effective stress was increased and decreased only by varying the pore pressure, while maintaining constant axial stress and confining stress at 60MPa (See pressure levels in Figure 3). Initially, the radial stress, axial stress and pore pressure were simultaneously increased to an in-situ condition of 60MPa in one hour. While maintaining the axial stress

at the in-situ conditions, the pore pressure was gradually dropped and then increased in a cyclic manner creating simulated reservoir injection and depletion process. The second experiment follows the same procedure as above but the increase in the effective stress is achieved by changes in the confining stress at constant pore pressure. This information was needed in the calculation of n using the formula by Todd and Simmons (1972). During the depletion and injection experiments ultrasonic signals were transmitted through the simulated reservoir using pulse echo techniques (Birch, 1960; Jonhson,1970) and the acoustic data collected was processed for velocity and quality factor using spectral ratio techniques (Toksoz et al., 1979) over a frequency range of 600–1000 KHz. The V_P, Q_P and the change in strain during the cyclic process were related to the pore pressure, confining pressure and the effective stress.

3.3. Test samples, laboratory equipment and setup

3.3.1 The sample characteristics

The quartz sandstone came from upper member of the Horton Bluff formation found in the Minas and Cumberland Basin of Nova Scotia, Canada. This sandstone is a reservoir rock that contains mainly natural gas under high pressure. The easily distinguishable unit is characterized by thick quartz-rich sandstone, which at some outcrop localities is pure enough to be used to manufacture glass (Ryan, 1998). Approximately 100 km to the north-east in the province of New Brunswick, this unit exists at a depth of approximately 2500 m where it is known for its high accumulation of natural gas (over-pressured gas

reservoir (Ryan, 1998)). The outcrop rock sample was originally under pressure from overburden stresses when it was under in-situ conditions. This pressure was released after uplift and thus it was necessary to bring the sample back to in-situ conditions again before starting the depletion and injection tests. The entire formation is dominated by 90% or more quartzarenites ranging from quartz pebble conglomerates to fine grained quartz sandstone (Ryan, 1998). Minor kaolinite, lithic fragment, traces of pyrites and some few ubiquitous plant detritus are the only component of the rock other than quartz. As stated above the quartz sandstone was very consistent and homogeneous and the drilling was done parallel to the bedding plane, the direction of maximum homogeneity. The microstructures of the quartz sandstone specimens were examined on thin section with particular attention to grain size distributions and the nature of the grain-scale distribution of any quenched melt quartz (Figure 3.1) It was found to contain fine grained rounded shapes of quartz with an average grain size of about 160 microns and very consistent trace of pyrite and minor kaolinite. It was prepared into cores of dimensions 108mm long by 54mm in diameter. The surfaces were ground smooth with the surface perpendicular to the core axis according to the American Standard of Testing Materials (ASTM, 2003). The samples have Uniaxial Compressive Strength (UCS) of approximately 100MPa (Table 1) and porosity of 15%, with permeability of 3.9mD. The initial benchtop measurements of the water-saturated properties of the sandstone at 2MPa initial pressure are shown in Table 3.1.

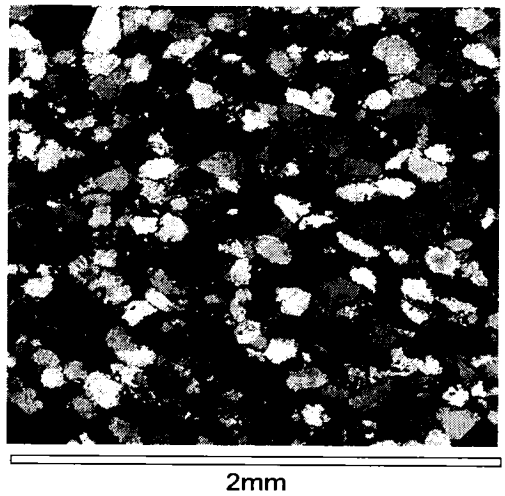

Figure 3.1: Thin section of quartz sandstone under cross polarized light (XPL)

Table 3.1 Geomechanical, petrophysical and ultrasonic properties of the glass sandstone

	GEOMECHANICAL PROPERTIES (SATURATED STATE)				
UCS	Static Modulus	Poisson Ratio	Shear Modulus	Bulk Modulus	Density
UCS (MPa)	E static (GPa)	v static	G static (GPa)	K static (GPa)	(g/cm3)
100	5.4	0.3	2.08	4.5	2.26
	SATURATED BENCH TOP ULTRASONIC PROPERTIES AT 1MHz FREQUENCY				
P wave velocity	S wave velocity	Dynamic Modulus	Poisson Ratio	Shear Modulus	Bulk Modulus
Vp(m/s)	Vs(m/s)	E dynamic (GPa)	v dynamic	G dynamic (GPa)	K dynamic (GPa)
3450	2650	18.5	0.049	8.82	6.84
	PETROPHYSICAL PROPERTIES				
Permeability	Porosity				
k (md)	(%)				
3.9	15				

3.3.2 Laboratory experiment and setup

Two sets of instruments, coupled together physically but functioning independently were used. These sets are (a) the pressure chamber which is basically a specialized tri-axial testing system that applies the axial, radial and pore pressure to the sample, and (b) the acoustic system that measures the acoustic properties of the sample. These are the arrival

times used to calculate the V_P and the attenuated signal used to calculate Q_P. Figure 3.2a is the schematic setup of the triaxial instrument, which is the same as used by Donald et al., (2004).

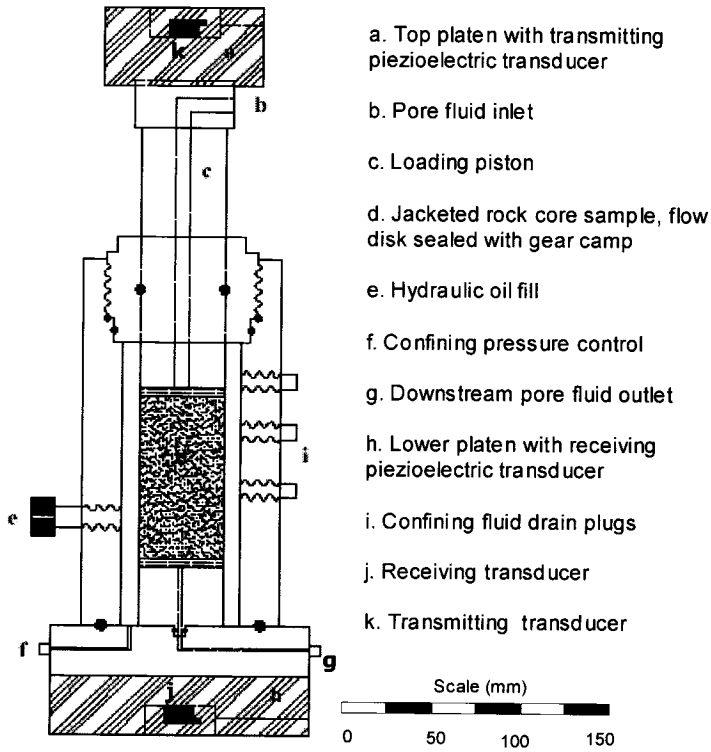

Figure 3.2a: Diagram of a triaxial equipment set up

The GDS Virtual Infinite Stiffness (VIS) Axial Loading System used in the experiment is a loading frame/compression machine with built in feedback control and continuous displays of axial load and platen displacement, with IEEE computer interface. These are microprocessor controlled with built-in feedback of axial load and platen displacement with Virtual Infinite Stiffness (VIS) that provides automatic correction for system compliance stored in ROM. It is then calibrated by computer to provide precise data on the load-deformation relationship of the entire load application and load measuring

system. These measurements are made with the adjustable upper cross beam in the maximum and minimum positions. The adjustable upper cross beam are built in mechanisms that can not be shown on our diagram in Figure 3.2a. The external component drawn to scale is shown in the Figure 3.2a. The only modification made in the equipment was the incorporation of the ultrasonic system and axially mounted platens that house the receiving and transmitting transducers. This system setup was verified both analytically and experimentally with both aluminum and lucite sample (Donald et al., 2004). Figure 3.2b also shows the picture of the VIS loading frame and the triaxial chamber. The loading piston has an insert with rubber O-ring seals to avoid communication between the confining and the pore pressure. The transducers were commercial piezoelectric acoustic emission sensors with a resonance frequency of 1 MHz and designed with peak sensitivity for displacement perpendicular to the transducer face and thus act as P wave transducers. Signals were digitally filtered to the range of 10 kHz to 3MHz band pass. The digitizer has a varying voltage amplifier which was applied to the data before it was recorded. The digitizing rate was 40MHz.

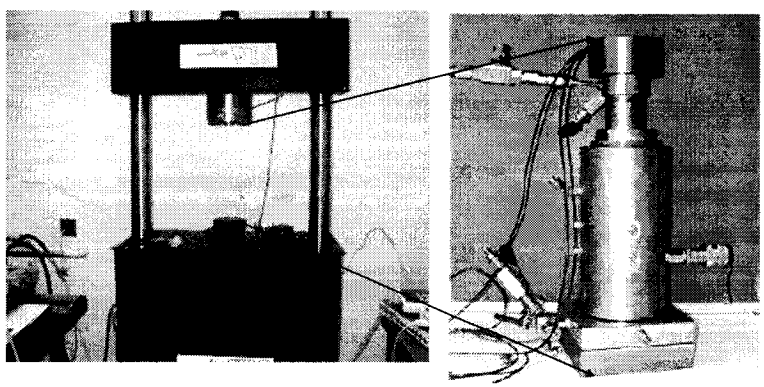

Figure 3.2b: Photograph of VIS machine with a triaxial cell

3.4 Testing procedure, methodology and data processing

3.4.1 Testing procedures and methods

Core samples were prepared according to the American Standard of Testing Material (ASTM, 2003) for laboratory tri-axial testing. The samples were fully saturated with water under a vacuum pump for 24 hours. One of the samples was oven dried. The oven dried state was achieved by drying the sample in 50°C oven for 24 hours. The oven dried and the water saturated densities of some of the cores were measured by weighing the samples in saturated state and in an oven dried state. The porosity was measured via the gas expansion method (Tiab and Donaldson, 2004). Unconfined compressive strengths of some of the samples were determined using the point load test. The initial characteristics of the samples are given in Table 3.1. Benchtop acoustic measurements were also done, with 2MPa axial load to ensure that there is a firm contact of the transducer end pieces with the sample (Myer et al., 1985). This was done to establish the benchtop property of the quartz sandstone since not much information of this type on sandstone is found in the literature. The sample was then jacketed with a 54mm diameter rubber tubing to isolate it from the oil acting as the confining pressure medium and water acting as pore fluid medium. The jacket was heat-shrunk around the cylindrical core sample. The flow disk, flow platens and the samples were loaded in the tri-axial chamber. The end faces of the acoustic platens were ground to a very fine surface finish according to ASTM standard referred earlier, and a thin layer of vacuum grease was placed between the platens and specimen ends to improve acoustic coupling under low axial load. Pulse transmission technique (Birch, 1960) was adapted and used to record the transmitted waves. P waves

piezoelectric transducers (1 MHz, 1.00"/25mm nominal element size, with part number V102-RM) were placed in the acoustic platens and mounted on top and bottom of the sample. This ensured that the transducers were in axially mounted position to the sample (Figure 3.1a and 3.1b). A high viscosity-bonding medium was used to bond the sensors to the center of the endplates. At the start of each test the loading ram was brought into light contact with the specimen and the radial stress, axial stress and pore pressure were simultaneously increased to a simulated insitu condition of 60MPa. This insitu condition was chosen to avoid the sample failing or developing artificial microcracks that would affect the results of the experiment. Figure 3.3 shows the individual radial, axial and pore pressure at the simulated insitu condition. The loading were done in stages – ramp up, depletion and injection. During the ramp up, an acoustic signal was transmitted at every increment of 10MPa pore pressure whilst ensuring that the differential stress remains constant at constant 2MPa (stage 1). At the insitu condition, the confining pressures and the axial stress were kept constant while the pore pressure was lowered gradually to 30MPa, under uniaxial strain condition (stage 2). This was done to simulate petroleum production far from the well bore where lateral displacement is considered negligible (Goulty, 2003). Thus effective stresses were increased and decreased only by variation in pore pressure, while maintaining constant axial load. The pore pressure was gradually dropped and then increased in a cyclic manner creating simulated injection and depletion processes as in a real reservoir.

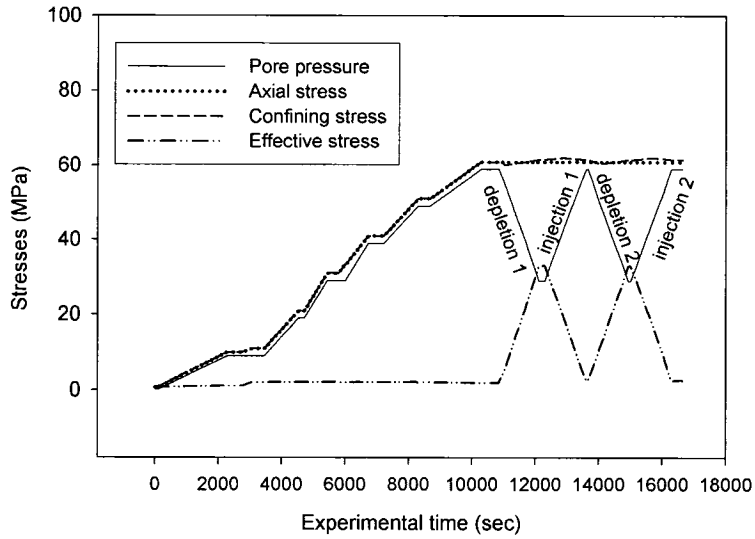

Figure 3.3: Confining stress, axial stress, pore pressure and effective stress behavior during the cyclic experiment (stage 1 to 5)

During the cyclic process, ultrasonic signals were again transmitted through the simulated reservoir every 2 minutes over the duration of the test. The acoustic data was recorded at a rate of 40MHz using the high speed digitizing card. After the experiment, the standard aluminum sample test was done and followed the same procedure as the actual test specimen. Because the aluminum standard has no porosity, only 2MPa effective stress was used to give good contact with the platens and transducers.

3.4.2 Data processing of acoustic data

Each signal was made up of digitized data of 50 waveforms. The 50 waveforms were stacked to improve the signal to noise ratio and to make it easier to pick the arrival times. The stacked waveform was plotted and any visible DC offset removed. The digitized data

falling in the first cycle was used for the analyses (Figure 3.4a). The velocity was found by simply dividing the length of the sample by the arrival time after subtracting the platen travel time and a 2μsec inherent delay of the pulser and oscilloscope. This intrinsic time delay was found by the travel time through the metal platens and the flow assembly without the sandstone sample. This travel time was validated with standard aluminum and acrylic samples and the accuracy of the velocity measurements were found to be 0.2%. The quality factor was found through spectral ratio techniques over a frequency range of 600 to 1000 KHz (Figure 3.4b and Figure 3.5). Details of this technique are found in (Toksoz et al., 1979).

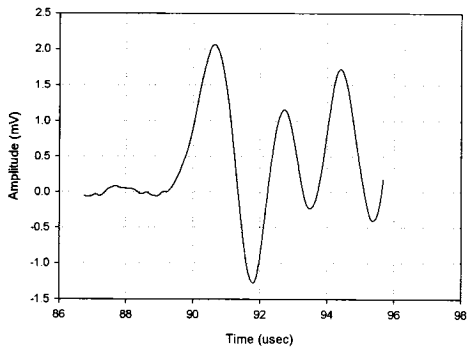

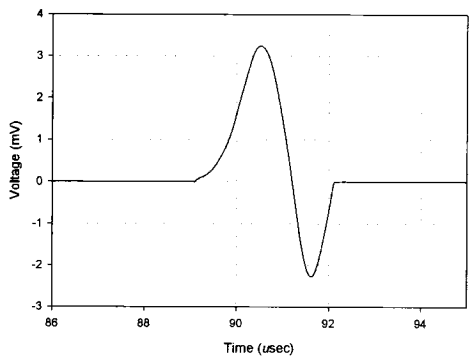

Figure 3.4a: Acoustic signal in time domain at 10MPa axial stress and a typical wave form used for the Fast Fourier Analysis

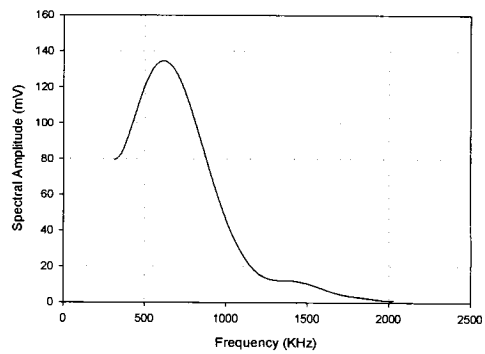

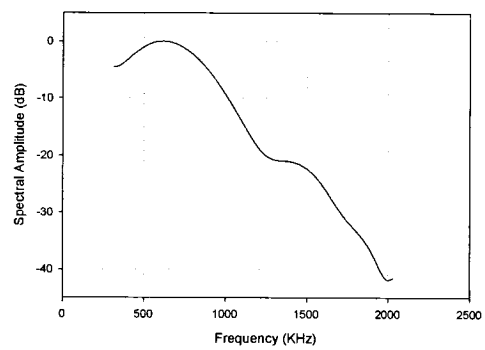

Figure 3.4b: Fast Fourier Transform with mV and dB spectral amplitude

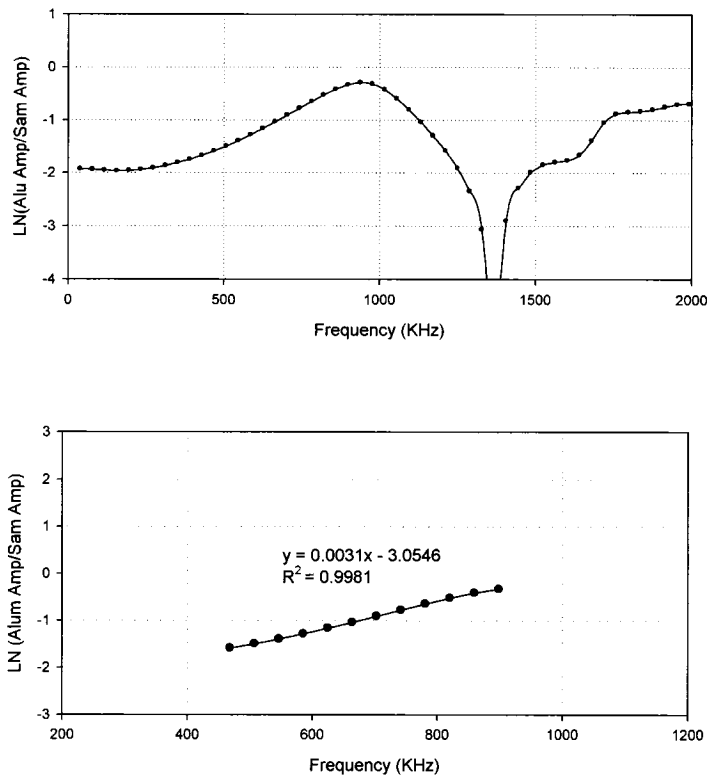

Figure 3.5: Spectral ratios and line of best fit for calculation of Q_p

The average material grain size was 160 microns and the length of the sample was 108mm. With the average P wave velocity of 3500m/s and a frequency range of 800 to 1000 KHz, the wave length is about 3.45mm. This gives enough wavelengths (32 cycles) within the 108mm sample length. It also gives wavelengths longer than the material grain size. The difference between log spectral ratio and its linear regression was used to calculate the error bar on Q_p. The regression coefficient was 0.9961 and at 95% confidence level, the Q_p values have an error of 0.38% (i.e. $Q_p \pm 0.38$).

3.5 Results, discussion and analysis

The quartz sandstone has a saturated benchtop V_P of 3500m/s when a nominal amount of effective axial stress (2MPa) was applied. The corresponding Q_P was 32. The slight lower values of the bench top measurements compared to that in the triaxial cell for V_p and Q_p may be due to reduction in water saturation level when the sample was taken out from the water for benchtop measurements. As described earlier, the quartz sandstone is well cemented and with few pores (porosity of 15%) and micro cracks. This implies less dispersion and thus corresponding high Q_P and V_p values (Kuster and Toksoz, 1974). These velocity and attenuation values compare well, though slightly lower, with published literature (Prasad and Manghnani, 1997) on other sandstone rocks such as Michigan and Berea sandstones.

The graph in Figure 3.6 shows the results of the V_P variation with pore pressure at constant effective stress of 2MPa. The V_P was found to be a function of both effective stress and pore pressure. Though the effective stress was constant, at 2MPa, V_P increased from 3390m/s at pore pressure of 10MPa to 3450m/s at pore pressure of 60MPa. The variation of V_P with pore pressure, at constant effective stress, indicates that the effective stress coefficient, n, is less than 1 (Gangi, 1991; Prasad and Manghnani, 1997; Khaksar et al., 1999). The curve also shows sharp increases in V_P in the initial stage of low pore pressures and gradual increases in V_p when the pore pressure reaches a peak of 60MPa. This also indicates that the effect of internal stress coefficient on the effective stress at

high pore pressures are more pronounced than at lower pore pressures and confining stress. Thus, it is important for the values of n to be accounted for in high pressure triaxial laboratory studies on acoustic velocity variation with pore pressure and confining stress. Again, as indicated on the graph the increase in V_P with pore pressure is non-linear. In fact, it behaves like the sandstone reported by Greenfield and Graham (1994). This indicates that the value of the internal coefficient is not constant for a particular rock but depends on the instantaneous value of confining and the pore pressures. It is again important to report n values with pore pressure and confining stress variables at all measurements. The velocity pore pressure curve (Figure 3.6) at constant effective stress during stage 1 of the experiment, follows a single three parameter exponential rise to a limit, similar to the one described by Greenfield and Graham (1994), for velocity effective stress variation. This variation of velocity at constant effective stress implies that $n \neq 1$. The velocity values have instrumental measurement accuracies of 0.21%.

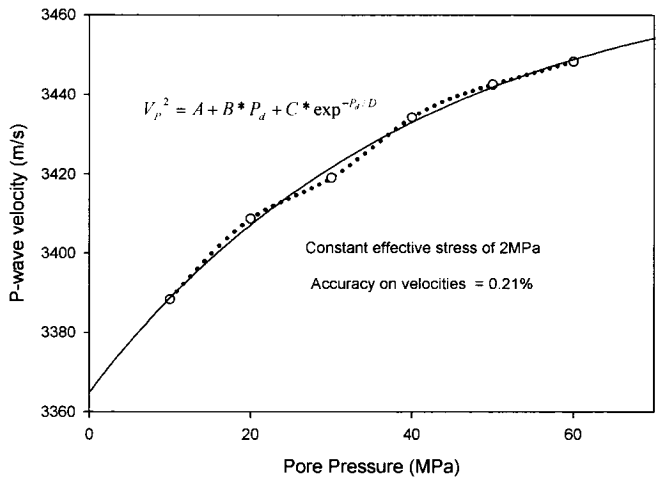

Figure 3.6: Variation of ultrasonic velocity with pore pressure at constant effective stress

The corresponding quality factor values for stage 1 of the experiment (Figure 3.7a) have similar behavior as velocities. Thus Q_P increases with pore pressure at constant effective stress. Q_P increases from 33 at pore pressure of 10MPa to 42 at pore pressure of 60MPa, at constant effective stress. The accuracy on the quality factor is 0.23%. The variation of pore pressure with Q_P is gradual at low pore pressure and steeper at high pore pressures. The difference between log spectral ratio and its linear regression was used to calculate the error bar for Q_p (Figure 3.7b). The regression coefficient was 0.9961 and at 95% confidence level the Q_p values have an error of 0.38%. (i.e. $Q_p \pm 0.38$). This travel time was also validated with standard aluminum and acrylic samples and the accuracy of the velocity measurements were found to be 0.21%. The best equation that describes the behavior of Q_P with pore pressure is a two parameter exponential growth without limiting value (Figure 3.7a). Equation 2 and 3 respectively describe the velocity and quality factor curve with pore pressure.

$$V_P^{\,2} = A + B \times P_p + C \times \exp^{-P_p / D} \tag{2}$$

$$Q_P^{\,2} = A \times \exp^{B \times P_p} \tag{3}$$

Where A, B, C, D depends on the type of rock and P_p is the pore pressure

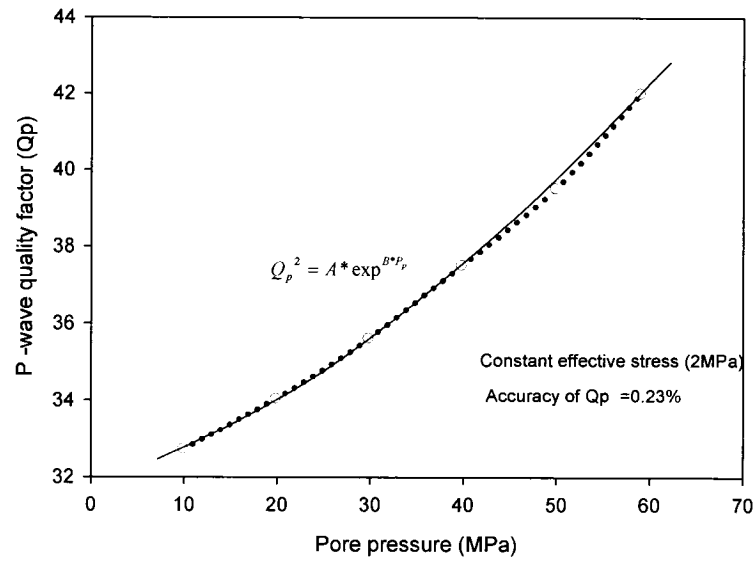

Figure 3.7a: Variation of quality factor with pore pressure at constant effective stress

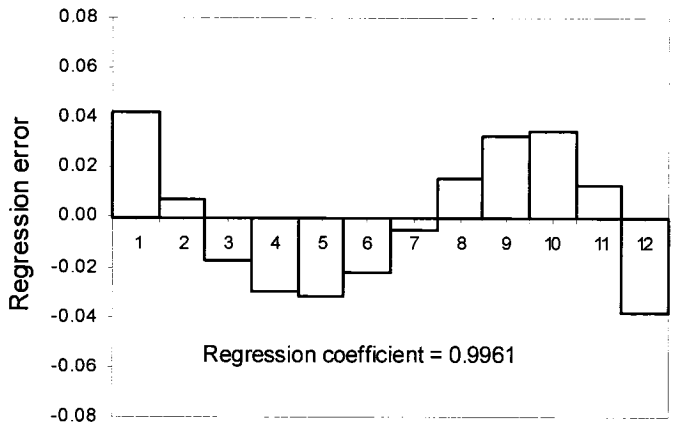

Figure 3.7b: Regression error of spectral ratio and its linear regression

3.5.1 Estimation of effective stress coefficient from velocity- pressure curves

Empirically, the gradient of the V_P - pore pressure curves and V_P - differential pressure curve can be used to determine n. From graphical point of view (Figure 3.6) a simple

empirical estimation of n could be the ratio of the gradient of the velocity-pore pressure curves at constant differential pressure and that of velocity differential pressure curve at constant pore pressure and more theoretical insight about this behavior are highlighted in Gurevich (2004). Todd and Simmons (1972) and Christensen and Wang (1985) have indicated that since both pore pressure and differential pressure have effect on the V_P and Q_P, a similar velocity differential pressure curve at constant pore pressure is needed to fully evaluate n. The mathematical equation to describe n based on these velocity pressure curves are given by Todd and Simmons (1972) as:

$$n = 1 - \left[\frac{\partial A}{\partial P_P}\right]_{P_d} \div \left[\frac{\partial A}{\partial P_d}\right]_{P_P}$$

A is the physical property in question, and in this case A takes the values of P-wave velocity (V_p) as well as attenuation quality factor (Q_p).

P_p is the pore pressure.

P_d is the differential pressure.

$\left[\frac{\partial A_P}{\partial P_P}\right]_{P_d}$ is the gradient of the velocity pore pressure curve at constant differential pressure.

$\left[\frac{\partial A_P}{\partial P_d}\right]_{P_P}$ is the gradient of velocity differential pressure curve at constant pore pressure.

The fact that these curves are not linear means that the ratios depend on the pore pressure values as well as differential pressure values. The gradient of the velocity verses differential pressure curve at constant pore pressure could be read from the velocity versus pore pressure curve at constant differential pressure at the point where pore pressure is equal to zero (Prasad and Manghnani, 1997). This involves an assumption that the curve is duplicated at higher pore pressures. Using this assumption, n was calculated to be 0.85 at 60MPa pore pressure. This assumption however could lead to a lower estimate of n especially at higher pressures with magnitude approaching the Uniaxial Compressive Stress (UCS) of sample, as a result of development of microcracks. This is not the case in this experiment since loading was carefully done to 60% of the UCS value. The cyclic experiments were therefore performed at lower insitu pressures below the strength of the rock sample. The low n value for the quartz sandstone may be due to the shapes and the pore-connectivity of the pore spaces as revealed in the thin section, but this was not qualitatively estimated. Most of the pores are not spherical and are not connected (low permeability, Table 3.1) and could not effectively provide the actual pore pressure to counterbalance the effective stress on the sample. This indicates that the shapes and the connectivity of the pores as well as the pore pressure levels are factors affecting the n value.

Figure 3.8 shows the trend in the changes in V_P during the depletion and injection processes. Depletion V_P are higher than injection V_P. This is because the depletion causes reduction in pore pressure and increases effective stress whilst injection increases pore

pressure and reduces effective stress. The sample in its natural state did not seem to have observable micro cracks so closure of natural pore spaces (porosity was 15%) was the cause of the increase in depletion velocity and the opening of pore spaces were the cause of reduction in injection velocities. The experiment did not introduce any observable microcracks in the sample since maximum stress on the sample was only 60% of its strength. Most of the opening and closing of the sample during the simulated injection and depletion process is due to closure and opening of pores rather than microcracks. This is because we could not substantiate the effect of microcracks. The same reason is true for quality factors where depletion Q_P are higher than injection Q_P (Figure 3.9). Figure 3.10 also shows depletion curves (first and second depletion cycle) with pore pressure. Velocity in the second depletion cycle is consistently higher than the velocity in the first depletion cycle though corresponding pore pressures and effective stresses are the same. The V_P in depletion 2 are very consistent at about 0.7% increases over the V_p in depletion 1. This may be attributed to (1) closure of pores after the first depletion loading and (2) the viscoelastic behavior of the rock, where time dependant strain during the first depletion (caused by increases in effective stress in the first cycle) still exists thus increasing the velocities in the second depletion (increases in effective stress in the second depletion).

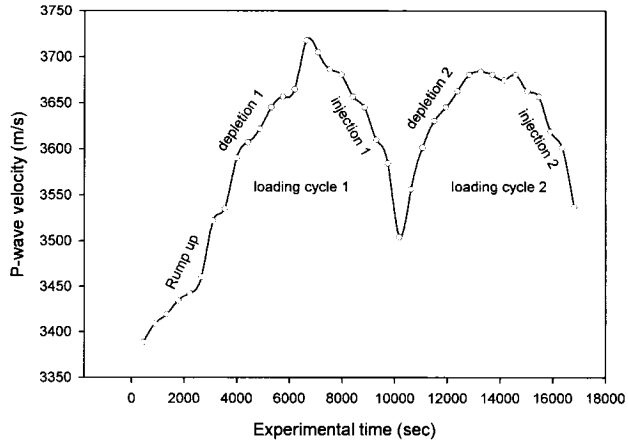

Figure 3.8: Velocity throughout the experiments

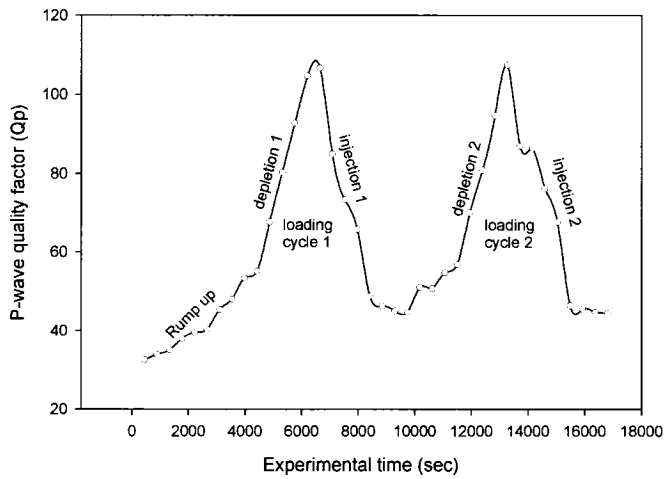

Figure 3.9: Quality factor throughout the experiments

This memory effect of the strain also affects the quality factors (i.e. second cycle quality factors are higher than the first cycle quality factors (Figure 3.11), and the percentage increase is more than the velocities increases (1.1%). Similarly, the reduction in strain during the first cycle contributes to the reduction of the V_P and Q_P during the second

injection (Figures 3.12 and 3.13). The comparison of the changes in the velocities to that of quality factors during the cyclic loading shows that the quality factors are more sensitive to changes in pore pressures and effective stress then the velocities. Sensitivity of quality factors are also more pronounced during the injection cycle than the depletion cycles. It could be argued therefore that Q_P may be better indicator for time-lapse reservoir monitoring than V_P. Q_P is more sensitive, though erratic to changes in petrophysical conditions than V_P (0.7% as against 1.1% over the same effective stress range). The higher Q_P values (30 to 102) for this quartz sandstone as compared to some published data for other sandstones (Prasad, 1998) may be due to the well cemented, fine grain nature of the quartz sandstone as well as lower clay content and absence of microcracks as indicated by the geology and the thin section analysis. Attenuation is therefore minimal thus resulting in higher Q_P values (Kuster and Toksoz, 1974).

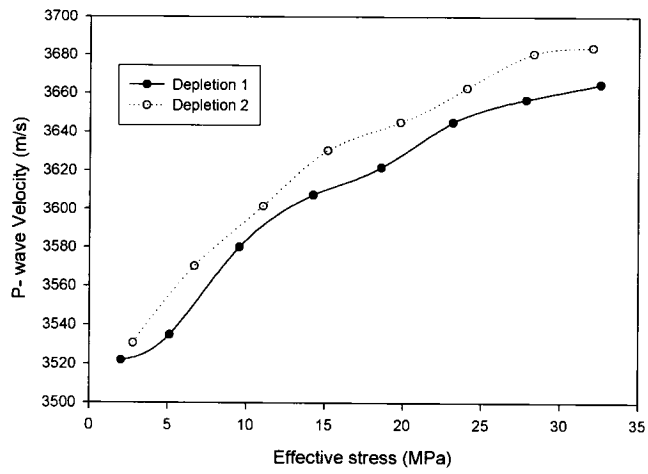

Figure 3.10: Velocities of the depletion cycle 1 and 2 with effective stress

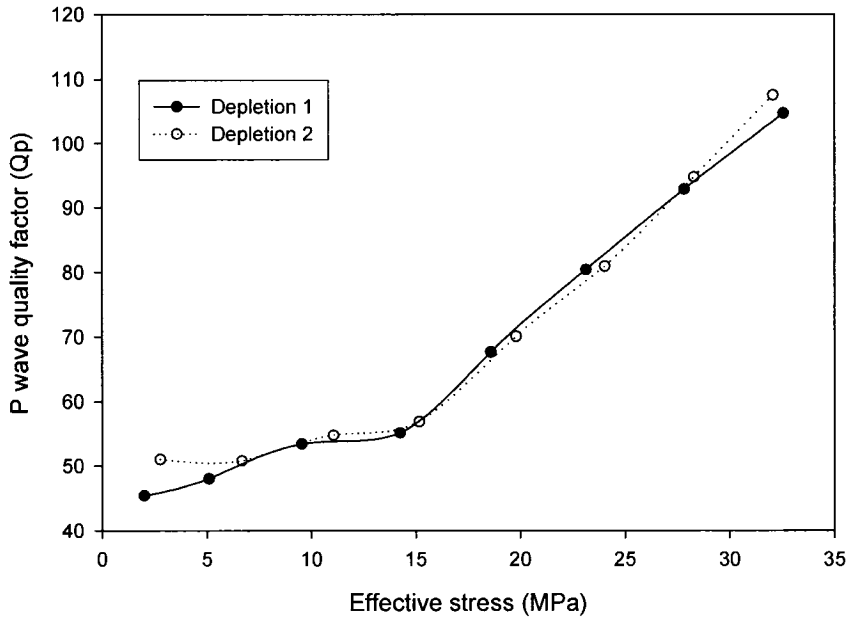

Figure 3.11: Quality factors of the depletion cycle 1 and 2 with effective stress

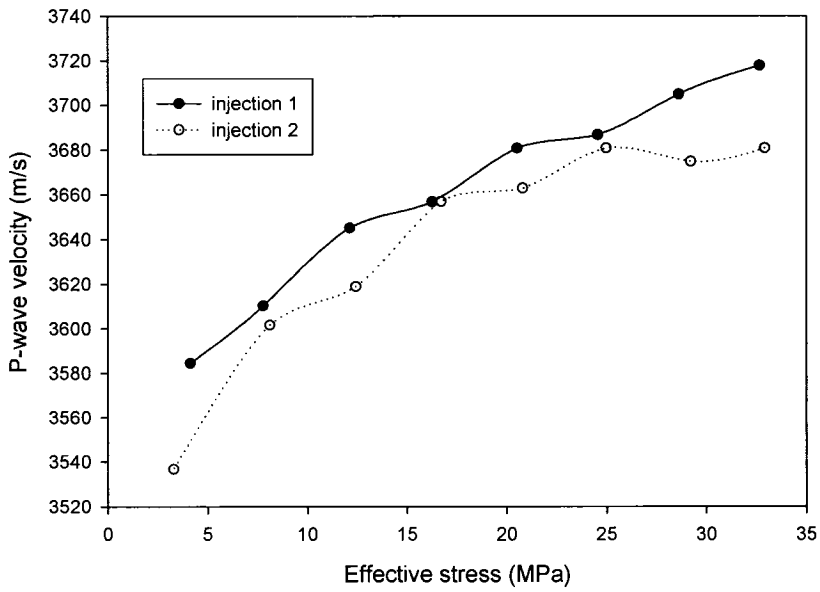

Figure 3.12: Velocities of the injection cycle 1 and 2 with effective stress

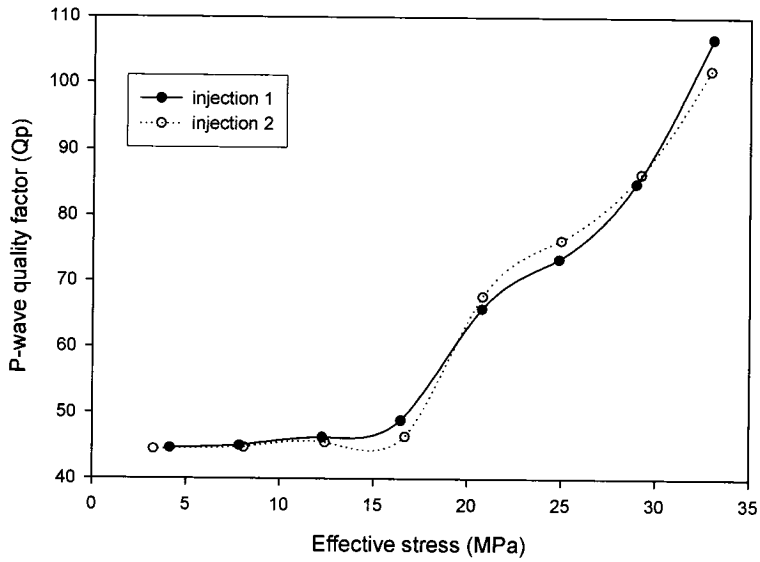

Figure 3.13: Quality factors of the injection cycle 1 and 2 with effective stress

In order to understand the history of loading and the strain weakening effect on velocity and quality factors, the strain on the sample was measured in the course of the experiment. The shortening of the sample length was quantified and the velocities recalculated taking into consideration the strain (shortening in length due to depletion) and compared the results to the second depletion (Figure 3.14). Figure 3.15a and 3.15b also specified the percentage difference due to strain and that due to pressure change. It was found that the viscoelastic relaxation is pronounced in the strain behavior where the media still remembers the history of loading. At every cycle there is an increase in strain despite removing all the effective stress by the previous injection cycle. This strain weakening behavior is responsible for the slight increases and decreases in V_P and Q_P with cyclic loading. This implies that lithology, porosity, permeability, pore fluids and

effective stress are factors that affect velocities and attenuation as highlighted by many writers (Wang, 2001; Berryman, 1992; Stoll, 1989; Prasad, 1998). However, as shown in this experiment, the relaxation time, hystersis, creep and the loading history also have effect on velocity and attenuation. However, the individual effect of these factors on the velocity and attenuation has not been qualitatively assessed.

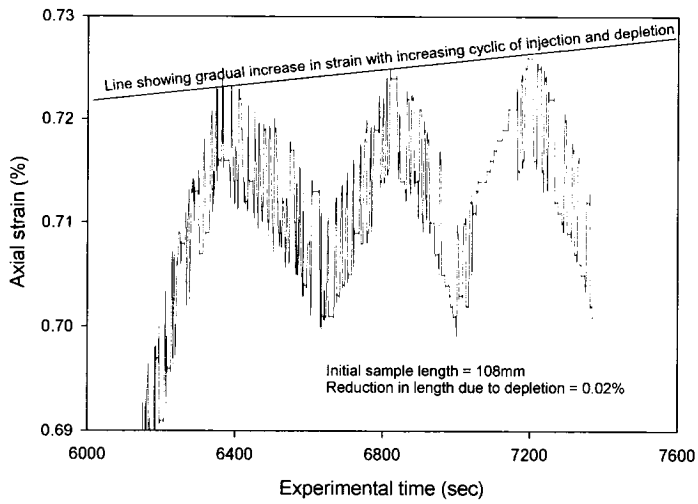

Figure 3.14: Strain behavior of the quartz sandstone during the whole experiment

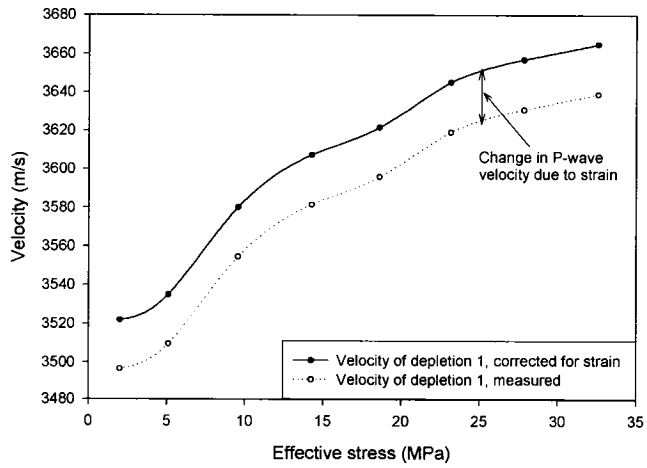

Figure 3.15a: Measured and corrected P wave velocities for depletion

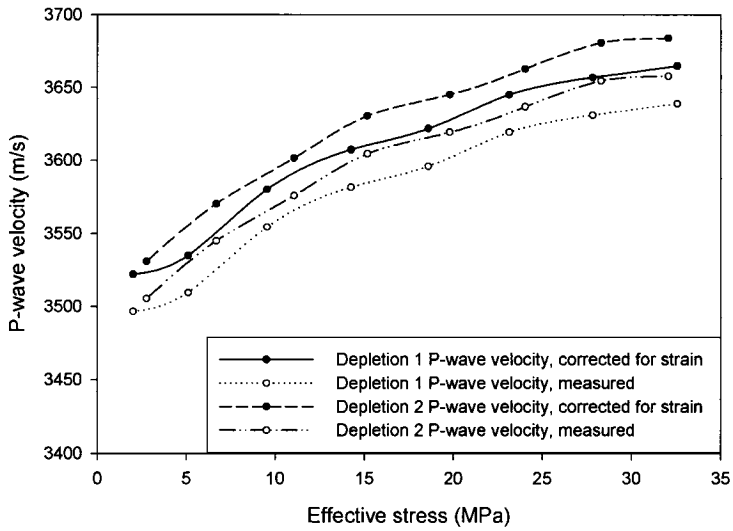

Figure 3.15b: Measured and corrected P wave velocities for injection and depletion for the entire experiment.

3.6 Conclusion

It was confirmed, as seen in the literature that V_P and Q_P increase with effective stress. However it was also found that, if the effective stress is constant, then V_P and Q_P would increase with pore pressure. This finding led to the conclusion that the effective stress coefficient was less than 1 for this quartz sandstone. Though V_P and Q_P were confirmed to increase with effective stress, they could still increase at constant effective stress based on the value of pore pressure. At a high pore pressures, there is a fairly constant V_P at constant effective stress but at low pore pressures, V_P variation with pore pressure

becomes pronounced. This was also true for Q_P. V_P curves follow a single three-parameter exponential rise to a maximum limit at the highest effective stress. On the other hand, Q_P curves have no clear limiting values. They follow the single two-parameter exponential growth without limit. The effective stress coefficient, n, was found to be less than 1 and it was pore pressure dependant. This was due the irregular shape of the pores as well as the pressure levels at which the experiment was performed. At low pore pressures, n approached 1. The depletion and injection cycle caused closure of micro cracks and pores and a viscoelastic relaxation, which resulted in an increased effect on the V_P and Q_P during the cyclic loading, thus making the rock less dispersive. However, we could not confirm the independent effect of microcracks on the velocity and attenuation. At every cycle there is an increase in strain despite removing the effective stress by injection. This creep and strain weakening behavior is responsible for the slight increase in velocities and Q_P with cyclic loading. Q_P was found to be more sensitive, though unstable in responding to the loading cycle and changes in pore pressures than V_P, leading to an argument that Q_P may be better indicator for time-lapse reservoir monitoring than V_P. However, stability of Q_P at high pore pressures and confining stress are in question. The instability may either be a natural tendency of attenuation to be more unstable in rocks than velocity or the assumption frequency independent Q_p. Further research on stabilities of V_P and Q_P is recommended.

3.7 Acknowledgements

Acknowledgements go to the Natural Sciences and Engineering Research Council of Canada (NSERC), Petroleum Research Atlantic Canada (PRAC) and Schlumberger Canada Limited for providing funding for this research.

3.8 References

ASTM Standard, (2003), Practice for preparing rock core specimens and determining dimensional shape tolerances: American Society for the Testing of Materials (ASTM), No 4543.

Berryman, J. G., (1992), Effective stress for transport properties for inhomogeneous porous rocks: J. Geophys. Res., 97, B12, 17409-17424.

Biot, M. A., (1956a), Theory of propagation of elastic waves in fluid saturated porous solids, Part I: Low frequency range: J. Acoust. Soc. Am., 28, 168-178.

Biot, M. A., (1956b), Theory of propagation of elastic waves in fluid saturated porous solids, Part II: High frequency range: J. Acoust. Soc. Am., 28, 179-191.

Birch, F., (1960), The velocity of compressional waves in rocks to 10Kilobars, Part I: J. Geophys. Res., 65, 1083-1102.

Christensen, N. I., and Wang, H. F., (1985), The influence of pore and confining pressure on dynamic elastic properties of Berea sandstone: J. Geophysics, 50, 207-213.

Donald, J. A., Butt S. D., and Iakovlev S., (2004), Adaptation of a triaxial cell for ultrasonic P-wave attenuation, velocity and acoustic emission measurements: Internat. J. Rock Mechs. Min. Sci., Vol. 41, 1001-1011.

Dvorkin J. Mavko G. and Nur A., (1995), Squirt flow in fully saturated rocks: Geophysics, 60, 97 – 107.

Dvorkin J. Nolen-Hoeksema R. and Nur A., (1994), The squirt-flow mechanism: microscopic description: J. Geophysics, 59, 428-438.

Dvorkin J. and Nur A., (1993), Dynamic poroelasticity: A unified model with the squirt and the Biot mechanisms: J. Geophysics, 58, 524-533.

Gangi A. F., (1991), The effect of pore fluid and pressure on the seismic velocity in cracks and/or porous rocks: SEG Research Workshop on Lithology, Tech. Abstracts, 35-38.

Goulty N.R, (2003), Reservoir stress path during depletion of Norwegian chalk oilfields: Petroleum Geoscience, Vol. 9, No. 3, 233-241.

Green, D. H., and Wang, H. F., (1986), Fluid pressure response to undrained compression in saturated sedimentary rocks: J. Geophysics, 51, 948-956.

Greenfield, R.J., and Graham, E.K., (1994), A Convenient functional form, consistent with elasticity theory, for fitting the velocities of rocks containing cracks: Trans. Amer. Geophys. Un. (EOS), 75, No. 16, 337-354.

Gurevich, B., 2004, A simple derivation of the effective stress coefficient for seismic velocities in porous rocks: J. Geophysics: 69, 393-397.

Johnson, C.F., (1970), A Pulse technique for the direct measurement of bar velocity: Twelfth Symp. on Rock Mechs. Proc., University of Missouri, Rolla, Missouri, Soc. of Min. Engs, New York.

Khaksar, A., Griffiths, C., and McCann, C., (1999), Effective stress coefficient for P and S waves velocity and quality factor in sandstone, example from Copper Basin Australia: SEG, Expanded Abstracts, 192-195.

Kuster T. K. and Toksoz M. N., (1974), Velocity and attenuation of Seismic waves in two phase media: Part II Experimental results: J. Geophysics, 39, 607 - 618.

Landro, M., and Kvam., O., (2002), Pore pressure estimation-What can we learn from 4D?: CSEG Recorder, 27, 83-87.

Myer, L. R., Hopkins, D., and Cook, N. G. W., (1985), Effect of contact area of an interface on acoustic waves transmission characteristics: 26th. US Symp. on Rock Mechanics, USA.

Nur, A., and Byrelee, J. D., (1971), An exact effective stress law for elastic deformation of rocks with fluid: J. Geophys. Res., 76, 6414-6419.

Nur, A and Simmons, G., (1969), The effect of saturation on velocity in low porosity rocks: Earth and Plan. Sci., 7, 183-93.

Plona, T. J., and Cook, J.M., (1995), Effects of stress cycles on static and dynamic Young's moduli in Castlegate sandstone: In J.J.K. Daemen & R.A. Schultz (eds.), Proceedings of the 35th U.S. Symposium on Rock Mechanics. Rotterdam: Balkema, 155-160.

Prasad, M., (1998), Empirical trends in velocity and quality factor properties of reservoir rocks: Department of Geophysics, Stanford University, Internal report, SRB project.

Prasad, M., and Manghnani, M.H., (1997), Effects of pore and differential pressure on compressional wave velocity and quality factor in Berea and Michigan sandstones: J. Geophysics, 62, 1163–1176.

Ryan, R. J., (1998), The Fall Brook Quarry near Three Miles Plains, In Classic Carboniferous Sections of the Minas and Cumberland Basin in Nova Scotia: The Soc. of Orga. Petro., Ann. Gen. Mtg, Field Trip, Open File Rept. ME 1998-5, NS Nat Resource Dept, NS, Canada.

Sabinin, V., Chichin-ina, T., and Ronquillo, J. G., (2003), Numerical model of seismic wave propagation in viscoelastic media: Conf. prog., Wave 2003, Sixth Internat Conf. on Mathematical. and Numerical Aspects of Wave Propagation, Finland.

Stoll, R.D., (1989), Sedment acoustics: Lecture note in earth science, 26, Springer Verlag.

Tiab D., and Donaldson, E. C., (2004), Petrophysics, theory and practice of measuring reservoir rock fluid transport properties: Gulf professional publ, 2nd. edition. p790.

Todd, T., and Simmons, G., (1972), Effect of pore pressure on the velocity of compressional waves in low porosity rocks: J. Geophys, Res., 77, 3731-3743.

Toksoz, M.N., Johnston, D.H., and Timur, A., (1979), Attenuation of seismic waves in dry and saturated rocks, Part I: Laboratory measurements: Geophysics, 44, 681-690.

Wang, Z., (2001), Fundamental of seismic rock physics, J. Geophysics, 66, 398-412.

Williams, P. R., and Ravji, S., (1999), Shear waves dispersion and mechanical relaxation spectra: J. Physics D: Applied Physics, 32, 1750-1758.

Chapter 4: Characterizing volumetric failure in weak sandstone reservoirs using P-wave quality factor, velocity and acoustic emissions

This paper was submitted to the journal of Geophysics and is currently under review. The main author is Mr. J. Adam Donald and co-authored by Mr. J. Adam Donald and Dr. Stephen D. Butt. The figure numbers and reference formats have been altered to match the formatting guidelines set out by Dalhousie University compared with the submitted manuscript to Geophysics. Sample names in the figure and table captions have been changed to be consistent with the rest of the thesis content. A list of Mr. Frempong's contributions to this paper is presented below.

- Sample preparation and manufacture of synthetic sandstone used for the experiment was done by Paul Frempong
- Developed experimental technique used for the experiment with Mr Donald,
- Software development and MATLAB code for data processing
- Performed all laboratory work with Mr. Donald Adam.
- Idea for investigating the effective stress coefficient originated from Mr. Paul Frempong during extensive literature review
- Editing and review of the manuscript.

4.1 Abstract

Simulated petroleum production tests were performed in the laboratory linking stress-strain behavior with P-wave velocity, quality factor and acoustic emissions in weak sandstone reservoirs. Stress sensitive reservoirs are associated with sand production and land subsidence contributing to costly problems in the oil industry. Comprehensive sets of experiments were performed in a triaxial compression cell to induce pore collapse in high porosity, weak synthetic sandstone core samples. The aim of this paper is to compare stress-strain behavior and ultrasonic parameters between two types of synthetic sandstone with different strengths of 3.5 and 7 MPa UCS, respectively. Piezoelectric sensors (1-MHz) were used for transmission and receiving ultrasonic waveforms pulsed through the core samples during the simulated production tests. Two tests pulsed P waves through the core axis measuring quality factor and velocity between 400 and 600 kHz, and two tests monitored acoustic emissions where ultrasonic b-values and cumulative AE events were calculated. A new approach for determining phase velocities using the cross-over spectra method was developed and verified using acrylic and aluminum samples. Experimental results indicate that velocity and quality factor show small variations with respect to effective stress changes for the 3.5 MPa sandstone. The 7 MPa sandstone, however, shows significantly larger changes in velocity and quality factor due to pore pressure variations, and pore collapse and compaction phases may be distinguished. Acoustic emission results correspond well to the stress-strain behavior for both samples and aid in the interpretation of results from wave transmission. The results highlight

variations in ultrasonic parameters and stress-strain behavior within weak sandstone reservoirs. Although much research has been done on the geomechanical behavior of this type of weak sandstone, very little experimental ultrasonic data have been presented. Time-lapse seismic and reservoir monitoring may benefit from laboratory tests such as these to assess problematic reservoirs.

4.2 Introduction

Understanding pore pressure conditions and its effect on pore structure in stress sensitive petroleum reservoirs is key for reservoir management. Mechanical damage near the wellbore has been characterized by decreasing acoustic wave velocities and significant velocity dispersion (Plona et al., 2002; Kane, 2001; Winkler, 1997) for intermediate strength rock (15-55 MPa UCS). However, stress sensitive reservoirs associated with sand production and subsidence are composed of relatively weak rock (<10 MPa UCS) where volumetric failure has been studied and identified as the main mode of failure contributing to rock deformation far from the well bore region (Tronvoll et al., 1997; Nouri et al., 2003). Identification of these sensitive areas using acoustics is important for the longevity and production efficiency of the reservoir. Coupling geomechanics with time-lapse seismic surveying and reservoir simulation are key relationships that need to be further examined. Recent advancements in reservoir simulators are considering geomechanical changes in reservoir conditions especially for stress sensitive reservoirs (Onaisi et al., 2002). Time-lapsed seismic surveys are being performed to image

changing conditions to aid in reservoir maintenance and development. Risk assessments are done for a given reservoir before proceeding with the 4-D survey and individual seismic and reservoir parameters are examined for their respective sensitivity under changing effective stress (Lumley et al., 1997). These parameters may need to be better calibrated for identifying effective stress changes in these problematic reservoirs where volumetric failure is likely to occur.

Elastic wave propagation is dependant on frequency and attenuating properties of the media, whether in the laboratory or the field. Wave velocity and attenuation measurements must be done with caution for low quality factor ($Q < 30$) material (Molyneux and Schmitt, 2000). Data processing artifacts such as the pedestal effect (Strick, 1970) may give unrealistic early travel times through the attenuating media. Identifying an appropriate frequency range for eliminating improbable data would also be helpful for modeling and inversion techniques associated with seismic processing.

Clamping acoustic listening devices are becoming more frequently used inside wellbores to characterize sand production as a real-time field measurement tool (Aldal et al., 2003). Acoustic emission characteristics may also be utilized to locate areas of mechanical damage (Maxwell and Urbancic, 2002). Laboratory studies of lower energy acoustic emissions (AE) during rock deformation and failure are often applied to the study of microseismic events recorded under field conditions. For data analysis, AE amplitudes

are considered to be proportional to stress release at the source and are used to infer the nature of rock deformation.

The main objective for this study is to link the stress-strain behavior just for pore pressure collapse observed in sandstone reservoirs during petroleum production to various seismic parameters used within industry today. To achieve this goal, a comprehensive set of simulated production experiments was performed in the laboratory to induce pore collapse in weak sandstones. Two types of synthetic sandstone with different strengths of 3.5 and 7 MPa UCS were used for comparison. Ultrasonic measurements were made on the core samples for four simulated production tests. Two tests measured P-wave velocity and quality factor, and two tests monitored acoustic emission (AE) where ultrasonic b-values and cumulative AE events were calculated. The AE results are used to aide in the interpretation of the velocity and quality factor data. Static elastic moduli were defined from UCS testing and petrophysical parameters were also found. A new method for determining phase velocity was developed and verified with acrylic and aluminum samples.

4.3 Experimental methods

4.3.1 Sample description

Synthetic sandstone comprised of Portland cement, silica sand and water, was used to represent the weak reservoir rock,. Table 4.1 shows the percentage composition by weight for Batches A and B. The grain size parameters of the silica sand are shown in

Table 4.2. D10, D20 and D60 refer to the diameter of the sand grain as percentage finer passed and CC and CU refer to the coefficient of curvature and uniformity respectively. From these parameters, the sand may be described as being fine grained and well sorted (CU <6 and CC ~ 1), with no clay size fraction (Bowles, 1992).

Table 4.1: Batch ratios by percent weight for the synthetic sandstone samples

Batch #	Silica Sand %	Portland Cement %	Water %
A	83	6	11
B	77	12	11

Table 4.2: Grain size parameters for the silica sand used in the synthetic samples.

D_{10}	D_{30}	D_{60}	C_C	C_U
0.170 mm	0.267 mm	0.360 mm	1.16	2.12

A sample thin section of the synthetic sandstone from Batch A is presented in Figure 4.1. Under polarized light, the grains appear angular to sub-angular in shape, with an average diameter of 0.288 mm, surrounded by the Portland cement matrix. The grain size of the silica sand is representative of natural clastic reservoir rock used in similar studies as outlined in other literature (Prasad and Manghnani, 1997; Sammonds et al., 1989). The samples were cast into cylindrical plastic molds, 52 mm in diameter and approximately 108 mm long, and left to harden for 24 hours at room temperature. They were then removed from the plastic molds and immersed in water and left to cure for 28 days.

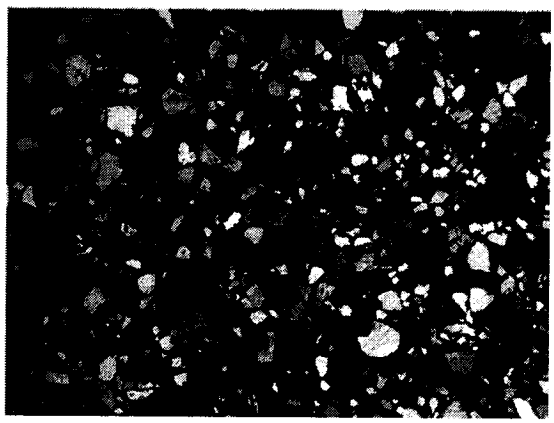

Figure 4.1: Microphotograph of a typical synthetic sandstone sample under cross-polarized light. The horizontal field of view is 11 mm.

Two cores from each batch (Samples A-3 and B-3) were subjected to some bench-top measurements to characterize the material properties. Results of these tests are summarized in table 4.3. UCS tests were done with axial and lateral displacement measurements to obtain static elastic moduli in order to classify their strength and stiffness. ASTM standards were followed for core sample preparation, as well as UCS test procedures. Porosity was calculated from the difference between dry and water saturated weights. The jacketed samples were placed within the triaxial cell under nominal (1 MPa) axial and confining pressures where pore fluid was passed through the long axis of the core. A flow rate and pressure gradient was obtained over a 5-minute constant flow period for determining sample permeability.

Table 4.3: Petrophysical and geomechanical properties of the synthetic core samples (A-3 & B-3).

Batch	Unconfined Compressive Strength (MPa)	Young's Modulus (GPa)	Poisson's Ratio (n)	Porosity (%)	Permeability (mD)
A	3.4	0.65	0.11	36	255
B	6.8	1.69	0.3	34	26

4.3.2 Experimental setup

Donald et al. (2004) gives an in-depth description of the exact experimental apparatus and techniques used for the simulated production tests. Figure 4.2 shows a scaled drawing of the apparatus. The jacketed core samples were placed inside the triaxial cell where axial stress, confining and pore pressure were increased to in-situ conditions. The servo-controlled pumps were configured for uniaxial strain condition to simulate petroleum production far from the well bore, where lateral displacement is considered negligible. Effective axial stress was increased and decreased only by variations in pore pressure, while maintaining a constant axial load. The 1-MHz Panametrics ultrasonic P-wave piezoelectric sensors are mounted inside custom platens sized to fit outside the triaxial cell, without modifying the cell itself. Sensors are centered and aligned with the core specimen axis.

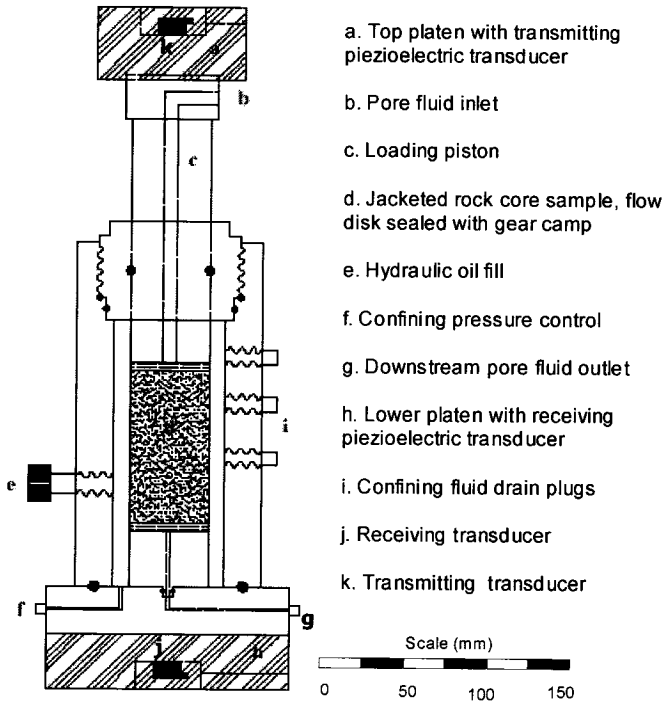

Figure 4.2: Scaled diagram of the experimental apparatus: triaxial cell and piezoelectric transducer platens.

Diffraction phase corrections as described by Khimunin (1972) and Papadakis (1972) for laboratory ultrasonic measurements were evaluated. The normalized distance (unit less) between sensors as a function of wavelength and transducer radius is 97.2. As shown by Khimunin (1972), the ratio of the average pressure on the transducer to the pressure of the continuous plane wave approaches zero as the normalized distance approaches 100. This indicates that the P-wave can be considered as a uniform pressure front as it passes through the apparatus, and no significant waveform curvature would be observed because of the relatively large distance between transmitter and receiver compared to the wavelength. Therefore the corrections were deemed to be unnecessary and not conducted.

Further, the geometry of the experimental set-up was evaluated to ensure that the first arrivals are P-waves and not resonant shape modes. For this set-up we assume a laterally extensive medium where the direct wave represents a pure longitudinal or compressional mode. The direct P-wave propagating through the apparatus will have a wavelength very small compared to the dimensions of the cylindrical platens and core sample. The strained portion of the medium, caused by the transmitted wave, is constrained by the surrounding mass and effectively stiffened. The possibility of measuring a resonant bar mode exists only when the ratio of the radius of the cylinder to the wavelength is less than 0.1 (Johnson, 1970). Therefore, for a frequency of 450 kHz, wave speed of 3500 m/s and a core radius of 27 mm, this ratio is 3.51, well above the value needed for resonant bar mode propagation.

4.3.3 Measurement techniques

Compressional waves were pulsed through the core samples at timed intervals throughout the simulated production tests for the velocity and attenuation measurements. At each interval, a set of 50 waveforms were acquired and stacked in order to improve the signal to noise ratio. Velocity determination in highly attenuating media is not a trivial exercise as indicated by Molyneux and Schmitt (2000). Wave dispersion was investigated for this situation and a modified cross-power spectrum analysis for time delay calculations was employed.

Phase velocity as a function of frequency ω may be obtained from the phase of the average cross power spectra G12 for two waves. Since there is only one receiving sensor for the wave Y2 (ω) propagating through the specimen, a second, non-dispersive waveform Y1 (ω) is obtained by replacing the rock core with an aluminum standard core of the same dimensions. The non-dispersive waveform Y1 (ω) represents a 'calibrated' input pulse for the triaxial cell, as it would be 'seen' entering the rock specimen. The cross power spectrum G12 is calculated from the product of Y1 (ω) and the complex conjugate of Y2 (ω). The phase of the cross power spectrum is calculated as follows:

$$\Theta_{12}(\omega) = \tan^{-1}\left(\frac{\mathrm{Im}(G_{12}(\omega))}{\mathrm{Re}(G_{12}(\omega))}\right) \tag{4.1}$$

The phase velocity then may be determined from the time delay between waveforms as a function of the unwrapped phase as shown below:

$$t(\omega) = \frac{\Theta_{12}(\omega)}{\omega} \tag{4.2}$$

$$V_P(\omega) = \frac{\Delta l}{t(\omega)} \tag{4.3}$$

The length of the rock sample is Δl, and the phase velocity is VP as a function of frequency ω. The use of the cross power spectrum for time delay calculations for phase velocity relies on the assumption that the wave group is propagated through the media as a single mode and therefore the velocity is only a function of frequency (Aki and Richards, 1980).

Verification of this new approach was done by comparing phase velocity results obtained by pulsing waves through material of different lengths as outlined by Molyneux and Schmitt (2000). Transmitted waveforms through two acrylic bars (ρ = 1.183 g/cm3), 108 mm and 148 mm in length respectively, are shown in Figure 4.3. Transducer platens were placed on either ends of the specimens and a nominal pressure was applied axially to ensure sufficient acoustic transmission. Figure 4.4 shows the waveforms obtained from the time-shifted aluminum standard and the same 108 mm long acrylic sample placed inside of the triaxial cell. The corresponding phase velocities over the frequency band of 100 to 1500 kHz are displayed in Figure 4.5. The percentage difference between the calculated velocities is less than 4% over the frequency range.

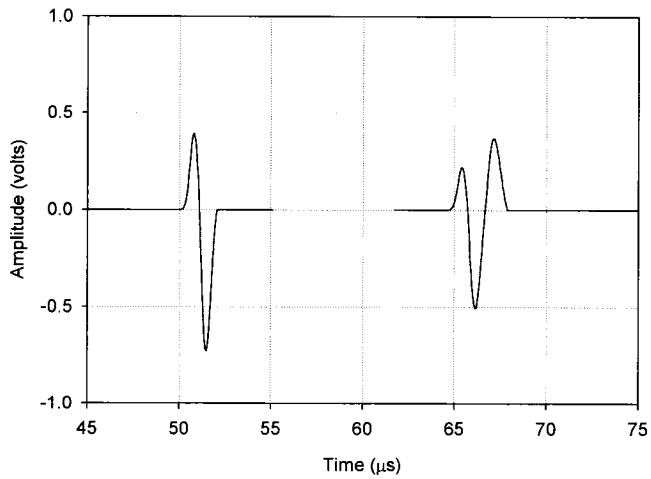

Figure 4.3: Waveforms transmitted through acrylic samples of 108 (left) and 148 mm (right) in length respectively.

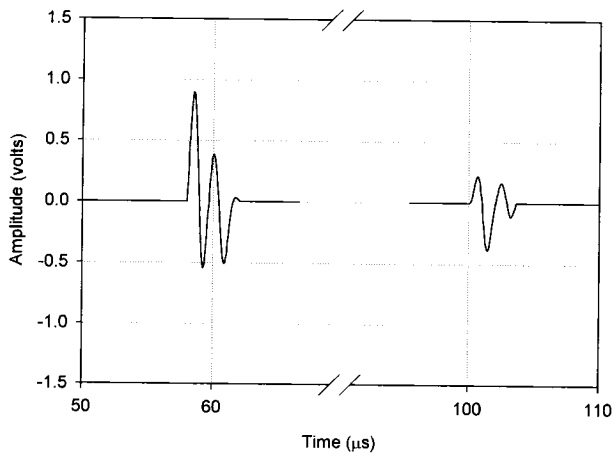

Figure 4.4: Waveforms transmitted through 108 mm long aluminum (left) and acrylic samples (right) inside the triaxial cell.

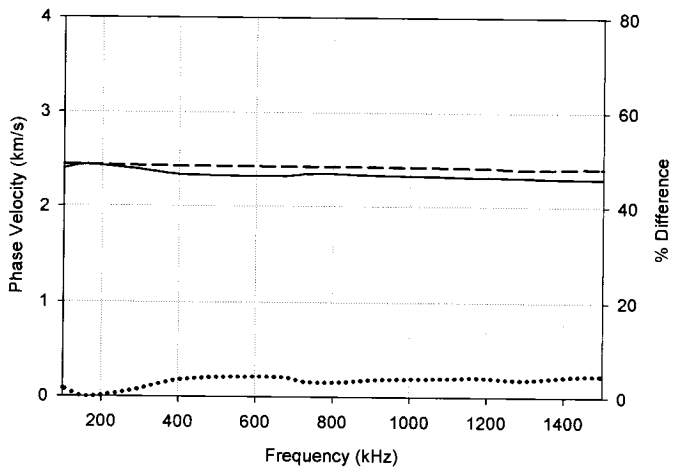

Figure 4.5: Comparison of phase velocities calculated from the two acrylic samples (dashed) and from the aluminum standard and acrylic sample inside the triaxial cell (solid). The percentage difference between the dispersion curves (dotted) is also displayed.

Quality factor was determined using the spectral ratios method derived by Toksoz et al. (1979). The same waveform acquired using the aluminum standard sample was used as the non-attenuating reference measurement shown in Figure 4.4. To be consistent when comparing velocity dispersion and attenuation, a frequency range between 400 and 600 kHz was found to be the most stable and therefore used in these calculations. Phase velocities are used in calculating quality factor for all of the test results.

Adjustments to the acquisition parameters were made for acoustic emission (AE) measurements as outlined by Donald et al. (2004). Line triggering thresholds were calibrated so that approximately 500 to 1000 acoustic emissions were detected over a 30 minute simulated production test. This gave enough acoustic data for further analysis. This number of events was found to give a representative data set. Seismic b-values represent the slope of the recurrence-magnitude relationship from earthquake studies and are inversely related to AE energy and peak amplitudes (Guttenburg and Richter, 1949; Scholz, 1968). This parameter is also used on smaller scale in the laboratory to help interpret mechanical damage in rock specimens (Butt, 1999; Butt and Calder, 1998; Sammonds et al, 1989).

4.4 Experimental results

4.4.1 Stress-strain results

Figures 4.6 and 4.7 show the stress-strain behavior observed during pore pressure reduction for all samples tested. The two main regions of these graphs are noted as the pore collapse and compaction phases and are distinguished by the distinct change in slope of the stress-strain relationship. Inter-particle bonds between grains begin to break down during the pore collapse phase and the strain-hardening behavior reaches its limit before entering the compaction phase. The average inter-granular stress increases on a different microstructure level than the original pore collapse phase, resulting in smaller strains being attained for higher stresses (Nouri et al., 2003; Tronvoll et al., 1997). The strength and stiffness of samples from Batch A (3.5 MPa UCS) and B (7 MPa UCS) are represented from their respective stress-strain behavior and elastic moduli. The inflection point between pore collapse and compaction phases occurs at much lower strain for the samples from Batch B. This inflection point is referred to as the critical pressure (David et al., 1998). The slopes of the pore collapse and compaction phases are also much steeper for samples with higher strength and stiffness. This behavior is to be expected, as the strength of each batch is a function of the amount of Portland cement used in the mixture. Batch B has twice the amount of cement than Batch A, corresponding to its higher elastic moduli.

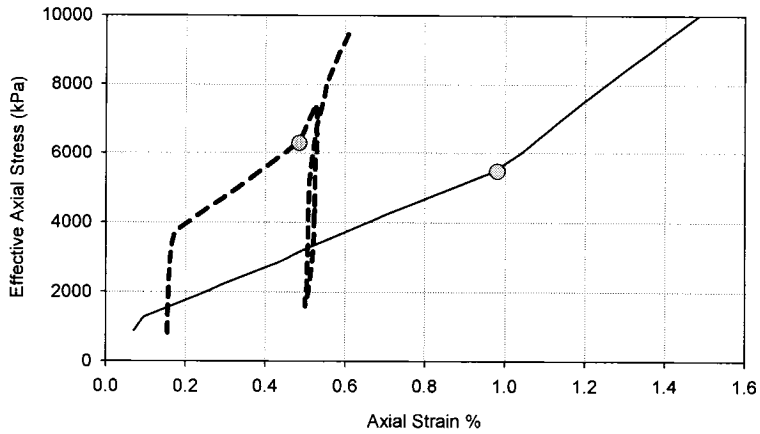

Figure 4.6 Stress-strain relationships for Samples A-1 (solid) and B-1 (dashed) during the simulated production tests. The grey dot represents transition between pore collapse and compaction phases during volumetric failure. P-wave velocity and attenuation data are shown in Figures 4.10 through 4.13.

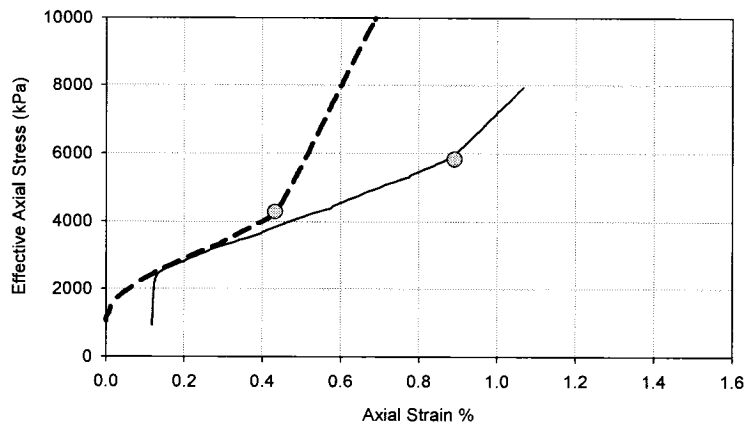

Figure 4.7 Stress-strain relationships for Samples A-2 (solid) and B-2 (dashed) during the simulated production tests. The grey dot represents transition between pore collapse and compaction phases during volumetric failure. Acoustic emissions were monitored during these tests were ultrasonic b-values and cumulative emissions were calculated. AE for these tests are shown in Figures 4.14 and 4.15.

4.4.2 P-wave transmission results

A series of waveforms acquired throughout the simulated production test of Samples A-1 and B-1 are shown in Figure 4.8. The compressional wave signal is relatively consistent at low effective stresses for both samples. Sample A-1 does not appreciably change with regards to its shape compared with B-1 as a function of increasing effective stresses.

First-break arrivals are not evident in this highly dispersive medium and are difficult to determine. Frequency dependence of the velocity measurement is shown in Figure 4.9 for both samples. P-wave velocity results are shown in Figures 4.10 and 4.11. Velocity and effective stresses are presented with respect to test time for the best data distribution. There is approximately 10% absolute difference in velocity between the A-1 and B-1 samples as a reflection of their respective strength and stiffness. For the range of effective stresses however, overall velocity changes were not significant for either sample and only slight variations were noticed for the duration of the test. Conversely, the quality factor data shown in Figures 4.12 and 4.13 give a different result. For Sample A-1, Q increases 30% from 18 to 24 and for B-1, Q increases by over 200% from 15 to 42. The significant change in waveform shape for Sample B-1 from Figure 4.8 is now represented in this dramatic increase of Q.

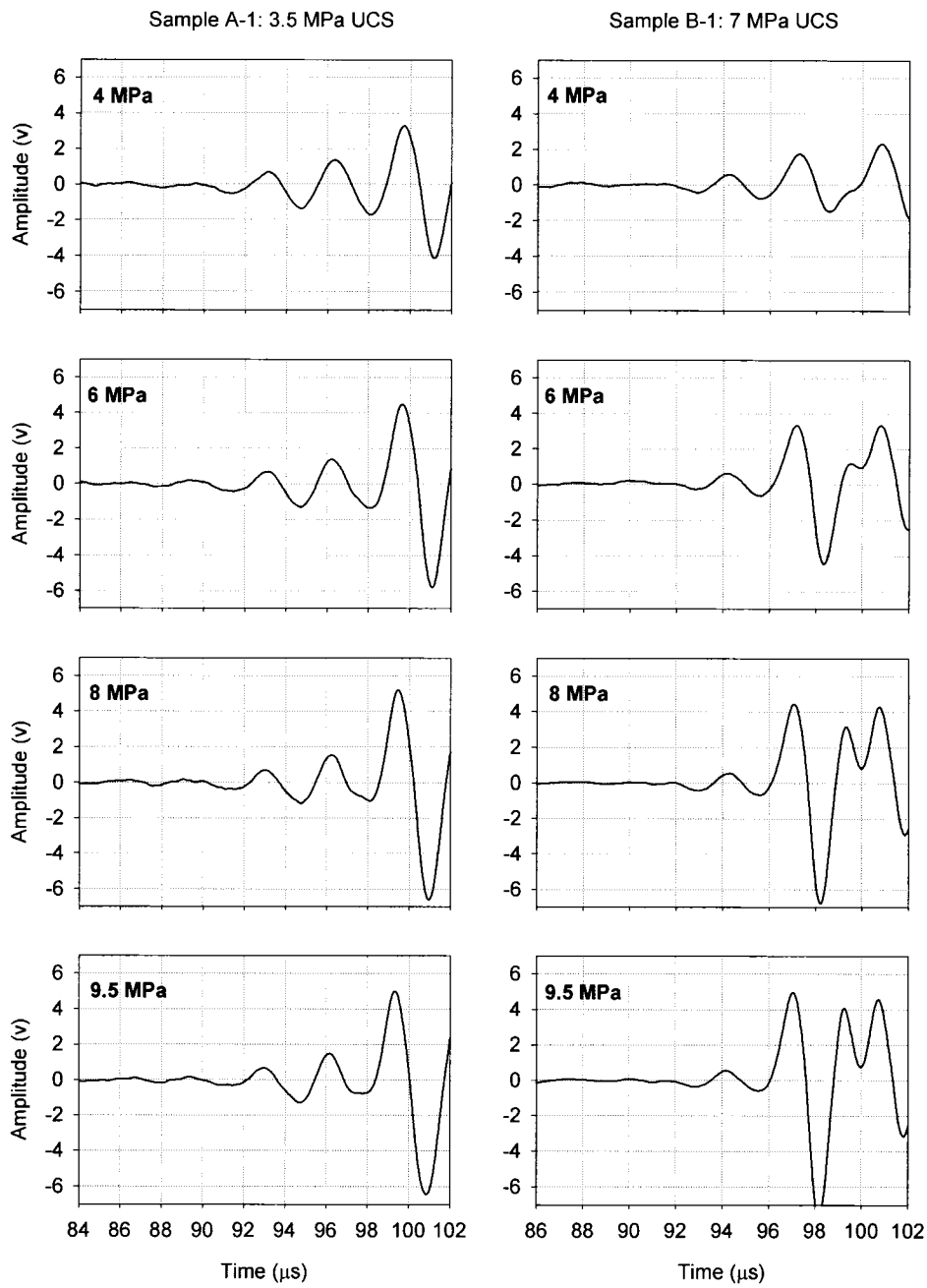

Figure 4.8: Transmitted waveforms through Samples A-1 (left panel) and B-1 (right panel) for successive effective stress increases as indicated (4, 6, 8 & 9.5 MPa). Initial lengths for the samples were 110.4 mm (A-1) and 118.5 mm (B-1).

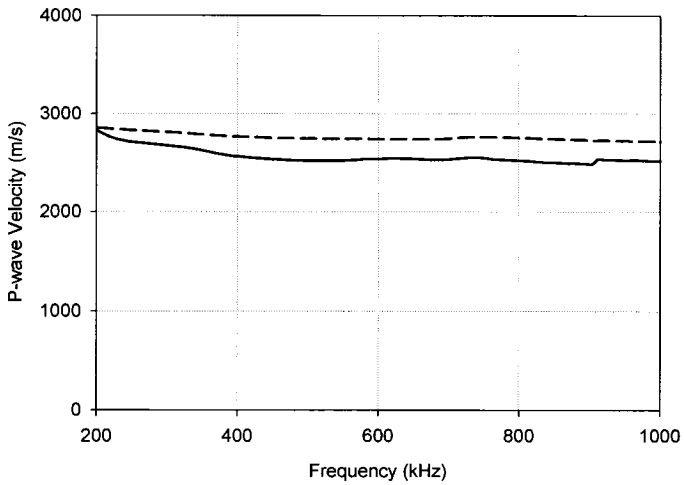

Figure 4.9 Sample velocity dispersion curves for Samples A-1 (solid) and B-1 (dashed) at 9.5 MPa of effective axial stress.

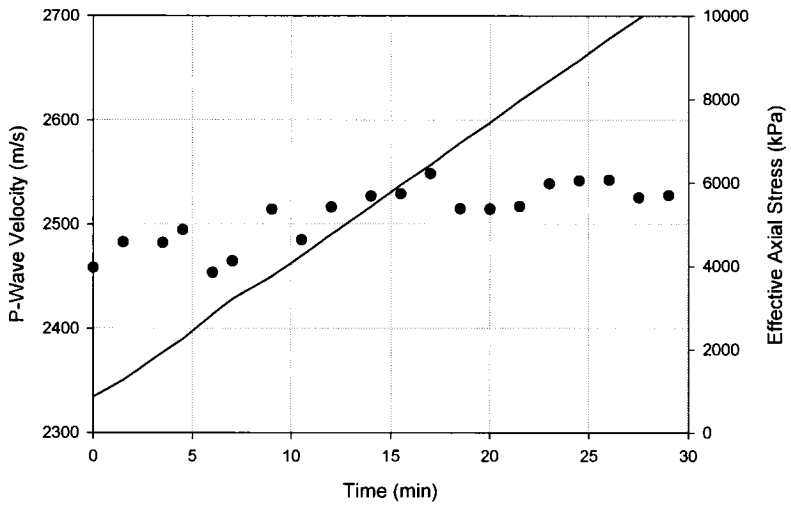

Figure 4.10: P-wave velocity (dots) over the frequency band 400-600 kHz and effective axial stress (solid line) versus simulated production time for Sample A-1.

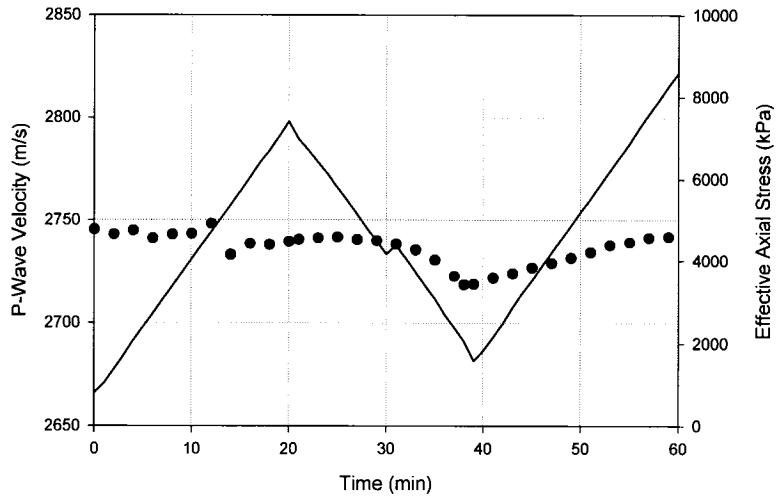

Figure 4.11: P-wave velocity (dots) over the frequency band 400-600 kHz and effective axial stress (solid line) versus simulated production time for Sample B-1.

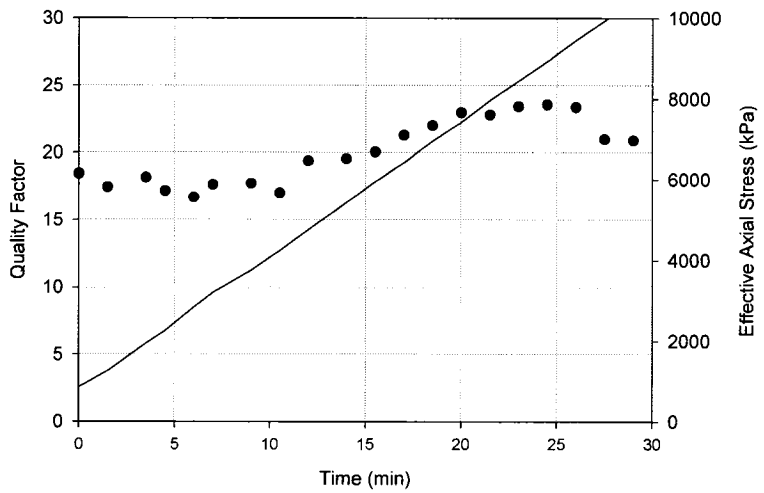

Figure 4.12: P-wave quality factor (dots) over the frequency band 400-600 kHz and effective axial stress (solid line) versus simulated production time for Sample A-1.

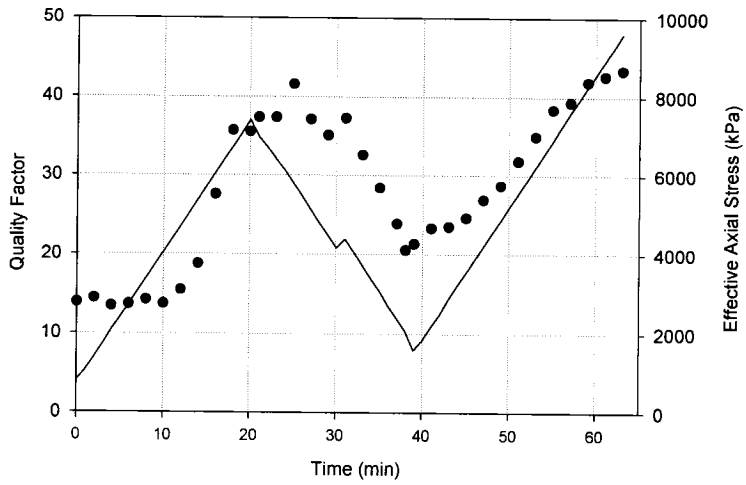

Figure 4.13: P-wave quality factor (dots) over the frequency band 400-600 kHz and effective axial stress (solid line) versus simulated production time for Sample B-1.

4.4.3 Acoustic emission results

Cumulative number of AE and ultrasonic b-values are the two parameters shown in Figures 14 and 15, for Samples A-2 and B-2, respectively. As the amount of total axial strain increases with time and effective stress, the cumulative number of AE also increases accordingly throughout the pore collapse phase. The rate of AE dramatically increases (indicated by the steeper slope of the cumulative AE curve) at the inflection point between phases for both samples. B-values were calculated using the peak amplitude of each AE detected from the sample. For Sample A-2, b-values increase accordingly with axial strain throughout pore collapse and suddenly decrease at the

critical pressure point when the compaction phase begins. This is a much different response than compared with Sample B-2, where b-values decrease throughout pore collapse and start to suddenly increase at the critical pressure point, continuing on through compaction.

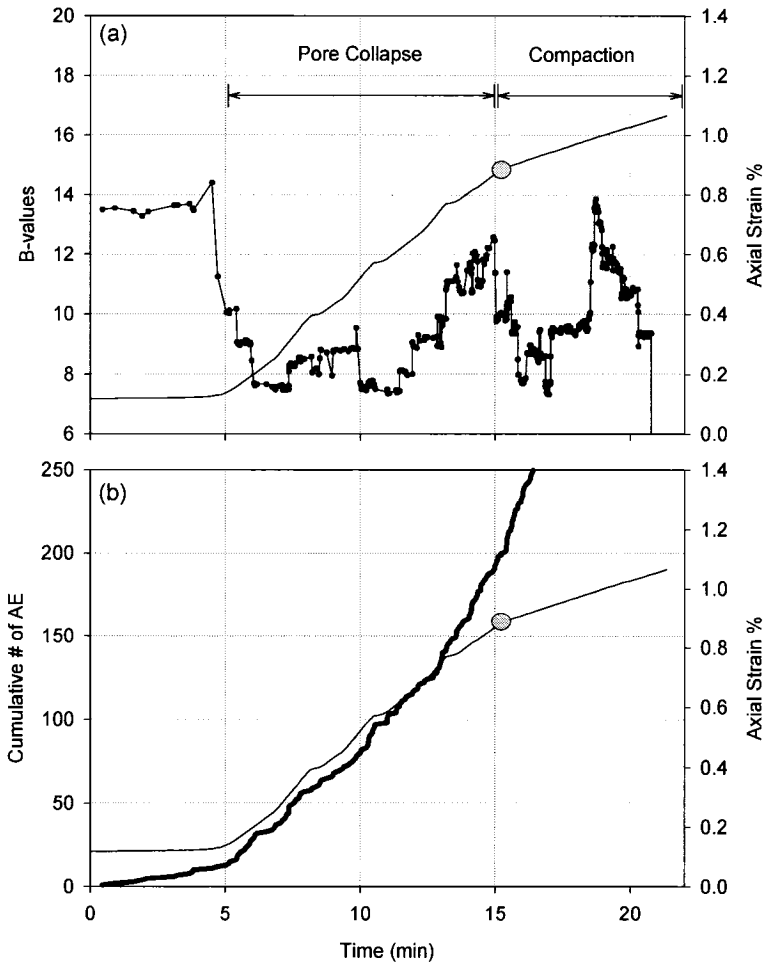

Figure 4.14: (a) Axial strain (solid line) and b-values (dots) versus test time for Sample A-2. (b) Axial strain (solid line) and cumulative number of AE (heavy line) versus test time for the same sample

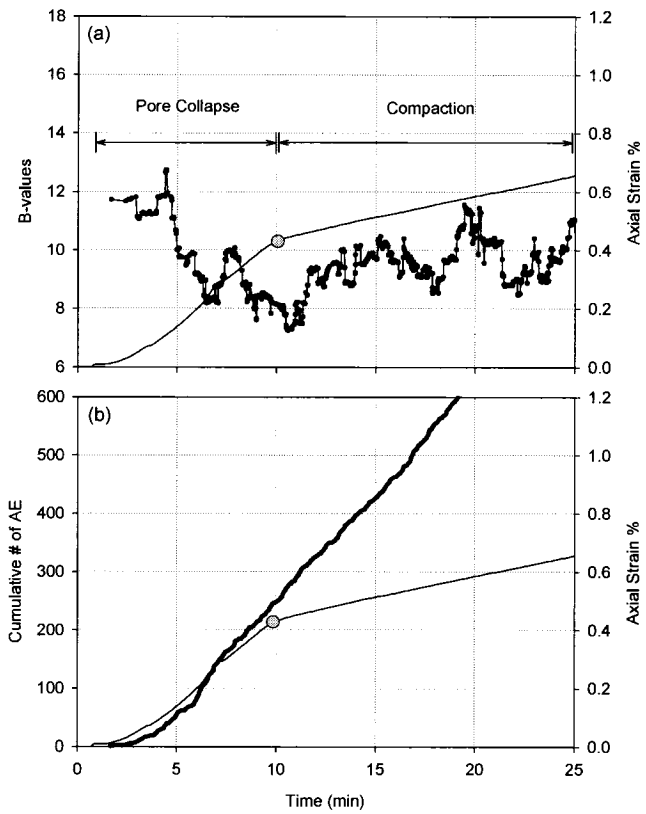

Figure 4.15: (a) Axial strain (solid line) and b-values (dots) versus test time for Sample B-2. (b) Axial strain (solid line) and cumulative number of AE (heavy line) versus test time for the same sample.

4.5 Discussion

P-wave velocity and quality factor measurements are very dependant on the frequency band of interest in high dispersive porous media. For this investigation, the frequency band between 400 and 600 kHz was found to have the most consistent signal strength and was therefore chosen for analysis. Molyneux and Schmitt (2000) used a similar frequency band of 200 to 600 kHz when interpreting their wave transmission results for tightly

packed silica sand. Velocity and quality factor data presented here are higher because of the Portland cement used as binder between sand grains, thereby increasing inter-granular elastic strength. The frequency band used for the results calculation is high enough to reduce the possibility of the pedestal effect abnormally affecting the phase velocity values. Strick (1970) first reported the pedestal effect as the theoretical onset of the wave at low frequencies, also shown in work by Molyneux and Schmitt (2000). As displayed in Figure 4.9, the P-wave velocity of Sample A-1 is the same as B-1 for the lower end of the frequency spectra (200 kHz) at 9.5 MPa of effective stress. As the frequency range approaches 400 kHz, the phase velocity of Sample A-1 becomes less dispersive and gives a more representative value of the true phase velocity.

At initial conditions, the pore pressure is supporting the sand and cement matrix against axial and confining stresses, maintaining it pore structure. At the beginning of simulated depletion, pore pressure is reduced resulting in the pore structure collapsing. The bonds between sand grains are relatively weak, and from observed AE, micro-cracking occurs at the onset of uniaxial strain. The critical pressure point corresponds well to the sharp increase in the rate of AE as also reported in a previous study by David et al. (1998), where AE were recorded during compaction of synthetic sandstone specimens.

B-values continuously rise throughout pore collapse from Sample A-2 indicating progressively weaker AE events (small amounts of strain energy being release at the source). At the critical pressure when the compaction phase begins, b-values sharply

decrease corresponding to larger amplitude AE events. Sammonds et al. (1989) reported the same trend in b-values with axial stress for more competent sandstone, pre- and post-failure of the specimen. B-values calculated with AE from Sample B-2 show a different response. The trend is exactly opposite, where the b-values progressively decrease during the pore collapse phase and start increasing throughout compaction. A comparison of these b-value characteristics suggests that for Sample A-2 (3.5 MPa sandstone), where the grains are more weakly cemented, resistance to pore collapse is less than in Sample B-2 (7 MPa sandstone).

In summary, a comparison of physical and ultrasonic properties for the two synthetic sandstone samples is made below:

- Unconfined compressive strength (UCS) and elastic moduli are higher for the samples from Batch B, indicating high grain-to-grain strength and directly proportional to the amount of Portland cement used in the mixture.
- Permeability and porosity are higher for samples from Batch A than Batch B.P-wave velocity and quality factors are overall higher for the samples from Batch B (7 MPa) than Batch A (3.5 MPa).
- B-values during pore collapse get progressively weaker for Batch A samples, indicating low resistance to volumetric failure.
- B-values during pore collapse get progressively stronger for Batch B samples, indicating greater resistance to volumetric failure.

4.6 Conclusions

Ultrasonic velocity, quality factor and AE parameters have been presented and compared for a set of simulated production experiments under the uniaxial strain condition for two different strength samples. The following conclusions may be drawn from the experimental results.

- Cumulative AE events show a direct correlation with strain behavior throughout the pore collapse phase and dramatically increase at the critical pressure when compaction begins.
- P-wave velocity and quality factor values are more representative of effective stress changes within the stronger (7 MPa) sample than the weaker sample (3 MPa).
- Different responses from ultrasonic b-values between the 3.5 (Sample A-2) and 7 MPa (Sample B-2) sandstones during pore collapse give relative indications of resistance to volumetric failure.
- A new method for calculating phase velocity in triaxial compression cells was applied to experimental data where only one transmitted wave was collected.

The experimental results suggest that 4-D seismic surveys can be better calibrated using continued experimental work as a means of improved characterization for weak sandstone reservoirs. Using quality factor differences as a tool for mapping pore pressure changes in the reservoir may provide more information than just velocity changes.

Further research should therefore be done in how to accurately measure Q *insitu*. Also, we have shown that slight variations in reservoir rock strength, within the ultra-weak range (<10 MPa), may play a bigger role for highly dispersive porous media than previously thought.

4.7 Acknowledgements

The authors would like to thank Petroleum Research of Atlantic Canada (PRAC), Schlumberger Canada Limited and the Natural Sciences and Engineering Research Council (NSERC) for providing funding. Technical assistance from Brian Liekens at the Dalhousie University Petroleum and Geomechanics Laboratory is also appreciated. Discussions with Ken Winkler and Tom Bratton with Schlumberger have been very helpful with the preparation of this work.

4.8 References

Aki, K. and Richards, P.G., (1980), Quantitative Seismology: Theory and Methods, W.H. Freeman publishers.

Aldal, D.A., Instanes, G. and Dahl, T., (2003), Sand Management by Using Ultrasonic Systems at Deep and Ultra Deepwater Installations: SPE 81439.

Bowles, J.E., (1992), Engineering Properties of Soils. Fourth Ed.: McGraw-Hill Inc.

Butt, S.D. and Calder, P.N., (1998), Experimental Procedures to Measure Volumetric Changes and Microseismic Activity During Triaxial Compression Tests: Int. J. Rock Mech. Min. Sci., 35, 249-254.

Butt, S.D., (1999), Development of an apparatus to study the gas permeability and acoustic emission characteristics of an outburst-prone sandstone as a function of stress: Int. J. Rock Mech. Min. Sci., 36, 1079-1085.

David, C., Menendez, B., and Bernabe, Y., (1998), The mechanical behavior of synthetic sandstone with varying brittle cement content: Int. J. Rock Mech. Min. Sci., 35, 759-770.

Donald, J.A., Butt, S.D. and Iakovlev, S., (2004), Adaptation of a Triaxial Cell for Accurate Ultrasonic P-wave Attenuation, Velocity and Acoustic Emission Measurements: Int. J. Rock Mech. Min. Sci. (*in press*).

Guttenburg, B. and Richter, C.F., 1949, Seismicity of the Earth: Princeton Univ. Press.

Johnson, C.F., (1970), A pulse technique for the direct measurement of bar velocity: Twelfth symposium on rock mechanics proceedings, University of Missouri, Rolla, Missouri, November 16-18. Society of Mining Engineers, New York.

Kane, M.R., (2001), Acoustic Rock Stress Estimation: M.S. thesis, Pennsylvania State University.

Khimunin, A.S., (1972), Numerical calculation of the diffraction corrections for the precise measurement of ultrasound absorption: Acustica, 27, 173-181.

Lumely, D.E., Behrens, R.A. and Wang, Z., (1997), Assessing the technical risk of a 4-D seismic project: The Leading Edge, 16, 1287-1291.

Maxwell, S.C. and Urbancic, T.I., (2002), Real-time 4D reservoir characterization using passive seismic data: SPE 77361.

Nouri, A., Vaziri, H., Belhaj, H. and Islam, R., (2003), Effect of volumetric failure on sand production in oil-wellbores: SPE 80448.

Onaisi, A., Samier, P., Koutsabeloulis, N. and Longuemare, P., (2002), Management of stress sensitive reservoirs using two coupled stress-reservoir simulation tools: ECL2VIS and ATH2VIS: SPE 78512

Papadakis, E.P., (1972), Ultrasonic diffraction loss and phase change for broad-band pulses: J. Acoust. Soc. Amer., 52, 847-849.

Prasad, M. and Manghnani, M.H., (1997), Effects of pore and differential pressure on compressional wave velocity and quality factor in Berea and Michigan sandstones, Geophysics, 62, 1163-1167.

Plona, T.J. and Cook, J.M., (1995), Effects of stress cycles on static and dynamic Young's moduli in Castelgate Sandstone: Daemen, J.J.K., and Schultz, R.A., Eds., Rock Mechanics, Proc. 35th U.S. Symp., 155-160.

Plona, T.J., Kane, M.R., Sinha, B., Walsh, J., (2002), Evaluating stress-induced anisotropy and mechanical damage from cross-dipole sonic data using dispersion analysis: SPE/ISRM 78233,.

Sammonds, P.R., Ayling, M.R., Meredith, P.G., Murrell, S.A.F. and Jones, C. (1989), A laboratory investigation of acoustic emission and elastic wave velocity changes during rock failure under triaxial stresses: Rock at Great Depth, Maury & Fourmaintraux, Balkema, Rotterdam.

Tang, X.M., (1993), Waveform inversion of seismic velocities and attenuation from low-frequency waves in cylindrical bars: Geophysics, 58, 1525-1531.

Toksoz, M.N., Johnston, D.H. and Timur, A., (1979), Attenuation of seismic waves in dry and saturated rocks; I, Laboratory measurements: Geophysics, 44, 681-690.

Tronvoll, J., Papamichos, E., Skjaerstein, A. and Sanfilippo, F., 1997, Sand production in ultra-weak Sandstones: Is sand control absolutely necessary?: SPE 39042.

Scholz, C.H., 1968, The frequency-magnitude relation of microfracturing in rock and its relation to earthquakes: Bull. Seis. Soc. Am., 58, 399-415.

Winkler, K.W., (1997), Acoustic evidence of mechanical damage surrounding stressed boreholes: Geophysics, 62, 16-22.

Chapter 5: Non destructive techniques to determine the effective stress coefficient of porous sandstone

This paper has been submitted to the Journal of Canadian Petroleum Technology (JCPT). The main author is Mr. Paul K. Frempong, co-authored by Dr. Stephen D. Butt. The figure numbers and reference formats have been altered to match the formatting guidelines set out by Dalhousie University compared with the submitted manuscript to JCPT. Sample names in the figure and table captions have been changed to be consistent with the rest of the thesis content.

5.1 Abstract

The concept of effective stress coefficient, 'n', is critical for the study of stress and pressure-dependent behaviour of rocks. However, there are some disagreements among different authors on the value, behavior and estimation methodology of the effective stress coefficient. Moreover, this parameter (n) is relatively unknown and very difficult to estimate. Most traditional methods of estimation give conflicting and unacceptable values. It is therefore often assumed to be equal to one, for convenience, thus compromising the accuracy of pore pressure and saturation predictions in reservoirs. We present a general review of 'n' and give a theoretical proof that 'n' is less than one for porous rocks. We also introduce a simple laboratory methodology to measure a more

reliable value of 'n' employing compressional ultrasonic wave velocity (V) and attenuation quality factor (Q). We then confirm the value of 'n' experimentally by using this laboratory method to estimate 'n' of quartz sandstone. We compare our experimental value of 'n' to both theoretical and practical results obtained from other literatures that used different estimation methodology. We argue from our experimental results that: (i) 'n' is not one but varies from zero to one, (ii) there is no single value of 'n' for a particular reservoir rock, (iii) 'n' depends on internal factors (porosity, pore geometry) and external factors (pore pressure and confining pressure) of the rock, (iv) velocity derived 'n' and quality factor derived 'n' are different for the same rock and (v) for this quartz sandstone, the velocity derived 'n' is smaller and also less sensitive to changes in pressure than quality factor derived 'n'.

5.2 Introduction

Most of the pioneering work on what is now known as the effective stress coefficient was done by Terzaghi (Terzaghi, 1943), who showed that most rocks are porous in a varying degree because of the pore spaces and micro cracks within them. The effect of these pores on the strength of rocks has widely been documented (Terzaghi, 1943; Brandt, 1955; Biot, 1955; Zimmerman et al., 1986; Berryman, 1992). A rock with a few or without pores is considerably stronger than the porous ones since pore spaces are unsupported within the rock. With the presence of unsupported spaces the intact rock between the pores has to take larger loads to sustain an overall applied stress. This

important phenomenon has a direct bearing on the effective stress of the rock (Figure 5.1a and 5.1b).

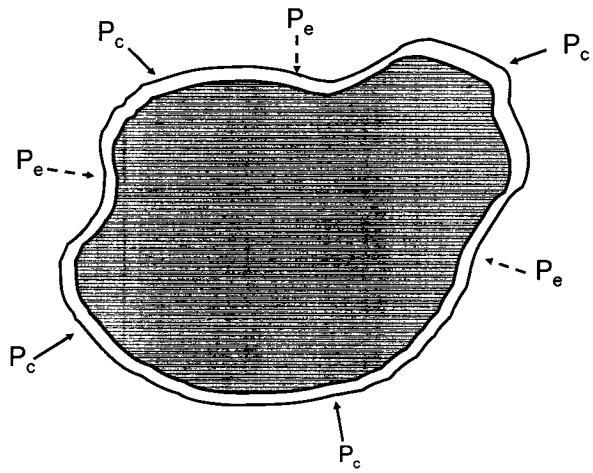

Figure 5.1a: Illustration of effective stress for isotropic, non porous, linear elastic rock subjected to confining pressure (P_c) on the outer surface. The effective stress (P_e) is equal to confining pressure (P_c)

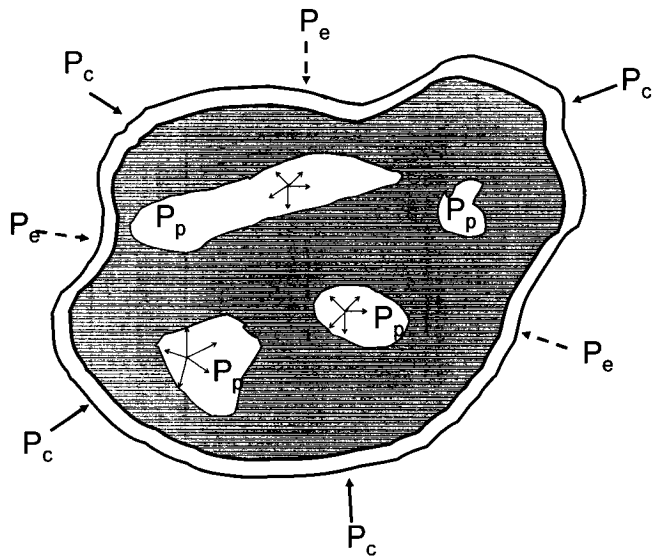

Figure 5.1b: Illustration of effective stress showing an ideal case of a porous rock subjected to confining pressure (P_c) on the outer surface and pore pressure at the inner pore surface.

Ideally $P_e = P_c - P_p$, but considering the effective stress coefficient, 'n', $P_e = P_c - nP_p$. Thus, the effective stress (P_e) is not directly equal to the differential pressure (P_d). Many writers (Landro and Kvam, 2002; Todd and Simmons, 1972; Robin, 1973; Carroll and Katsube, 1983; Christensen and Wang, 1985; Zimmerman et al., 1986; Gangi, 1991; Berryman, 1992; Gurevich, 2004) have highlighted the problem caused by this phenomenon and it includes increase in the uncertainties associated with the estimated pressures and saturation in reservoirs. According to Prasad and Manghnani (1997), the relation between effective stress (P_e), pore pressure (P_p) and confining pressure (P_c) should properly be written as:

$P_e = P_c - nP_p$

Where, 'n' is the effective stress coefficient or coefficient of internal deformation,

P_c is the confining pressure

P_p is the pore pressure

Thus, effective stress is equal to the differential pressure in a special case when 'n'=1 (i.e. $P_d = P_e = P_c - P_p$). This proposition has widely been embraced both in practice (Prasad, 1998) and in theory (Gurevich, 2004). In fact, most laboratory measurements show that effective stress coefficients are lower than one (Todd and Simmons, 1972; Christensen and Wang, 1985; Prasad, 1998; Siggins and Dewhurst, 2003). However, some authors disagree and postulate that 'n' is equal to one (Zimmerman et al., 1986). These are not the only disagreements on the value of 'n'. There are also questions like:

(i) What are the appropriate methods that should be used to estimate 'n'?

(ii) Does 'n' vary or remain constant for one type of reservoir rock?

(iii) What external and internal factors of rocks, if any, influence the value of 'n'? Few answers to these questions are found in the literature and the objective of this paper is to provide answers to these questions that are of general interest to the reservoir engineer. Most traditional methods of estimation give conflicting and unacceptable values of 'n'. It is therefore often assumed to be equal to one, for convenience, thus compromising the accuracy of pore pressure predictions in reservoirs. Recent theoretical work by Gurevich (2004) on effective stress coefficient suggests that further experimental work should be done on real and natural rocks to establish the effective stress coefficient. In this study, both a theoretical derivation and a laboratory experiment have been performed on natural rocks having low-permeability and high-porosity in order to estimate the effective stress coefficient and to establish the factors that affect this parameter.

5.3 Reviews and theoretical derivation of 'n'

In this section, we present how the theory of elasticity could be modified when the fluid in the pore spaces is exerting opposite pressure during rock compression deformation process. For simplicity, all deformations are assumed to take place under constant temperature (isothermal). In the deformation of isotropic, linear, elastic and non porous rocks, the stress and strain are related by Hooke's law as:

$$\sigma_{ij} = \lambda \delta_{ij} \varepsilon_{aa} + 2\mu \varepsilon_{ij} \qquad (5.1)$$

Where, ε_{ij} are the elements of the strain tensor,

σ_{ij} are the elements of the stress tensor,

ε_{aa} is the volumetric strain summed over repeated index,

δ_{ij} is the Kroenecker's delta and is equal to 0 if $i \neq j$, and 1 if $i = j$,

and λ is the Lame constant.

From equation 1, the strain is given by:

$$\varepsilon_{ij} = \frac{\sigma_{ij}}{2\mu} - \frac{\lambda \delta_{ij} \varepsilon_{aa}}{2\mu} \tag{5.2}$$

The bulk modulus, 'K', is defined as the ratio of hydrostatic stress, 'σ_o' to volumetric strain, thus:

$$\sigma_0 = \frac{1}{3}\sigma_{aa} = K\varepsilon_{aa} \tag{5.3}$$

Equation (5.3) implies that:

$$\varepsilon_{aa} = \frac{1}{3K}\sigma_{aa} \tag{5.4}$$

The shear modulus, 'μ', is defined as the ratio of shear stress to shear strain, thus:

$$\sigma_{ij} = 2\mu\varepsilon_{ij} \text{ for } i \neq j \tag{5.5}$$

The young modulus, 'E', is also defined as the ratio of extensional stress to extensional strain in a uni-axial stress state, thus:

$$\sigma_{zz} = E\varepsilon_{zz} \tag{5.6}$$

The stresses in all the other directions are zero (for example $\sigma_{xx}=\sigma_{yy}=\sigma_{xy}=\sigma_{xz}=\sigma_{yz}=0$).

Substituting equation (5.4) into (5.2) yields:

$$\varepsilon_{ij} = \frac{\sigma_{ij}}{2\mu} - \frac{\lambda\sigma_{aa}}{6\mu K}\delta_{ij} \tag{5.7}$$

But the relationship between the elastic constants, 'K', 'λ' and 'μ' is given by:

$$\lambda = K - \frac{2}{3}\mu \qquad (5.8)$$

Also for a rock under various compression forces the total effective stress, 'P_e' is given by (Geertsma, 1953: Gurevich, 2004):

$$P_e = -K\theta \qquad (5.9)$$

Where, θ is the total dilatation and 'K' is the Bulk modulus as defined above (i.e. fractional change in volume)

Substituting equation (5.8) into equation (5.7) yields

$$\varepsilon_{ij} = \frac{1}{2\mu}(\sigma_{ij} - \frac{1}{3}\sigma_{aa}\delta_{ij}) + \frac{1}{9K}(\sigma_{aa}\delta_{ij}) \qquad (5.10)$$

Equation 5.9 represents a case where the rock has no pore pressure exerted on the pore surfaces (Figure 5.1a). In a situation where the pore pressure has effect on the strain as in figure 5.1b, then, the pore pressure should be incorporated into the isotropic condition in equation 5.10. Assuming the strain is linearly related to the pore pressure, then, the general tensor expression for strain in terms of stresses and pore pressure can be written as:

$$\varepsilon_{ij}^{P_p} = \frac{1}{3H}(P_p\delta_{ij}) \qquad (5.11)$$

Where, ε_{ij}^{Pp} is the strain due to pore pressure which depends on a new effective modulus H introduced by Biot (1941). In other words, there is an incremental pore pressure induced in the rock that resists the volumetric strain. Thus the total strain, taking pore

pressure into consideration, is given by the sum of all the pressures (equation 5.10 and 5.11). Thus:

$$\varepsilon_{ij} = \frac{1}{2\mu}(\sigma_{ij} - \frac{1}{3}\sigma_{aa}\delta_{ij}) + \frac{1}{9K}(\sigma_{aa}\delta_{ij}) - \frac{1}{3H}(P_p\delta_{ij}) \qquad (5.12)$$

The negative sign represents the direction of the pore pressure with respect to the confining pressure. From equation 5.12, it is clear that, when a piece of porous rock is subjected to stresses, there are three terms that contribute to the total strain.

The first term is the strain due to deviatoric stress given by:

$$\varepsilon_{ij}(1) = \frac{1}{2\mu}(\sigma_{ij} - \frac{1}{3}\sigma_{aa}\delta_{ij}) \qquad (5.13)$$

This strain depends on the effective shear modulus, 'μ', of the rock without pores pressure.

The second term is the strain due to hydrostatic stress given by:

$$\varepsilon_{ij}(2) = \frac{1}{9K}(\sigma_{aa}\delta_{ij}) \qquad (5.14)$$

This strain depends on the effective bulk modulus, 'K', of the rock without pore pressure.

The last term in equation 5.12 is the strain due to pore pressure given by:

$$\varepsilon_{ij}(3) = -\frac{1}{3H}(P_p\delta_{ij}) \qquad (5.15)$$

This strain depends on the new effective modulus, 'H', defined by Biot in 1941. From equation 5.12, the total volumetric strain, 'θ', which takes into account the effect of all the pressures, including pore pressure, is given by:

$$\theta = \varepsilon_{11} + \varepsilon_{22} + \varepsilon_{33} = \frac{1}{K}(\frac{\sigma_1 + \sigma_2 + \sigma_3}{3}) - \frac{1}{H}P_p \qquad (5.16)$$

But the confining pressure is the average of the three principal stresses, thus:

$$P_c = \frac{1}{3}(\sigma_{11} + \sigma_{22} + \sigma_{33}) \tag{5.17}$$

Therefore substituting equation 5.17 into 5.16 implies that

$$\theta = \frac{1}{K}(P_c - \frac{K}{H}P_p) \tag{5.18}$$

From equation 5.18, it is seen that the volumetric strain has been expressed as a linear combination of pore pressure and confining pressure. This volumetric strain, according to equation 5.18, increases with confining pressure and decreases with pore pressure. This shows that, both pore pressure and confining pressure affect the volumetric strain of the total aggregate of the rock. A single new variable, 'P_e' that describes the effective deformation of the whole solid in terms of the confining stress and pore pressure can therefore be defined from equation 5.18 as;

$$\theta K = (P_c - \frac{K}{H}P_p) \tag{5.19}$$

But θK is the volumetric strain times the Bulk modulus, which is equal to effective stress, 'P_e', given in equation 5.9. This implies that:

$$P_e = (P_c - \frac{K}{H}P_p) \tag{5.20}$$

Thus:

$$P_e = P_c - nP_p \tag{5.21}$$

where, 'n' is the effective stress coefficient and its value depends on both H and K. K and H are themselves defined in accordance with laboratory test. This parameter 'n' is not well known and its value has been a source of disagreement among researchers.

5.4 Experimental value of 'n'

Based on laboratory experimental results from soil samples, Terzaghi (Terzaghi, 1943) suggested that, 'n' should be equal to one. His interpretation was that both grain boundaries and grain contacts have an effective porosity of one, which is to say, water at a pressure P_p fills all space between grain contacts. Other writers (Brandt, 1955; Biot, 1955) dispute Terzaghi's interpretation. According to Brandt (1955), 'n' varies from zero to one and depends not only on pore spaces but also on pore geometry and the physical properties of the constituent matrix of the rock. Biot pore elastic theory (Biot, 1955) also predicts 'n' to be less than one and can be calculated from the formula:

$$n = 1 - c_r / c_b \tag{5.22}$$

Where, c_b is the bulk compressibility and,

c_r is the compressibility of the rock matrix.

However, Biot (1955) suggested an approximate constant value of 'n' to be 0.90 for all rocks. This value is known in the literature as Biot constant or Biot coefficient, 'α'. Other researchers (Geertsma, 1953; Skempton, 1960) have suggested similar relationship for calculating 'n'. For example, Geertsma (1953) and Skempton (1960) proposed that 'n' can be calculated from the formula:

$$n = 1 - K / K_0 \tag{5.23}$$

where K and K_0 are the effective and grain bulk modulus respectively. The derivation of Geertsma (1953) was disputed by Suklje (1969) who included porosity (ϕ) as part of the Geertsma's relation and showed that:

$$n = 1 - (1 - \phi)K / K_0 \qquad (5.24)$$

Nur and Byerlee (1971) also suggested that 'n' varies between zero and one using a different derivation method. They assume an isotropic aggregate of solid material with connected pores. The outside of the solid is subject to confining pressure P_c and the pores are subject to pore pressure P_p. According to Nur and Byerlee (1971) both of these pressures have opposing effect on the volumetric strain of the aggregate, leading to a conclusion that 'n' should not be equal to one. The disagreements among various researchers on the value of 'n' and how it should be estimated still continues. Recently, Gurevich (2004) presented impressive and very detailed theoretical insights into the value of 'n' and concluded that, for most variety of rock properties, 'n' could be assumed to be one. However, his theory was based on two main assumptions:

(i) the grain matrix material was assumed to be homogeneous.

(ii) the material is linearly elastic within the range of stresses and pressures that were considered.

However these two assumptions are not valid in practical situation for real natural rocks. Other empirical relationships have been put forward by many authors (Todd and Simmons, 1972; Christensen and Wang, 1985; Prasad, 1998) relating 'n' to some physical properties like acoustic wave velocity, attenuation quality factors and dispersion characteristics. Todd and Simmons (1972) stated that 'n' could empirically be determined, and that the mathematical equation to describe 'n' based on particular physical quantity, 'A' is given by:

$$n = 1 - \left[\frac{\partial A}{\partial P_P}\right]_{P_d} \div \left[\frac{\partial A}{\partial P_d}\right]_{P_P} \tag{5.25}$$

where A is the physical property in question

P_p is the pore pressure

P_d is the differential pressure

$\left[\frac{\partial A_P}{\partial P_P}\right]_{P_d}$ is the gradient of the quantity 'A' verses pore pressure curve at constant differential pressure,

$\left[\frac{\partial A_P}{\partial P_d}\right]_{P_P}$ is the gradient of the quantity 'A' verses differential pressure curve at constant pore pressure.

Depending on the particular physical property 'A' of the rock, these pressure curves may or may not be linear. For non linear ones, it indicates that, the gradient of the pressure curve depends on the pore pressure and the differential pressure. This is the case for the acoustic velocities and attenuation quality factor that we investigated.

5.5 Laboratory experiment to determine 'n'

The theoretical value of 'n' was verified experimentally on real natural sandstone rocks as suggested by Gurevich (2004). This was done to establish the experimental value of the effective stress coefficient of natural rocks and to find the factors that affect this parameter. The parameter 'A' in equation 5.25 was assumed to be:

(i) P-wave velocity (V_p)

(ii) Attenuation quality factor (Q_p)

5.5.1 The sample

A suite of geo-mechanical and acoustic laboratory experiments were performed under varying degree of pore pressure and confining pressure. The samples (Figure 5.2a) used for the experiments were high-porosity, low-permeability sandstone core of dimensions 54mm by 108mm. The geo-mechanical and petrophysical properties of the sample are given in table 5.1. The samples were from the Cumberland Basin onshore Nova Scotia. It was found to contain fine grained rounded shapes quartz of average size of about 160 microns. The thin section is shown in Figure 5.2b. The sample was strongly cemented and very tight with few pores. Samples were drilled perpendicular to the lamination/bedding plane so that samples of maximum heterogeneity are achieved.

Table 5.1 Properties of the quartz sandstone

Porosity	Permeability	UCS	E_{static}	υ_{static}
15%	17 mD	100 MPa	5.2 GPa	0.3

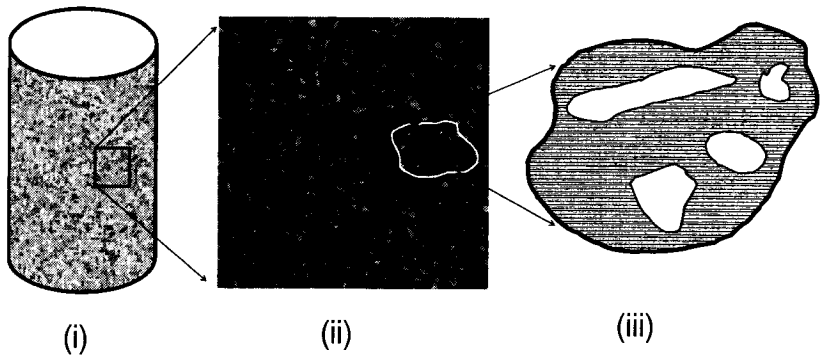

Figure 5.2a: Schematic of the: (i) 108 by54 mm core sample used in the experiment with (ii) the thin section and (iii) some distribution of pore spaces within the samples (not to scale)

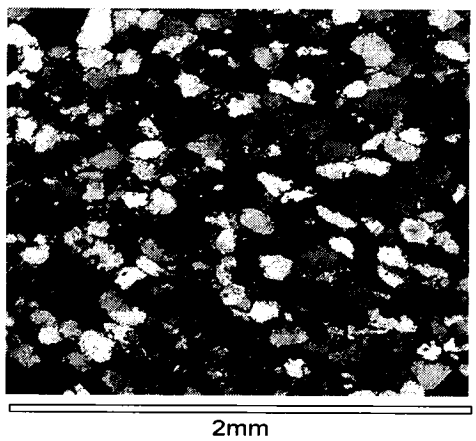

Figure 5.2b: Thin section of the sample (quartz sandstone) under cross polarized light (XPL)

The sample preparation, coring, grinding and polishing are not detailed in this paper. However, such details can be found in the ASTM standard (ASTM, 2004). Again the detailed geological, petrophysical and geomechanical properties of this type of sandstone sample have been documented elsewhere (Ryan, 1998; Frempong and Donald, 2003).

The core sample with the thin section and pore geometry are shown in Figure 5.2a and 5.2b.

5.5.2 Experimental apparatus

The experimental apparatus was developed purposely for the study of P-wave velocity, attenuation quality factor and acoustic emissions during triaxial tests (Donald et al., 2004). It is made up of a triaxial apparatus coupled with acoustic system that can simultaneously measure the acoustic, geomechanical and petrophysical characteristics of a rock core sample. The scaled triaxial cell is shown in figure 5.3a and the photograph of the whole apparatus is shown in figure 5.3b. It operates on a jacketed core sample placed inside the triaxial cell. The axial stress, confining pressure and pore pressure may be increased to *in-situ* conditions. The pressures can also be increased and decreased whilst simultaneously sending acoustic signals through the sample. Two 1-MHz P-wave piezoelectric transducers were mounted inside custom platens positioned outside the triaxial cell, which are centered and aligned with the core axis of the sample. This arrangement enables the pulsing of direct P-waves along the axes of the core samples. Validation of this apparatus has been done by both numerical and experimental modelling (Donald et al., 2004) to ensure that unwanted resonant shape modes (Johnson, 1970) and diffraction errors (Khimunin, 1972; Papadakis, 1972) are eliminated. Therefore the waveforms recorded at the receiving transducers can be considered as plane compressional waves that propagated along the lengths of the core samples.

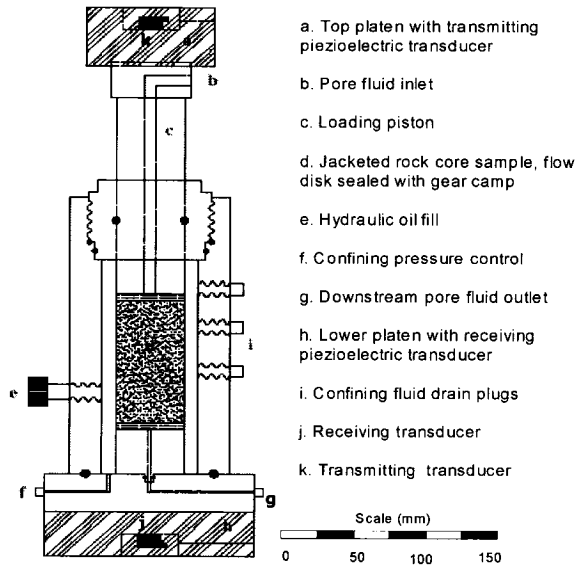

Figure 5.3a: The triaxial cell with centrally mounted acoustic transducers used for the experiment

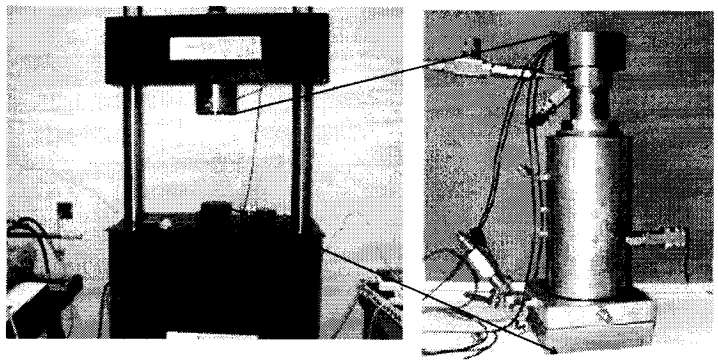

Figure 5.3b: Photograph of the loading Machine with a triaxial cell

5.5.3 Experimental methods

The experiments were performed according to the ASTM standard (ASTM, 2004) for triaxial testing. Two sets of experiments were conducted. The plan of each of the

experiment and the pore pressure, confining pressure and differential pressure variation is shown in table 5.2. Figure 5.4 and 5.5 also show the pressure regime during test 1 and test two respectively. The sample was first jacketed with rubber tubing to isolate it from the confining pressure fluids during the experiment. It was then heat shrunk before it was loaded into the tri-axial chamber and connected to the various pressure pumps that control pore pressure and confining pressure. Two 1-MHz transducers were connected and glued to two steel plates and were axially mounted on top and bottom sample with platens. The leads of the transducers were connected to a computer based acoustic system. A pulse transmission technique (Birch, 1960) was used to send waves through the sample. In the first experiment, the confining pressure was kept constant at 2MPa whilst the pore pressure and the differential pressure were increased to 60MPa and 62MPa respectively. In the second experiment the pore pressure was kept constant at 2MPa and the confining pressure and differential pressure were increased to 100MPa and 98MPa respectively. Ultrasonic signals were passed through the rock at every 5 minutes interval. The acoustic data were collected at the rate of 25ns per sample (40MHz) on a PC based digitizer.

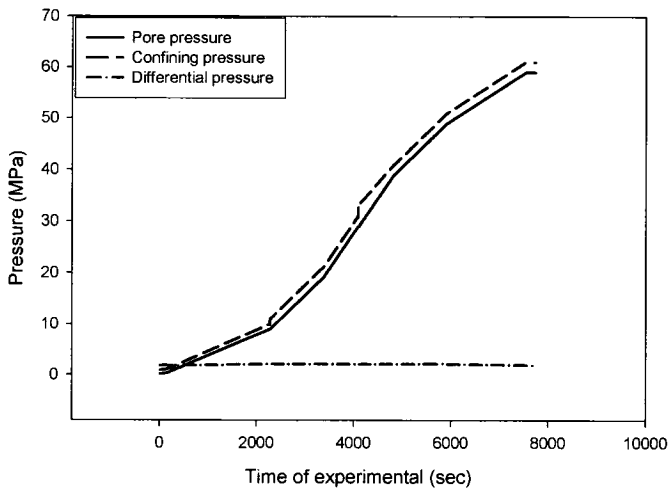

Figure 5.4: Pressure changes during experiment 1: Confining and pore pressure increase whilst differential pressure remains constant.

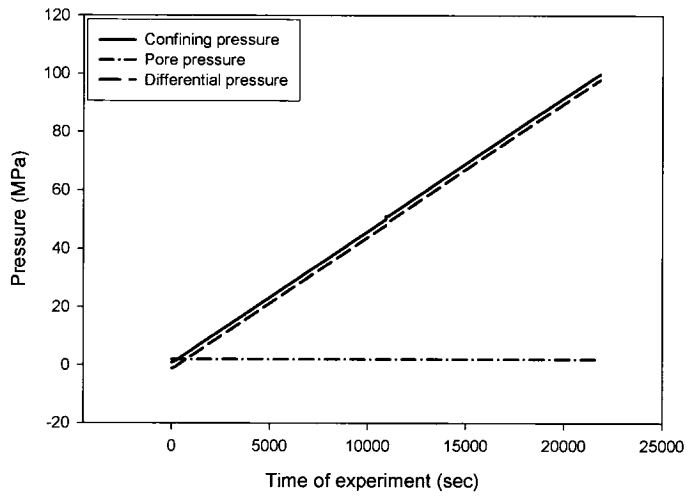

Figure 5.5: Pressure changes during experiment 2: Confining and differential pressure increase whilst pore pressure remains constant.

Table 5.2: Experimental plan

	Pore Pressure	Confining Pressure	Differential Pressure
Experiment 1	Constant pore pressure at 2MPa	Increasing confining pressure up to 100MPa	Increasing differential pressure up to 98MPa
Experiment 2	Increasing pore pressure up to 60MPa	Increasing confining pressure up to 62MPa	Constant differential pressure up to2MPa

5.5.4 Data analysis and calculations

The digitized waveforms collected were stacked to improve signal to noise ratio and to make it easier to pick arrival times. The acoustic signals at varying confining pressure is shown in Figure 5.6. The stacked waveform was plotted and any visible DC offset removed (Figure 5.7). The velocity was found by simply dividing the length of the sample by the arrival time after subtracting the platen travel time and a 2μsec inherent delay of the pulsar and oscilloscope. The quality factor was found through spectral ratio techniques (Toksoz et al., 1979) over a frequency range of 600KHz to 1400KHz. The spectral ratio technique was used because it has been known to be a very robust method in the estimation of attenuation quality factor (Butt et al., 2000) Moreover, the acoustic amplitude varies depending on sample conditions and there was no need for correction with regard to sample geometry and or diffraction error (Butt, 2001). The details of the spectral ratio technique are given elsewhere (Toksoz et al., 1979, Butt et al., 2000). Comparison of the sandstone and aluminum signal is shown in Figure 5.7. The Fast

Fourier Transform (FFT) of the acoustic signal, the spectral ratios between sample and aluminum standard and the line of best fit are shown in figures 5.8, 5.9, 5.10 respectively.

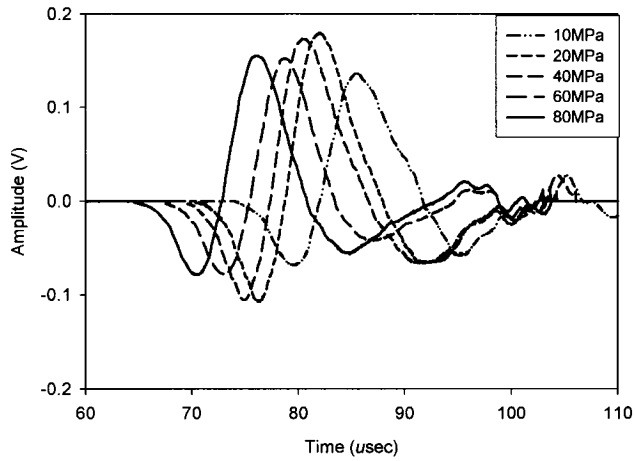

Figure 5.6: Comparison of acoustic signal at different confining pressure

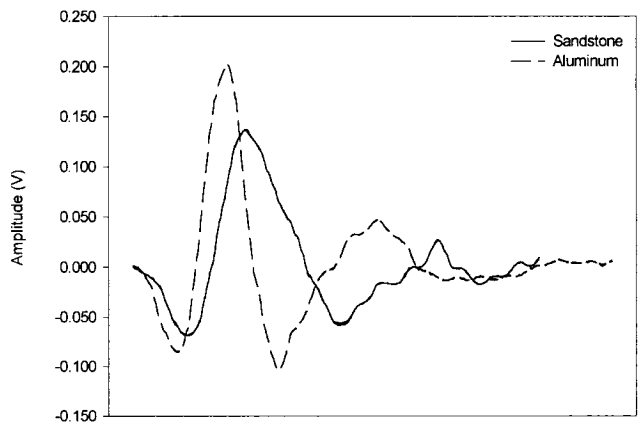

Figure 5.7: Comparison of aluminum and sandstone signals at 10MPa confining pressure

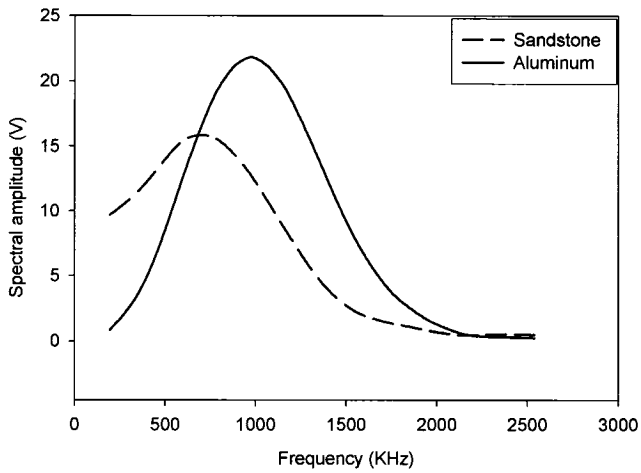

Figure 5.8: FFT of both aluminum and sandstone signals – Spectral amplitude in voltage

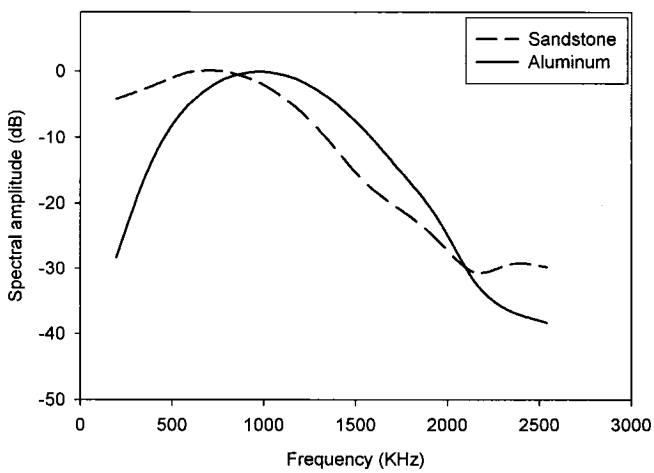

Figure 5.9: Comparing the FFT of aluminum and sample signal at decibel scale.

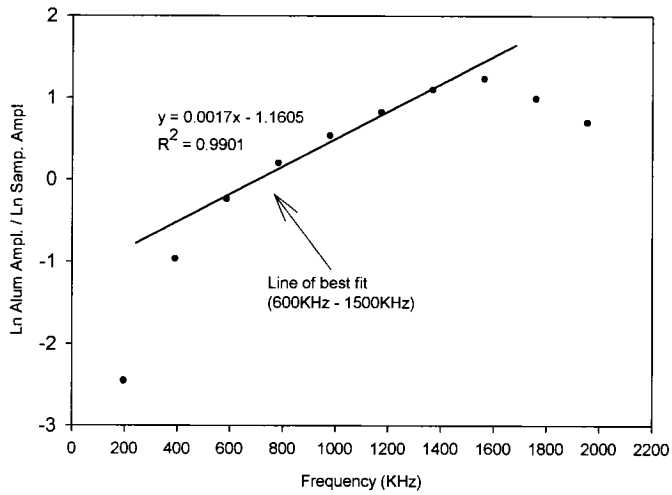

Figure 5.10: Estimation of quality factor – The line of best fit is in the greatest signal energy concentration (600KHz -1500KHz)

5.6 Results and discussions

The V and Q values were considered as the physical property 'A' of the reservoir rock. Gradients of the graphs of velocity versus pore pressure at constant differential pressure (Figure 5.11) and that of velocity versus differential pressure at constant pore pressure (Figure5.12) were used to calculate 'n', applying equation 5.25. Similar graphs for attenuation quality factors are also shown in Figures 5.13 and 5.14. Gradients of the graphs of quality factors versus pore pressure at constant differential pressure and that of quality factor versus differential pressure at constant pore pressure were also used to calculate 'n'. Some writers (Prasad and Manghnani, 1997) believe that the two curves duplicate themselves at higher pore pressures. They argue therefore that, the gradient of

the velocity verses differential pressure curve at constant pore pressure could be read from the velocity versus pore pressure curve at constant differential pressure, at the point where pore pressure is equal to zero. This assumption was not followed because it could lead to a lower estimate of 'n' especially at higher pressures close to the Uni-axial Compressive Strength (UCS) of the rock.

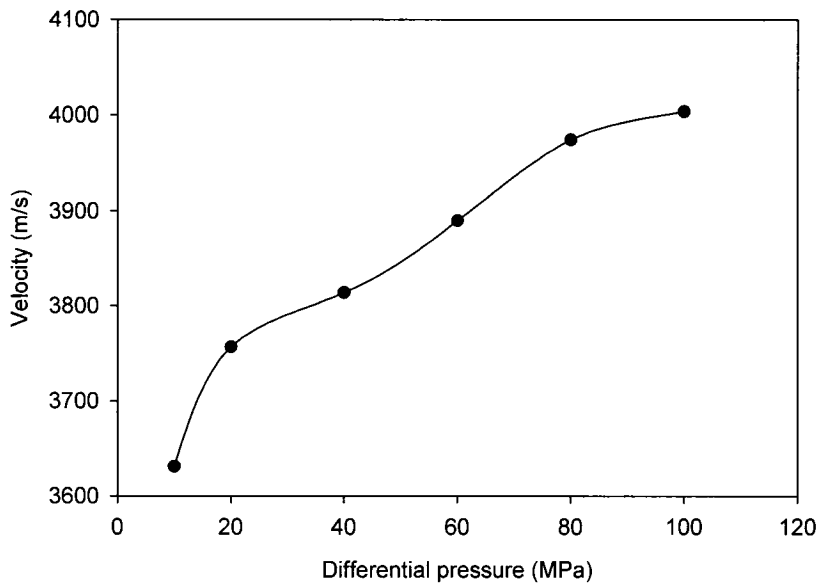

Figure 5.11: Velocity verses differential pressure at constant pore pressure. Note that increasing differential pressure at constant pore pressure amounts to increasing confining pressure.

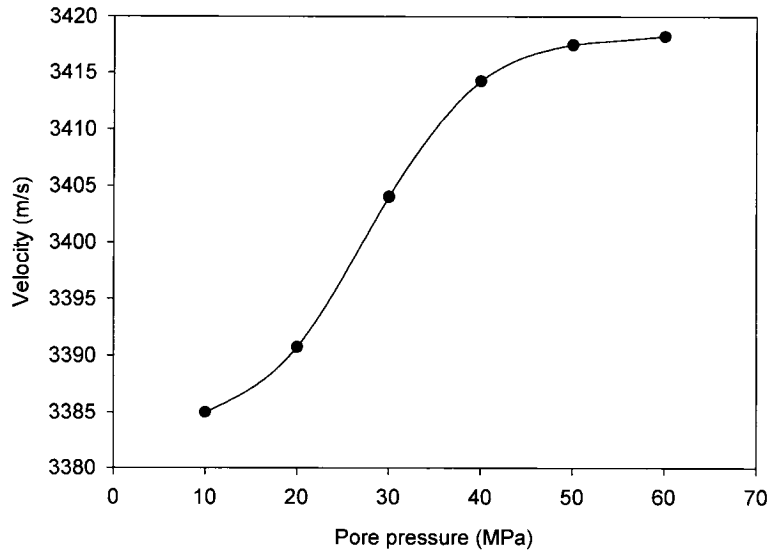

Figure 5.12: Velocity verses pore pressure at constant differential pressure. Constant differential pressure means an equivalent change in both pore pressure and confining pressure

.

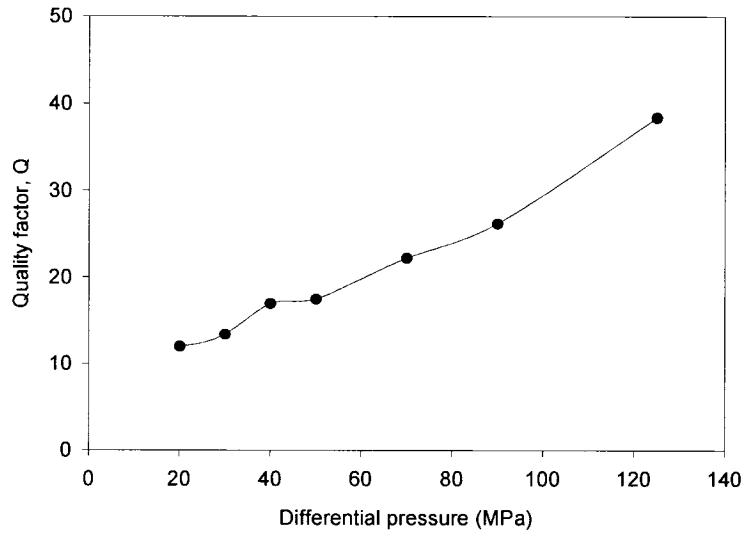

Figure 5.13: Quality factor verses differential pressure at constant pore pressure.

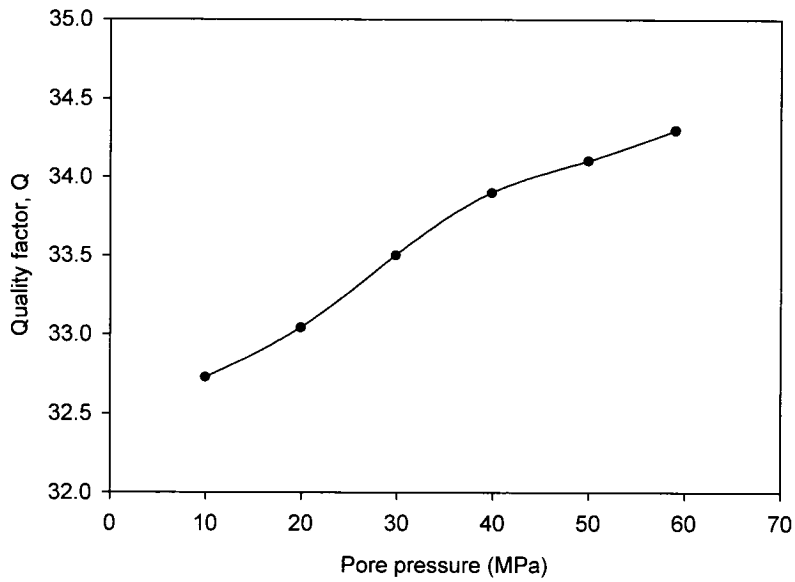

Figure 5.14: Quality factor verses pore pressure at constant differential pressure.

The cyclic experiments were therefore performed at lower *insitu* pressures below the strength of the rock sample. From Figures 5.11, 5.12, 5.13 and 5.14 it is confirmed that changing pore pressure, confining pressure and differential pressure influence both velocity and attenuation on the sandstone sample. In Figure 5.11 and 5.13, where the pore pressure is kept constant, acoustic velocity and attenuation increase due to the increases in the differential pressure. This is to be expected since the overall effective stress on the sample is increased, thus increasing both velocity and attenuation. However, in Figure 5.12 and 5.14, where differential pressure is kept constant, acoustic velocity and attenuation increase. This would only occur in a situation where the differential stress and

effective stress are not equal in magnitude. If the differential pressure and the effective stress were equal, one would not expect changes in velocity and attenuation at constant differential pressure, but this is not the case. Both pore pressure and confining pressure have different influence on acoustic velocity and attenuation quality factor. This is shown in Figure 5.15 and 5.16 where the two graphs are superimposed. The different influence of the pore pressure and confining pressure on acoustic velocities and attenuation of the sandstone led to a conclusion that 'n' is not one and therefore the effective stress is not just the difference between confining pressure and pore pressure for this sandstone sample. The stress dependant nature of 'n' as in equation 4 implies that 'n' may also vary from rock to rock, depending on a particular pore structure and mineral composition. The influence of pore pressure on velocity and attenuation are less pronounced than the influence of confining pressure on velocity and attenuation. This is indicated by a sharp increase in the gradient of the two curves in Figure 5.15 for velocities and that in Figure 5.16 for attenuation. Comparing the changes in velocity with differential pressure and that of attenuation with differential pressure (Figure 5.11 and 5.13), it is observed that attenuation is more sensitive than velocity to changes in differential pressure. At higher pressure, velocity becomes insensitive to changes in differential pressure while the changes in attenuation with pressure increases even at higher differential pressure. The velocity curve therefore follows a three parameter exponential decay, (Figure 5.11), similar to that given by Prasad and Manghani (Prasad, 1998) whiles attenuation (Figure 5.13) follows a three parameter exponential rise, with no limiting value in the pressure range of the experiment.

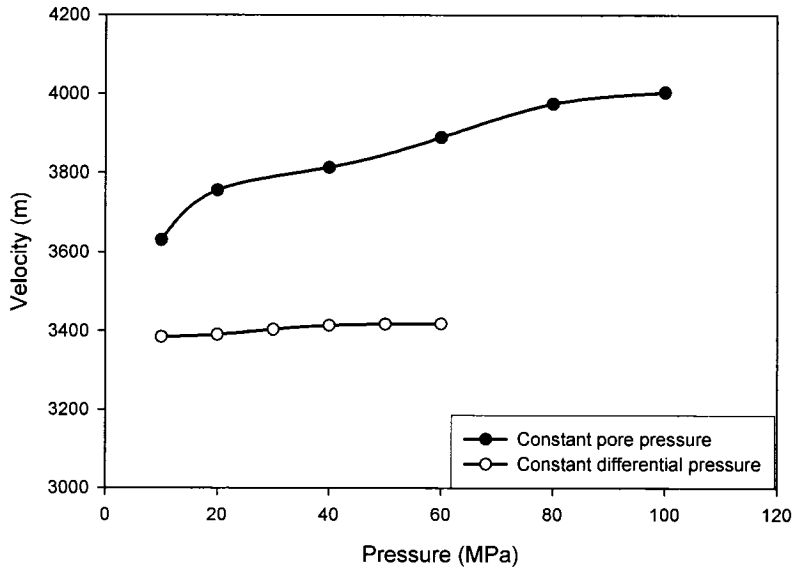

Figure 5.15: Comparing velocity response with changes in pore pressure, differential pressure and confining pressure

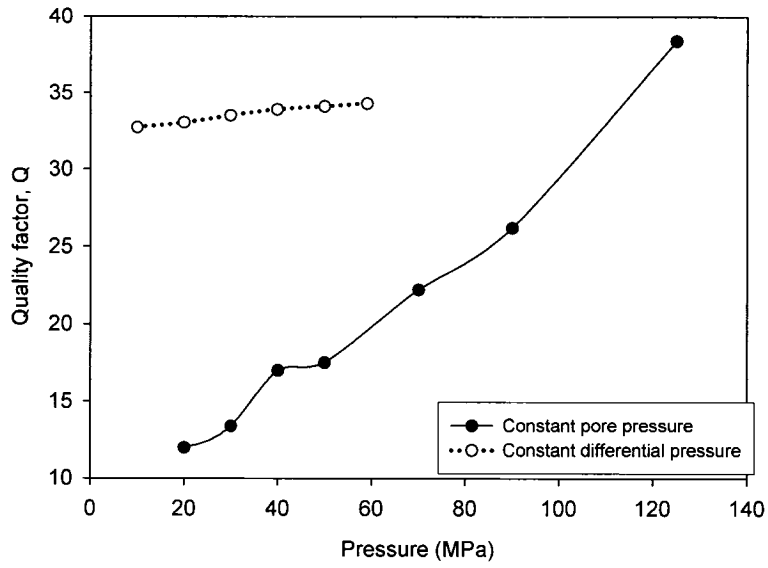

Figure 5.16: Comparing quality factor response with changes in pore pressure, differential pressure and confining pressure

The gradient of the two curves (i.e. velocity at constant pore pressure and velocity at constant differential pressure (Figures 5.17 and 5.18)) were used to calculate the value of 'n' as per equation 5.1. It was found that 'n' is 0.82 for the glass sandstone, using velocity as the physical quantity. Similar calculation with attenuation quality factor (Figures 5.19 and 5.20) yielded 'n' as 0.86. Since the variation of velocity with pressure is not completely linear, only the average gradients were used for the calculation of 'n'. Incremental values of 'n' at specific pore pressure and differential pressure increments were also calculated and it was found that 'n' decreases with pressure (Figure 5.21). Thus 'n' is inversely proportional to both pore pressure and confining pressure. This indicates that the value of 'n' for a particular rock is not constant. At low pore pressure 'n' approaches 1 and reduces to about 0.80 at high pore pressure for this sandstone rock. This implies that both porosity and pore structure play a significant role in the value of 'n'. In fact, at high pore pressure the pores spaces expand and induce a temporal high porosity and thus 'n' decreases. This is in essence the same argument put forward by Biot (1955) who calculated n using the bulk compressibility and the compressibility of the rock matrix and suggested an approximate value of n to be 0.9 for all rocks. At low pore pressure, the pores spaces contract by the confining stress and thus a temporal low porosity is induced resulting in high value of 'n'. In theory 'n' should approach one at zero pore pressure though this was not confirmed by our experiment. The values of 'n' obtained from this experiment were compared with the values obtained in other literature (Prasad and Manghnani, 1997) on similar sandstone rocks under similar experimental pressures conditions and similar results were obtained (Table 5.3).

Table 5.3: Comparison of the current results (quartz sandstone), with previous study (Berea sandstone (Prasad and Manghnani, 1997), Michigan sandstone (Prasad and Manghnani, 1997))

	Berea Sanstone		Michigan Sandstone		Quartz Sandstone	
	Pc (MPa)	n	Pc (MPa)	n	Pc (MPa)	n
	5	0.946	5	0.977	20	0.981
	10	0.986	10	0.928	40	0.910
	15	0.969	15	0.850	60	0.876
	20	0.858	20	0.831		
	25	0.796	25	0.615		
Bulk density (g/m3)	2.282		2.362		2.26	
Porosity (%)	21.18		16.94		15	
Grain size(um)	150-250		300-400		160-200	
Permeability(md)	1000		---		17	

The higher increases in 'n' for the quartz sandstone may be due to the elevated pressures at which this experiment was performed. It may also be due to comparatively low porosity values of this rock. For non porous rock, 'n' is 1 as indicated by Gurevich (2004). The above 'n' values have confirmed the results in some of the literature which argue (Todd and Simmons, 1972; Christensen and Wang, 1985; Prasad, 1998; Siggins and Dewhurst, 2003) that, the value of 'n' is between one and zero. It has also been found that there is no single value of 'n' for a particular rock. We can deduce from the experimental results that 'n' is affected by both internal and external factors, which are themselves inter-related. The external factors include pore pressure and confining pressure whilst internal factors include porosity and pore structure. The changes in the internal factors are brought about by the external factors. This confirms the work of other authors who have suggested that 'n' is not always constant but may depend on confining stress and pore pressure (Prasad and Manghnani, 1997)). This also brings more validity to the work of Suklj (1969) that includes porosity in his empirical calculation for 'n'. What

was not mentioned in his work was the influence of the pore pressure and confining pressure on the value of 'n'. This has been clarified in this research by the changing value of 'n' with both pore pressure and confining pressure. Analyzing the values of 'n' obtained from this study and that in various literatures for different sandstone rocks, (Prasad and Manghnani, 1997), Biot 0.90 constant seems to be a reasonable value for 'n' for most sandstone rocks. Therefore for all practical purposes, Biot constant of 0.9 is a reasonable value for the effective stress especially for quick calculations. However, since different sandstones have different porosities and mineralogical characteristics, it is recommended that a simple laboratory experiment be carried out to estimate the average value of 'n' used for the calculations of saturations and pore pressure predictions. In today's pore pressure predictions where accuracy is of great concern, running a quick experiment like this to estimate the exact value of 'n' for the reservoir rock in question should be a priority. Another characteristic of 'n' is that different quantities used to calculate 'n' has different values. In this study, velocity derived 'n' is larger than quality factor derived 'n'. Other acoustic properties of the rock could be used to derive 'n' and that would make it possible to compare the behavior of 'n' derived from different physical properties.

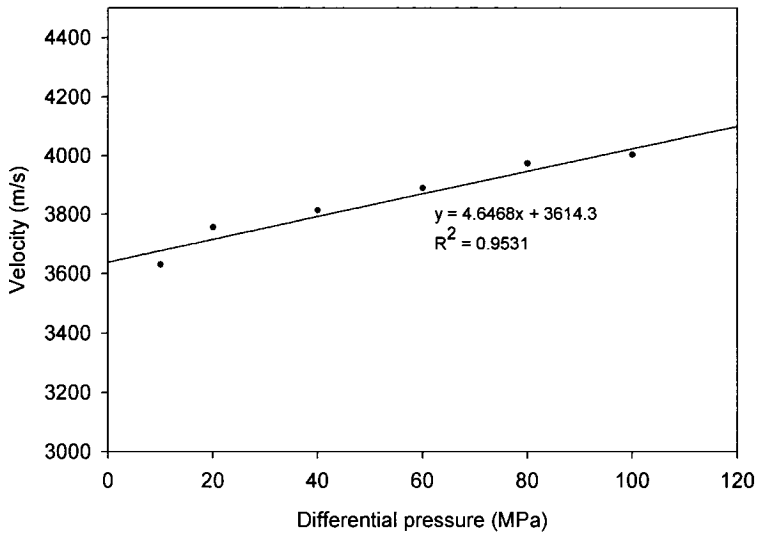

Figure 5.17: Best fit line to estimate the gradient of velocity differential pressure curve.

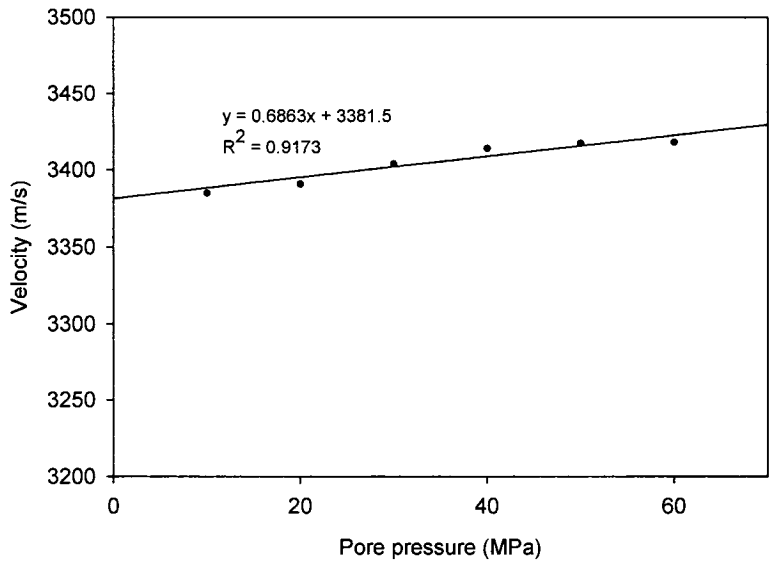

Figure 5.18: Best fit line to estimate the gradient of velocity pore pressure curve

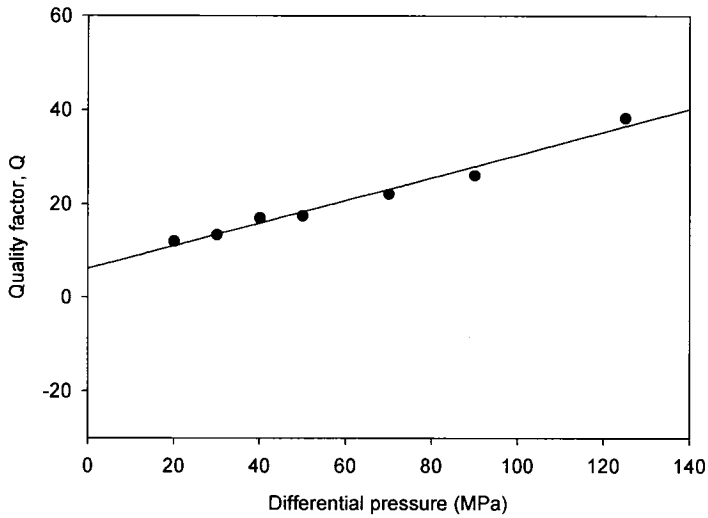

Figure 5.19 Best fit line to estimate the gradient of quality factor differential pressure curve

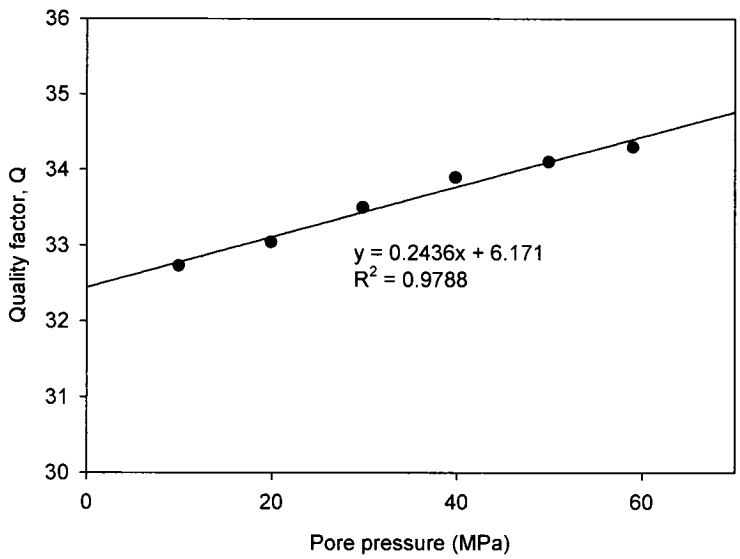

Figure 5.20: Best fit line to estimate the gradient of quality factor pore pressure curve

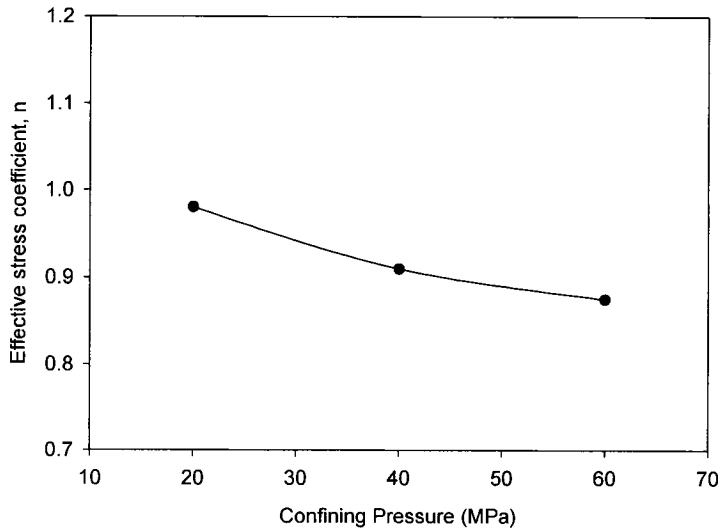

Figure 5.21: Values of 'n' with increasing pore pressure and differential pressure

5.7 Measurement and experimental accuracy

The exact accuracy, precision and repeatability of our measurements, at any pressure during the experiment may never be known for certain. However, accuracy in some of the calculations and measurements were quantified in order to increase the confidence in our data. These include:

(i) The travel time was validated with standard aluminum and acrylic samples and the accuracy of the velocity measurements were found to be within 0.25%.

(ii) One of the sources of error in the calculation of attenuation quality factor (Q) using spectral ratio technique is the frequency independent assumption. The frequency range

was from 500 KHz to 1500 KHz (Figure 5.8). This may introduce some error in our Q estimates. The magnitude of this error was analyzed using an error bar for Q. The error bar was based on the difference between log spectral ratio and its linear regression. The regression coefficient was 0.97 and at 95% confidence level the Q values have an error of 0.5% (i.e. Q±0.5%). This is within experimental error. Calibration of the whole experimental set up was also done with both aluminum standard and a Lucite sample and the results were in perfect agreement with published velocity results of Lucite and aluminum. Validation of this apparatus has been done by both numerical and experimental modeling(Donald et al., 2004) to ensure that unwanted resonant shape modes (Johnson, 1970) and diffraction errors (Khimunin, 1972; Papadakis, 1972) are eliminated. Therefore the waveforms recorded at the receiving transducers can be considered as plane compressional waves that propagated along the lengths of the core samples. The calibration methodology is given in Donald et al., (2004). This shows the reliability of our experimental set up and measurements.

5.8 Conclusions

We have confirmed the value of 'n' theoretically and experimentally by using a laboratory acoustic method at high frequency, to estimate 'n' of quartz sandstone. The review indicated that, the disagreements and the perceptions surrounding the value of 'n' still exist. Although most of the theoretical literature has shown that the value of 'n' is one, practical and laboratory studies have consistently found the value of 'n' to be less

than one. This discrepancy between the theory and practice may be due to the two main assumptions that are normally made in the theoretical derivation of 'n'. These are the:

(i) The homogeneity assumption of the grain matrix material and,

(ii) The linear elasticity assumption of the rock material, within the range of stresses and pressures in operation.

Our theoretical derivation and laboratory results at high frequency have revealed that:

(i) The effective stress is not equal to the differential stress. They could be equal only in a special case where there are no pore spaces and thus pore pressure is equal to zero.

(ii) 'n', is basically the effectiveness of the pore pressure in counteracting the total applied stress on the material. This effectiveness would in part depend on the porosity of the material as well as the shape and the sizes of the pores.

(iii) The value of 'n' is not one but varies from zero to one,

(iv) There is no single value of 'n' for a particular reservoir rock

(v) 'n' is inversely proportional to both pore pressure and confining pressure

(vi) 'n' decreases from one at low pore pressure and confining pressure to zero at high pore and confining pressures.

(vii) It was also found that 'n' depends on internal factors (porosity, pore geometry) and external factors (pore pressure and confining pressure) of the rock.

(iv) Velocity derived 'n' and quality factor derived 'n' are different for the same rock. For the quartz sandstone, the velocity derived 'n' is smaller and also less sensitive to changes in pressure than quality factor derived 'n'.

We compared our experimental value of 'n' to both theoretical and practical results obtained from other literature that used different methodology. We found that they are in agreement. The slight increase in our estimated value of 'n' was attributed to the elevated pressures at which we performed our experiments. It was also attributed to the comparatively low porosity values of this rock. Note that, the limit of 'n' as porosity goes to zero is 1. With the increasing demand of high accuracy in pore pressure and saturation predictions, running a quick experiment to estimate the exact value of 'n' for the rock, following the above procedure, should become a priority.

5.9 Acknowledgements

We would like to thank the Natural Sciences and Engineering Research Council of Canada (NSERC), Petroleum Research Atlantic Canada (PRAC) and Schlumberger Canada Limited for providing funding for this research.

5.10 Nomenclature

P_e	Effective stress
P_d	Differential pressure
P_c	Confining pressure
P_p	Pore pressure
n	Effective stress coefficient (Coefficient of deformation)

V	Compressional wave velocity
Q	Attenuation quality factor
c_b	Bulk compressibility of the rock
c_r	Compressibility of the rock matrix
α	Biot coefficient
K	Effective Bulk moduli
K_0	Grain Bulk moduli
ϕ	Porosity
A	Physical quantity of the rock
ε_{ij}	Elements of the strain tensor,
σ_{ij}	Element of the stress tensor
ε_{aa}	Volumetric strain summed over repeated index,
δ_{ij}	Kroenecker's delta
λ	Lame constant
K	Bulk modulus
σ_o	Hydrostatic stress
σ_{aa}	Mean stress times 3 sum over repeated index
μ	Shear modulus
E	Young Modulus
σ_{zz}	Extensional stress
ε_{zz}	Extensional strain
ε_{ij}^{Pp}	Strain due to pore pressure

H	Biot effective modulus due to pore pressure
θ	Total volumetric strain with pore pressure effect

5.11 References

ASTM Standard 4543, (2004) Practice for Preparing Rock Core Specimens and Determining Dimensional Shape Tolerances: American Society for the Testing of Materials.

Berryman, J. G., (1992), Effective Stress for Transport Properties of Inhomogeneous Porous Rock: Journal of Geophysical Research, Vol. 97, pp. 17409–17424.

Biot M. A., (1955), Theory of Elasticity and Consolidation for a Porous Anisotropic Solids: Journal of Applied Physics, Vol. 26, pp. 182-197.

Birch, F., (1969), The velocity of compressional waves in rocks to 10Kilobars, Part I: J. Geophys. Res., 65, 1083 -1102.

Brandt H., (1955), A Study of the Speed of Sound in Porous Granular Media: Trans ASME, Vol. 77, pp. 479-485.

Butt, S.D., Mukherjee, C., and G. Lebans, (2000), Evaluation of Acoustic Attenuation as an Indicator of Roof Stability in Advancing Headings: International Journal of Rock Mechanics and Mining Science, Vol. 37, pp.1123-1131.

Butt, S.D., (2001), Experimental Measurement of P-wave Attenuation Due to Fracture over 100 to 300 kHz Bandwidth: Journal of Pure and Applied Geophysics, Vol. 158, pp.1783-1796.

Carroll, M. M., and Katsube, N., (1983), The Role of Terzaghi Effective Stress in Linearly Elastic Deformation: ASME Journal of Energy Resources and Technology, Vol. 105, pp. 509–511.

Christensen, N. I., and Wang, H. F., (1985), The Influence of Pore and Confining Pressure on Dynamic Elastic Properties of Berea Sandstone: J. Geophysics, Vol. 50, pp. 207-213.

Donald, J. A., Butt S. D., and Iakovlev S, (2004), Adaptation of a Triaxial Cell for Ultrasonic P-wave Attenuation, Velocity and Acoustic Emission Measurements: International Journal of Rock Mechanics and Mining Science, Vol. 41, pp. 1001-1011

Frempong, P. K. and Donald, J. A., Properties of Natural and Artificial Sandstone, Internal Report, Dalhousie University, Mining Engineering Department, Halifax, 2003.

Gangi, A. F., (1991), The Effect of Pore Fluid and Pressure on the Seismic Velocity in Cracks and/or Porous Rocks: SEG Research Workshop on Lithology, Technical Abstracts, pp. 35-38.

Geertsma, J., (1953), The Effect of Fluid Pressure Decline on Volumetric Changes of Porous Rocks: Trans AIME, pp. 331-340.

Gurevich, B., (2004), A Simple Derivation of the Effective Stress Coefficient for Seismic Velocities in Porous Rocks: J. Geophysics, Vol. 69, No. 2, pp. 393-397.

Johnson, C.F., (1970), A Pulse Technique for the Direct Measurement of Bar Velocity: Twelfth Symposium on Rock Mechanics Proceeding, University of Missouri, Rolla, Missouri, Society of Mining Engineers, New York.

Khimunin, A.S., (1972), Numerical Calculation of the Diffraction Corrections for the Precise Measurement of Ultrasound Absorption: Acustica, Vol. 27, pp. 173-181.

Landro, M., and Kvam., O, (2002), Pore Pressure Estimation-What can we Learn from 4D?, CSEG Recorder, Vol. 27, pp. 83-87.

Nur, A., and Byrelee, J. D., (1971), An Exact Effective Stress Law for Elastic Deformation of Rocks with Fluid: Journal of Geophysical Research, Vol. 76, pp. 6414-6419.

Papadakis, E.P., (1972), Ultrasonic Diffraction Loss and Phase Change for Broad-Band Pulses: Journal of Acoustic. Society of America, Vol. 52, pp. 847-849.

Prasad, M., (1998), Empirical trends in velocity and quality factor properties of reservoir rocks, Department of Geophysics, Stanford University, Internal report, SRB project.

Prasad, M., and Manghnani, M.H., (1997), Effects of Pore and Differential Pressure on Compressional Wave Velocity and Quality Factor in Berea and Michigan Sandstones: J. Geophysics, Vol. 62, pp. 1163–1176.

Robin, P.Y. F., (1973), Note on Effective Pressure: Journal of Geophysical Research, Vol. 78, pp. 2434–2437.

Ryan, R. J., (1998), The Fall Brook Quarry near Three Miles Plains: Classic Carboniferous Sections of the Minas and Cumberland Basin in Nova Scotia., The Society of Organic Petrology, Annual General Meeting and Field Trip, Open File Report, ME 1998-5, NS Natural Resource Department, NS, Canada.

Siggins, A. F., and Dewhurst, D. N., (2003), Saturation, Pore Pressure and Effective Stress from Sandstone Acoustic Properties: Geophysical Research Letters, Vol. 30, pp. 1089.

Skempton, A. W., (1960), Effective Stress in Soils, Concrete and Rocks-Pore Pressure and Suction in Soils: Butterworth, London, pp. 123.

Skulje, L., (1969), Rheological Aspects of Soil Mechanics: New York, pp. 123.

Terzaghi, K., (1955), Theoretical Soil Mechanics: John Wiley and Sons, New York, 1943.

Todd, T., and Simmons, S G., (1972), Effect of Pore Pressure on the Velocity of Compressional Waves in Low Porosity Rocks: Journal of Geophysical Reserve, Vol. 77, pp. 3731-3743.

Toksoz, M.N., Johnston, D.H. and Timur, A., (1979), Attenuation of Seismic Waves in Dry and Saturated Rocks, I, Laboratory Measurements: J. Geophysics, Vol. 44, pp. 681-690.

Zimmerman, R. W., Somerton, W. H., and King, M. S., (1986), Compressibility of porous rocks, Journal of Geophysical Research, No. B12, Vol. 91, pp. 765-777.

Chapter 6: Characterization of the permeability and acoustic properties of an outburst-prone sandstone

This paper is has been accepted for publication in the journal of Applied Geophysics (ref no. APPGEO770). The main author is Dr Steve Butt and Mr Paul Frempong is the co-author. The figure numbers and reference formats have been altered to match the formatting guidelines set out by Dalhousie University compared with the submitted manuscript to APPGEO770. Sample names in the Figures and Table captions have been changed to be consistent with the rest of the thesis content. Mr Frempong's contributions to the papers are given below:

- Processing of the acoustic data
- Performed part of the experiment work (aluminum standard test)
- Produced the draft of writeup

6.1 Abstract

Two underground coal mines in the Sydney Coalfield, Nova Scotia, Canada have encountered gas outbursts from sandstone formations overlying the coal seams. These have consistently occurred while driving mine roadways into virgin ground at and below mining depths of 700 m. In this investigation, triaxial compression tests were conducted

on samples of the outburst-prone sandstone from one of these mines, the Phalen Colliery, while simultaneously measuring gas permeability, acoustic emissions and ultrasonic P-wave velocity and attenuation. Experimental results characterized these sandstone properties over the full range of axial stresses up to compressive failure. These data were intended to assist with i) evaluating the potential for degassing the sandstone, and ii) evaluating the results of in-seam seismic surveys which were conducted to map the sandstone ahead of mining. At the estimated in situ conditions in virgin rock at 700 m depth, the sandstone permeability is expected to be in the 0.005 to 0.04 mD range, the P-wave velocity is approximately 4000 m/s and the attenuation quality factor in the 20 to 25 range. Near mine openings at 700 m depth, where the lateral confining pressures are reduced, the permeability can be several orders of magnitude higher in the 4 to 15 mD range, the P-wave velocity is 3800 m/s and the attenuation quality factor is in the 10 to 15 range. Experimental data suggests that microcracking in the sandstone prior to compressive failure does not significantly enhance permeability but there may be local pockets of higher permeability within the sandstone.

6.2 Introduction

Gas outbursts are the rapid ejection of gas and rock material from rock strata at underground mines. They are a major safety hazard because of the danger posed by the fragmented rock ejected into the mine opening and because much of the expelled gases are explosive e.g. methane. Worldwide, these outbursts have been reported at several

types of underground soft-rock mines, but the majority occur at coal mines when openings are excavated in close proximity to low permeability strata containing gas under high pressure and are more frequent when excavation is occurring in virgin rock such as near the face of an advancing roadway or tunnel (Sheppard et al., 1981). Most reported gas outbursts at coal mines occur from the coal face. However, two coal mines in the Sydney Coalfield, Nova Scotia, Canada, have encountered outbursts from sandstone formations that overlie the coal seams. These sandstone-hosted outbursts are more often referred to as rock gas outbursts to distinguish them from the more common coal gas outbursts.

In the Sydney Coalfied, 37 of these rock gas outbursts were recorded from 1977 to the mine's closure in 1984 (Aston et al., 1990). The great majority of these outbursts occurred during the advancing of new roadways at or below a mining depth of 700 m. Beginning in 1994, the nearby Phalen Colliery encountered gas outbursts from overlying sandstone formations during the advancing of new roadways upon reaching a mining depth of approximately 700 m. The similarity between the depth at which outbursting began to occur at these two mines suggested that some critical combination of stress-controlled *in situ* sandstone permeability and gas pressure were significant factors in outburst occurrence. In fact, at the Phalen Colliery, the outburst sandstone unit was mined against at shallower depth updip and did not exhibit outburst behaviour. Underground coal mines in the Ukraine and Germany have also reported the occurrence of sandstone-hosted gas outbursts upon reaching a similar depth (Devco, unpub. reports). Research

conducted on the outburst-sandstones of the Sydney Basin at that time focused on characterizing the *in situ* permeability, porosity, gas pressures and compositions, etc.. for these formations (e.g. Golder Associates, 1985; Gibling et al., 1999; Devco, unpub. reports). Major conclusions from this work include: i) gas in the outburst-prone sandstone is predominantly methane, ii) this gas is normally pressured, and iii) the *in situ* permeability is generally less than 0.02 mD.

The research described in this paper is an extension of earlier work by Corbett, (1997) and Butt, (1999). It investigates the permeability, acoustic emissions and ultrasonic velocity and attenuation properties of the outburst-prone sandstone from the Phalen Colliery over a range of triaxial stress conditions up to compressive failure. The intended applications of this data were i) to assist with evaluating the potential of degassing operations for the outburst-prone sandstone, and ii) to assist with the interpretation of in-seam seismic surveys (King and Greenhalgh, 1979) which were conducted to map the outburst sandstone ahead of the advancing roadways. The Phalen Colliery closed shortly after this investigation (in part, due to these outbursting hazards and other ground control problems) but the experimental results can be applied to other mines in the Sydney Coalfield and elsewhere in the world where similar sandstone-hosted gas outbursts are a problem.

6.3 Outburst history, Phalen Colliery

A total of 5 sandstone-hosted gas outbursts occurred at the Phalen Colliery from 1994 to the mine's closure in 2000. All of these occurred during the advancing of the main slope roadways. The first outburst occurred on Sept. 28, 1994 in No. 3 Slope when the roadway was being advanced at a depth of 697 m using a mechanical roadheader. This event ejected 20 m^3 of debris into the roadway, released 1300 m^3 of methane, dislodged 8 steel arch supports, moved the roadheader back 3 m and injured the machine operator. Ironically, a local microseismic system was operating near this heading and recorded some of the events associated with the outburst. Details about this microseismic activity are provided in other sources (Corbett, 1997; Forrester et al., 1994). After this incident, the mine adopted an outburst hazard Code of Practice which required roadway excavation using shotfiring methods when near or below a depth of 600 m. The next four outbursts all occurred in the adjacent No. 4 Slope during the roadway advance over a 12 m interval from October 15 to November 11, 1997 (Woodland, 1997). These four outbursts occurred at mining depths from 697 m to 699 m and were triggered by shotfiring following the mine's outburst Code of Practice. These four outbursts occurred with increasing severity, as evidenced by a significant increase in the volume of outburst cavity, the ejected methane gas and the displacement of outburst material from the first to last events (Table 6.1). Figure 6.1 is a sketch of the outburst cavities resulting from these bursts. The final outburst in No. 4 Slope was so rapid that although fragmented rock debris and 9 steel arches were ejected 19 m back into the roadway, the debris completely underfilled three

chock wooden cribs supporting the roof of the #3 outburst cavity before they could fall (Figure 6.1). Roadway excavation in this slope was halted shortly after this event and did not resume before the closure of the mine.

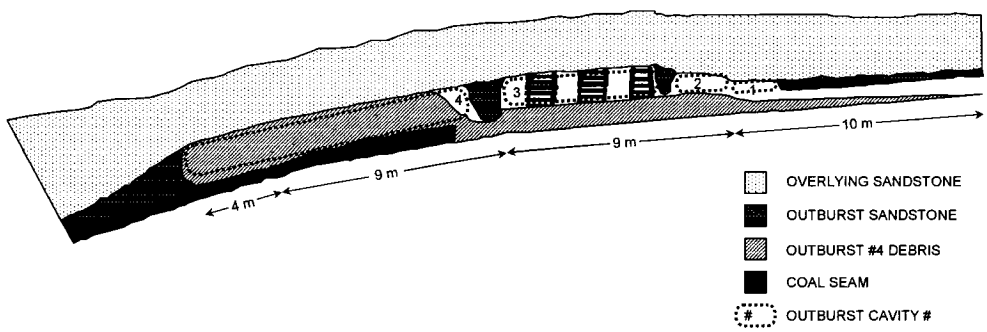

Figure 6.1: Vertical section showing the location of the cavities produced by the four outbursts in the No. 4 Slope and the ejected debris field resulting from Outburst #4. Note the three timber cribs in the Outburst #3 cavity which remained in place during Outburst #4.

Table 6.1: Summary of the sandstone-hosted gas outbursts in #4 Slope, Phalen Colliery in 1997.

Outburst #	1	2	3	4
Date	Oct. 15	Oct. 21	Oct. 23	Nov. 4
Mining depth (m)	697	697	698	699
Coal seam thickness (m)	2.8	2.8	2.8	2.6
Outburst sandstone thickness (m)	0.7	1.2	3	3.5
Estimated cavity size (m^3)	6	14.4	307	792
Volume methane released (m^3)	42	86	180	1250
Distance material ejected from face (m)	0	0	5	19
Number of arches displaced	0	0	2	9

6.4 Sandstone samples

The outburst-prone sandstone is described as a river-channel sandstone that has eroded the upper portion of the coal seam (Forgeron et al., 1986). In many locations, the outburst-prone sandstone is overlain by a visually different sandstone formation that is not outburst-prone. The sandstone samples consisted of 35.0 mm diameter cores which were recovered from boreholes drilled from the coal mine workings. Several samples were recovered near the outburst locations in the No. 3 and No. 4 Slopes while others were recovered updip at a lower mining depth (Table 6.2). The samples were a medium grained, poorly sorted argillaceous sandstone with an estimated porosity of 3%. Test specimens were prepared as right circular cylinders with a length to diameter ratio of 2 in accordance with the procedures and shape tolerances as outlined in ASTM D4543.

Table 6.2: Summary of tested sandstone samples.

Borehole name and description		Tested Sample
PH403	•Borehole drilled into a longwall pillar specifically to recover sandstone samples. •Samples recovered from ~640 m depth.	PH403-A PH403-B PH403-D PH403-E PH403-G
H5	•In-seam exploration borehole drilled ahead of advancing roadways. •Samples recovered from ~700 m depth near the outburst in No. 3 Slope.	H5-R H5-V
PH472	•Borehole drilled above mine roadway specifically to recover sandstone samples. •Samples recovered from ~700 m depth near Outburst # 1 in the No. 4 Slope.	PH472-N PH472-M
PH473	•Borehole drilled ahead of advancing roadway specifically to recover sandstone samples. •Samples recovered from ~700 m depth near Outburst #1 in the No. 4 Slope.	PH473-K PH473-L

6.5 Experimental setup

The stress-flow-acoustic triaxial system used for this research was developed in-house and is described in detail in a related publication (Butt, 1999). In brief, the triaxial cell (Figure 6.2) consists of a closed cylindrical chamber with a loading piston the same diameter as the tested samples, an internal system of flow tubes, ports and platens to flow air through the samples for permeability measurement and specialized platens to enable direct transmission of ultrasonic waves along the sample axis. Hydraulic oil is used to apply confining pressure to the samples which are sealed against the oil using heat shrink vinyl tubing. The cell assembly is mounted in a servo-controlled loading frame to apply axial force to the sample. The air flow measurement system (Figure 6.3) was designed in accordance with ASTM D4525. It delivers filtered, desiccated air at room temperature at regulated pressures less than 70 kPa gauge pressure to the upstream end of the sample and measures the flow rate exiting the downstream end of the sample. Separate static flow lines measure the air pressures on the upstream and downstream ends of the samples.

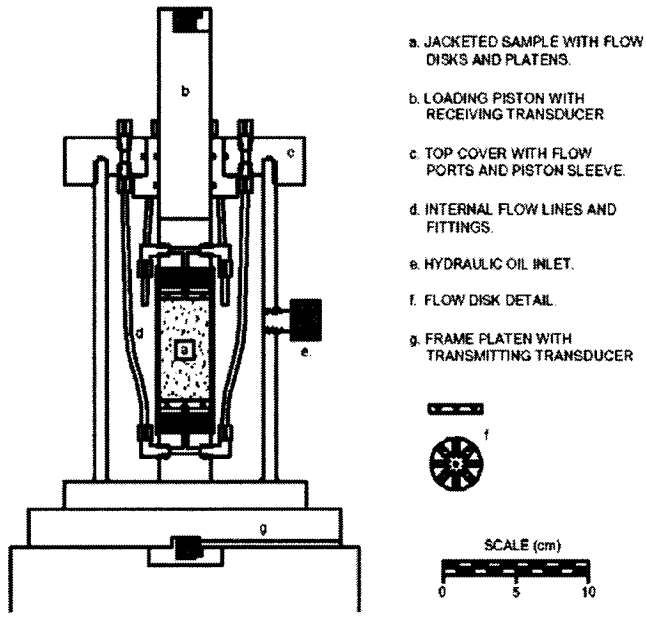

Figure 6.2: Schematic of the stress-flow-ultrasonic triaxial cell.

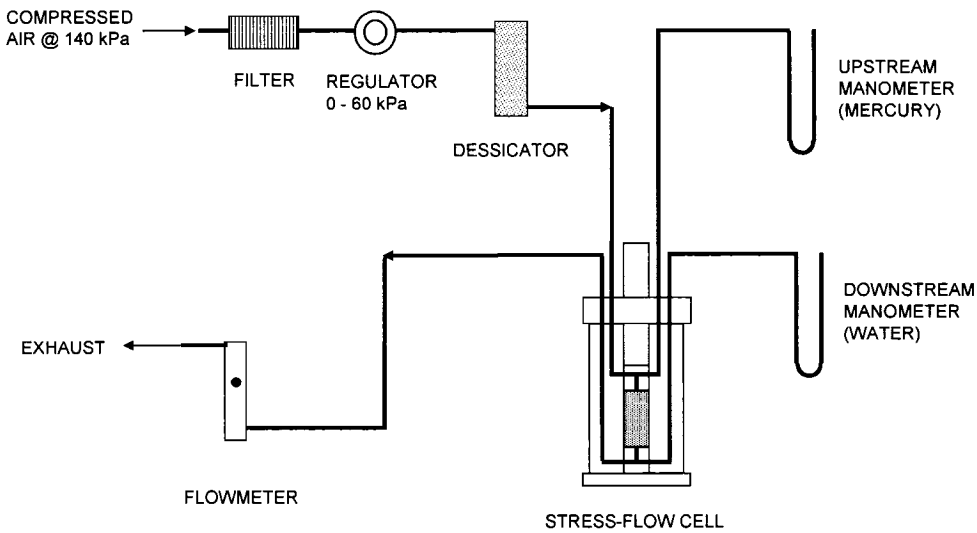

Figure 6.3: Schematic of the air flow measurement system

The acoustic measurement system is sketched in Figure 6.4. Two ultrasonic P-wave sensors are mounted in-line with the sample axis in cavities machined into the cell loading piston and the lower frame platen. The upper sensor is configured as a receiving sensor and is connected to a PC-based digital recording system that amplifies and filters the signal over frequency range of 100 to 400 kHz and records the waveforms at a sampling rate of 1 MHz. For any test, the acoustic system is configured to operate in one of two modes:

1) Acoustic Emission (AE) detection. In this mode, the receiving sensor is configured to trigger on signal amplitude and passively detects and records the AE generated within the sandstone samples in response to applied stress.
2) Ultrasonic transmission measurement. In this mode, a pulse-calibration unit strobes the lower sensor with a high voltage, short duration pulse which generates a source P-wave. This waveform propagates through the cell and sandstone sample and to the upper receiving sensor. Recording at the receiving sensor is triggered using a synchronization signal generated by the pulse-calibration unit.

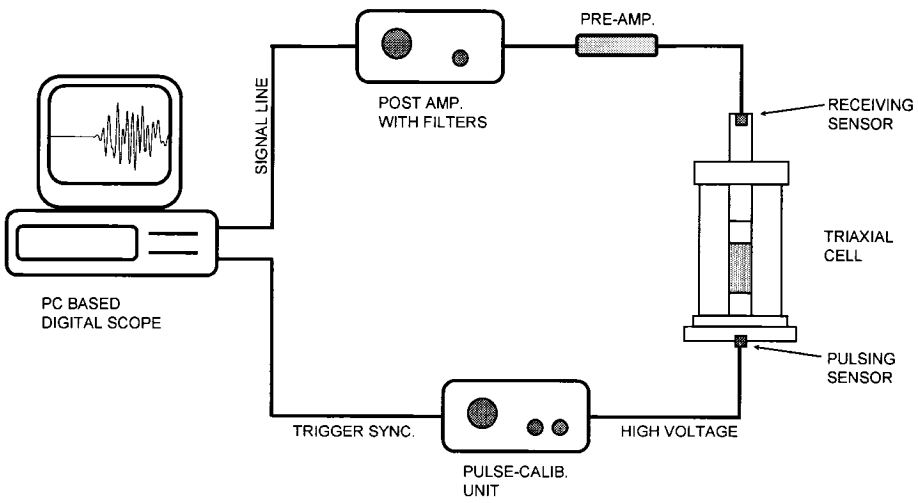

Figure 6.4: Schematic of the acoustic measurement system

6.6 Experimental procedure

The sandstone samples were compressed to failure in the loading frames at constant displacement rates of 2 or 4 mm/hour. These tests were conducted at confining pressures of 1, 5 and 10 MPa. The tests at 1 MPa simulated uniaxial compression tests since the 1 MPa pressure was just sufficient to seal the heat shrink tubing against the sample to prevent air flow along the outside of the sample but not high enough to significantly influence the compressive strength. The tests at confining pressures at 5 and 10 MPa simulated the behaviour of the sandstone under *in situ* conditions and represent the range of expected lateral pressures at a depth of 700 m in virgin ground with an estimated overburden pressure of 20 MPa. During these tests, the following measurements were recorded:

- Applied axial force at a rate of several readings per second.
- Measurements of upstream air flow pressure, downstream pressure and downstream flow rate at an approximate period of 10 seconds.
- For AE monitoring, digitized waveforms detected by the receiving sensor at a maximum rate of approximately 5 events per second.
- For ultrasonic transmission measurements, the digitized waveforms recorded by the receiving sensor at an approximate rate of one per second.

All of these measurements were indexed with respect to elapsed test time to facilitate evaluation and comparison during post-test data analysis.

6.7 Data analysis procedures

6.7.1 Stress-permeability

The axial force and displacement measurements were converted to axial stress and strain by dividing through by the initial sample cross-sectional area and length, respectively. The flow measurements were used to compute gas permeability k_g using:

$$k_g = \frac{2Q_d P_d \mu L}{(P_u^{\,2} - P_d^{\,2})A} \tag{6.1}$$

where Q is flowrate, P is absolute gas pressure, μ is air viscosity at the test temperature, L is the sample length, A is the corssectional area, and the subscripts d and u indicate upstream and downstream measurements, respectively. Due to the gas slippage effect described by Klinkenberg (1941), the gas permeability measured under the low gas

pressures used for these experiments is higher then the intrinsic permeability that would apply for gas under much higher *in situ* pressure. Therefore, the intrinsic permeability k_∞ was then computed using:

$$k_g = k_\infty \left(1 + \frac{b}{P}\right) \tag{6.2}$$

where P is the average of the absolute upstream and downstream pressures, and b is the gas slippage factor. For this computation, b was estimated using an empirical relationship derived from a study using approximately 100 low permeability sandstone samples (Jones and Owen, 1980):

$$b = 0.86 k_\infty^{-0.33} \tag{6.3}$$

where b is in units of atmospheres and k_∞ is in units of mD.

6.7.2 Acoustic emissions

The acoustic emissions were evaluated by examining the pattern of cumulative AE recorded during a test. The rate of AE would be proportional to the slope of graphs of cumulative AE versus test time. Periods of little or no AE would be indicated by flat traces on these graphs.

Ultrasonic Waveform Analysis

Prior to the computation of P-wave velocity or attenuation, the recorded waveforms were processed to improve the signal to noise ratio and to isolate the desired wave components. First, every 16 consecutive waveforms were checked to remove bad events

(due to sporadic triggering errors) and then stacked. Each stacked waveform was examined and all waveform amplitudes after the initial P-wave arrival were zeroed to remove the later wave arrivals. The arrival time and a 128 point Fast Fourier Transform were then determined for each these stacked, isolated P-waveforms. These processing steps are outlined in figure 6.5.

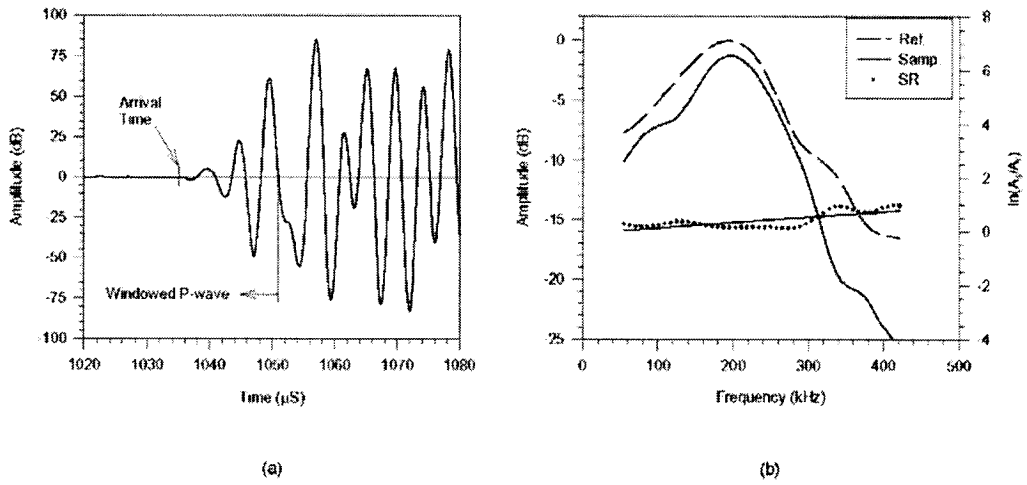

Figure 6.5: Details of the ultrasonic waveform processing procedures showing (a) picking of arrival times and P-wave windowing, and (b) example waveform FFTs and corresponding spectral ratios.

For each waveform the group P-wave velocity V_p was computed using:

$$V_p = \frac{L}{t - t_0} \tag{6.4}$$

where L is the sample length, t is the arrival time, and t_0 is the zero arrival time computed by pulsing a waveform through the triaxial cell and platen stack without any sample being present. The value of $t - t_0$ is therefore the time-of-flight through the sample.

The method used to compute the P-wave attenuation is the spectral ratios method (Tosköz et al., 1979) which utilizes the spectral amplitudes recorded by propagating a waveform through a non-attenuating reference sample with the same dimensions as the sample. For this research, an aluminum standard was used. Previous work (e.g. Butt, 2001) has shown that the spectral ratios method is robust for this type of laboratory attenuation measurement since it is relatively insensitive to the variations in wave amplitude that result from the changing contact pressure between the sample, loading piston and platens throughout a test.

The attenuation of the P-wave can be described using:

$$A_2(f) = G(x)A_1(f)\exp\left(-\frac{\pi x f}{cQ}\right) \tag{6.5}$$

where the A is the spectral amplitude, the subscripts 1 and 2 indicate two locations along the same raypath separated by distance x, $G(x)$ is the geometrical spreading function, c is the phase velocity and Q is the attenuation quality factor. Dividing equation 6.5 for the sample by equation 6.5 for the reference sample gives:

$$\ln\left(\frac{A_r(f)}{A_s(f)}\right) = \left(\frac{\pi x}{c_s Q_s} - \frac{\pi x}{c_r Q_r}\right) f + \ln\left(\frac{G_r(x)}{G_s(x)}\right) \tag{6.6}$$

where the subscripts s and r indicate the sample and reference values, respectively. Assuming that $1/Q_r \approx 0$, this reduces to:

$$\ln\left(\frac{A_r(f)}{A_s(f)}\right) = \frac{\pi x}{c_s Q_s} f + \ln\left(\frac{G_r(x)}{G_s(x)}\right) \tag{6.7}$$

where $\pi x/c_s Q_s$ is the linear slope of a plot of $\ln(A_r/A_s)$ as a function of frequency. For the determination of Q the phase velocity c was assumed to be the same as the group velocity V_p computed in Equation 6.2. A typical spectral ratios dataset is shown in figure 6.5.

6.8 Experimental results

6.8.1 Permeability-stress

Stress-strain curves for the tested samples are given in figure 6.6. Most samples had a Young's Modulus in the range of 8 to 10 GPa and a failure strength in the range of 100 to 165 MPa. In general, the samples tested at 10 MPa confining pressure (e.g. PH403-B and PH473-L) had the greatest stiffness and failure strength with both parameters decreasing at lower confining pressures. The two weakest samples, PH403-D and H5-V, had the lowest Young's Modulus of 6 and 7 GPa, respectively.

Permeability-stress data for the tested samples are given in figure 6.7. For some tests, permeability measurements were partially or entirely out of range due to incorrect configuration of the flowmeter, as noted on the graphs. In general, sample permeability decreases logarithmically with increasing axial stress. For samples tested at 1 MPa confining pressure, permeability ranges between 10 to 20 mD at low axial stress and decreases to as low as 0.1 mD at an axial stress of 125 MPa. For samples tested at 5 and 10 MPa confining pressure, permeability is generally less than 0.1 mD and, where data is available, the measured permeability decreases to as low as 0.003 mD before falling out

of measurement range. At approximately 700 m depth, the permeability in virgin ground is expected in the range of 0.005 to 0.04 mD, and near mine openings, where lateral confining pressures are reduced, the permeability can be several orders of magnitude higher in the 4 to 15 mD range.

Several additional observations can be made from the permeability-stress data. First of all, sample H5-V tested at 5 MPa confining pressure showed anomalously high permeability (with respect to the general permeability patterns noted above) with values 2 to 3 orders of magnitude higher than expected. This suggests that pockets of higher permeability may be present in the sandstone. Secondly, both of the samples recovered from borehole H5 show permeabilities that are less sensitive to changes in axial stress than the other samples. This is shown as the slope of the fitted logarithmic relationship for these two samples which is less than the consistent slope for all other samples where stress-permeability data are available. Since borehole H5 was the only borehole drilled in-seam and parallel to sedimentary bedding (Table 6.2), this suggests that horizontal permeability is less sensitive to stress than vertical permeability.

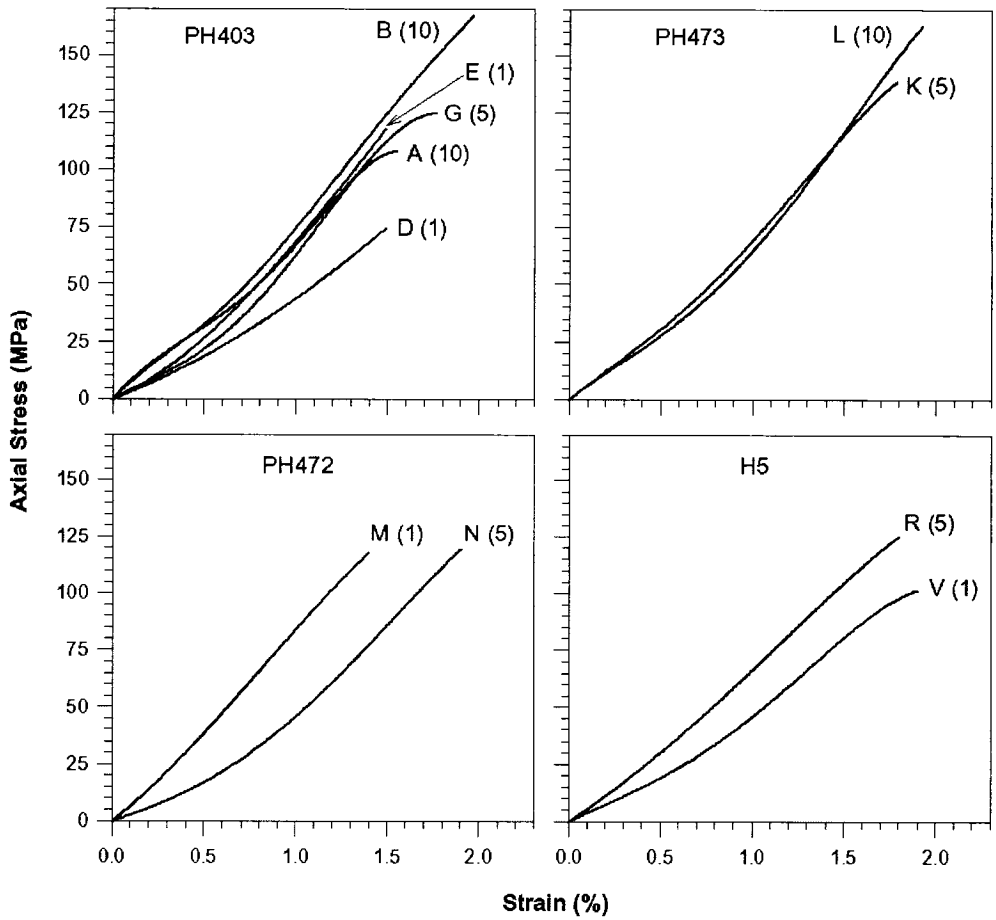

Figure 6.6: The stress vs. strain measurements for the tested sandstone samples prior to failure. The number in brackets after each sample label indicates the confining pressure in MPa.

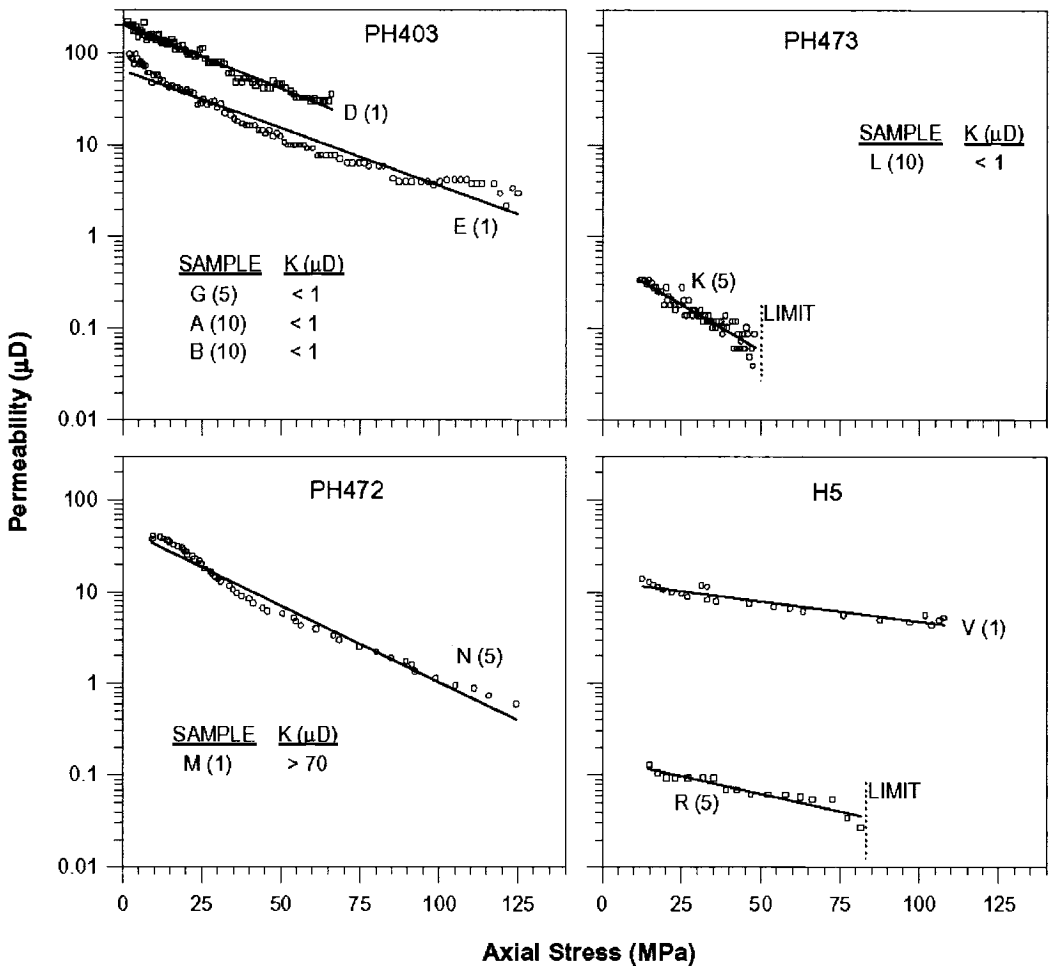

Figure 6.7: The permeability vs. stress measurements for the tested sandstone samples prior to failure. The number in brackets after each sample label indicates the confining pressure in MPa. Samples with measurements partially or completely out of range are indicated on each graph.

Acoustic Emissions

The samples from boreholes PH403 and PH473 were tested with the acoustic monitoring system configured to record AE. The patterns observed for all of these samples was

consistent with two distinct periods of AE activity: i) during the first few minutes at the start of each test when confining pressure was applied and the stress-strain curve was curling upwards, and ii) during the final few minutes of each test when the stress-strain curve was beginning to roll over before sample failure. There were generally no AE detected outside these two periods. These patterns of AE are shown in figure 6.8 for three of the PH403 borehole samples tested over the range of confining pressures along with there corresponding stress-time curves.

The first AE period is interpreted as seating of the sample platens and the closure of recovery-induced microcracks, while the second period is interpreted as microcracking of the sample matrix or cemented grain contacts during the period of plastic deformation preceding failure. This interpretation is supported by the permeability measurements shown in figure 6.7 with many samples showing permeability measurements decreasing at a rate greater then the logarithmic trend during the first AE period (due to closure of microcracks) and permeability measurements decreasing at a rate less than the trend during the second AE period (due to permeability enhancement from new microcrack formation). The permeability measurements during the aseismic period of the linear stress increase generally follow the logarithmic trend and suggest that the permeability decrease is due to elastic compression of the sample matrix and pore spaces during this interval.

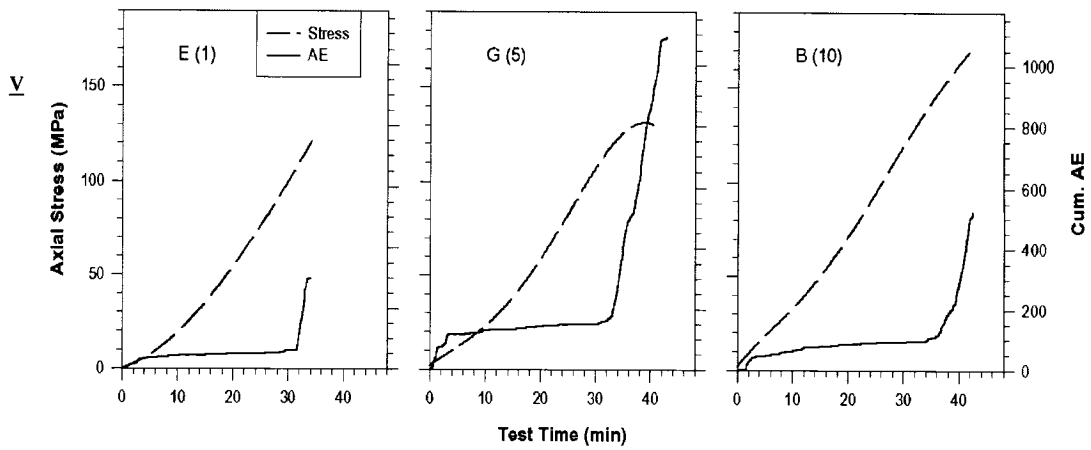

Figure 6.8: The cumulative number of acoustic emissions and the axial stress for samples taken from the PH403 borehole. The number in brackets after each sample label indicate the confining pressure in MPa.

Velocity and Attenuation

The samples form the PH472 and H5 boreholes were tested with the acoustic monitoring system configured for ultrasonic transmission measurements. Due to a system configuration error, the waveforms recorded for sample H5-V had poor signal-to-noise ratio and no data for these waveforms are presented here.

The computed P-wave velocities and attenuation quality factors for the remaining three samples are presented in figures 6.9 and 6.10, respectively. The V_p data show initial velocities between 3000 and 3500 m/s at low axial stress which increase to maximum values in the range of 5200 to 5500 m/s just before sample failure at 120 MPa axial stress. Increases in velocity are generally proportional with increases in axial stress after an initially higher rate. In general, samples tested at higher confining pressure have

higher initial velocities reflecting the higher initial stress conditions for these tests. The Q_p data show average attenuation quality factors in the range of 10 to 20 at low axial stress which increases to average values in the range of 30 to 40 just before sample failure. The high level of scatter in the Q_p values for sample PH472-N is the result of difficulties separating the initial P-wave arrival from a later wave arrival; this problem has been corrected in later research by significantly increasing the digital sampling rate and hence the number of P-wave samples (Donald et al., in pres). As with the velocity data, samples tested at higher confining pressure have initially higher Q_p values.

At approximately 700 m depth, the P-wave velocity and attenuation quality factors in virgin ground are expected to be 4000 m/s and 20 to 25, respectively. Near openings, where lateral confining pressures are reduced, these parameters are expected to be somewhat lower at 3800 m/s and 10 to 15, respectively.

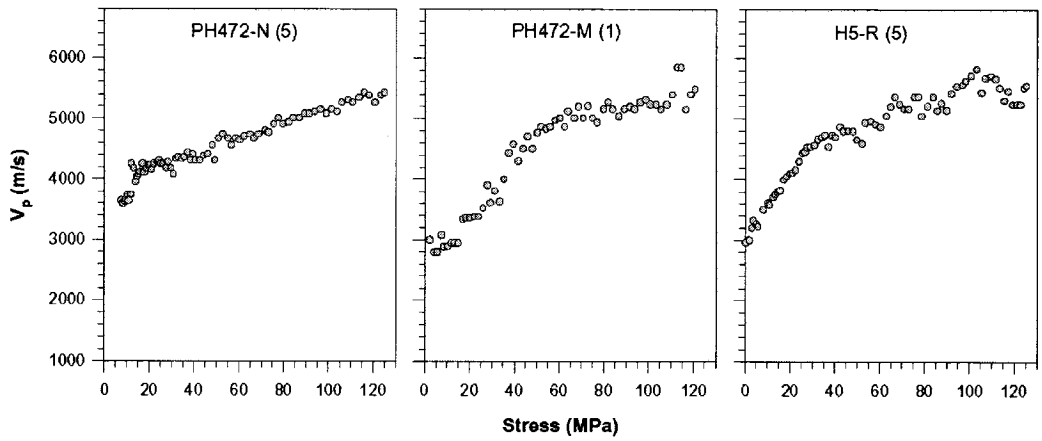

Figure 6.9: P-wave velocity vs. stress measurements for the tested samples prior to failure. The number in brackets after each sample label indicate the confining pressure in MPa.

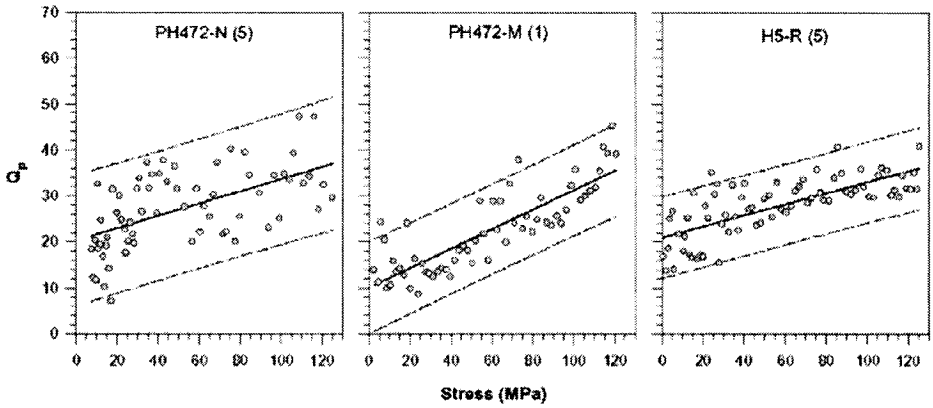

Figure 6.10: P-wave quality factor vs. stress measurements for the tested samples prior to failure. The number in brackets after each sample label indicates the confining pressure in MPa. The solid lines are the linear trend fitted by least-squares regression and the dashed lines bound the 95% prediction interval.

6.9 Conclusions

From this investigation, the patterns of permeability, acoustic emissions, ultrasonic velocity and ultrasonic attenuation for samples of the outburst-prone sandstone have been characterized over a range of triaxial pressures and axial stresses up to failure. From these data, several observations can be made regarding the characteristics of the sandstone at approximately 700 m depth with an estimated overburden pressure of 20 MPa:

- The permeability in virgin ground is less than 0.1 mD and probably in the range of 0.005 to 0.04 mD.
- Near mine openings, where lateral confining pressures are reduced, the permeability can be several orders of magnitude higher in the 4 to 15 mD range.
- Horizontal permeability is less sensitive to changes in stress than vertical permeability.

- P-wave velocity is expected to be approximately 4000 m/s in virgin ground and approximately 3800 m/s under reduced lateral confining pressure near mine openings.
- P-wave attenuation quality factor is expected to be in the 20 to 25 range in virgin ground and in the 10 to 15 range under reduced lateral confining pressure near mine openings.

In addition, several observations regarding permeability enhancement can be made:

- Microcracking of the sandstone prior to compressive failure does not result in significant permeability enhancement.
- Local pockets of higher permeability may be present in the sandstone.
- These observations can be applied in the field by installing transducers in the mine opening and analyzing the acoustic velocity of waves. As indicated higher speed above 4000m/s indicates higher stresses which signify an unsafe, outburst prone area and an onset of rock outburst.
- De-stressing therefore has to be done in these areas before mining proceeds.

6.10 Acknowledgements

The authors would like to thank former staff of the Phalen Colliery for collaboration in this investigation, in particular Stephen Forgeron, Senior Mine Geologist, Pleman Woodland, Senior Outburst Engineer, and Robert MacDonald, Mine Manager. The assistance of Jack Touseull of ASTM International regarding clarification of gas permeability measurement procedures is greatly appreciated.

6.11 References

ASTM Standard D4525, (1990), Standard test method for permeability of rocks by flowing air, ASTM International Annual Standards, Vol. 04.08, West Conshohocken, Pa.

ASTM Standard D4543, (1985), Standard practice for preparing rock core specimens and determining dimensional and shape tolerances, ASTM International Annual Standards, Vol. 04.08, West Conshohocken, Pa.

Aston, T., Kullman, D. and Barron, K., (1990), Modelling of outbursts at #26 Colliery, Glace Bay, Nova Scotia. Part 1: outburst history and field data, *Min. Sci. Tech.*, Vol. 11, p. 253-260.

Butt, S. D., (1999), Development of an apparatus to study the gas permeability and acoustic emission characteristics of an outburst-prone sandstone as a function of stress, *Int. J. Rock. Mech. & Min. Sci.*, Vol. 36, No. 8, p. 1079-1085.

Butt, S. D., (2001), Experimental measurement of P-wave attenuation due to fractures over the 100 to 300 kHz bandwidth, *Pure Appl. Geophys.*, Vol. 58, No. 9/10, p. 1783-1796.

Corbett, G. R., (1997), *The development of a coal mine portable microseismic monitoring system for the study of rock gas outbursts in the Sydney coal field, Nova Scotia*, unpub. M.Eng. thesis, McGill University, Canada, 177 pages.

DEVCO (Cape Breton Development Corporation), 1994-2000. Unpublished internal reports.

Donald, A., Butt, S. D. and Iakevlov, S., in pres., Adaptation of a triaxial cell for ultrasonic P-wave attenuation, velocity and acoustic emissions measurements, *Int. J. Rock. Mech. & Min. Sci.*

Forgeron, S, Mackenzie, B. and Macpherson, K., (1986), The effects of geological features on coal mining, Sydney Coalfield, Nova Scotia, *CIM Bulletin*, Vol. 79, No. 891, p. 79-87.

Forrester, D., Cain, P., Corbett, G. and Plouffe, M., (1994), *CBCRL monitoring of outburst incident at Phalen Colliery of September 28, 1994*, unpub. report, CANMET-MRL.

Gibling, M. R., Nguyen, M. H., Martel, A. T. and Naylor, R. D., (1999). Chapter 4 – Porosity and permeability of sandstones in the Phalen and Prince Mines, in *Geology and hydrogeology of the subsea mining district, Sydney Coalfield, Nova Scotia*, Centre for Marine Geology, Dalhousie University, unpub. Tech. Rep. 14.

Golder Associates, (1985). *Development and use of triaxial rock testing procedures for*

samples of the Sydney Coalfield, Phases One and Two, unpublished report to CANMET for DSS Contract OSQ83-00214.

Jones, F. O. and Owens, W. W., (1980), A laboratory study of low permeability gas sands, *J. Pet. Tech.*, Sept., p. 1631-1640.

King, D. and Greenhalgh, S., (1979). In-seam seismic methods; a review, *Bulletin – Australian Society of Exploration Geophysicists*, Vol. 10, No. 3, p. 222.

Klinkenberg, L. J., (1941), The permeability of porous media to liquids and gases, *API Drilling and Production Practice*, p. 200-213.

Sheppard, J., Rixon, L. K. and Griffiths, L, (1981), Outbursts and geological structures in coal mines: a review, *Int. J. Rock. Mech. & Min. Sci.*, Vol. 18, p. 267-283.

Tosköz, M. N., Johnston, D. H., and Timur, (1979), Attenuation of seismic waves in dry and saturated rocks: I. laboratory measurements, *Geophysics*, Vol. 44, No. 4, p. 681-690.

Woodland, P., (1997), Overview of gas outbursts in No. 4 Slope, Phalen Colliery, unpub. internal Devco report.

PART III

NUMERICAL MODELING, DIFFRACTION, ATTENUATION AND SCALING DEVELOPMENT

III: Overview

This chapter contains two technical papers. All the papers are based on numerical modeling of wave propagation, attenuation, scaling developments and multi-frequency data integration. The first paper is with the journal of Acoustical Society of America for consideration. The second paper is with International Journal of Mathematical Geology. These papers are on numerical modeling and linked directly with laboratory experimental and validations.

Chapter 7: Laboratory experiment and modeling to study the effect of diffraction on velocity and attenuation measurements in rock materials

This paper is submitted to the Journal of Acoustical Society of America for publication. The lead author for this paper is Mr Paul Frempong with one co-author, Dr. Stephen D. Butt.

7.1 Abstract

Deviation in geometrical optics contributes significantly to errors, in the form of diffraction losses, in acoustics experiments. Rock materials, by their nature, have high intrinsic and scattering attenuation properties. There is therefore the tendency to neglect diffraction loss in attenuation and velocity measurements in rocks. This paper presents a laboratory velocity and quality factor measurements in rocks that take into account diffraction losses due to non standard shapes and sizes of the rock sample. A model of diffraction correction factors calculated numerically for non standard geometries were used to correct the laboratory measured velocities and attenuation values. Results show that, transducers of larger diameter, higher central frequency and shorter wavelength cause more diffraction loss in rocks than their opposite counterparts. Measurements in shorter rock samples result in high diffraction errors than that of longer rock samples. Diffraction errors reduce the measured velocities and increase the measured quality

factor. Rocks of high acoustic velocities and low quality factors are more susceptible to diffraction losses than rocks of low velocity and high quality factor. Although the percentage diffraction corrections for the rock materials were generally small, they were still considered significant, especially given the present increasing demand for high accurate and precise acoustic measurements at a MHz frequency range, to identify microscopic structures in rocks.

7.2 Introduction

Diffraction loss is one of the factors that affect the accuracy of velocity and attenuation measurements during acoustic laboratory experiments. Any deviation from geometric optics results in energy leak around the sides and rear of the rock sample, thus affecting the travel time and the amplitude. Laboratory acoustic measurements are particularly prone to diffraction loss effect because of the shapes and sizes of sample and transducer characteristics used in these measurements. The measurements are based on the response of the complex pressure fields between the emitting transducer and the receiving transducer (William, 1951). The pressure transfer between these two surfaces is inefficient because of losses of energy due to wave spreading. This phenomenon is known as diffraction loss. Diffraction losses in various industrial materials were studied extensively in the past (William, 1951; Seki et al., 1956; Papadakis, 1972; Khimunin, 1972; Benson and Kiyohara, 1973). Corrections have been applied in most acoustic measurements of low loss materials. However, diffraction loss has rarely been applied in

the laboratory acoustic measurements on rocks, where it has been known to have high intrinsic and scattering attenuation. Diffraction losses in these materials are usually neglected (Adam, 2004). The reasons normally given are: (i) the small amount of measurements of diffraction loss as compared to the visco-elastic and scattering loss, particularly in rocks (Adam, 2004), and (ii) the amount of accuracy needed in the measurements of acoustic properties of rocks makes considering diffraction loss insignificant (Johansson and Martinsson, 2001). With the increasing demand of high accurate measurements of acoustic velocities (V) and attenuation quality factors (Q) in rock materials, coupled with measurements in some low absorption rock media, in the MHz frequency range, to identify microscopic fractures, diffraction loss may no longer be ignored. This paper presents a laboratory study and numerical modeling of diffraction loss in rocks of different shapes and sizes. Compressional ultrasonic wave velocities (V_P) and attenuation quality factors (Q_p) were measured in rocks of different shapes and sizes under varying degrees of effective stress. A model of diffraction correction factors based on the methods by Papadakis (1966) was then used to correct the measured V_p and Q_p. It was found that the impacts of diffraction loss on the measured velocity and attenuation were small. However it was still significant, especially given the present increasing demand for high accurate acoustic measurements at a MHz frequency range, to identify microscopic structures in rocks.

7.3 Review of diffraction loss

Generally, the estimation of diffraction loss requires the evaluation of complex pressure values at the surface of the transducers: one at the emitting transducer and the other at the receiving transducer (Khimunin, 1972). Knowledge of these temporo-spatial pressure patterns of acoustic radiation is therefore important in defining the performance and efficiency of the acoustic measurements. For efficient and accurate acoustic measurements, many factors have to be carefully considered to minimize diffraction loss. These include:

- Using standard sizes and shapes of the rock sample (minicores, or large cores with specific length-to-diameter ratio)
- Using standard size of the transducer, for example the physical diameter of the transducer.
- Carefully choosing transducer's position on the surface of the sample so that the axis of the transducer coincides with the axis of the core sample under study.
- Choosing right wave characteristics (wavelength and central frequency of the transducer).

Even if the above precautions are taken, and a perfect experimental arrangement is in place, minor intrinsic beam spread could occur because the vibrating particles of the material, through which the wave travels, do not always transfer all of their energy in the direction of wave propagation. Therefore it is important to model diffraction loss and include it in laboratory acoustic measurements. Many modeling techniques are available.

Some numerical methods are also available for the estimation of the average pressure. These include rigorous calculations by numerical integration and spectral representation of the field of the transducer source. Other numerical methods found in the literature include using Lommel and Bessel functions (Benson and Kiyohara, 1974), Simpson method (Khimunin, 1972), numerical integration with trapezium method and a rapid impulse method that requires only one numerical integration per point field (Pinttinen and Luukkala, 1977). Like many numerical methods, the choice of technique is based on three main criteria:

(i) The required accuracy and acceptable errors,

(ii) The theoretical and mathematical complexity,

(iii) The computer time and ease of coding the algorithm.

Published tables and graphs of diffraction loss and phase shift angles are available for correction of measured velocities and attenuation. All these tables are based on the original diffraction loss modeling by William (1951) and later by Papadakis (1966, 1972) and Khumunin (1972). The tables are universal in that they can be used to correct diffraction loss on any combination of transducer and sample size and shapes. The only difference the calculated values may be (i) the accuracy of the numerical calculations and (ii) the small errors that may results in the extrapolation and interpolation of diffraction loss values for a case where the exact transducer diameter and the corresponding wavelength (ka values) may not appear in the published tables. To avoid such extrapolation and interpolation errors, a similar numerical calculation employing Simpson formula was used to generate a diffraction loss model based on the exact 'ka'

value of 13.9 used in the current study. To examine the validity of this numerical approach, the amplitude loss and phase advance due to the diffraction effect was applied on a second experiment with different ka values and results were in good agreement.

7.4 Numerical calculations of diffraction loss

7.4.1 Diffraction modeling procedure

Modeling diffraction loss comprises the evaluation of the values of the complex acoustic pressure at a sufficient number of points on the receiver's surface. The diagram in Figure 7.1 is an acoustic beam from a transducer that sweeps over a cylindrical volume along the z axis, so that at any distance, z, the cylindrical coordinates at any location P is given by (r, θ, z). The first coordinate (r), describes the distance from the z-axis to the point (p) and the second coordinate (θ), describes the angle from the positive xz-plane to the point, p. The third coordinate (z), is the usual z-coordinate from the transducer face along the positive z direction of which the beams travel. The surface of the cylinder, which in this experiment represents a sandstone sample, is imparted with wave energy with velocity amplitude υ_0 by the transducer. The transducer has a central frequency (f), wavelength (λ), and wave number (k).

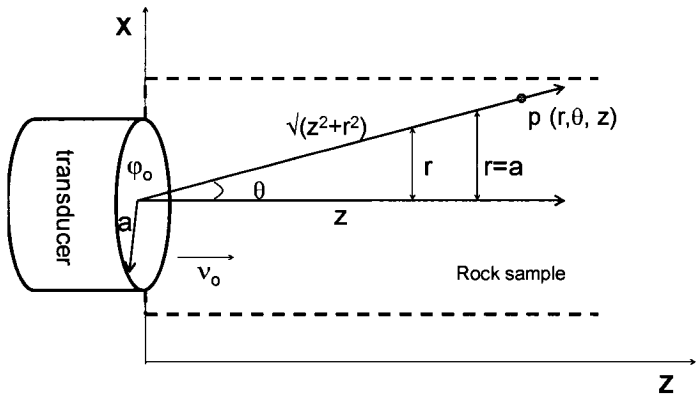

Figure 7.1: Acoustic beam from a transducer through an imaginary cylindrical sample volume along the z axis

The P-wave causes the sample particles at the surface to vibrate with the same velocity amplitude, υ_0, along the z axis. The exact expression of the initial axial velocity potential at the surface between the transducer and the sample in this arrangement (Figure 7.1) is given by Williams (1951) as φ_0 where:

$$\varphi_o = (\upsilon_o / ik)(e^{-ikz} - e^{ik(z^2+a^2)}) \tag{7.1}$$

The approximate velocity function can be expressed in terms of basal function at any distance through an acoustic beam centered at z axis as:

$$\varphi = \upsilon_o a \int_0^\infty \mu^{-1} e^{-\mu z} J_o(\eta r) J_1(\eta a) d\eta \tag{7.2}$$

where $\mu = (\eta^2 - k^2)^{1/2}$

η is an integration variable,

J_0 and J_1 are ordinary Bessel functions.

Inspecting equations 7.1 and 7.2, it is noted that:

$$\varphi = a\int_0^{\infty} \mu^{-1} e^{-\mu z} J_1(\alpha a) d\alpha = (ik)^{-1}(e^{ikz} - e^{ik(z^2+a^2)}) \tag{7.3}$$

If the two transducers have equal radius *a*, facing each other along the distance, z, Williams (1951) showed that the average pressure, P, can be deduced from the velocity potentials, φ, in equation 7.1, 7.2 and 7.3 as:

$$P = \rho c v_0 e^{ikz} - \frac{4\rho c v_0}{\pi}\int_0^{\pi/2} \exp[-ik(z^2 + 4a^2\cos^2\theta)^{1/2}]\sin^2\theta d\theta \tag{7.4}$$

Where, k is the wave number ($k=2\pi/\lambda$),

λ the wavelength,

z is the distance between transducers,

υ_0 is the velocity amplitude of the initial vibration on the transmitting transducer.

According to William (1951), the plane wave term (from equation 4) is given by:

$$P_0 = \rho c v_0 \exp[i(\omega t - kz)] \tag{7.5}$$

As discussed earlier, the diffraction loss then becomes the ratio of the spatially averaged acoustic pressure received at the receiving transducer front face from the transmitter (*P*, in equation 7.4), to a plane wave with the same initial pressure emanating from the full infinite plane of the transmitter front face (P_0 in equation 7.5). This is mathematically given by: $\left|\frac{P}{P_0}\right|$

Therefore diffraction loss is given by:

$$\left|\frac{P}{P_0}\right| = \left| \frac{\{\rho c v_0 e^{ikz} - \frac{4\rho c v_0}{\pi} \int_0^{\pi/2} \exp[-ik(z^2 + 4a^2\cos^2\theta)^{1'2}]\sin^2\theta d\theta\}}{\{\rho c v_0 \exp[i(\omega t - kz)]\}} \right| \tag{7.6}$$

As stated earlier many writers have used different techniques to calculate equation 7.6. The technique employed in this research is Simpson method. Equation 7.6 is first decomposed into simpler equations and each is evaluated with Simpson's formula to get an approximate estimate of the diffraction loss.

Decomposition method:

$$\text{Let} \quad D = \int_0^{\pi/2} \sin[k(z^2 + 4a^2\cos^2\theta)^{1'2}] \times \sin^2\theta d\theta \tag{7.7}$$

$$C = \int_0^{\pi/2} \cos[k(z^2 + 4a^2\cos^2\theta)^{1'2}] \times \sin^2\theta d\theta \tag{7.8}$$

$$B = D\frac{4}{\pi}\cos kz - C\frac{4}{\pi}\sin kz \tag{7.9}$$

$$A = 1 - C\frac{4}{\pi}\cos kz - D\frac{4}{\pi}\sin kz \tag{7.10}$$

Then:

$$\left|\frac{P}{P_0}\right| = (A^2 + B^2)^{1/2} \tag{7.11}$$

The diffraction phase angle (ϕ) in radians, is also given by the tangent inverse of the real and imaginary part of the average pressure and the pressure of the plane waves.

Thus:

$$\phi = \tan^{-1}(B/A) \tag{7.12}$$

The diffraction attenuation (α) in decibel is expressed as the logarithmic of expression of the dimensionless ratio of the diffraction loss (P/P_0) given by:

$$\alpha = -20\log_{10}(\frac{P}{P_0}\} \tag{7.13}$$

Simpson method was applied to each term of the diffraction loss (equation 7.7 and 7.8) to estimate the integral C and D. It is then used to evaluate the values of A, B, P/P_0, ϕ and α. The computation of the integrals (Equation 7.7 to 7.11) was programmed numerically in MATLAB (see Appendix A), and the iteration of the algorithm was continued above m=100 until a convergence within $1*10^{-6}$ was obtained. This has to be done to take into account the low absorption nature of the glass sandstone so that small diffraction errors could be mapped accurately.

7.4.2 Diffraction modeling results

The results of the modeling are presented in the form of tables and graphs that can be used for diffraction loss for ka of 13.9. The diffraction loss dependant parameters (sample length, z, wavelength, λ and radius of transducer, *a*), were normalized as dimensionless distance S, given by, $S= z\lambda /a^2$. The central value for 'ka' for the transducer is 13.09. The parameters were input into the Simpson algorithm for the estimation of diffraction loss for 'ka' =13.09. The diffraction phase shift ϕ for the sandstone was also calculated using equation 7.12. This calculation were repeated for other experiments with same ka values but different values of k and a. Table 7.3 shows the integral, A and B and the estimated values of diffraction loss, P_0/P, diffraction phase shift, ϕ, and diffraction loss in decibels,

α, for 'ka'=13.09 and dimensionless distance, S, up to 50. The losses are also plotted graphically in figures 7.7 and 7.8 with the normalized distance, S, up to 14.

7.5 Laboratory experiment

7.5.1 General

In the study of reservoir imaging, laboratory acoustic measurements of reservoir rocks under deformational stress are conducted routinely using a triaxial chamber, coupled with acoustic instruments. The main aim is to find the acoustic properties (velocity, attenuation, impedance, quality factors and acoustic emission) and link them to the petrophysical and geomechanical characteristics of the rocks. Such experiment demands that, the effective stress on the rock sample is varied whilst ultrasonic waves are transmitted through the sample in the triaxial chamber. The strict conditions on the geomechanical experiments and the size, shape and the dimensional tolerance on the sample may result in the deviation of geometrical optics when the two experiments (acoustic and geomechanics) are coupled together. The setup and the experimental arrangements may therefore cause diffraction losses that would affect the accuracy of the velocity and attenuation values. Some authors (Donald et al., 2004) have iterated that diffraction phase corrections as described by Khimunin (1972) and Papadakis (1972) are not required in ultrasonic velocity and attenuation measurements of rocks because the diffraction loss is small enough to be considered negligible. However, as shown by Khimunin (1972), the ratio of the average pressure on the transducer to the pressure of

the continuous plane wave would only approach zero only when the normalized distance becomes so large (infinite) which is not the case for the samples used in this experiment. This indicates that the P-wave can not be considered as a uniform pressure front as it passes through the rock sample, and therefore small diffraction would be observed because of the relatively small distance between transmitter and receiver.

Suits of laboratory experiments were conducted to illustrate diffraction loss correction in attenuation and velocity measurements in rock samples subjected to deformational forces. The samples were of the same type of rock (quartz sandstone) with different sizes and shapes. The physical size and the characteristics of the transducers for each experiment were also different. This was done to practically quantify the diffraction loss in attenuation and velocity measurements of the quartz sandstone using the modeling method presented above.

7.5.2 The rock samples

The samples were high-porosity, low-permeability sandstone rock core of different sizes (Figure 7.2). The geomechanical and petrophysical properties of the sample are given in Table 7.1. The rock contains fine grained rounded shapes of quartz of average size of about 175 microns. The samples were strongly cemented and very tight with few pores. They were drilled perpendicular to the lamination/bedding plane so that cores of maximum heterogeneity were achieved. The sample preparation involving coring, grinding and polishing are not detailed in this paper. However, such details can be found

in the ASTM standard (ASTM, 2004). The detailed geological, petrophysical and geomechanical properties of this type of sandstone rocks have also been documented elsewhere (Ryan, 1998). The shapes and sizes of the core samples for all the experiments are given in Figure 7.2. The transducer characteristic frequency and physical dimensions are also given in Table 7.2

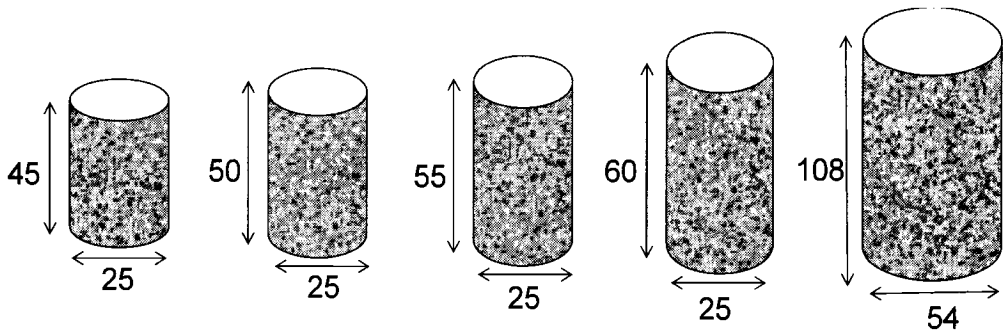

Figure 7.2: Sizes of samples used in the experiment

Table 7.1 Physical properties of quartz sandstone

PROPERTIES OF THE ROCK SAMPLE	
Uniaxial Compressive Stress (MPa)	102.83
Young Modulus E, (MPa)	5435.00
Bulk Modulus K (MPa)	4530.00
Shear Modulus G (MPa)	2078.91
Density ρ (g/cc)	2.30
Poisson Ratio	0.31
Porosity (%)	16.20
Permeability k (md)	4.10
Unconfined P Wave Velocity Vp (m/s)	3450.00
Unconfined S Wave Velocity Vs (m/s)	2650.00

Table 7.2: Transducer characteristic and sample parameters used in the experiments

Transducer Property	Radius (a) 7.19, 12.5 mm	Central frequency (fc) 1000KHz	
Wave Property	Type P-Wave Wavelength (λ) 3.45, 4.00 mm	Velocity (v) 3450000, 4000000 mm/s Wavenumber (k) 1.8212, 1.571 /mm	Frequency (f) 1000000Hz
Sample Property	Type Quartz sandstone Dimensionless distance (S) 7.2	Length (z) 45, 59, 55, 60, 108 108 mm ka 13.09, 19.64	Diameter (d) 25, 54 mm

7.5.3 Experimental set-up and apparatus

The equipment is made up of a high pressure triaxial cell, equipped with an array of pressure vessels that can be used for pressure-curing and velocity measurements. The principal cell (Figure 7.3) is a 7 ton, double-walled steel vessel with 40 cm long by 10 cm diameter working cavity, which can operate to a hydrostatic confining pressure of 1.4 GPa. The pressure medium consists of light hydraulic oil pumped into the working cavity by means of a two-stage intensifier. Electrical communication to samples in the working cavity is maintained through eight insulated cone feed-throughs in the vessel's end closure, allowing as many as six samples to be measured at a time. The system is housed in a double-reinforced concrete vault and monitored from control panels in an adjacent laboratory. The digitizer is a Nicollet 4094 digital oscilloscope that can be operated in different modes from 5ns to 500ns at 8 to 12 bit. The digitizer has a varying voltage amplifier which can be applied to the data before it is recorded.

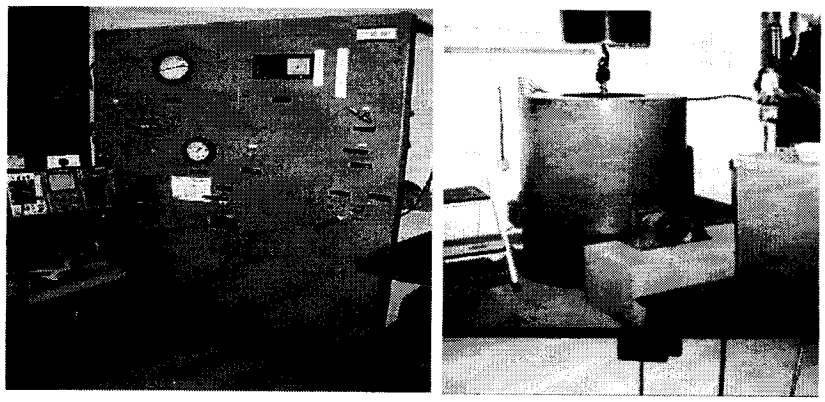

Figure 7.3 Photograph of apparatus: Tri-axial chamber apparatus with pressure control system coupled to the oscilloscope

7.5.4 Experimental methodology

Core samples were prepared according to the American Standard of Testing Material (ASTM, 2004) for laboratory tri-axial testing. The initial characteristics of the samples are given in Table 1. Bench top acoustic measurements were made with a nominal amount of effective axial stress (2MPa), applied to adequately close rock boundaries and ensure efficient acoustic transmission. This measurement was to establish the bench top property of the quartz sandstone. The samples were fully saturated with water under a vacuum pump for 24 hours. Each sample was then jacketed with a rubber tubing (Figure 7.4) to isolate it from the oil acting as the confining pressure medium. The samples were then loaded in the tri-axial chamber. Velocities were measured on pieces of minicore samples of different sizes (Figure 7.2), using the pulse transmission technique of Birch (1960), and Christensen and Wang (1985). 1 MHz lead zirconate transducers mounted on backup electrodes were used to send and receive P-waves through the samples. To

prevent the pressure medium from invading the samples during the pressure run, the minicores were sheathed in thin copper foil and the entire sample/transducer/electrode assembly was enclosed in neoprene tubing. Once the sample assembly was sealed in the pressure vessel and the pressure raised, the transmitting transducer was excited by a high voltage spike from a pulse generator and the time of flight to the receiving transducer was measured at specified pressure intervals using a digital oscilloscope. The velocity was then calculated from the time of flight and the length of the sample. After the experiment, the standard aluminum sample test was done following the same procedure as the rock specimen. The accuracy was estimated to be 0.5% for the velocity. In a typical pressure run, the velocity increases rapidly from 0 to about 200 MPa in response to the closure of microcracks and linearly at higher pressures in response to the intrinsic elastic properties of the minerals in the rock. Since velocities at any given pressure are typically higher during decompression than during compression and the decompression cycle is more representative of insitu conditions, the velocities reported below were read from decompression curves. A typical signal through the sandstone during decompression at various confining pressure is given in figure 7.5a and that of aluminum standard is given in figure 7.5b. All samples were measured wet after saturation in water to simulate insitu conditions as closely as possible. The sizes of the samples and traducer characteristics used for the experiments are shown in Figure 7.2 and Table 7.2

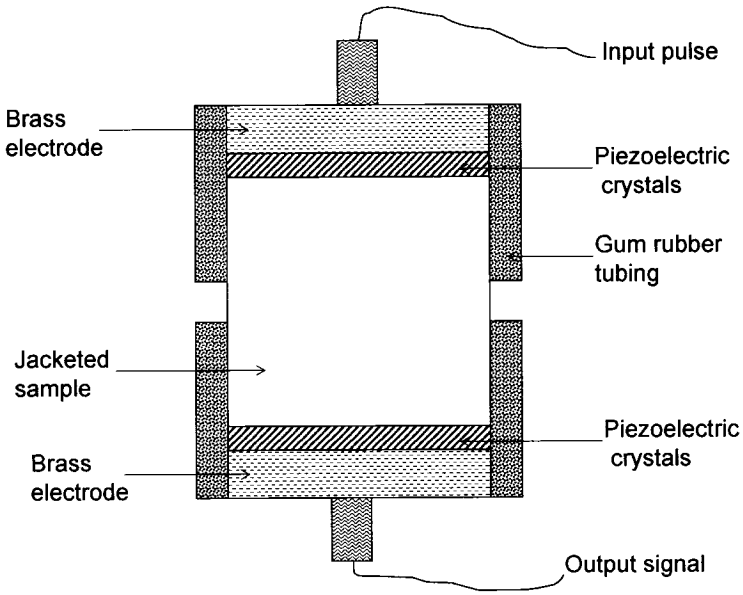

Figure 7.4: Sample assembly: jacketed sample with transducers and brass electrodes

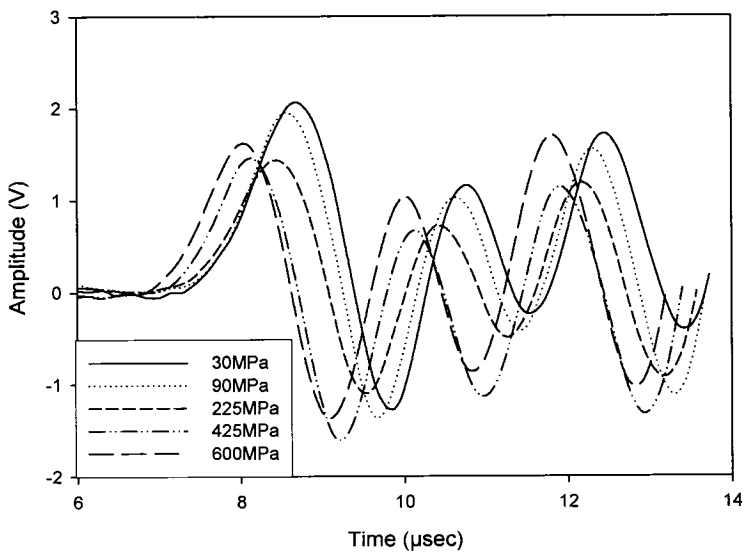

Figure 7.5a: Typical signal through the sandstone at pressures from 30MPa to 600MPa

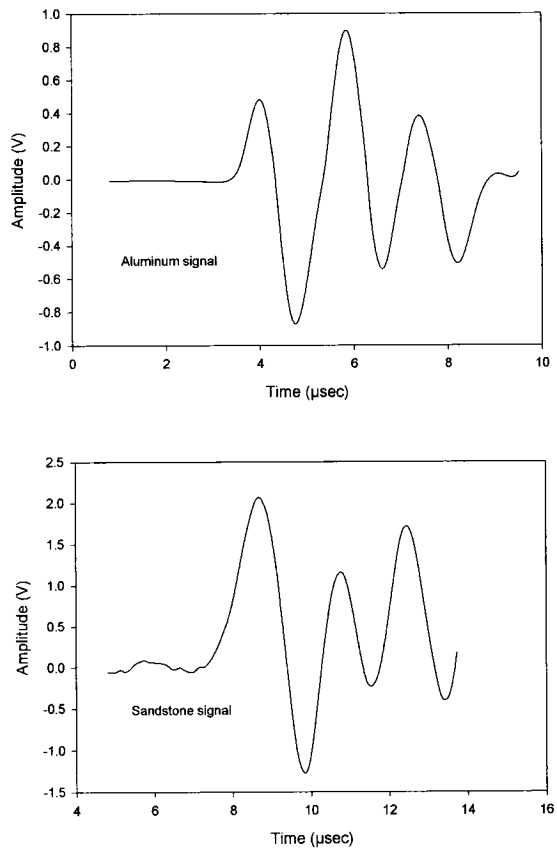

Figure 7.5b: Typical signal through the sample and the aluminum standard

7.5.5 Estimation of travel time and velocity

The technique used here is quite similar to those mentioned in Prasad and Manghnani (1997). The receiving signal amplitude will depend on the sample density and wave speed. The 'first break' of the P-wave is easily detected as it is passed through the rock sample. Prior to the computation of P-wave velocity or attenuation, the recorded waveforms were processed to improve the signal to noise ratio and to isolate the desired

wave components. First, every 50 consecutive waveforms were checked to remove bad events (due to sporadic triggering errors) and then stacked. Each stacked waveform was examined and all waveform amplitudes after the initial P-wave arrival were zeroed to remove the later wave arrivals. The arrival time and a 128 point Fast Fourier Transform were then determined for each of these stacked, isolated P-waveforms. For each waveform the group P-wave velocity V_p was computed using:

$$V_p = \frac{L}{t - t_0} \tag{7.14}$$

Where L is the sample length,

t is the arrival time,

t_0 is the zero arrival time computed by pulsing a waveform through the triaxial cell and platen stack without any sample being present.

The value of $t - t_0$ is therefore the time-of-flight through the sample.

7.5.6 Calculation of attenuation and quality factor

The method used to compute the P-wave attenuation is the spectral ratios method (Toksöz et al, 1979) which utilizes the spectral amplitudes recorded by propagating a waveform through a non-attenuating reference sample (realistically with $Q_{reference} >> Q_{rock}$) with the same dimensions as the sample. For this research, an aluminum standard was used. Previous work by Butt (2001) has shown that this spectral ratios method is robust for this type of laboratory attenuation measurement and relatively insensitive to the variations in wave amplitude that result from the changing contact pressure between the sample, loading piston and platens throughout a test. The attenuation of the P-wave

can be described using:

$$A_2(f) = G(x)A_1(f)\exp\left(\frac{\pi x f}{cQ}\right) \tag{7.15}$$

where the A is the spectral amplitude,

the subscripts 1 and 2 indicate two locations along the same raypath separated by distance x,

$G(x)$ is the geometrical spreading function, c is the phase velocity

Q is the attenuation quality factor.

Dividing equation 7.15 for the sample by equation 15 for the reference sample gives:

$$\ln\left(\frac{A_r(f)}{A_s(f)}\right) = \left(\frac{\pi x}{c_s Q_s} - \frac{\pi x}{c_r Q_r}\right) f + \ln\left(\frac{G_r(x)}{G_s(x)}\right) \tag{7.16}$$

where the subscripts s and r indicate the sample and reference values, respectively. Assuming that $1/Q_r \approx 0$, this reduces to:

$$\ln\left(\frac{A_r(f)}{A_s(f)}\right) = \frac{\pi x}{c_s Q_s} f + \ln\left(\frac{G_r(x)}{G_s(x)}\right) \tag{7.17}$$

where $\pi x/c_s Q_s$ is the linear slope of a plot of $\ln(A_r/A_s)$ as a function of frequency. For the determination of Q, the phase velocity, c, was assumed to be the same as the group velocity V_p computed in equation 7.14. A typical spectral ratios dataset is shown in Figure 7.6.

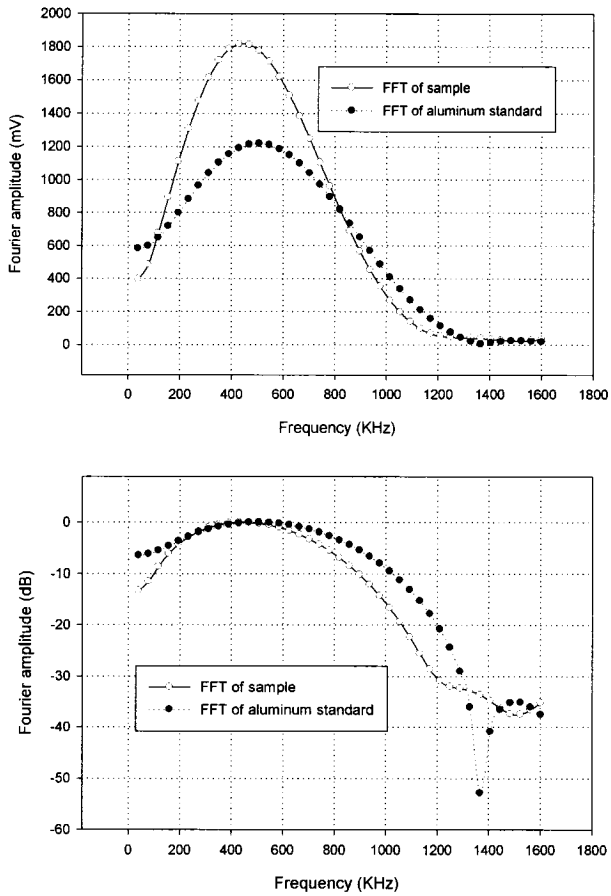

Figure 7.6: Fast Fourier Transform of the signal and the aluminum

7.6 Diffraction correction procedures

7.6.1 Effect of diffraction on the measured travel time

The diffraction errors were corrected by means of the curves in Figure 7.7 and 7.8 and Table 7.3. The diffraction would cause a phase shift, so that the measured time is not the true time of travel of the signal but actually made up of the true travel time less the time due to diffraction. This is because of the differences in phase caused by diffraction. Thus,

if ϕ is the phase shift in radians, with S the normalized distance, then the corrected time is given by:

$$t_c = \phi(S)/2\pi f_c \tag{7.18}$$

Where $\phi(S)$ is the phase shift in radians at a normalized distance of S

f_c is the central frequency of the transducer

$\phi(S)$ is read from the diffraction phase shift values (table 7.3). In this experiment, f_c was 1000 KHz. The diffraction correction time (t_c) is then added to the measured time (t_m) to estimate the true travel time (t_t). Thus;

$$t_t = t_m + t_c \tag{7.19}$$

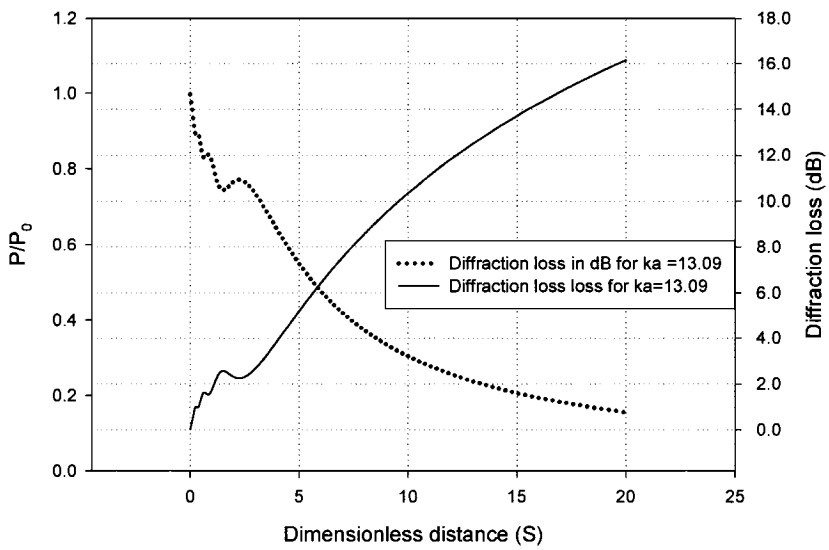

Figure 7.7: Diffraction loss curves for ka=13.09

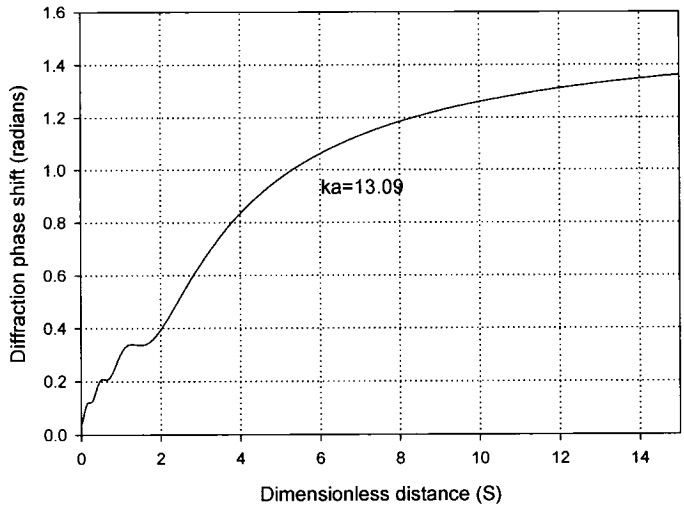

Figure 7.8: Diffraction phase shift angles in radians for ka=13.09

7.6.2 Effect of diffraction on attenuation and quality factor

The attenuation that was measured was not the true attenuation because of the diffraction. The true attenuation is modeled by subtracting the corrected attenuation from the measured attenuation. Thus:

$$\alpha_t = \alpha_m - \alpha_c$$

where α_c, is corrected attenuation

α_m is the measured attenuation

α_t is the true attenuation

α_t is read from Table 7.3.

Applying the corrected velocities and corrected attenuations to the measured travel time and attenuation yielded the corrected values in table 4. The graphs in Figures 7.9, 7.10 and 7.11 show the measured travel time, velocity and attenuation quality factors with the

corresponding corrected values for the quartz sandstone. The application of the diffraction correction decreased the measured velocities by 0.62% and increased the quality factor by 1.3%. It is also noted that the percentage diffraction loss increases with increasing velocity but decreases with increasing quality factor. This is an interesting result since it indicates that there is more concern for diffraction loss correction in high acoustic velocity measurements and low quality factor measurements. Although there could be an argument that the correction factors are small and therefore be neglected, it would still be better than no correction, especially given the type of accuracy needed in today's measurements of acoustic properties of rocks. Diffraction correction should therefore be routinely considered in all attenuation and velocity measurements of rocks.

Table 7.3: Diffraction loss and phase shift for 'ka' =13.09

Dimensionless distance (S)	A	B	Diffraction Loss	Diffraction Phase shift (rad)	Diffraction Attenuation (dB)
0.0	0.99675	0.03725	0.99745	0.03735	0.02221
0.2	0.89305	0.10881	0.89965	0.12124	0.91849
0.4	0.87209	0.15411	0.88560	0.17491	1.05523
0.6	0.81333	0.17044	0.83100	0.20657	1.60801
0.8	0.81433	0.19413	0.83715	0.23403	1.54395
1.0	0.77899	0.24387	0.81627	0.30339	1.76328
1.2	0.72890	0.25557	0.77240	0.33724	2.24312
1.4	0.70518	0.24706	0.74721	0.33699	2.53118
1.6	0.70436	0.24745	0.74656	0.33784	2.53871
1.8	0.70924	0.26480	0.75706	0.35733	2.41738
2.0	0.70839	0.29445	0.76714	0.39393	2.30247
2.2	0.69791	0.32916	0.77164	0.44070	2.25173
2.4	0.67836	0.36336	0.76955	0.49176	2.27528
2.6	0.65197	0.39383	0.76168	0.54340	2.36451
2.8	0.62120	0.41913	0.74937	0.59355	2.50609
3.0	0.58814	0.43897	0.73390	0.64117	2.68730
3.2	0.55439	0.45367	0.71635	0.68581	2.89749
3.4	0.52102	0.46382	0.69757	0.72738	3.12830
3.6	0.48877	0.47012	0.67817	0.76595	3.37328
3.8	0.45806	0.47321	0.65860	0.80167	3.62757
4.0	0.42913	0.47372	0.63918	0.83474	3.88747
4.2	0.40206	0.47214	0.62014	0.86539	4.15024
4.4	0.37687	0.46893	0.60160	0.89382	4.41380
4.6	0.35350	0.46445	0.58367	0.92022	4.67663
4.8	0.33187	0.45899	0.56640	0.94478	4.93758
5.0	0.31186	0.45280	0.54981	0.96766	5.19582

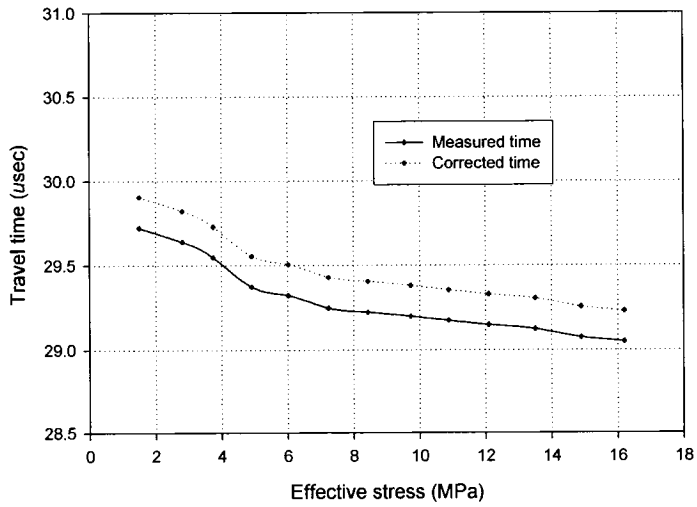

Figure 7.9: Measured and corrected travel time with effective stress

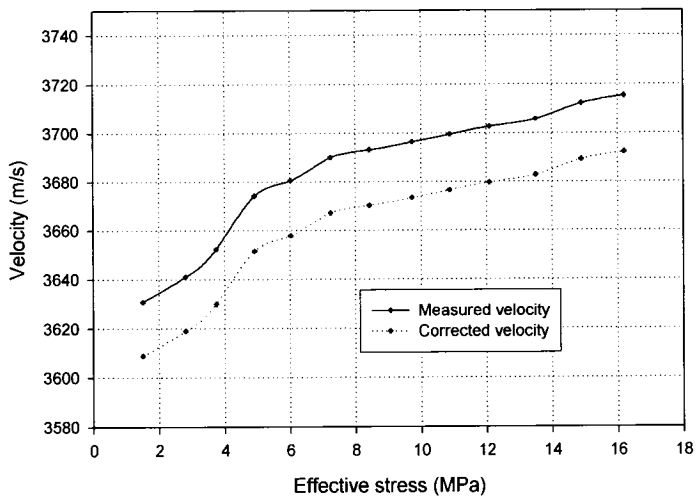

Figure 7.10: Measured and corrected velocity with effective stress

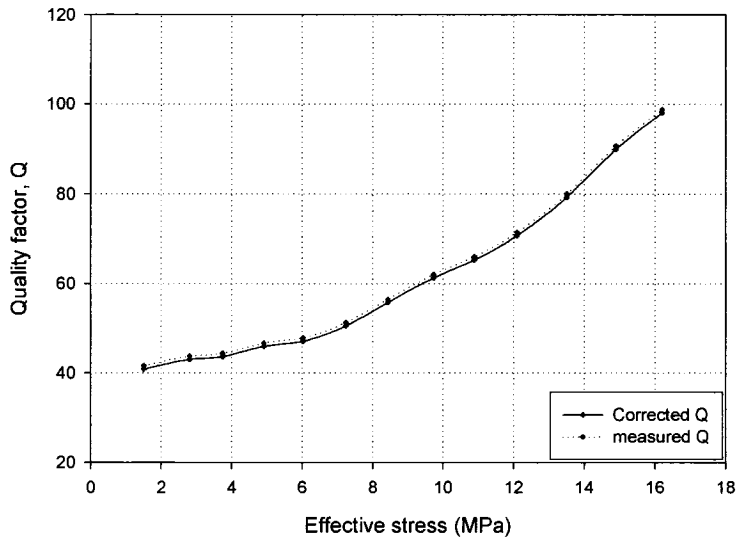

Figure 7.11: Measured and corrected quality factors with effective stress

Table 7.4: Corrected values of travel time, velocity and quality factors

Effective Stress KPa	Measured Time (μs)	Measured Velocity (m/s)	Measured Q	Diffraction Time correction (μs)	Diffraction Q correction	True time (us)	True velocity (m/s)	True Q	% change in velocity	% change in Q
1505.0	29.7222	3630.95	40.84	0.1819	0.7243	29.9041	3608.86	41.57	0.608	1.773
2811.0	29.6391	3641.13	42.99	0.1819	0.7243	29.8210	3618.93	43.71	0.610	1.685
3749.0	29.5473	3652.45	43.60	0.1819	0.7243	29.7292	3630.11	44.32	0.612	1.661
4917.0	29.3723	3674.21	45.90	0.1819	0.7243	29.5542	3651.60	46.62	0.615	1.578
6026.0	29.3223	3680.48	47.05	0.1819	0.7243	29.5042	3657.79	47.77	0.617	1.539
7241.0	29.2473	3689.91	50.56	0.1819	0.7243	29.4292	3667.11	51.28	0.618	1.433
8431.0	29.2223	3693.07	55.72	0.1819	0.7243	29.4042	3670.23	56.44	0.619	1.300
9732.0	29.1973	3696.23	61.25	0.1819	0.7243	29.3792	3673.35	61.97	0.619	1.183
10882.0	29.1723	3699.40	65.23	0.1819	0.7243	29.3542	3676.48	65.95	0.620	1.110
12090.0	29.1473	3702.57	70.68	0.1819	0.7243	29.3292	3679.61	71.40	0.620	1.025
13505.0	29.1223	3705.75	79.31	0.1819	0.7243	29.3042	3682.75	80.03	0.621	0.913
14894.0	29.0723	3712.12	89.93	0.1819	0.7243	29.2542	3689.04	90.65	0.622	0.805
16203.0	29.0473	3715.32	98.01	0.1819	0.7243	29.2292	3692.20	98.73	0.622	0.739

7.6.3 Sources of error and experimental accuracy

The exact accuracy, precision and repeatability of our measurements, at any pressure level during the experiment may never be known for certain. However, accuracy in some of the calculations and measurements were quantified in order to increase the confidence in our data. These include:

(i) The travel time, which was validated with standard aluminum and acrylic samples and the accuracy of the velocity measurements were found to be 0.50%.

(ii) One of the major sources of errors in the calculation of attenuation quality factor (Q) using spectral ratio technique is the assumption that the quality factor is independent of frequency. The frequency range was from 600 KHz to 1200 KHz, but a central frequency of 1Mhz was used in our calculations. This may introduce some error in the Q estimates. The magnitude of this error was analyzed using an error bar for Q. The error bar was based on the difference between log spectral ratio and its linear regression. The regression coefficient was 0.96 and at 95% confidence level the Q values have an error of 0.45%. (i.e. Q±0.45%). This is within experimental error. Calibration of the whole experimental set up was also done with both aluminum standard and a Lucite sample and the results were in perfect agreement with published velocity results of Lucite and aluminum.

7.7 Discussions

Non destructive evaluation of microscopic structures and properties of reservoir rocks demand high accurate and measurements of acoustic velocities and attenuation quality factors at a MHz frequency range. For such a high accuracy, diffraction corrections should not be ignored but must be applied to make a precise and accurate ultrasonic evaluation. The modeling procedure shows that different modeling techniques are available for the evaluation of diffraction loss. These techniques give the same results, the only difference being the precision. A model of diffraction correction curves and factors, calculated numerically for non standard geometries, and for specific transducer characteristic values (ka) are available for diffraction correction. This makes it easier to routinely apply diffraction losses in laboratory ultrasonic measurements without going through for modeling process. The causes of diffraction losses were mainly attributed to deviations in geometric optics, brought about by the choice of non standard shape and sizes of the rock sample and a wrong choice of transducer characteristic. Diffraction losses in non standard geometry and the transducer are very large. Therefore for very short rock samples, there is more need to apply diffraction corrections. The diffraction loss curves, presented in Figures 7 and 8, are undulating at the short distances of S and become smooth as the S increases. The undulation is due to the pronounced interference effect giving rise to multiple maxima and minima. As the frequency of the source is reduced for a fixed transducer radius the main acoustic beam becomes broader and side lobes begin to appear. The higher the frequency of the transducer the larger is the near

field zone and so, for a short sample, diffraction correction is large. It is noted that diffraction loss is a function of the radius of the transducers, 'a', the wave number 'k', the frequency, 'f' and the length of the sample 'z'. These values are standardized by a dimensionless distance, S. For a particular value of S, the diffraction loss is affected by the values of 'ka'. The number of undulations increases with increasing value of 'ka'. This is an indication of increasing diffraction loss with increasing 'ka'. It implies that transducers of larger diameter, higher frequency and shorter wavelength would cause more diffraction loss than their opposite counterparts. The calculated values of P/P_0, ϕ and α, are in agreement up to five decimal places with the calculation methodology of Benson and Kiyohara, (1973) that applied Lommel and Bessel functions. Table 3, Figure 7 and Figure 8 provide quantitative value of diffraction correction expected when a specific transducer and sample geometry are chosen during laboratory acoustic experiment. The table is a useful tool for researchers to use to plan experiments in anticipated acceptable diffraction loss. The issue of symmetry effect of 'ka' raised by Khimunin (1972) was also investigated and it was confirmed that 'ka' values are symmetrical. This indicates that the results achieved with 'ka' of, say 20, do not matter what multiple combination of 'k' and 'a' gives 'ka' of 20. For example, k=4 and a=5 would give the same results as k=5 and a=4. This would give the flexibility of choosing a combination of smaller or larger size transducer, at higher or lower central frequency, and vice versa. Thus, this would eliminate limitations for specific physical measurement of the sample and transducer size and wave frequency. It is confirmed from the laboratory experiment that different sizes of samples and sensor dimensions need different

correction factors because of differences in the values of 'ka'. The symmetry effect of ka makes diffraction loss tables universal and can be used for all diffraction corrections for all combination of transducer sizes, characteristic frequency and different sample sizes and shapes.

7.8 Conclusions

The objective of this work was achieved by presenting an efficient technique of modeling diffraction loss using Simpson method and providing a table of diffraction correction factors that can be applied to different sample sizes and transducer characteristics. It was confirmed from the laboratory experiments that different sizes of samples and sensor dimension needs different correction factors. However, the symmetrical nature of the 'ka' values makes the diffraction tables universal and can be used for all diffraction corrections for all combination of different transducer sizes, wave characteristics and sample sizes. The results were confirmed with similar experiments from the same rock sample but different sizes of the rock core and different sizes and characteristics of the transducers and the results were in agreement. Diffraction errors reduce the measured velocities and increase the measured quality factor. Rocks of high acoustic velocities and low quality factors are more susceptible to diffraction losses than rocks of low velocity and high quality factor. Although the percentage diffraction corrections for the rock materials were generally small, they were still considered significant, especially given the present increasing demand for high accurate and precise acoustic measurements at a MHz

frequency range, to identify microscopic structures in rocks.

7.9 Appendix: MATLAB code for calculation of diffraction loss

% input, n = number of iteration for Simpson Quadrature
Pie, pi = 3.142
Input Velocity, V = 6000000mm/s
Central frequency of sensor, f = 1000000Hz
Wavelength, lamda, λ = 6mm
Wave number, k = 2pi/λ =1.04719755
Radius of transducer, a = 12.5mm
'ka' Value, 'ka' = 1, 5, ..100
Dimensionless distance, S = 0:0.01:20
Actual distance between transducers, z = S/λa^2
Changing frequency would change λ and therefore S and 'ka' values. Changing these parameters would change the distance and produce the Loss curve with distance at a fixed frequency. Changing the frequency would also change the 'ka' curve and produce the loss curve with frequency and fixed distance.
Parameter definitions

```
u=0; v=pi/2; ii=0; iii=0; n=100; pi= 3.142; a=12.5; lamda=6.0000; k=2*pi/lamda;
ka=k*a;
for S=0:0.01:20
 z=S/(lamda/a^2);
Tsimp=(sin(k*(z^2+4*a^2*(cos(u)^2))^0.5)*(sin(u)^2))+(sin(k*(z^2+4*a^2*(cos(v)^2))
^0.5)*(sin(v)^2));
h = (v-u) / n;
Tsum4 = 0.0;
for i = 1:2:(n-1)
x = u + i*h;
Tsum4 = Tsum4 + (sin(k*(z^2+4*a^2*(cos(x)^2))^0.5)*(sin(x)^2));
end
Tsum2 = 0.0;
for i = 2:2:(n-2)
x = a + i*h;
Tsum2 = Tsum2 + (sin(k*(z^2+4*a^2*(cos(x)^2))^0.5)*(sin(x)^2));
end
Tsimp = (h/3.0)*(Tsimp + 4*Tsum4 + 2*Tsum2);
D1=Tsimp;
simp=(cos(k*(z^2+4*a^2*(cos(u)^2))^0.5)*(sin(u)^2))+(cos(k*(z^2+4*a^2*(cos(v)^2))^
0.5)*(sin(v)^2));
```

```
h = (v-u) / n;
sum4 = 0.0;
for i = 1:2:(n-1)
x = u + i*h;
sum4 = sum4 + (cos(k*(z^2+4*g^2*(cos(x)^2))^0.5)*(sin(x)^2));
end
sum2 = 0.0;
for i = 2:2:(n-2)
x = a + i*h;
sum2 = sum2 + (cos(k*(z^2+4*a^2*(cos(x)^2))^0.5)*(sin(x)^2));
end
simp = (h/3.0)*(simp + 4*sum4 + 2*sum2);
C1=simp;
-------------------------------------------------
3 CALCULATION OF B
B1= D1*(4/pi)*cos(k*z)-C1*(4/pi)*sin(k*z);
 -------------------------------------------------
CALCULATION OF A
A1=1-C1*(4/pi)*cos(k*z)-D1*(4/pi)*sin(k*z);
 -------------------------------------------------
iii=iii+1;
ii=ii+1;
test(ii)=A1;
exam(iii)=B1;
end
test=test';
exam=exam';
save C:\LOSSA test /ascii
save C:\LOSSB exam /ascii
Plot the graph of the results
 t=0:0.01:20;
  t=1:501;
 clf
 plot(t,test,'r-')
 xlabel('Dimensionless Dist. S')
 ylabel('|P/Po|')
 Title('Results of Diffraction Loss for K=13.09')
 Grid
```

7.10 References

ASTM Standard 4543, (2004), Practice for preparing rock core specimens and determining dimensional shape tolerances: American Society for the Testing of Materials.

Benson G.C., and Kiyohara, O., (1974), Tabulation of some integral functions describing diffraction effects in the ultrasonic field of a circular piston source: J. Acoust. Soc. Am., 55, 184 -185.

Birch, F., (1960), The velocity of compressional waves in rocks to 10 kilo bars, Part 1: J. Geophys. Res., 65, 1083–1102.

Butt S.D., (2001), Experimental measurement of P-wave attenuation due to fracture over 100 to 300 kHz bandwidth, J. Pure & Appl. Geophysics, 158, 1783-1796

Christensen, N. I., and Wang, H. F., (1985), The Influence of pore and confining pressure on dynamic elastic properties of Berea Sandstone: Geophysics, 50, 207-213.

Donald, J. A., Butt S. D., and Iakovlev S., (2004), Adaptation of a triaxial cell for ultrasonic P-wave attenuation, velocity and acoustic emission measurements: Internat. J. Rock Mechs. Min. Sci., 41, 1001-1011

Johnson, C.F., (1970), A Pulse technique for the direct measurement of bar velocity: Twelfth Symp. on Rock Mechs. Proc., University of Missouri, Rolla, Missouri, Soc. of Min. Engs, New York.

Johansson, J., Martinsson, P., (2001), Incorporation of diffraction effects in simulations of ultrasonic systems using P-spice models: IEEE Ultrasonics Symp., 405 - 410.

Khimunin, A. S., (1972), Numerical calculation of the diffraction corrections for the precise measurement of ultrasonic absorption: Acustica, 27, 173-181

Khimunin, A. S., (1978), Ultrasonic propagation parameter measurements incorporating exact diffraction corrections: Acustica, 39, 87-95,

Papadakis, E. P., (1966), Ultrasonic diffraction loss and phase change in Anisotropic materials: J. Acoust. Soc. of Am, 40, 863-876

Papadakis, E. P., (1972), Ultrasonic diffraction loss and phase change for broad band pulse: J. Acoust. Soc. of Am, 525, 847-849

Pinttinen, A., and Luukkala, M., (1977), Diffraction loss associated with curved ultrasonic transducers: J. Phys. D: Appl. Phys., 10, 665-669.

Prasad, M., and Manghnani, M.H., (1997), Effects of pore and differential pressure on compressional wave velocity and quality factor in Berea and Michigan Sandstones: Geophysics, 62, 163–1176,

Ryan, R. J., (1988), The Fall Brook Quarry near Three Miles Plains: Classic Carboniferous Sections of the Minas and Cumberland Basin in Nova Scotia., The Society of Organic Petrology, Annual General Meeting and Field Trip, Open File Report, ME 1998-5, NS Natural Resource Department, NS, Canada,

Seki, H, Granato, A., and Truell, R., (1956), Diffraction effect in the ultrasonic field of a piston source and their importance in acoustic measurement of attenuation: J. Acoust. Soc. Am., 28, 230-238.

Toksoz, M.N., Johnston, D.H., and Timur, A., (1979), Attenuation of seismic waves in dry and saturated rocks, Part I: Laboratory measurements: Geophysics, 44, 681-690.

William, Jr. A. O., (1951), Piston source as high frequencies: J. Acoust. Soc. Am., 23, 1-6

7.11 Acknowledgements

Acknowledgements go to the Natural Sciences and Engineering Research Council of Canada (NSERC), and Petroleum Research Atlantic Canada (PRAC) for providing funding for this research.

7.12 Symbols and abbreviations

1. V = Velocity
2. Q = Attenuation quality factors
3. V_p = Compressional wave Velocity
4. Q_p = Compressional wave Attenuation quality factors
5. P/P_0 = Diffraction Loss
6. ϕ = Diffraction phase shift angle
7. P = Spatially averaged acoustic pressure
8. φ = Velocity potential
9. s = Surface area of a transducer
10. ρ = Density of the medium
11. t = Time
12. (t) = Transducer
13. p = Arbitrary point on the cylindrical coordinate

14.	(r, θ, z)	= Cylindrical coordinates
15.	r	= First coordinate describing the distance from the z-axis to an arbitrary point p
16.	θ	=The second coordinate that describes the angle from the positive xz-plane to the point p.
17.	z	=The third coordinate is the z coordinate from the transducer face along the positive z direction.
18.	f	= Frequency
19.	f_c	= Central frequency
20.	λ	= Wavelength
21	k	= Wave number
22.	υ_0	= Velocity amplitude
23.	η	= Integration variable
24.	J_o and J_1	= Ordinary Bassel functions
25	φ_o	= Initial axial velocity potential
26	a	= Radius of transducer
27	P_0	= Initial pressure emanating from the full infinite plane of the transmitter front face
28	α	= Diffraction attenuation in decibel
29	S	= Dimensionless distance
30	t_c	= Diffraction correction time
31	t_m	= Measured arrival time

32 t_t = True travel time

33 α_c = Diffraction attenuation correction

34 α_m = Measured attenuation

35 α_t = True attenuation

36 d = Diameter of sample

37 l = Length of sample

Chapter 8: Numerical Spectral discretization modeling of non linear wave in quartz sandstone

8.1 Abstract

Numerical spectral discretization technique is used to quantify the effect of frequency on the wave velocity in quartz sandstone. The dispersion model is based on damped Klein Gordon wave equation that considers energy losses as the wave travels through the rock. Attenuation quality factor is described by constant Q and used to model both the high and low frequency behavior of the wave propagation. The results are used to model wave propagation in the visco-elastic medium (quartz sandstone) that models dispersion using the damped Klein Gordon wave propagation model to predict wave velocities over a broad frequency band. Comparison of modeled predictions with multi-frequency laboratory data shows good agreement.

8.2 Introduction

The issue of how to scale data derived from multi-frequency seismic velocities, used across the various frequency bands has been a major problem in acoustic imaging (Landro and Kvam, 2002; Imhof, 2003; Wang and Dodds, 2003). Different dispersion mechanisms based on differences in wave frequency, wavelength, and reservoir flow units and thicknesses cause differences in acoustic velocity (Parra et al., 1999). For example, the laboratory velocity (core scale) is greater than the seismic velocity (log

scale) and in turn greater than vertical seismic profiling velocity (seismic scale), simply because the frequencies of the waves used in estimation of these velocities are different (Carcione and Tinivella, 2001). Figure 8.1 shows a schematic of compressional wave velocity as a function of frequency for a typical sandstone rock (Winkler, 1986). As indicated in the figure, the velocity in dry rock was assumed to be independent of frequency and the velocity in liquid-saturated rock increases with frequency. This is because the water in the saturated rock causes dispersion because of fluid motion and the high frequency components travel and becomes the first arrivals, thus increasing the measured group velocity. The fluid motion is caused by pressure equilibration as the seismic wave passes through the rock (Pride et al., 2003) and depends on the viscosity and bulk modulus of the pore fluid, and the permeability of the rock (Batzle et al., 2003, Kumar et al., 2003). If the pore space is completely filled with fluid, the fluid has less mobility than if there is some gas saturation and it has been shown that attenuation is highest in a partially fluid saturated rock (Kumar et al 2003; Winkler and Nur, 1982). Total velocity dispersion is the fractional increase of the high-frequency velocity in the saturated rock relative to the low-frequency velocity.

Generally, waves exhibit different dispersion characteristics in different materials resulting in corresponding variations in travel times and velocities. Table 8.1 shows the frequency, wavelength and corresponding velocities at various scales in acoustic imaging. If the data from these frequency ranges (Lab/Log/Seismic data) are to be integrated, there is the need for the velocities to be scaled by developing appropriate scaling models and methodologies.

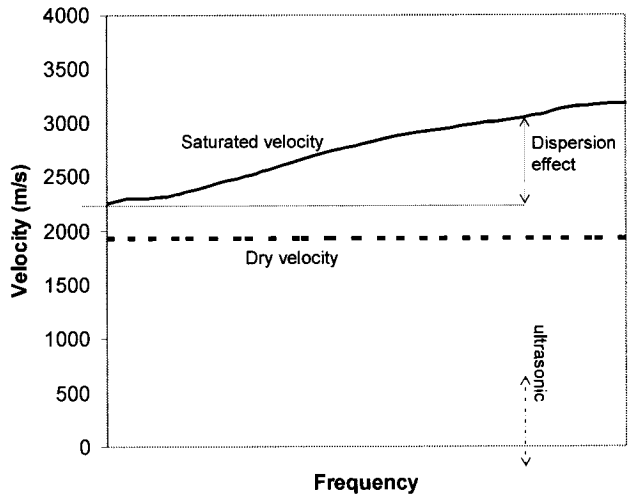

Figure 8.1: Schematic of compressional wave velocity as a function of frequency for a typical sandstone. (after Winkler, 1986)

Table 8.1: Various acoustic measurements across the frequency-wavelength band

Measurements	Thickness	Frequency	Wavelength
Laboratory Measurements (Core scale)	Millimeters to Centimeters	100KHz to 1MHz	0.008 Meters
Field Measurements (Log scale)	Centimeters to Meters	100Hz to 15KHz	0.027 Meters
Field Measurements (Seismic scale)	Meters to Killometers	1Hz to 100Hz	20 Meters

To date, there are limited practical scaling laws between imaging across the various frequency bands. It is important to consider the theoretical and practical differences of measuring acoustic wave velocity. Theoretical analyses that link elastic properties to wave propagation phenomena are almost exclusively based on the motion of single

frequency plane waves traveling at the frequency-dependent phase velocity. However, in many real laboratory and field situations wave velocities are determined by charting the picked transit times versus propagation distance of a band-limited wave packet, the general assumption being that such methods yield group velocity. However, phase and group velocities only coincide with certainty when there is no wave-velocity dispersion. There is therefore the need to scale the velocities down from the laboratory to the field and vice versa, if these multi-frequency acoustic data are to be integrated. Backus averaging (Backus, 1962) provides a finely foliated velocity model in an attempt to solve the scaling problems. However, as Para et al. (1999) indicated, Backus averaging has three major shortcomings and limitations: (i) Backus averaging is restricted to zero-frequency limit (low frequency limit), (ii) there is no source of intrinsic energy dissipation such as friction or viscosity (attenuation) catered for in the model, (iii) the model requires that layer thickness of the media must be larger than the seismic wavelength: how much greater is still a question of disagreement among practitioners. The authors believe that the way to reconcile the various velocity disparities is to develop a model that would scale the velocities depending on the type of waves used in the measurement (frequencies and wavelength characteristics) and the type of propagation medium. This research, thus, provides the opportunity to numerically examine the velocity dispersion of elastic waves over a wide frequency range. The objective of this is to develop practical scaling models and methodology that take into account intrinsic energy dissipation. The numerical method applied uses Numerical Fourier discretization (NSD) which is discretization in the Fourier domain at a short numerical interval. The

NSD method was used to develop wave propagation in a visco-elastic medium that utilizes the Klein Gordon wave propagation model, to predict wave over a broad spectrum of frequencies. Laboratory experimental were used to evaluate the results of the numerical model.

8.3 Linear and non linear waves

8.3.1 Linear waves

A wave propagating in a medium is governed by a three-dimensional wave equation which is a second-order linear partial differential equation that relates the temporal and spatial derivatives of the pressure field (Elmore and Heald, 1985):

$$u_{tt} - c^2(u_{xx} + u_{yy} + u_{zz}) = 0 \qquad (8.1)$$

Where, u_{tt} is the second derivative of the displacement amplitude, u, with respect to time, t.

u_{xx} u_{yy} u_{zz} are the second derivative of the displacement amplitude, u, with respect to distance, x, y and z respectively.

c is the velocity of the wave

The equation was derived from fundamental Newton momentum law and energy conservation of a particle moving in a medium. The assumptions underlying the derivation of the equation are:

(i) there is no frictional resistance to particle motion

(ii) the displacement of the particle is small and does not exceed the elastic limit

of the material.

Therefore, the waves propagate through the medium without loss of energy or change in shape. Such a wave travels infinitely at a constant speed, c, called the phase velocity. Waves of this nature are described as linear waves. The medium in which they travel may be described as frictionless and offers no resistance to wave motion. However this is not the situation typically encountered for the propagation of elastic waves in geologic media.

8.3.2 Non Linear waves

Non linearity is rather a more common state of affairs in wave travel (Elmore and Heald, 1985). For many media a more complicated non linear wave equation describes the wave propagation through them. The non linearity is as a result of opposing forces such as the frictional forces that oppose particle displacement, causing loss of energy, spreading of energy and dispersion. The velocity of the elastic waves is not constant but depends on the wave frequency or equivalently on wavelength. Such a medium is then said to possess the property of dispersion. Dispersion is a phenomenon where waves either traveling in different directions or having different frequencies propagate with different speeds.

8.3.3 Dispersion of non linear waves

Dispersion is a phenomenon where waves either traveling in different directions or having different frequencies propagate in different speeds. Dispersion is known to fall

into two basic classes: (i) intrinsic, which is based on energy loss due to friction. Grain to grain friction in sedimentary rock causes some attenuation. However the major source of intrinsic attenuation in porous rocks such as sand, shale or carbonate occurs when motion of the rock and the fluid in the pores becomes uncoupled, (ii) scattering, which is based on local wavelength-scale variations in the rock formation. Intrinsic dispersion is a local property of the rock while scattering dispersion is a property of a neighborhood of rocks, and includes the effects of reflections, refractions, and the law requiring continuity of displacement (Parra et al., 1999). Dispersion does not result in energy loss, but energy spread. However, because attenuation is intrinsically linked to dispersion (Aki and Richards, 1980), it is very difficult to separate them.

8.4 Effect of dispersion

The effects of dispersion often include:

(i) waves traveling along coordinate axes propagating slower than in diagonal directions,

(ii) high-frequency waves propagating faster than lower-frequency waves, in the case of body waves.

It is possible to analyze the dispersion introduced by a numerical method either directly by substituting certain "test waves" into the discretized equation or by frequency domain analysis. In both dispersive and non dispersive media, the wave velocity for sinusoidal waves of a particular frequency is termed the phase velocity, and it is related to frequency

and wave number by:

$$c = \frac{k}{\omega} \tag{8.2}$$

Where, c is the speed of the waves

k is the wave number given by $2\pi/\lambda$

λ is the wavelength given by $2\pi/k$

ω is the angular frequency given by $2\pi f$

f is the frequency of oscillation given by $\omega/2\pi$

The relationship between k and ω as in Equation 8.2 is called the dispersion relation. For linear waves, the ratio of k and ω is constant, c, called the phase velocity and thus k is inversely proportional to ω. There is no dispersion in this type of waves. For non linear waves, c varies and it depends on ω and k. In non linear waves, if the phase velocity, c, decreases with frequency, in some frequency range, the medium is said to possess normal dispersion in this range. On the other hand if c increases with frequency, in some frequency range, it is said to possess anomalous dispersion in this range. Both normal and anomalous dispersions are observed for elastic waves and are common in nature.

8.5 Effect of the elastic wave non-linearity on the numerical modeling

The non linearity of waves would result from adding a damping term or frictional term to the linear wave equation. This damping term depends on many factors including the

nature of the material, the state, density, modulus etc. The damping term would reduce the amplitude and the velocity of the waves as it moves through the material. For inhomogeneous material this damping term may also vary from one point of the material to another. Thus the general form of a nonlinear wave equation is given by:

$$u_{tt} - c^2 u_{xx} = q(x,t) \tag{8.3}$$

Where $q(x,t)$ is the damping term or resistance function

In theory, there is no restriction on the mathematical form of $q(x,t)$. However, there should always be a practical justification for adopting a very complex and complicated model for $q(x,t)$ (Howard, 1993; Cooper, 1998; Elmore and Heald, 1985). The fracture system of the material may dictate the complexity of the dumping resistance and the corresponding energy losses. Other factors like the density, homogeneity, modulus etc may also come into play. $q(x,t)$ can be a constant, a linear, or non linear damping and could be modeled to damp only the amplitude, the phase speed or both. The simplest form is when the non linear term $q(x,t)$ is zero which means there is no friction and the classical wave equation is retrieved.. When $q(x,t)$ is constant it presents the simplest form of the non linear equation. The damping function could also be quadratic, cubic or higher functions. It may even take the form of sinusoidal or exponential function and so on. The function may depend on the frequency, wavelength and the amplitude or combination of any of the properties of the waves. Based on the nature of $q(x,t)$ many common forms of non linear wave equations encountered in nature can be modeled. These are reviewed in section 8.6.

8.6 Review of common form of linear and non linear wave models.

Several types of linear and non linear wave model have been applied to the propagation of elastic wave in geologic media.

1. The classical wave model is given by:

$$\frac{\partial^2 u(x,t)}{\partial t^2} - c^2 \frac{\partial^2 u(x,t)}{\partial x^2} = 0 \tag{8.4}$$

The non linear term is zero and therefore there is no frictional resistance to wave motion in the medium and the amplitude of vibration with respect to elastic limit is very small. There is no energy loss and the wave velocity is constant. There is no dispersion and the frequency does not change. Most of the wave modeling in the literature that uses final difference and finite element rely heavily on this type equation that describes the physics of the wave (Alford et al., 1974; Kelly et al., 1976; Cejan et al., 1985). It is normally describes as 'pure' linear wave.

2. Klein Gordon (KG) wave model

$$\frac{\partial^2 u(x,t)}{\partial t^2} - \frac{\partial^2 u(x,t)}{\partial x^2} = u(x,t) \tag{8.5}$$

$$\frac{\partial^2 u(x,t)}{\partial t^2} - \frac{\partial^2 u(x,t)}{\partial x^2} - mu(x,t) = 0 \qquad (8.6)$$

Klein considers the wave equation from quantum mechanics point of view where all forms of energy losses are taken into consideration. It is one of the simplest models for non-linear wave interaction. It is derived from the relativistic energy, for a particle with rest mass m resulting in the generalized non linear wave equation. (Elmore, 1985: Cooper, 1998). Anno (1992) showed that the Klein Gordon model is mathematically equivalent to the acoustic variable density wav equation and thus applicable for the modeling of P-wave dispersion.

3. Sine Gordon wave model

$$\frac{\partial^2 u(x,t)}{\partial t^2} - \frac{\partial^2 u(x,t)}{\partial x^2} = \sin u(x,t) \qquad (8.7)$$

It is Klein Gordon wave equation with sinusoidal frictional term, *sin (u(x,t))*

4. Double sine Gordon wave model

$$\frac{\partial^2 u(x,t)}{\partial t^2} - \frac{\partial^2 u(x,t)}{\partial x^2} = \sin u(x,t) + \frac{1}{2}\sin u(x,t)/2 \qquad (8.8)$$

It is Klein Gordon wave equation with double sinusoidal frictional terms. It is used in

situation where the frictional resistance becomes a complex sinusoid.

5. Damped Sine Gordon wave model

$$\frac{\partial^2 u(x,t)}{\partial t^2} - \frac{\partial^2 u(x,t)}{\partial x^2} = \sin u(x,t) + 2d\frac{\partial u(x,t)}{\partial t} \tag{8.9}$$

It is Klein Gordon wave equation with a sinusoidal and non sinusoidal frictional term.

6. Korteweg- de Vries (KdV) wave model

$$\frac{\partial u(x,t)}{\partial t} - 6u(x,t)\frac{\partial u(x,t)}{\partial x} + v\frac{\partial^2 u(x,t)}{\partial^2 x} + \mu\frac{\partial^3 u(x,t)}{\partial x^3} = 0 \tag{8.10}$$

or

$$\frac{\partial u(x,t)}{\partial t} - 6u(x,t)\frac{\partial u(x,t)}{\partial x} + \mu\frac{\partial^3 u(x,t)}{\partial x^3} = 0 \tag{8.11}$$

KdV was first formulated as part of an analysis of shallow-water waves in canals, it has subsequently been found to be involved in a wide range of physics phenomena, especially those exhibiting shock waves, traveling waves, and solitons (Chanteur and Raadu, 1987; Van Groesen and De Jager, 1994; Van der Blij, 1978). Certain theoretical physics

phenomena in the quantum mechanics domain are explained by means of a KdV model (Van der Blij, 1978). It has many applications ranging from its use in fluid dynamics, aerodynamics, and continuum mechanics as a model for shock wave formation, solitons, turbulence, boundary layer behavior, and mass transport. It has been studied and applied for many decades. Many different closed-form, series approximation, and numerical solutions are known for particular sets of boundary and initial conditions. The Korteweg-deVries equation encountered in many problems involves weak nonlinearity (Hokstad, 2004) and therefore was not used for this model. Examples of its application includes surface waves in shallow water, acoustic waves in a plasma of ions and electrons, large-scale waves in the atmosphere caused by the rotation of the earth (so-called Rossby waves), and electric circuits with a nonlinear capacitor (Hokstad, 2004). However the KdV was programmed as an option tools in the NFD computer program given in the appendix and can be used for the dispersion analysis in different phenomenon.

8.7 The KG model used in the dispersion analysis

As presented above, there are many forms of the non linear wave equations. The nature of the non-linearity really depends on the model adopted for the non linear frictional resistance. In theory, any frictional model based on the frictional resistance of the medium under study and all the opposing forces and energy losses of the wave in the material can be formulated and included in the non linear wave equation.

The initial non linear wave model used in this research is a modified form of the Klein Gordon wave equation with linear frictional term based on the rest mass (γ) of the vibrated particles. Klein considers the wave equation from quantum mechanics point of view where all forms of energy losses are taken into consideration. It is one of the simplest models for non-linear wave interaction. It is derived from the relativistic energy, for a particle with rest mass m resulting in the generalized non linear wave equation. The KG model adapted was very applicable because all the energy losses (intrinsic and scattering and diffraction) were quantified in terms of a single attenuation quality factor, Q, and was included in the model. Equation 8.3 considers a frictional resistance to motion. This resistance introduces fast variation in the phase and thus the speed of the wave. This is to ensure the relatively higher attenuation property of the glass sandstone. This equation is solved using the Fourier transform and the differential evaluated for an asymptotic stationary phase. Then a wave packet is found traveling at a phase velocity $\omega(k)/k$ and at a group velocity $\omega'(k)$ or $d\omega/dk$.

$$\frac{\partial^2 u(x,t)}{\partial t^2} - \frac{\partial^2 u(x,t)}{\partial x^2} = \gamma u(x,t) \tag{8.12}$$

where γ is the rest mass for particle.

8.7.1 Model of dispersion relation in KG wave equation

The theoretical group and phase velocities [$(\omega'(k))$ and $(\omega(k)/k)$] can be found by considering a plane non linear wave (equation 8.12). Looking for a solution in the form

of complex exponential, it implies that:

$$u(x,t) = e^{i(kx-\omega(k)t)} \tag{8.13}$$

Where k is the wave number given by $2\pi/\lambda$

λ is the wavelength given by $2\pi/k$

ω is the angular frequency given by $2\pi f$

f is the frequency of oscillation given by $\omega/2\pi$

x is the distance travel

t is the time

u the amplitude

e is an exponential function

i is a complex number notation $i = \sqrt{-1}$

Substituting equation (8.13) into the wave equation (8.12) we see that equation 8.13 would be solution to equation 8.12 only and only if:

$$-\omega(k)^2 + k^2 - \gamma^2 = 0 \tag{8.14}$$

so that

$$\omega(k) = \pm\sqrt{k^2 - \gamma^2} \tag{8.15}$$

Taking ω(k) to denote the plus root, we see that if waves of the form

$$u(x,t) = e^{i(kx \pm \omega(k)t)} \tag{8.16}$$

would solve the modified non linear Klein Gordon wave equation, then,

$$\omega(k) = \pm\sqrt{k^2 - \gamma^2} \tag{8.17}$$

Equation 8.17 is called the dispersion relation for the KG wave equation (equation 8.12)

The speed of propagation of this plane wave is

$$\frac{\omega(k)}{k} = \pm\frac{\sqrt{k^2 - \gamma^2}}{k} \tag{8.18}$$

This is called the phase velocity. The group velocity, ω'(k), which is differential of the dispersion relation is given by:

$$\omega'(k) = \pm\frac{k}{\sqrt{k^2 - \gamma}} \tag{8.19}$$

Similarly various dispersion relations can be derived for any of the non linear wave equations models presented in equation 8.4 to 8.11. For example the dispersion characteristics for some common non linear waves are given in the next section.

Dispersion relation for the non linear wave model discussed earlier include:

$\omega = \sqrt{(k^2+1)}$ Klein-Gordon

$\omega = k^3$ Korteweg-de Vries

8.7.2 Solution of the modified KG waves by Numerical Fourier Discretization

Boundary Conditions:

Due to the requirement of periodicity by the Fourier transform we are limited to three types of boundary conditions:

(i) periodic boundaries (real to complex FT),

(ii) free boundaries (real to real FT: imaginary parts are set to zero <=> cosine transform),

(iii) fixed boundaries (real to imaginary: real parts are set to zero <=> sine transform).

The wave is allowed the wave to move freely in a free boundary condition so that imaginary part of the wave is set to zero (real to real FT: imaginary parts are set to zero <=> cosine transform), thus, limiting these numerical experiments propagating in the positive x direction

Initial conditions:

$u(x_n,0)$ and $v(x,0)$ are used as initial displacements and initial velocity, to analyze how the initial displacement evolves in time. The complex Fourier representation of $u(x_n,t)$ can be found numerically as:

$$u(x_n,t) = \sum_k \tilde{u}(k_j,t)e^{ik_j x_n} \tag{8.20}$$

where

$$\tilde{u}(k_j,t) \tag{8.21}$$

is the Fourier transform of the wave at any time t

But the Fourier transform at a time t is given by

$$\tilde{u}(k_j,t) = u(k_j,0)e^{i\omega_j t} \tag{8.22}$$

where

$$\tilde{u}(k_j,0) \tag{8.23}$$

is the Fast Fourier Transform (FFT) of the initial wave.

The method now considers a non linear wave of the form:

$$u(x,t) = e^{i(kx\pm\omega(k)t)} \tag{8.24}$$

where the ω changes with respect to k,

This implies that the wave at a time t is given by:

$$u(x,t) = \frac{1}{2\pi}\int U(k)e^{i(kx-\omega(k)t)}dk \tag{8.25}$$

Knowing that the initial wave is

$$u(x,0) = \frac{1}{2\pi}\int U(k)e^{ikx}dk \tag{8.26}$$

Where

U(k) is the Fourier Transform of u(x,0)

The method considers a non linear wave of the form:

$$u(x,t) = e^{i(kx\pm\omega(k)t)} \tag{8.27}$$

where the ω changes with respect to k,

This implies that the wave at a time t is given by:

$$u(x,t) = \frac{1}{2\pi}\int U(k)e^{i(kx-\omega(k)t)}dk \tag{8.28}$$

Knowing that the initial wave is

$$u(x,0) = \frac{1}{2\pi}\int U(k)e^{ikx}dk \tag{8.29}$$

Where

U(k) is the Fourier Transform of u(x,0)

Because ω(k) is greater than zero, u(x,t) is a wave which moves to positive x direction. Negative wavenumbers are set to zero. This boundary condition is necessary to avoid reflected waves at the boundaries otherwise the resulting waves would form standing

waves. To describe the behavior of the function as time goes to infinity we consider dispersion from the KG equation. Because of the dispersion relation, this wave would change shape as t increases and the frequency component would tend to separate, or disperse.

The wave at time t is then given by

$$u(x,t) = \frac{1}{2\pi}\int U(k)e^{i(kx-\omega(k)t)}dk \tag{8.30}$$

$$= \frac{1}{2\pi}\int U(k)\cos(kx-\omega(k)t)dk \tag{8.31}$$

To demonstrate this modeling, let the initial wave be :

$$u(x,0) = Ae^{-\alpha x^2} \times \cos(2x) \tag{8.32}$$

Where

A is the initial amplitude of the wave, in this case, taking as the trigger voltage for our experiment, 50mV

$e^{-\alpha x^2}$ is a model of non linear amplitude reduction with distance x due to frictional forces.

The amplitude reduction model takes into account all the energy losses and it is quantified by the attenuation coefficient of the quartz sandstone. In the desktop measurement, the quality factor was 24 (i.e. Q=24) and therefore the attenuation coefficient, α, is 1/24. When x=0, t=0 and the amplitude reduction is 1. This is initial pulse sent through the quartz sandstone. As the wave travels and x increases (i.e. x =0, 1, 2, 3....), the reduction in amplitude increases and eventually the wave losses its energy

when A=0 at a distance x=n. cos (2x) is the sinusoidal nature of the wave, and his can also be taken as sin (2x) based on the whether one is considering periodic boundaries, free boundaries or fixed boundaries.

Taking attenuation quality factor into consideration, the initial pulse u(x,0) is given by:

$$u(x,0) = 50e^{-\frac{1}{24}x^2}\cos(2x) \qquad (8.33)$$

The Fourier transform of this initial pulse is therefore given by:

$$\tilde{u}(k,0) = 50\sqrt{24\pi}\exp(-6(k-2)^2) \qquad (8.34)$$

The range of k chosen is up to 100 (i.e. k = 0, 1, 2 .....256). Since the $\omega(k)$ is greater than zero, it implies that u(x, t) is a wave pocket moving to the right only as t increases.

8.8 Numerical Spectral decomposition procedure

The NFD procedure is summarized in the following four steps:

Step 1: Set the initial and boundary conditions based or material and experimental conditions under study:

a $u(x,0) = A_0 e^{-\alpha x^2}\cos(2x)$ for t =0

b $\frac{\partial u}{\partial t}(x,0) = 0$ for t=0

c. A_0 =50mV for t=0

d. Attenuation coefficient α =1/Q =1/24

Steps 2: Perform a real to complex Fourier Transform on the initial displacement $u=(x_n,0)$ to get Fourier coefficients $\breve{u}=(k_j,0)$

$$u = (x_n,0) \qquad \bar{u} = (k_j,0)$$

Step 3: Calculate the Fourier coefficient at the time t:

$$\bar{u}(k_j,t) = \bar{u}(k_j,0)e^{iw_j t}$$

Substituting the dispersion relation

$$\omega_j = \sqrt{k^2 - 1}$$

$$\frac{\omega_j}{k_j} = \frac{\sqrt{k_j^{\,2} - 1}}{k_j} = c_j$$

Where c_j is the phase velocity

Step 4: Perform a complex to real inverse FT to get the displacement field at time t,

$$u = (x_n,t)$$

$$u(x_n,t) = \sum_k \tilde{u}(k_j,t)e^{ik_j x_n}$$

or

$$u(x_n,t) = \frac{1}{2\pi}\int U(k)e^{i(kx-\omega(k)t)}dk$$

The above steps are coded and implemented in the MATLAB program given in the appendix.

8.9 Results and discussions

The results of the numerical model are shown in the following figures. Figure 8.2a shows the initial wave, u_0, ($[u(x,0) = 50\, e^{-\frac{1}{24}x^2} Cos\ (2x)]$) sent through the rock. It is a wavelet of amplitude A=50mV, centered at x=0 and t=0. Figure 8.2b also shows the same wave after traveling through the rock for 15μs. This is superimposed (Figure 8.2c) and compared with the wave that travels through a rock with no dispersion (Figure 8.2d). The dispersive waves become broader as it travels through the rock, with the high frequency components traveling faster at front of the wave train and the low frequency wave traveling slower at the tail. Figure 8.3 shows dispersion effect quantified in the form of distance travel.

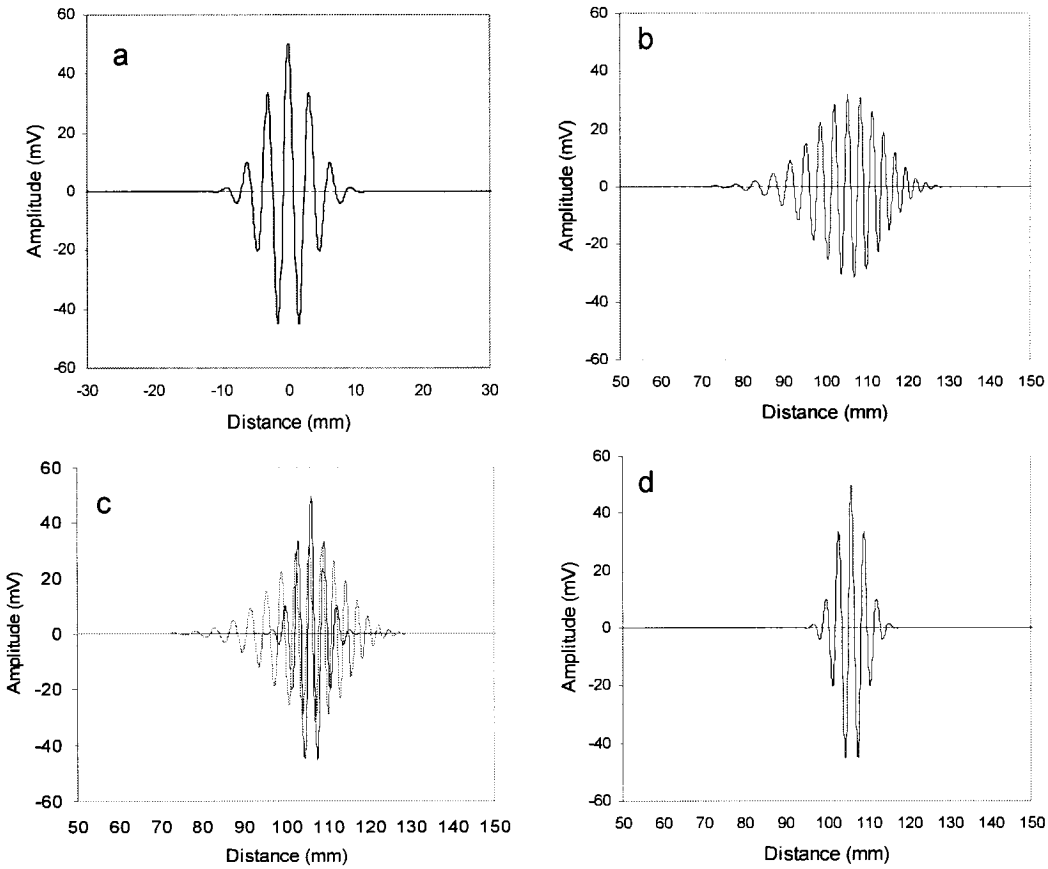

Figure 8.2 (a) the initial wave, u_0 sent through the rock at time 0 and distance 0 (b) the same wave after traveling through the rock for 15μs. (c) Comparison with a dispersive and non dispersive waves (d) wave that travels through a rock for 15μs. with no dispersion.

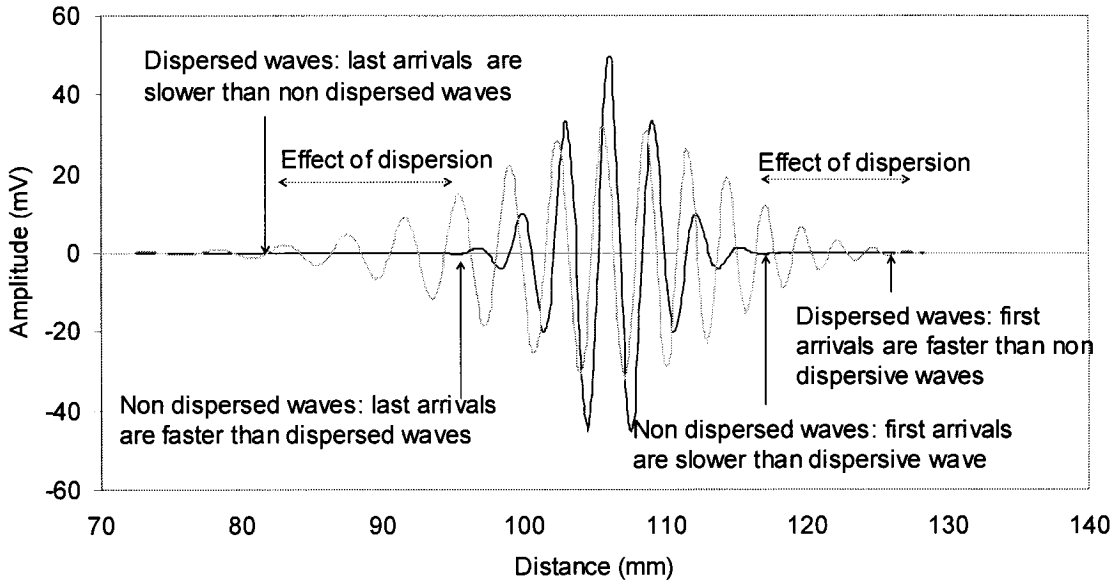

Figure 8.3: Analysis of the arrival of the dispersed and non-dispersed waves after traveling for 15us. The effect of dispersion caused the high frequency wave to arrive earlier ahead of the non dispersed waves. The effect of dispersion also caused the low frequency wave to arrive later behind the non dispersed waves. The distance between the two is quantified as the effect of dispersion.

In Figure 8.4 the wave is plotted at increasing distances from x=0 to study how it behave and broadens with travel through the rock. It is seen that the original initial wave disperses with propagation with high frequency component traveling faster and broadening the wave pocket. The low frequency components travel slower as the wave disperses and emerges at the end of the wave pocket. Simultaneously, the wave also losses energy due to attenuation as it travels through the medium.

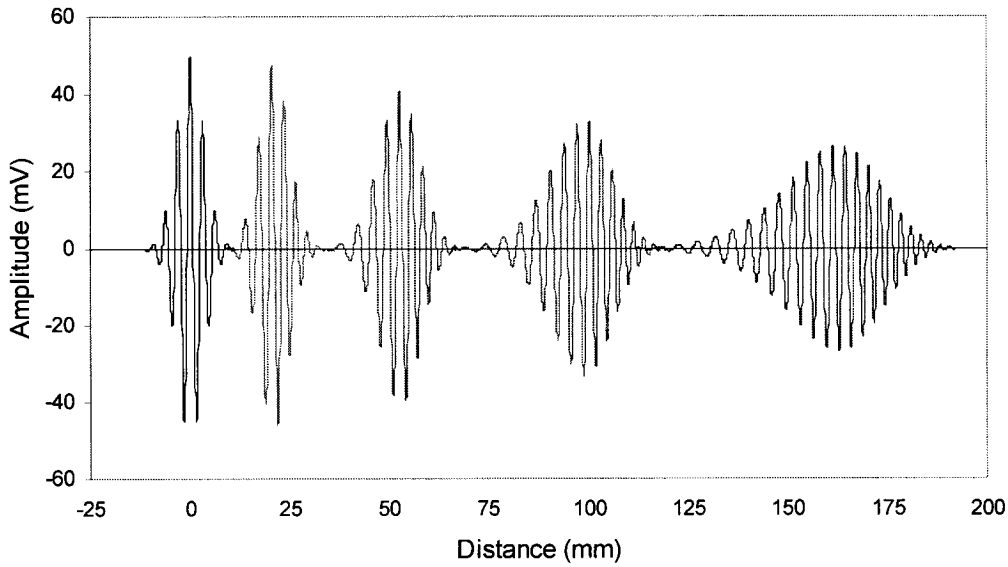

Figure 8.4: Tracking of the wave pocket with increasing propagation distance

Figure 8.5 shows the frequency scaling results and gives the w-k diagram for both dispersive and non dispersive rock (a), and the velocity relationship with wavelength (b), frequency (c) and wavenumber (d). It is seen that velocity increases with frequency and reduces with wavelength and that these relationships are non linear. It is seen that at the initial stage, for the few 100KHz frequency, the velocity is very crucial since the rate of change in velocity at these lower frequencies up to the MHz frequency range are relatively large. At a very high frequency range (MHz range) the rate of velocity change is very low and almost flat.

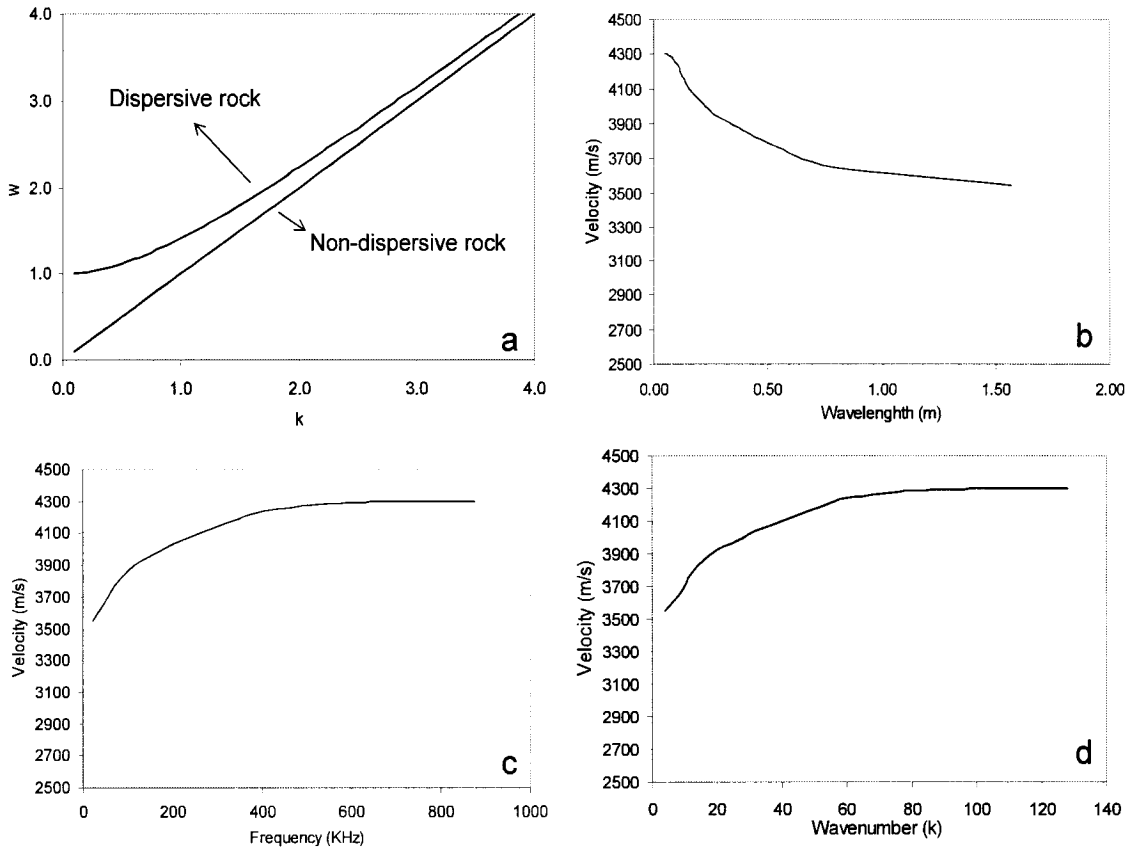

Figure 8.5: (a) w-k diagram for dispersive (quartz sandstone rock) compared to a theoretical non dispersive material. (b) Velocity - wavelength relationship. (c) Velocity-frequency relationship and (d) Velocity -wavenumber relationship.

The above results show that the differences in wave velocities are due to the use of different frequency waves in the acoustic imaging systems (core/log/VSP). Basically, all the waves used are non linear with a frequency band around a central frequency. These waves tend to disperse when they travel through the formation (mostly visco-elastic dispersive rocks). When they disperse, the different frequency components travel with different velocities. The results of this modeling show that, in general, the high frequency

wave bands disperse more than low frequency wave bands. The accuracy of measuring velocity therefore depends on the dispersion characteristics of the waves and the nature of the rocks that disperse the waves. High frequency waves tend to present more problems and inaccuracies in velocity measurements because of highly dispersive nature of these waves. Anomalous dispersion occurred in some of the experiments where the phase velocities decrease with frequency. This occurs mostly in the very high dispersive media (saturated, high porosity, weak synthetic sandstone that was prepared in the laboratory). These synthetic high attenuating sandstone rocks act as filters to remove all the high frequency waves and slow down the low frequency velocity, before it reaches the arrival point. A laboratory test (not shown here) on a highly attenuating synthetic sandstone shows this anomalous characteristics (Donald et al., 2004). These weak, loose, inhomogeneous and incompetent rocks present more inaccuracies in velocity measurements than competent homogenous and strong rocks, because the latter tends to disperse waves more than the former. Therefore the accuracy of measuring velocity, in part, depends on the dispersion characteristics of the rock as well as the nature of the wave (frequency range). The problem is compounded with longer travel distances of these high frequency waves.

Using alternate numerical modeling technique, such as conventional finite difference to analyze wave propagation gives a velocity profile but does not resolve the issue of dispersion which is central to scaling. The spectral discretization technique presented above is able to break the waves down in frequency domain so that different frequency

components can be analyzed. The model that is chosen or adopted for the non linear nature of the wave in the rock in question plays a very important role on the final dispersion model and thus the velocity measurements. The attenuation coefficient and the initial non linear model are, key to identifying anomalies in the final dispersion model. The relationship between velocity and frequency that was found in this experiment would work for sandstones with similar attenuation characteristics. For different rocks, the attenuation values are needed as inputs into the spectral discretization model developed, in order to predict changes in velocity with frequency.

8.10 Validation of the model and comments on the experimental work

Laboratory acoustic experiments were performed and the laboratory results were used to verify the results of the numerical modeling. Experiments were conducted using the glass sandstone described previously in chapter 3 using acoustic sensors in direct contact with the ends on the core. These experiments were conducted either on the bench top specimens with no stresses applied or under a normal 1Mpa hydrostatic stress using the hydrostatic cell described in chapter 3. Four experimental data points have been plotted in figure 8.6. The velocity assigned for each experimental data point was the group velocity measured at a maximum energy and correspond to the frequency at that peak energy level of the Fourier spectrum. Four experimental data points were plotted. The size of sample, transducers characteristics and measurement conditions of each experimental data point used in the validation are given below:

(1) Desktop measurement from a 2.5mm by 60mm cylindrical dry quartz sandstone sample. A 350Khz microdot transducer was used and the frequency at the maximum peak energy was 300khz.

(2) Desktop measurement from a 2.5mm by 60mm dry sample. A 1Mhz transducer was used and the frequency at the maximum peak energy was 500khz.

(3) Hydrostatic pressure of 1MPa on a rock sample of 54mm by 108 mm quartz sandstone and a 1 Mhz transducer. The frequency at the peak energy was 850kHz.

(4) Hydrostatic pressure of 1MPa on a dry rock sample of 2.5mm by 60mm using a 1.5 Mhz transducer. The peak energy at was at a frequency of 1300kHz.

The numerical model was validated with the above four experimental multi-frequency data of 300khz, 500khz, 850khz and 1300khz and they were in good agreement within an acceptable experimental error (Figure 8.6). This shows the applicability of the KG model for dispersion in this sandstone over the MHz frequency band.

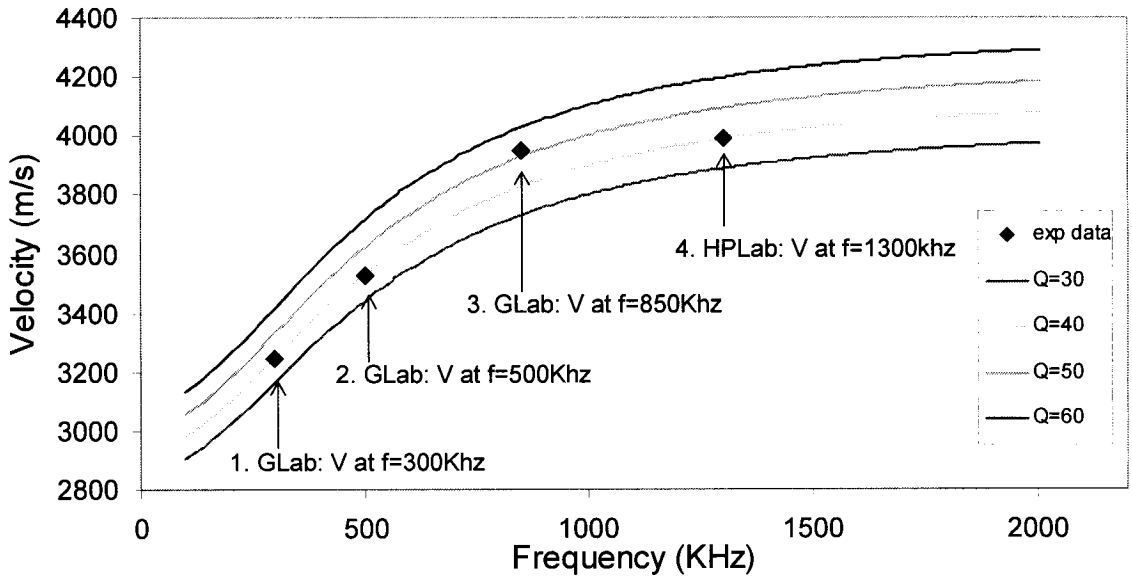

Figure 8.6: The measured velocities for the quartz sandstone using at 4 different dominant frequencies.

8.11 Conclusions

The objective of this investigation was to develop dispersion modeling methodology that takes into account intrinsic energy dissipation. The model uses spectral ratio techniques to break multi-frequency non linear waves into individual components. Frequency analyses confirms that the problem of scaling is due to the different dispersion and attenuation mechanisms in the rocks caused by intrinsic anelasticity of the rock material and scattering. These mechanisms are responsible for the velocity disparities across the

different frequency waves throughout the spectrum. The accuracy of measuring velocity across the frequency spectrum therefore depends on the dispersion characteristics of the waves and the nature of the rocks (modulus, density, saturation, etc) that disperse the waves. When normal dispersion occurs, the high frequency waves tend to travel faster than low frequency waves. Again the high frequency wave attenuate faster (travel at a shorter distance) than the low frequency waves. The spectral discretization technique adopted in this research was able to decompose these traveling waves into the frequency domain. Thus, different frequency components were analyzed and accurate velocity differences quantified for a particular frequency. The model that was developed for the multi-frequency velocity analysis scales the velocities across a broad frequency bands as confirmed from experimental validation.

This model relates velocities with frequencies throughout the rock imaging frequency band (Lab, Log and Seismic). Since the attenuation quality factor targeted for the sandstone was the model parameter, responsible for the attenuation, the results of the velocity-frequency relationship would be applicable for sandstones of similar attenuation characteristics. For different rock types, the attenuation values are needed as inputs into the spectral discretization model developed, in order to predict changes in velocity with frequency. The model was evaluated with the experimental multi-frequency data between 300KHz and 1.5MHz and they were in good agreement. Recommendation has been given to further investigate this method over a lower frequency spectral. It is also recommended that further research utilizing wavelet transforms instead of Fourier

transform to analyze the dispersion, be carried out. The two results can then be compared with the laboratory results to see which of the transformation produces the best results.

8.12 Appendix

The above models are implemented in the MATLAB (Math Works, 2001) program below:

```
% PROGRAM:  Numerical Fourier Discretization
% PAUL FREMPONG    11 JANUARY 2005

% The above models are implemented in the MATLAB program below:
% This program uses the (inverse) fast Fourier transform to compute the solutions of 6
% different dispersive equations with the same initial data u(x,0). The three equations
are:
%       ω = √ (k^2-1)          Current model
%       ω = √ (k^2+1)          Klein-Gordon
%       ω = k^3                Korteweg-de Vries
%       ω = sin (k)*k^2        Benjamin-Ono
%       ω = k^2                Schroedinger
%       ω = k / (1+k^2)        Regularized Long Wave
%
%  The initial data for each is
%      u(x,0) = 50exp(-((x**2)/24))*exp(2ix)
%  In the transform variable the initial data is
%      u(k,0) = 50exp(-6*(k-2)**2)*sqrt(24*pi)
%  The data is sampled on the interval  k in [0,K]. K is set to 100.
%  The number of sample points is N (set to 4096), so delk = 100/4096 = 0.016.
%  The result is displayed on the interval x in [-pi/delk, pi/delk]
%  intervals delx = 2*pi/K.
%
%  The values of u(x,t) go into the vector u
%  The values of u(x,0) go into the vector u0
%  The values of u(x,0) translated to the right with speed
%  equal to the group velocity at k = 2 go into the vector v.
%  The latter can be used to compare how the wave is being
%  deformed by the dispersion process.
%  The values of the group velocities for all k goes to Vg
%  The values of the group velocities for all k goes to Vp
```

```
%
%  There are seven supporting mfiles:
%       0. Initial.m          For initial data and boundary conditions
%       1. CSModel.m:         Dispersion relation for the current model
%       2.KGModel.m:          Dispersion relation for the Klien Gordon model
%       3.KdVModel.m:         Dispersion relation for the Korteweg-de Vries model
%       4.BOModel.m:          Dispersion relation for the Benjamin-Ono model
%       5.SModel.m:           Dispersion relation for the Schroedinger model
%       6.RLWModel.m:         Dispersion relation for the Regularized Long Wave model

disp(' ')
disp(' There are six choices of dispersion relations ')
disp(' Enter 1 for the Current Scaling Model')
disp(' Enter 2 for the Klein-Gordon equation ')
disp(' Enter 3 for the Korteweg-deVries equation ')
disp(' Enter 4 for the Benjamin-Ono equation  ')
disp(' Enter 5 for the Schroedinger equation ')
disp(' Enter 6 for the Regularized Long Wave equation ')
m = input('Enter the choice of dispersion relation   ')

t = input('Enter the time t at which you wish to view the solution   ')

% Note that, in theory, the time can be anywhere between zero and infinity but care must
% be taken not to enter a time when the wave has already lost energy and does not exist
% in the medium. This can be deduced from the attenuation coefficient and the Initial
% amplitude given in  the initial condition

K = 100;                              % Maximum wavenumber considered
N = 4096;                             % Maximum sampling points considered
delk = K/N;                           % Diescretization interval of the wavenumber
k = 0:delk:K - delk;                  % k from zero incrementing by delk to K
delx = 2*pi/K;                        % equivalenth discretization in terms of length x
x = -N*pi/K: delx : N*pi/K -delx;     % from –ve value incrementing to positive values.
                                      % This is because of the ifft that produce both
                                      % negative and positive values
W = Initial(k);

if m == 1

ww = exp(-i.*CSModel(k).*t).*W        %  The wave in Fourier domain at time t and with
                                      % dispersive relation substituting w for k

z = exp(-i*k*t*2/sqrt(2)).*W;         % A vector v which is the original wave u0
                                      % translated by the quantity t*omega'(2)
```

```
 elseif m ==2
   ww = exp(-i.*KGModel(k).*t).*W;
   z = exp(-i.*2/sqrt(5)*k.*t).*W;
elseif m=3
  ww = exp(-i.*KdVModel(k).*t).*W;
  z = exp(-i*12*k*t).*W;
elseif m=4
  ww = exp(-i.*BOModel(k).*t).*W;
  z = exp(-i*(1.973)*k*t).*W;
elseif  m=5
  ww = exp(-i.*SModel(k).*t).*W;
  z = exp(-i*4*k*t).*W;
else
ww = exp(-i.*RLWModel(k).*t).*W;
  z = exp(-i*(26/25)*k*t).*W;
end
  uu = real(ifft(ww));
  u = (N*delk/(2*pi))*[uu((N/2)+1:N),uu(1:N/2)];
  uu0 = real(ifft(w));
  u0 = (N*delk/(2*pi))*[uu0((N/2)+1:N), uu0(1:N/2)];

  vv = real(ifft(z));
  v = (N*delk/(2*pi))*[vv((N/2)+1:N),vv(1:N/2)];
% save C:\MATLAB6p1\Christmas2004\fresult.txt v /ascii
c=w/k      %Phase velocity ( c) calculations
%    Group velocity (g) calculations
if m == 1
        g= k*(k^2-1)^(-0.5)
elseif  m=2
        g=k*(k^2+1)^(-0.5)
elseif  m=3
        g=3k^2
elseif  m=4
        g=2k
elseif  m=5
        g=(2*k*sin(k))+(k^(2)*cos(k))
else
        g= (1/(1+k^2))*(((2*k^2)/(1+k^2))+1)
 %      Transposition of data
   transu0=u0';
   transx=x';
   transv=v';
   transu=u';
   transc=c';
```

```
  transg=g';
  transw=w';
  transk=k';
%       Save all dats in ASCII for further analyses
 save C:\MATLAB6p1\Christmas2004\u0result.txt transu0 /ascii /tabs
 save C:\MATLAB6p1\Christmas2004\xresult.txt transx /ascii /tabs
 save C:\MATLAB6p1\Christmas2004\uresult.txt transu /ascii /tabs
 save C:\MATLAB6p1\Christmas2004\vresult.txt transv /ascii /tabs
 save C:\MATLAB6p1\Christmas2004\cresult.txt transc /ascii /tabs
 save C:\MATLAB6p1\Christmas2004\gresult.txt transg /ascii /tabs
save C:\MATLAB6p1\Christmas2004\wresult.txt transw /ascii /tabs
save C:\MATLAB6p1\Christmas2004\kresult.txt transk /ascii /tabs

% Plot them in MATLAB, view and anlyse.
plot(x,u0,x,u,'g')
plot(k,w)
plot(k,c)
plot(x,u0)
plot(x,v)
plot(x,u)
plot(x,u,x,v)
plot(x,u0,x,u,'g')
plot(k,g)
axis([0 250 -1 1])
 plot (x,u0,x,u,'g')

%       SUPPORTING FILES: These files should be in different files nad placed in the
same directory as the main file

% File 1. Initial pulse
function y = Initial(k)
  y = 50*exp(-6*(k-2).^2)*sqrt(24*pi);

% File 2. Current Scaling Model
function w = CSModel(k)
w = sqrt( k.^2 -1);

%  File 3. Klein-Gordon Model
function w=KGModel(k)
w = sqrt( k.^2 + 1);

%  File 4. Korteweg-deVries  Model
function w = KdVModel(k)
    w =  k.^3;
```

```
% File 5. Benjamin Ono Model
function w = BOModel(k)
ω = sin (k)*k^2;

% File  6. Schroedinger model
function w=SModel(k)
   w = k.^2;

% File 7. Regularized Long Wave model
function w = RLWModel(k)
    w = k / (1+k^2)
END
```

8.13 Acknowledgements

We would like to thank the Natural Sciences and Engineering Research Council of Canada (NSERC), Petroleum Research Atlantic Canada (PRAC) and Schlumberger Canada Limited for providing funding for this research. Thanks to Dr C. Zhang at Taiyuan University of Technology, China for helping in writing the computer codes.

8.14 Reference

Anno, P., (1992), A Klein-Gordon acoustic theory, Unpublished Ph.D. thesis, Colorado School of Mines, T4326, CWP-117

Aki, K., and Richards, P.G., (1980), Quantitative seismology, theory and practice, 1:W. H. Freeman Co.

Backus, G.E., (1962), Long-wave elastic anisotropy produced by horizontal layering. Journal of Geophysical Research, 67, 4427–4440.

Butt, S., Frempong, P. K., Mukherjee, C. and Upshall, J., (2005), Experimental measurement of the ultrasonic velocity, attenuation and permeability characteristics of outburst prone sandstone, Journal of Applied Geophysics, (accepted, February 2005, Manuscript No: APPGEO770)

Carcione J. M. and Tinivella, U, (2001), The seismic response to overpressure: a modelling study based on laboratory, well and seismic data, Geophysical Prospecting, V. 49, pp. 523-539

Cooper, M. J., (1998), Introduction to partial differential equations with MATLAB, Birkhauser publishers, Boston, MA, USA, 540p

Donald, J. A., Butt S. D., and Iakovlev S., (2004), Adaptation of a triaxial cell for ultrasonic P-wave attenuation, velocity and acoustic emission measurements: Internat. J. Rock Mechs. Min. Sci., 41, pp. 1001-1011

Elmore, W.C. and Heald M. A., (1985), Physics of waves, Dover Publications Inc, New York. 477p

Frempong, P. K., and Butt, S., (2004), Modeling of diffraction loss and phase shift angels in a low adsorption media: example of a quartz sandstone, Geophysics, (in press) paper no: GEO 2004 0114

Frempong, P. K. and Butt, S., (2004), Non destructive techniques to determine the effective stress coefficient of porous sandstone Canadian Journal of Petroleum Technology, CJPT, (submitted)

Frempong, P. K., Donald, A. and Butt, S., (2004), The effect of injection and depletion cycles on ultrasonic velocity and quality factor in glass sandstone, Geophysics, (in press) paper no. GEO 2004 0096-R1

Howard, G., (1993), The physics of waves, Prentice Hall Publishing, New Jerssey, 421p

Imhof, M., G., (2003), Scale dependence of reflection and transmission coefficients, Geophysics Vol. 68, No.. 1, p. 322–336

Landro, M., and Kvam., O., (2002), Pore pressure estimation-What can we learn from 4D?: CSEG Recorder, 27, 83-87.

MathWorks, (2001), Matlab, 6: The MathWorks, Inc

Mavko, G., Mukerji, T. and Dvorkin, J., (1998), The rock Physics Handbook-Tools for Seismic Analysis in porous media, Cambridge University Press, New York, 329p.

Parra, J.O., Hackert, C. L., Ababou, R., and Sablik, M. J., (1999), Dispersion and attenuation of acoustic waves in randomly heterogeneous media, Journal of Applied Geophysics, Vol. 42, pp. 99–115

Wang X. and Dodds, K., (2003), Viscoelastic wave modelling using a staggered high-order finite-difference in inhomogeneous media, Proceedings of the 6th SEGJ of International Symposium: Imaging and Technology, Tokyo, Japan.

Winkler, K. W., (1986), Estimates of velocity dispersion between seismic and ultrasonic frequencies, Geophysics, Vol. 51, No. 1, pp. 183-189.

Alford, R. M., Kelly, K. R., and Boore, D. M., (1974), Accuracy of finite-difference modeling of acoustic wave propagation: Geophysics, v. 39, no. 6, p. 834-842.

Kelly, K. R., Ward, R. W., Sven Treitel, and Alford, R. M., (1976), Synthetic Seismograms: A finite-difference Approach: Geophysics, v. 41, no. 1, p.2-27.

Cerjan, C., Kosloff, D., Kosloff, R., and Reshef, M., (1985), A nonreflecting boundary

condition for discrete acoustic and elastic wave equations: Geopgysics, v. 50, no. 4, p. 705-708.

Chanteur, G., Raadu, M., (1987), Formation of shocklike modified Korteweg-de Vries solitons - Application to double layers, J. Physics of Fluids, vol. 30, p. 2708-2719.

Van Groesen, E., and de Jager , E. M., (1994), Mathematical Structures in Continuous Dynamical Systems; Studies in Mathematical Physics, 617pp., North Holland Publishing Cy, Amsterdam, 617pp.

Van der Blij, F., (1978), Some Details of the History of the Korteweg-de Vries Equation; Nieuw Archief voor Wiskunde, no 3, Vol. 26, pp. 54 -64.

Hokstad, K (2004) Nonlinear and dispersive acoustic wave propagation, Geophysics, Vol. 69, N0.3 p. 840–848.

Berryman, J. G. and Greenet, R.R., (1980), Discrete inverse methods for elastic waves in layered media, Geophysics, Vol. 15, No.2 p. 213-233.

Belokolos E. D., (1995), General formulae for solutions of initial and boundary value problems for sine-Gordon equation, Theor. & Math. Phys., 1995, Vol. 103, No. 3, pp. 613–620.

Benjamin, T. B., Bona, J. L., and Mahony, J. J., (1972), Model equation for long waves in nonlinear dispersive systems, Philos. Trans. Roy. Soc. London, Vol. 272A, pp. 47–78, 1972.

Burt, P. B., (1978), Exact, multiple soliton solutions of the double sine-Gordon equation, Proc. Roy. Soc. London, Ser. A, Vol. 359, pp. 479–495, 1978.

PART IV

DISCUSSIONS, ANALYSES AND CONCLUSIONS

IV: Overview

This chapter discusses all the work done in the thesis and gives detailed analysis of the results and findings of the research. It explains how the introduction and the preceding chapters and technical publications link together with the conclusions and the appendices. The discussion takes into account how the results from the research achieved the objectives outlined in the introductory chapter. Practical applications and the value of the thesis have been explained. Pertinent areas have been highlighted and recommendations given with regard to further research that needs to be done. New research areas have also been identified which could be considered for further studies.

Chapter 9: Analyses and discussions of results, conclusions and recommendations

9.1 Introduction

There were four main objectives that this research set out to achieve: (i) to generate a database of acoustic data under different pore pressure and effective stress conditions, in the laboratory, (ii) to find how the various acoustic properties used in acoustic imaging relate to pore pressure and in-situ stress conditions, (iii) to evaluate the factors that contribute to accurate velocity differences across a broad frequency bands, (iv) to develop a wave propagation model incorporating both attenuation and dispersion for acoustic imaging and reservoir characterization. These objectives were achieved by laboratory experimental techniques and numerical modeling. The research also resulted in new findings and other scientific developments that are discussed in the subsequent sections in this Chapter.

9.2 Discussion on literature review and previous work

Detailed review of the pore pressure imaging and current laboratory-field scaling methodologies used in acoustic imaging indicated that, although the non invasive determination of wave velocity can be used to some extent to derive some mechanical

properties of rocks, there is no construction of general acousto-mechanical model. The pertinent areas of concern were some inconsistencies in the equations that were used to link the mechanical behavior of the materials to their sonic and ultrasonic characteristics. Most of the acousto-mechanical modeling equations were empirical in nature with many assumptions and material specific information. Their use and practical applications are therefore limited. The two main problematic issues were the assumptions of material homogeneity and isotropic conditions.

Rocks are heterogeneous, complicated and variable from one field location to another. It is therefore very difficult to get a universal rock physics theory or empirical relationship. Probably few drill cores if tested in the laboratory can pass this homogeneity and isotropic test. However, for a general field application, being widely advocated, there is some push for oversimplification. This problem has also been identified by other writers. For example Lu and McMechan (2002) argued that the theoretical models to estimate gas hydrate saturation from seismic data predict significantly different acoustic/elastic properties of sediment containing gas hydrate that, it is not known which results to use. The shortcoming is due to the generality with which some of these rock physics theories are applied, with little attention to the various limitations. The review recommended further studies including pore pressure predictions and development of scaling models, of which the objectives of this research, explained in Chapter 1, were based.

9.3 How the review impacted on the experimental design and techniques

The experiments were designed to further test some of the rock physics theories with a range of materials (artificial and natural sandstone) under varying geomechanical, petrophysical and acoustic characteristics. (The list of all the laboratory experiments and experimental conditions are found in Chapter 1, and in the Appendices). The experiments simulated both in-situ field conditions and laboratory conditions. This helped verify and analyze the response and behavior of reservoir rocks with regard to changing pore pressure and effective stress conditions. The new direction of our experiments took into consideration some of the limitations and the findings to this review. As a matter of scientific need, studies were extended to the petrophysical and mineralogical (grain size distribution, degree of compaction etc.) levels of these rock materials. In doing so, a database was established, (explained later in this chapter) of real factors and properties of rocks, their correlation and auto-correlation of factors that can be used in rock classification.

9.4 The scaling problem

On the issue of scaling model, the review identified that, there are problems on how to resolve the differences between, core, log and vertical seismic profile velocity (seismic) wavelength scales. This velocity disparity, discussed intensively in scientific literature, is

referred to as the scaling problem. Extensive literature review indicated that, to date, Backus averaging is the only practical method that provides a finely foliated velocity model in an attempt to solve the scaling problems. However, it was found that Backus averaging has three major shortcomings and limitations: (i) Backus work was restricted to zero-frequency limit (low frequency limit), (ii) there was no source of intrinsic energy dissipation such as friction or viscosity (attenuation), catered for, in the model, (iii) the model requires that layer thickness of the media must be larger than the seismic wavelength: how greater is still a question of disagreement among practitioners. It was in the light of this the author developed a model to reconcile the various velocity disparities and scaled the velocities depending on the type of waves used, at a given frequencies and wavelength characteristics. This research provided the opportunity to examine the dispersion of elastic wave velocity over a wide frequency range. The aim of the literature review was to identify the current practices, the shortcomings on scaling models, to accumulate knowledge, study the fundamental science underlying seismic propagation in reservoir rocks and develop ideas and techniques which were applicable and relevant to the current practicing methods of reservoir imaging. The results of the thesis answer the two most important questions: (i) what factors contribute to acoustic velocity differences across a broad frequency band, and (ii) and how does one develop practical scaling models and methodology that take into account intrinsic energy dissipation. The results, findings and answers to these two questions, that forms the heart of this research, are discussed in the next sections.

9.5 Development of the experimental techniques and equipment design

Another sub objective was to perform suites of petrophysics, geomechanics and acoustics laboratory experiments on natural and artificial sandstone to measure porosity, permeability, saturations, P-wave velocity, attenuation and quality factor, under both hydrostatic and deviatoric stresses. In order to accomplish this, equipment was designed and, new experimental techniques for ultrasonic wave measurements on core samples, under in-situ stress and pore pressure conditions, in the laboratory were developed. This resulted in a wealth of acoustic imaging data consisting of mechanical, petrophysical, acoustical and dynamic rock properties. Details of this database are discussed in section 9.6.

Traditionally, coupling geomechanics, acoustic and petrophysical experiments present challenges, especially regarding the issue of where transducers should be attached in the presence of high confining pressure around the rock material. Experimental measurement techniques were developed to accurately determine quality factor and velocity for rock samples within a triaxial cell. This includes the design of ultrasonic acquisition system to measure arrival time through the pulse echo techniques during compression testing. Traditional velocity and attenuation measurements adheres the piezoelectric transducer directly onto the rock surface. However, such arrangement when coupled with confining pressure, exerts high pressure on the transducer and affect the vibrational mode of the

transducer, and thus the acoustic results. To avoid this problem, triaxial compression cell was adaptations to accommodate axially mounted ultrasonic P-wave transducers. The ultrasonic piezoelectric sensors were mounted in custom platens sized to fit outside the existing triaxial pressure cell without any alterations to the cell itself. All sensors were centered and aligned with the core specimen axis. The transducers were further away from the rock sample and the transmitted wave propagated through the loading piston, flow disks and base plate. P-wave amplitude decreased and frequency spectral changed slightly as a result of this extended path the wave followed. However, the validity of this experimental arrangement was verified by numerical modeling and they were in perfect agreement with measurements. The lower and upper platens that house the 1 MHz Panametrics P-wave piezoelectric transducers were custom designed for the thick walled triaxial cell rated to 69 MPa (10 Kpsi). The contact surfaces between the platens, loading piston and base plate were machined flat and a thin film of high vacuum grease was applied to ensure maximum ultrasonic signal transmission. Flow disks, made of steel, were used on either ends of the sample to distribute the pore fluid on either ends of the core sample.

9.6 The geo-scientific database

The experiment and numerous investigations carried out in other coordinated research projects, resulted in a wealth of data from various disciplines of geosciences, including

geology, geophysics, petrophysics and acoustics. To allow a comprehensive survey of the data available, and to facilitate direct access to information, this data catalogue was set up on the local server at the Mining Engineering department. The database includes a database guide that renders the possibility of checking easily for the desired information. Data are first subdivided according to geographical location, then to scientific subject. The description of each available data set starts with a header containing information about global location and type of data. More detailed information like the exact dataset content, data structure, file size and format, data source and manipulation as well as a short example of the original data file are included. The database also include the results of the experiments done in this investigation and data already collected in a related research projects (Donald et al., 2004). The ultrasonic and acoustic data, in particular, were recorded in several frequency bands ranging over two orders of magnitude from 350 KHz to 1500 KHz, which assisted with the scaling components of this research project.

This local database adds information on attenuation and diffraction loss factors to the High Pressure Geophysics Laboratory (HPLab) database in the Department of Earth Science at the Dalhousie University (http://gsca.nrcan.gc.ca/pubprod/rockprop /intro_e.php). This is to develop a common data repository for all academic and industry geo-scientific data. The HPLab database at the geology department spans over 25 years of collaborative research work. During this period, the HPLab acquired, enhanced, archived and disseminated regional geological, geophysical, geochemical, mineral and

petroleum data as a fundamental component of its work. The geo-scientific database provides improved access to a single source of data for a variety of needs including quality hardcopy information and remote access to seamless geo-scientific datasets. By linking our experimental database (Mining department) with the HPLab database and making the geo-scientific information readily available within Dalhousie, these data can be incorporated into decision-making processes thereby promoting mineral and petroleum exploration in Atlantic Canada and around the world. The objective is therefore to centralize relevant data from various sources for better project coordination and to facilitate future planning. The database will be of significant value to geophysicist, planners, scientists, engineers, and others interested in rock characteristics of rocks around the world. It would also be useful for student's teaching and research in Dalhousie University.

9.7 The velocity measurements

Elastic wave propagation through porous media has been studied in the laboratory over the past 50 years. Various techniques have been utilized for wave velocity and attenuation measurements at high frequencies (500 Hz to 1.5 MHz). The measurement of velocity used in this research was based on the pulse transmission technique by Birch (1960). This is the standard laboratory acoustic velocity measurements. Generally, the elastic-wave velocities are determined by picking the time of a certain feature of a

propagating pulse, such as the first amplitude maximum. Velocity values as a function of rock type, degree of saturation and pressure were found (appendices). The results indicated that many factors affect acoustic velocity, and can be grouped into three broad heading: rock properties, fluid properties and environmental conditions. These factors have been discussed in details in the next sections. The pulse transmission technique by Birch (1960) used in the experiment and possible source of errors have also been discussed in section 9:19.

9.8 Ultrasonic imaging of pore pressure

As highlighted earlier, one of the objectives of this research was also to produce acoustic images in the laboratory under different stress conditions. To achieve this objective, a number of acoustic experiments were performed on both natural and artificial sandstones rock using the designed equipment and experimental techniques explained above. The stress chosen ranges from 0 MPa to 60MPa. This high stress gives opportunity to investigate imaging within and beyond the current depth (around 3 to 4 km) of reservoir operation. Figure 9.1 taken from Carcione and Hellev, (2002) shows depth-net overburden pressure relationship of a typical reservoir. This geo-pressure information gave some experimental guidelines of the type of simulated insitu pressure that was used in the laboratory test, so that it can be easily related to field applications. It was found that acoustic properties behave differently under different stress and pore pressure

conditions. The experimental results indicated that the main parameters controlling acoustic velocities and attenuation can be grouped into three main categories: rock properties, fluid properties and environmental conditions.

The rock properties include factors like the density, texture and mineralogy, clay content, micro-cracks, fractures, porosity, lithology and pore shapes. Most of these factors, for example micro cracks, porosity, fractures pore shapes etc. are in turn controlled by the stress exerted on the rocks. The thin section study confirmed that these factors are important rock properties that affect the acoustic velocities. At great depth, these factors are altered by the high overburden pressure which in turn affects the acoustic velocity.

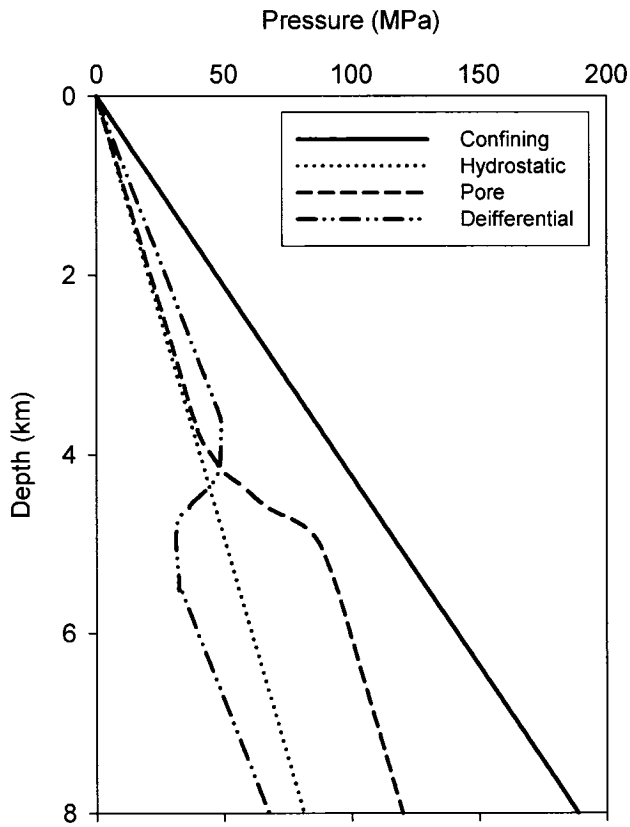

Figure 9.1: Typical pressure-depth plot where the different pressure definitions are illustrated (after Carcione and Hellev, 2002)

9.9 Stress - acoustic velocity relationship

In order to link the experimental stress conditions to practical field reservoir applications, the various stresses that exist in reservoirs in relation to the overburden depth were analyzed. The analysis of geo-pressure (Figure 9.1) indicates that, in a reservoir, there

always exist two distinct pressures: overburden pressure and reservoir pressure. The net overburden pressure (Po), also called confining pressure, is the pressure exerted by the total overburden rock strata, whereas the reservoir pressure (P_p), also called fluid pressure or pore pressure, is exerted by the fluid mass. This confining stress normally has two components; the total vertical stress which is normally equivalent to the maximum principal insitu stress, and the total horizontal stress which is the insitu minimum principal stress. In region without much tectonic activities, the maximum total horizontal stress is approximately equal to the minimum total horizontal stress. The difference between the overburden pressure and reservoir pressure is called the net overburden pressure (Pd), which is also called differential pressure or sometimes effective pressure (Pe). Strictly speaking, the net overburden pressure is slightly lower than the effective stress because of the effective stress coefficient which was found to be equal to 0.82 for the quartz sandstone. Therefore it is the net overburden pressure that controls the seismic properties of reservoir rocks because the pore fluid pressure supports a part of the overburden pressure, thereby decreasing the load supported by the total rock strata. As shown in the diagram (Figure 9.1) the overburden pressure responsible in changing these rock properties increases with depth. The confining pressure, pore pressure, hydrostatic pressure and differential pressure increase linearly with depth to about 4km, the pore pressure suddenly increases, thud decreasing the differential pressure.

The general stress relationship with velocity from the experiments is shown below

(Figure 9.2). Results show that V_p varies with pore pressure as well as confining pressure giving a net overall effective stress velocity relationship. The variation of V_p with pore pressure, at constant effective stress, indicates that the effective stress coefficient, n, is less than 1. This result confirms earlier research on V_p - pore pressure relationships (Gangi, 1991; Prasad and Manghnani, 1997; Khaksar et al., 1999). Thus, it is important for the values of n to be accounted for in high pressure triaxial laboratory studies on acoustic velocity variation with pore pressure and confining stress. This was done in this experiment. The V_p variation with the overall effective stress is non linear and is quantified by a new model

$$V_P^{\,2} = A + B * P_p + C \times \exp^{-P_p / D} \qquad 9.1$$

Where A, B, C, D depends on the type of rock and Pp is the pore pressure. This equation is similar to the one reported by Greenfield and Graham (1994). The fact that V_p changes with pore pressure at constant effective stress indicates that the value of the internal coefficient is not 1 but varies from 0 to 1 for a particular rock. In fact, the experimental results show that the value depends on the instantaneous value of the confining and the pore pressure.

The general trend of velocity effective stress is that seismic velocities increase as the net overburden pressure increases. However, the relationship between seismic properties and the net overburden pressure is nonlinear. Seismic properties increase faster (higher slope)

in low net overburden pressure regions. In most samples (both the synthetic and artificial sandstone), rate of change of V_p is greater at low pressures (up to 15 MPa) than at higher pressures. The different behavior of V_p gives indications of the type of pores in the samples. A steep increase in V_p at low pressures is indicative of the closing microcracks or pores with large aspect ratio.

From the graph (Figure 9.2), it is seen that imaging pore pressure with velocity is effective in low overburden pressure where changes to velocities are as high as 8% during the first 18MPa (about 1km depth). However, the velocity barely changes at high pressures. In fact the velocity is insensitive to changes in pressure at high pressures. This occurs at a depth of approximately 3 to 4km and beyond. Imaging with velocity beyond this point is very limited and presents challenges. There are several possible explanations for this; the most significant is probably the gradual velocity change with pressure, mentioned above. The thickness and the depth of the over-pressured unit are crucial factors strongly impacting our ability to use velocity analysis as a tool for pressure prediction. The sensitivity for detecting abnormal velocity changes decreases rapidly with depth, while the uncertainty in velocity estimation increases rapidly with depth.

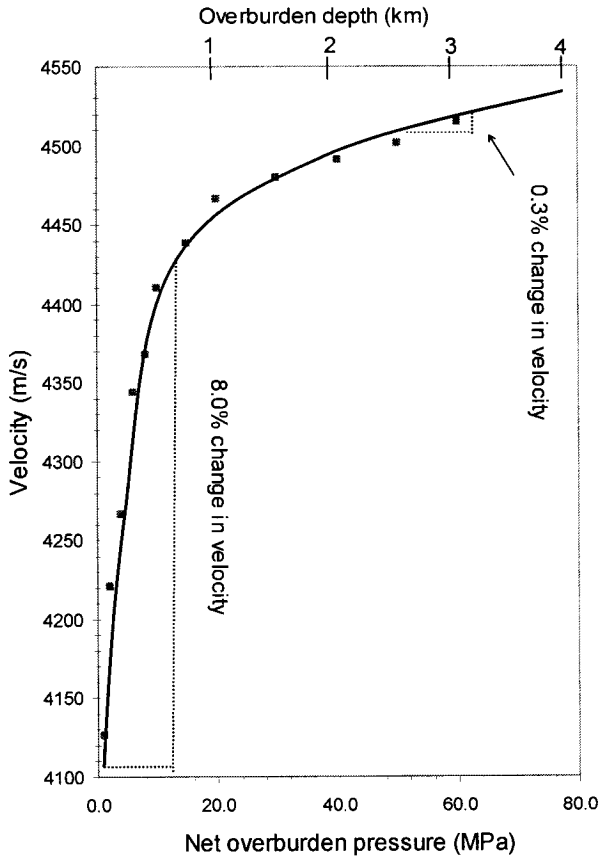

Figure 9.2: One relationship between acoustic velocity and net overburden pressure derived from this research

9.10 Stress - attenuation quality factor relationship

The results indicate that quality factor increases with pore pressure as well as effective stress or net overburden pressure. The variation of pore pressure with Q_p is gradual at low pore pressure and steeper at high pore pressures. The best equation that describes the behavior of Q_p with stress is a two parameter exponential growth without limiting value. Equation 9.2 describes the quality factor-pressure curve. It is noted that Q increases with

stress.

$$Q_P^{\ 2} = A \times \exp^{B*P_p} \tag{9.2}$$

Where A, B, C, D depends on the type of rock and Pp is the pore pressure

The relationship between Q and the overburden pressure is also shown in Figure 9.3

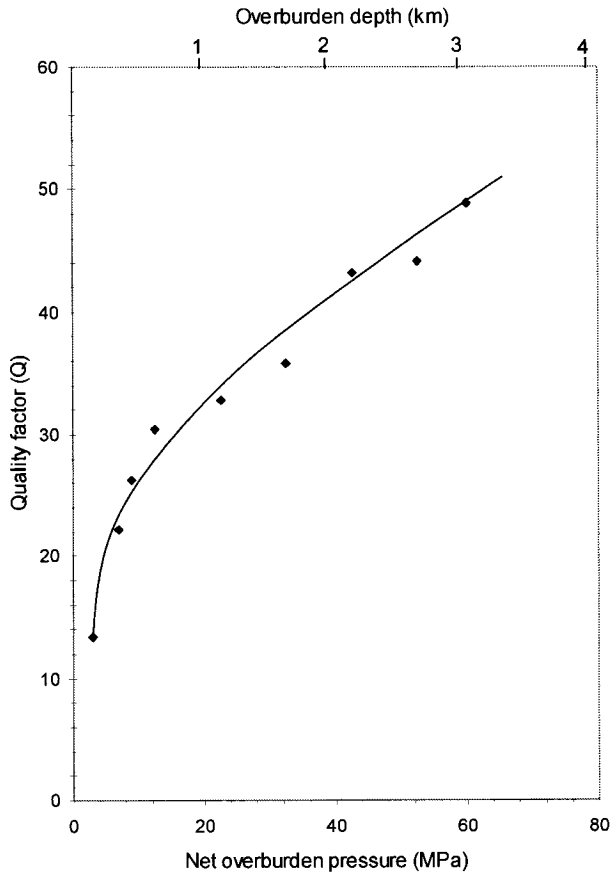

Figure 9.3: One relationship between attenuation quality factor and net overburden pressure derived from this research

9.11 Comparison of imaging pore pressure with velocity and with attenuation quality factor

Variation of velocity and quality factor to pore pressure and effective stress changes under simulated production scenarios was examined for artificial and natural sandstone. It is found that both velocities and attenuation change with net overburden stress. Therefore both of these acoustic properties can be used as an index for imaging and characterizing rock properties. However, the research indicated that the variations in attenuation with effective stress are greater than the variation in velocity with effective stress (Figure 9.4). For example in Figure 9.5, a change in effective stress from 0 to 20 MPa results in 8% velocity while Figure 9.6 shows an 80% change in attenuation for the same pressure change. This indicates that attenuation is far more sensitive than velocity to changes in pore pressure. Thus traditional velocity models are inadequate for high pore pressure imaging. New evaluation methods based on other acoustic properties are needed to fill the knowledge gap within these rock types if acoustic imaging at such deep depth and high pressure is to be guaranteed. However, .attenuation values are also more difficult to obtain experimentally than velocities and insitu measurements are even more difficult. As highlighted in the preceding technical publications, the method used in attenuation measurement is the spectral ratio technique, which assumes frequency independence of Q. This assumption would impact on the accuracy of the attenuation measurements. Attempt were made to correct some of the errors in the form of diffraction and resulted in

1% change in the frequency. However, the effect of dispersion on the spectral ratio techniques in attenuation methods remains an unsolved problem probably because of the physics linkage between attenuation and dispersion. On the other hand, our experiment has shown that at high pressures, velocity data does not often provide the resolution needed for identifying slight changes in the physical state of rock over varying insitu conditions. These small changes however, can be incorporated into reservoir monitoring using attenuation instead of velocity, if accurate insitu attenuation measurements techniques are developed. Further research is recommended for attenuation measurement. If successful, then the real time pore pressure prediction during drilling operations that currently incorporates sonic and seismic velocities may use attenuation in addition, in order to help gather more information. Simultaneously linking geomechanical measurements with both velocity and attenuation variations would present a more meaningful, higher resolution picture of changing reservoir conditions. The issue of finding more appropriate way of estimating both laboratory attenuation and insitu is discussed below and can be looked into as a future research area.

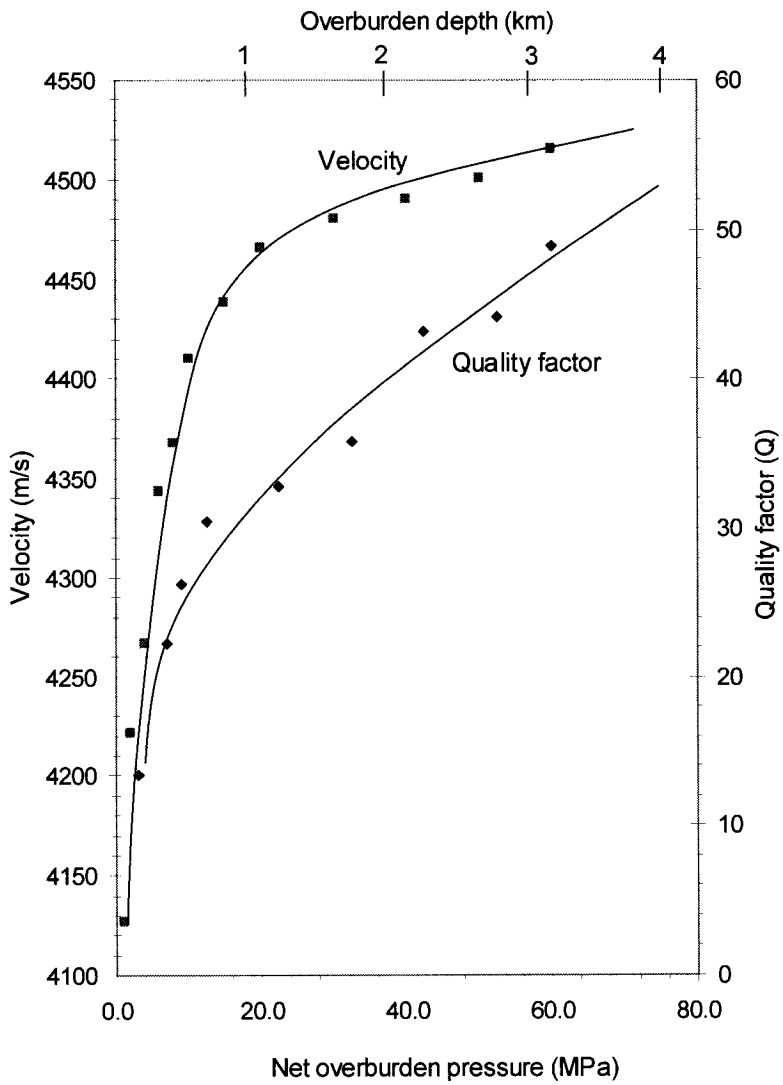

Figure 9.4: Comparison of acoustic velocity and quality factor with the net overburden pressure

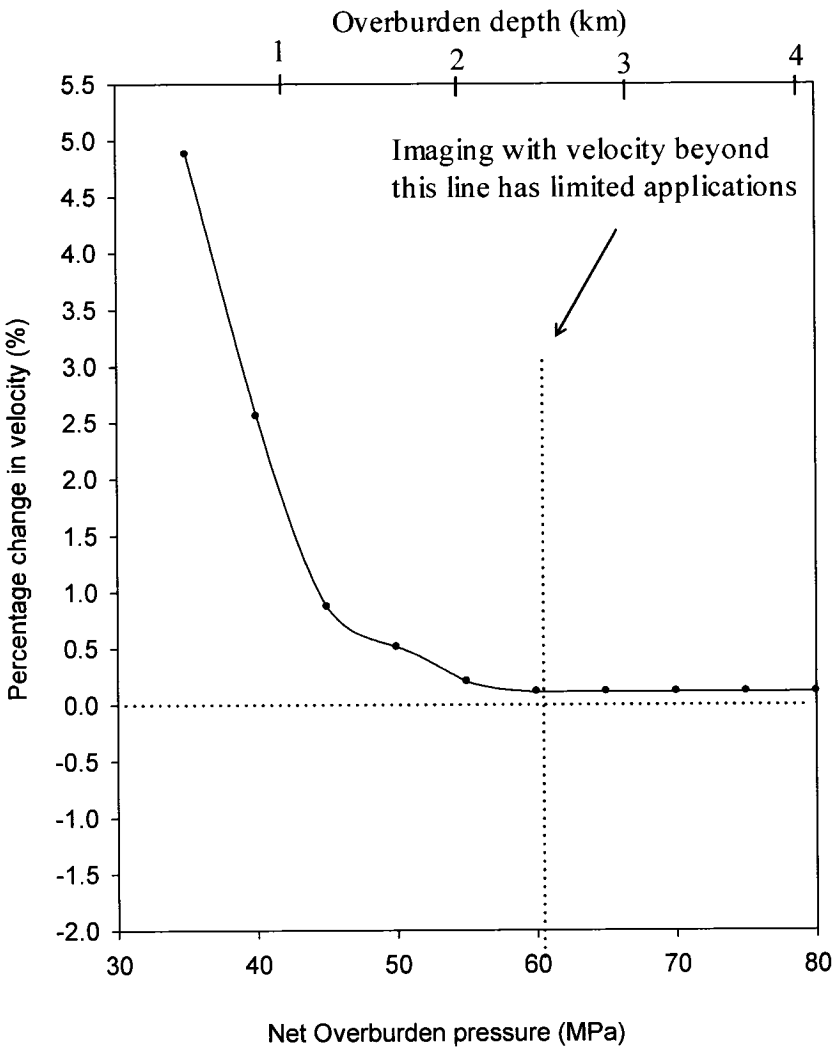

Figure 9.5: Sensitivity of acoustic velocity with depth

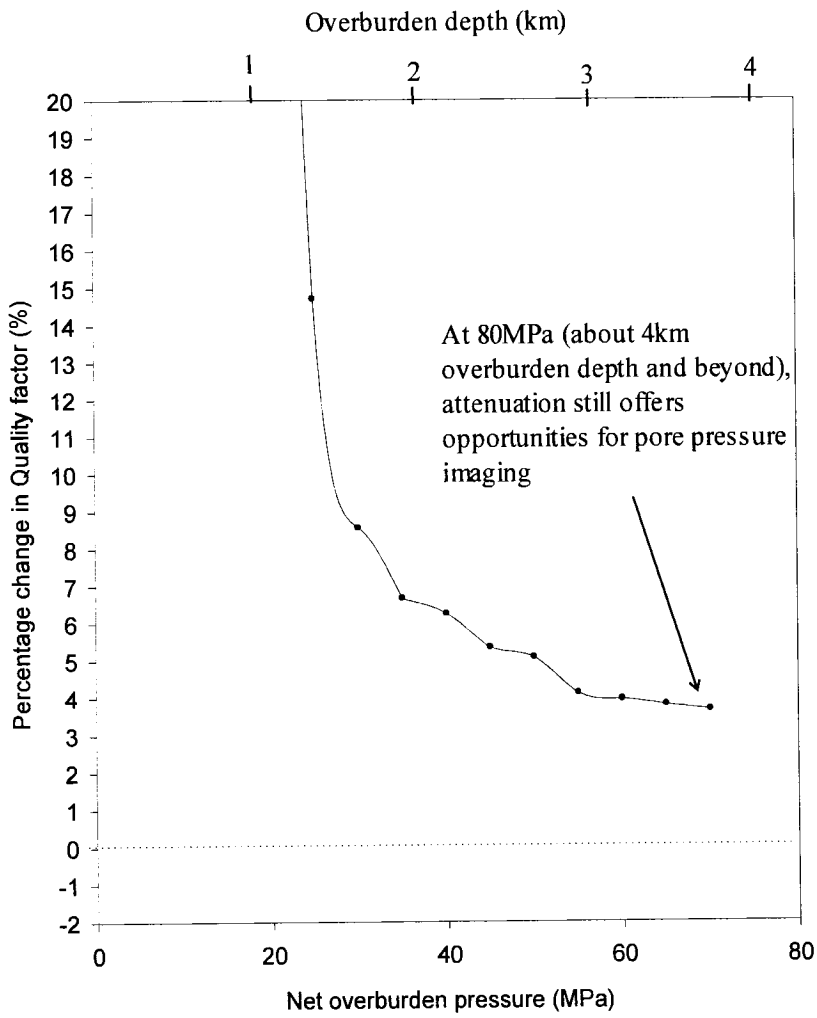

Figure 9.6: Sensitivity of attenuation quality factor with depth

9.12 Fluid properties and dispersion

The fluid properties were also identified as one of the factors that affect seismic velocity. These include factors such as dry or saturated velocity, saturated with liquid (water, oil,

brine) or gas and degree of saturation (i.e. saturation level or percentage saturation). Investigation was only done for dry and water saturated velocity. The degree of saturation varies from 0% (dry) to 100% (fully saturated). It was found that fluid effect on velocity depends on the saturation. It was also confirmed that velocity in the saturated rock was higher than velocity in dry rocks. This was due to the effect of dispersion. From previous studies, the fluid motion is caused by pressure equilibration as the seismic wave passes through the rock. Therefore the attenuation depends on the fluid mobility, which in turn depends on the viscosity and bulk modulus of the pore fluid, and the permeability of the rock. If the pore space is completely filled with fluid, the fluid has less mobility than if there is some gas saturation. Thus attenuation is highest in a partially fluid saturated rock Therefore the presence of water causes the wave train to disperse. When that happens, the high frequency waves move faster than the low frequency waves. The wave train becomes broader, with the slower waves from the lower frequency modes at the tail of the wave train and faster waves from the higher frequency mode at the front of the wave train. During the laboratory experiments, the velocities were measured using the first arrival phase velocity of the wave train which is obviously the fastest frequency waves when dispersion takes place. This is the fundamental reason why dispersion causes increases in first arrival phase velocity and delay in last arrival and group velocities. In fact, dispersion may decrease the group velocity but not the phase velocity of the first arrival. The numerical model presented in the subsequent section throw more light on this preposition. The research did not investigate the effect of different type of fluid on the

velocity, but many authors have confirmed that, high density waves increases dispersion and thus increases velocity whiles low density fluid reduces dispersion and reduces velocity. The third factor affecting velocity was the environment factor which typically includes the state of in-situ stress (pore pressure, confining stress, effective stress) surrounding the rocks. This has already been explained above. The final property which was investigated and in fact forms the major part of the research is the effect of frequency of the waves used in the imaging. The frequency of the wave is explained in details in the next section on the scaling model below. Other environmental factors like temperature, fluid composition wettability etc. were not investigated and were outside the scope of this research.

9.13 Dispersion and attenuation at low frequency limit

Acoustic waves create relative motion between the fluid and the solid frame due to inertial effects. This phenomenon was first introduced by Biot (Biot, 1956a; 1956b). As the rock matrix is accelerated, the fluid lags behind, resulting in viscous dissipation of acoustic energy. However at low frequencies, the viscous skin depth is much larger than the pore size and fluid and solid are virtually locked together, moving in phase. Velocity is minimum and there is little attenuation. At high frequencies, the viscous skin depth is very small and the fluid and solid are essentially decoupled. Velocity is a maximum, and attenuation is low. For water-saturated rocks, the critical frequency in the Biot theory

where attenuation and dispersion are maximum, is often on the order of 100 kHz. It is been shown by many authors that at such frequency and for all practical purposes, dispersion is negligible. Increasing viscosity pushes the critical frequency even higher. Therefore seismic waves and sonic logging are almost always in the low-frequency range of Biot theory. This research did not investigate dispersion at such low frequencies and thus could not confirm the negligible dispersion at low frequency limit. The low-frequency limit of Biot theory gives Gassmann's equations. An interesting prediction of Biot theory is the existence of a second compressional wave dominated by the properties of the pore fluid (often called the Biot slow wave). At low frequencies this wave is diffusive and at high frequencies it is propagatory. The propagating wave is very difficult to observe in rocks, though it has been seen in synthetic materials.

9.14 Numerical modeling and Dispersion Analyses

The heart of the thesis is the development of the wave propagation model that is detailed in Chapter 8. The answer to the question of what factors contribute to velocity differences in acoustic imaging across the various frequency band has been made clear from the preceding publications cited in Chapter 8. The Numerical Spectral Discretization model identified a sufficient discrepancy between theory and practice of wave propagation which is explained below.

The physics that describes waves is a three-dimensional second-order linear partial differential equation that relates the temporal and spatial derivatives of the pressure field.

$$u_{tt} - c^2 u_{xx} = 0 \qquad (9.3)$$

Where, u_{tt} is the second derivative of the displacement amplitude, u, with respect to time, t of wave's travel.

u_{xx} is the second derivative of the displacement amplitude, u, with respect to distance, x of wave's travel.

c is the velocity of the wave

The equation was derived from fundamental Newton's law of momentum and energy conservation of a particle with a rest mass, m, moving in a medium. The assumptions used in the derivation of the equation are:

(i) There is no frictional resistance or any opposing force to particle motion. This is linked to the homogeneity assumption of the grain matrix material

(ii) The displacement amplitude of the particle vibration is small and does not exceed the elastic limit of the material. This is linked to the linear elasticity assumption of the rock material, within the range of stresses and pressures in operation.

With these two assumptions, the waves propagate through the medium without loss of energy or change in shape. Such a wave travels infinitely at a constant speed, c, called the phase velocity. Waves of this nature are described as linear waves. The medium in which they travel are described as frictionless and it offers no resistance to wave motion. One example of this type of waves is light waves traveling in vacuum with a constant speed of

light, c.

However, the above assumptions result in a drastic simplification of waves in nature. All the waves that were used from frequency of 300KHz to 1300MHz show some forms of dispersion through the materials. The results show that most waves in materials media are dispersive. However, literature indicates that the dispersion effect in rocks of low frequency wave is negligible. This was not investigated. Thus, as the waves are transmitted through the material, they are bound to change in a manner that the wave energy is more spatially spread out or dispersed. It is noted that non linearity is rather a more common state of affair in wave travel in practice. These media (rocks) have a more complicated non linear wave equation that describes the wave propagation through them. The non linearity is as a result of opposing forces such as the frictional forces (strictly speaking, the frictional forces are the elastic modulus) that oppose particle displacement, causing loss of energy (attenuation) and spreading of energy (dispersion), and the two are linked together. The velocity of the waves we studied therefore changes with the frequencies, or equivalently, on wavelength. The material is considered to possess the property of dispersion. The rock (natural and artificial sandstone) used in the experiment possess dispersion property.

Dispersion is a phenomenon where waves having different frequencies propagate with different speeds. Dispersion is known to fall into two basic classes: intrinsic, which is

based on anelasticity; and scattering, which is based on local wavelength-scale variations in the rock formation. Intrinsic dispersion is a local property of the rock while scattering dispersion is a property of a neighborhood of rocks, and includes the effects of reflections, refractions, and the law requiring continuity of displacement. Dispersion does not result in energy loss, but energy spread. However, because attenuation is intrinsically linked to dispersion, it is very difficult to separate them. The "pure" linear wave equation presented above is nondispersive and therefore fails to capture this phenomenon which is common for many acoustic waves

9.15 The effect of dispersion

The effects of dispersion often include:

The effects of dispersion often include:

(i) waves traveling along coordinate axes propagating slower than in diagonal directions,

(ii) high-frequency waves propagating faster than lower-frequency waves, in the case of body waves.

Thus, the more a wave disperses, the faster the high frequency waves travels ahead of the wave pulse and the slower the low frequency wave travels behind the wave pulse. Thus, any property that causes dispersion would cause increased velocity of the first arrival (high frequency) and decrease velocity in the last arrival (low frequency). However, for a very highly attenuation material, the material acts as filters and remove all the high

frequency component. In this case, only the low frequency wave would be present and the wave would move slower. For example, velocities in saturated rocks, described above, were higher than velocities in dry rocks. This was due to the effect of dispersion. The presence of water causes the wave train to disperse. When that happens, the high frequency waves move faster ahead of the wave train increasing the velocity and the low frequency waves moves slower behind the waves reducing the velocity. The wave train becomes broader with slower waves from low frequency modes at the tail of the wave and faster waves from high frequency modes at the front of the wave train. What is practically measured in the laboratory or for that matter in the field or any acoustic velocity experiment is the phase velocity of the first arrival of the wave train or pulse, which is obviously the fastest frequency waves. That is why dispersion causes increase in velocity. So a wave originally made through a higher frequency excitation (MHz range) would disperse more and travel faster than a wave produced by a low frequency excitation (KHz range). This indicates that dispersion reduces with frequency and becomes very low at extremely low frequencies. Thus, confirming some findings in the literature that indicates that the dispersion effect on low frequency wave is negligible.

It is possible to analyze the dispersion introduced by a numerical method either directly by substituting certain "test waves" into the discretized equation or by frequency domain analysis. The former was the numerical methods used in the research. Summary of the steps involved are given in section 9.15 and the whole technique and methodologies are

explained in appendix 4 and in the technical paper in Chapter 8. This technique was used to develop wave propagation in visco-elastic medium (quartz sandstone) that unifies the dispersion theory, and frequency dependant velocity approaches to velocity predictions at all frequencies and wavelengths.

9.16 Phase and group velocity issue

In both dispersive and non dispersive media, the wave velocity for a pure sinusoidal wave of a particular frequency is termed the phase velocity, and it is related to frequency and wave number by:

$$c = \frac{k}{\omega} \tag{9.4}$$

Where, c is the speed of the waves

k is the wave number given by $2\pi/\lambda$

λ is the wavelength given by $2\pi/k$

ω is the angular frequency given by $2\pi f$

f is the frequency of oscillation given by $\omega/2\pi$

The relationship between k and ω as in Equation 9.7 is called the dispersion relation. For linear waves, the ratio of k and ω is constant, c, called the phase velocity. Thus k is directly proportional to ω for linear waves. There is no dispersion in this type of waves. However, in non linear waves, c varies with ω and k, either in an increasing manner or

decreasing manner. If the phase velocity, c, decreases with frequency, in some frequency range, the medium is said to possess normal dispersion in this range. On the other hand, if c increases with frequency in some frequency range, it is said to possess anomalous dispersion in this range. Both normal and anomalous dispersions are observed for acoustic waves.

9.17 Numerical Spectral Discretization procedure

The NSD procedure is summarized in the following four steps:

Step 1: Set the initial and boundary conditions based or material and experimental conditions under study

Steps 2: Perform a real to complex Fourier Transform on the initial displacement to get Fourier coefficients

Step 3: Calculate the Fourier coefficient at the time t and substitute the modeled dispersion relation.

Step 4: Perform a complex to real inverse FT to get the displacement field time t,

Step 5: The above steps are then coded and implemented in any computer programming language of choice.

9.18 Discussion and results of the modeling

The results of the numerical model are shown in the following figures. Figure 9.7a shows the initial wave, u_0, ($[u(x,0) = 50\, e^{-\frac{1}{24}x^2} Cos\ (2x)]$) sent through the rocks. It is a wavelet of amplitude A=50mV, centered at x=0 and t=0. Figure 1b also shows the same wave after traveling through the rock for 15μs. This is superimposed (Figure 9.7c) and compared with the wave that travels through a rock with no dispersion (Figure 9.7d). The dispersive waves become broader as it travels through the rock, with the high frequency components traveling faster at front of the wave train and the low frequency wave traveling slower at the tail.

In figure 9.8a, the wave is plotted at increasing distances from x=0 to study how it behaves and broadens with travel through the rock. It is seen that the original initial wave disperses with propagation with high frequency component traveling faster and broadening the wave pocket. The low frequency components travel slower as the wave disperses and emerges at the end of the wave pocket. Simultaneously, the wave also losses energy due to attenuation as it travels through the medium. Figure 9.8b, is the analysis of the arrival of the dispersed and non-dispersed waves after traveling for 15us. The effect of dispersion caused the high frequency wave to arrive earlier ahead of the non dispersed waves. The effect of dispersion also caused the low frequency wave to arrive later behind the non dispersed waves. The distance between the two is quantified as the

effect of dispersion.

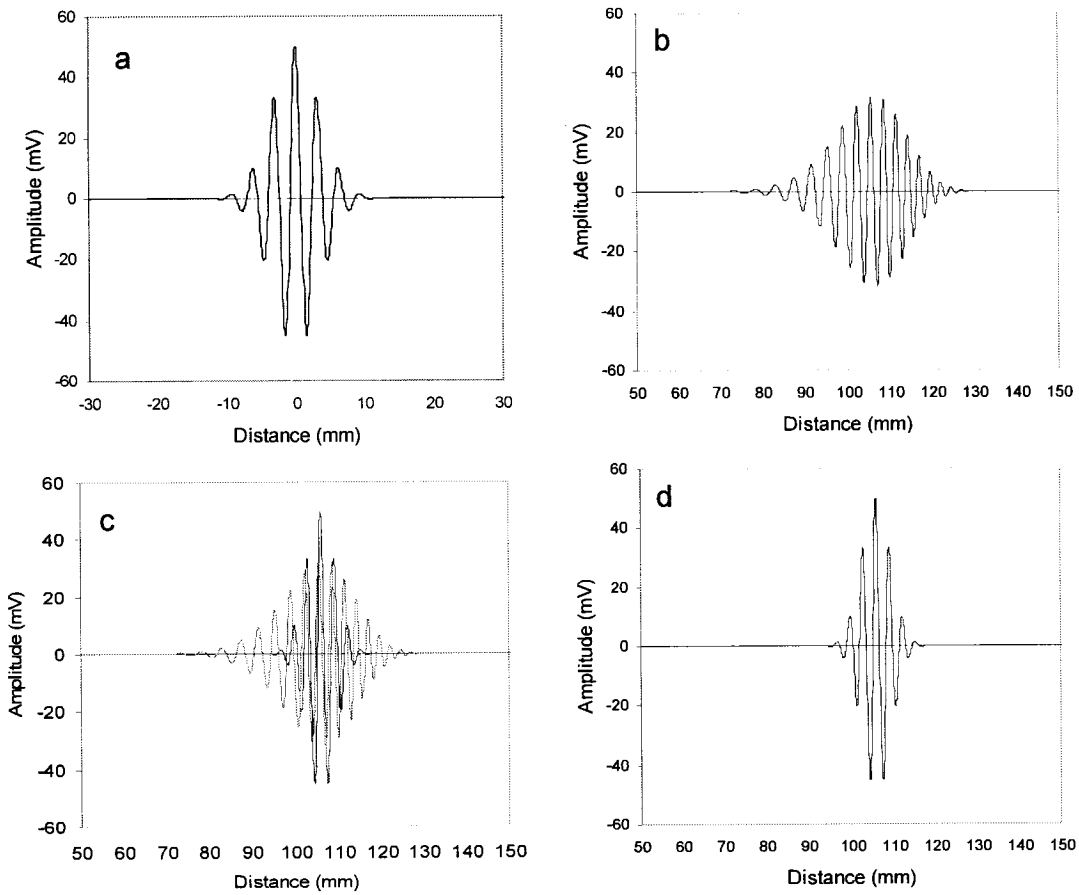

Figure 9.7 (a) the initial wave, u0 sent through the rocks at time 0 and distance 0 (b) the same wave after traveling through the rock for 15μs. (c) Comparison with a dispersive and non dispersive waves (d) wave that travels through a rock for 15μs. without dispersion

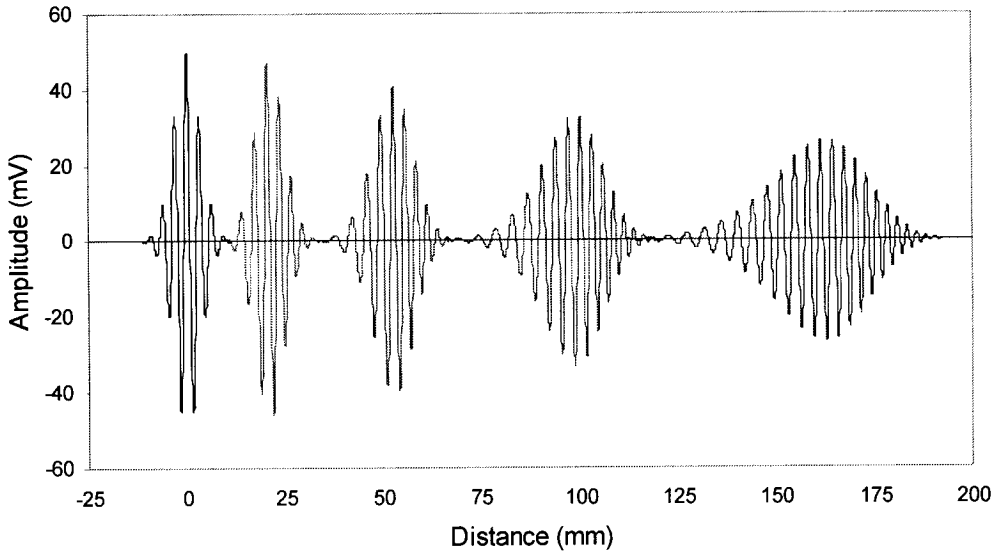

Figure 9.8a: Tracking of the wave pocket with increasing propagation distance

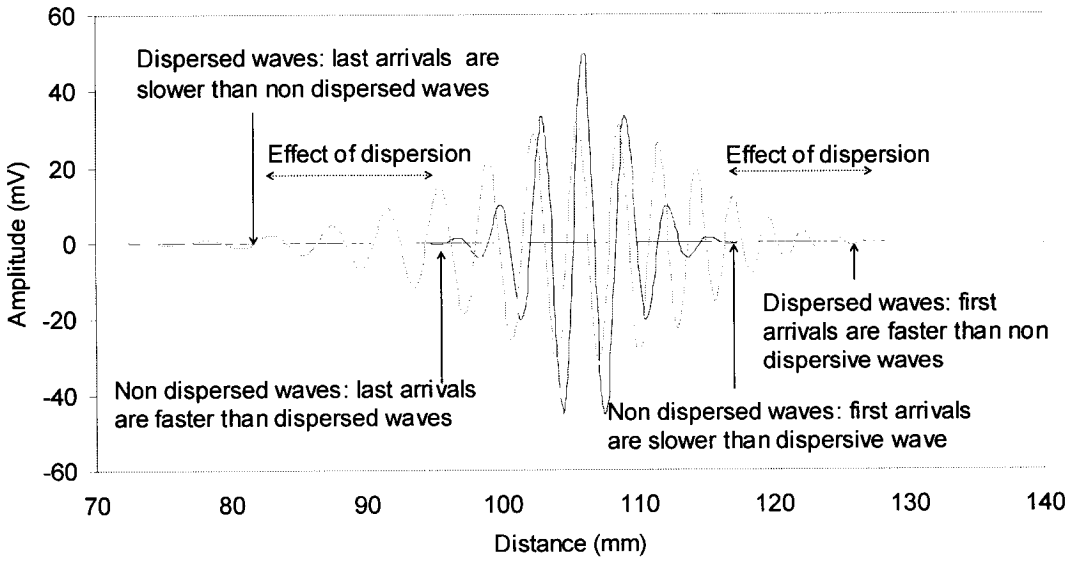

Figure 9.8b: Analysis of the arrival of the dispersed and non-dispersed waves after traveling for 15us. The effect of dispersion caused the high frequency wave to arrive earlier ahead of the non dispersed waves. The effect of dispersion also caused the low frequency wave to arrive later behind the non dispersed waves. The distance between the two is quantified as the effect of dispersion.

Figure 9.9 shows the frequency scaling results and gives the w-k diagram for both dispersive and non dispersive rock (a), and the velocity relationship (b), frequency (c), and wavenumber (d). It is seen that velocity increases with frequency and reduces with wavelength and that these relationships are non linear. It is seen that at the initial stage, for the few 100KHz frequency, the velocity is very crucial since the rate of change in

velocity at these lower frequencies to the MHz frequencies are relatively large. At a very high frequency range (MHz range) the rate of velocity change is very low and the curve is almost flat.

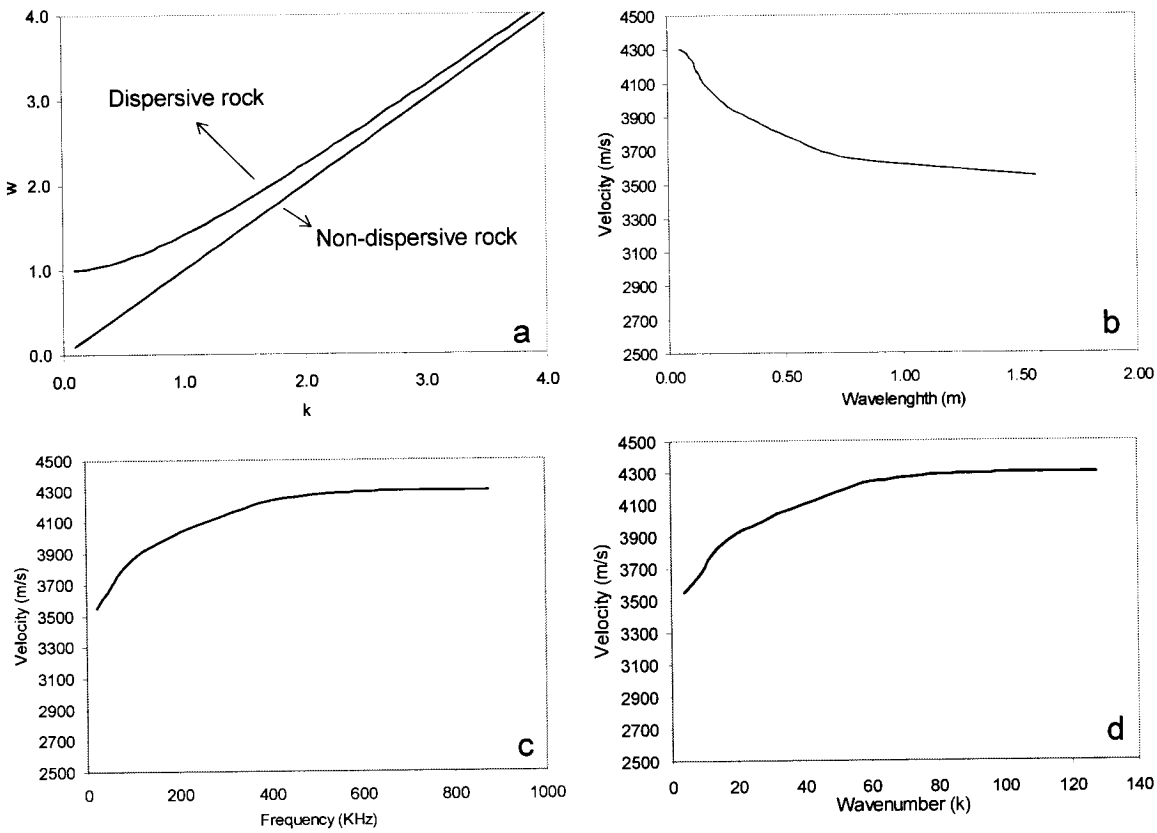

Figure 9.9: (a) w-k diagram for dispersive (quartz sandstone rock) compared to theoretical non dispersive material, (b) Velocity wavelength relationship, (c) Velocity frequency relationship and (d) velocity wave number relationship.

The difference in wave velocities is due to the use of different frequency waves in these three imaging systems. Basically, all these waves are non linear so they tend to disperse when they travel through the formation. When they disperse, the different frequency components travel with different velocities. The results of the modeling show that, the in general, the high frequency wave bands disperse more than low frequency waves bands. The accuracy of measuring velocity therefore depends on the dispersion characteristics of the waves and the nature of the rocks that disperse the waves. High frequency waves tend to present more problems and inaccuracies in velocity measurements because of highly dispersive nature of these waves. Anomalous dispersion occurred in some of the experiments where the phase velocities decrease with frequency. This occurs mostly in the very high dispersive media (saturated, high porosity, weak synthetic sandstone that was prepared in the laboratory). These synthetic high attenuating sandstone rocks act as filters to remove all the high frequency waves and slow down the low frequency velocity, before it reaches the arrival point. A laboratory test (not shown here) on a highly attenuating synthetic sandstone shows this anomalous characteristics (Donald et al., 2004). These weak, loose, inhomogeneous and incompetent rocks present more inaccuracies in velocity measurements than competent homogenous and strong rocks, because the latter tends to disperse waves more than the former. Therefore the accuracy of measuring velocity, in part, depends on the dispersion characteristics of the rock as well as the nature of the wave (frequency range). The problem is compounded with longer travel distances of these high frequency waves. Using finite difference to analyze

the wave gives a velocity profile and does not resolve the issue of dispersion which is central to scaling. The spectral discretization technique is able to break the waves down in frequency domain so that different frequency components could be analyzed. The model that is chosen or adopted for the non linear nature of the wave in the rock in question plays a very important role on the final dispersion model and thus the velocity measurements. The attenuation coefficient and the initial non linear model are key, to identifying anomalies in the final dispersion model.

The relationship between velocity and frequency was found to be non linear. It is seen that at the initial stage, for the few 100KHz frequency, the velocity is very crucial since the change in velocity at these lower frequencies up to the MHz frequency range are very large. At a very high frequency range (MHz range) the change in frequency with velocity is very low and almost flat. The relationship between velocity and frequency that was found in this experiment would work for sandstones with similar attenuation characteristics. For different rocks, the attenuation values are needed as inputs into the developed spectral discretization model, in order to predict changes in velocity with frequency.

9.19 Validation of the NSD model

Laboratory acoustic experiments were performed and the laboratory results were used to

verify the results of the numerical modeling. Experiments were conducted using the glass sandstone described previously in Chapter 3 using acoustic sensors in direct contact with the ends on the core. These experiments were conducted either on the bench top specimens with no stresses applied or under a normal 1MPa hydrostatic stress using the hydrostatic cell described in Chapter 3. Four experimental data points were plotted. The velocity assigned for each experimental data point was the group velocity measured at a maximum energy and correspond to the frequency at that peak energy level of the Fourier spectrum. Four experimental data points were plotted. The size of sample, transducers characteristics and measurement conditions of each experimental data point used in the validation are given below:

(1) Desktop measurement from a 2.5mm by 60mm cylindrical dry quartz sandstone sample. A 350Khz microdot transducer was used and the frequency at the maximum peak energy was 300khz.

(2) Desktop measurement from a 2.5mm by 60mm dry sample. A 1Mhz transducer was used and the frequency at the maximum peak energy was 500khz.

(3) Hydrostatic pressure of 1MPa on a rock sample of 54mm by 108 mm quartz sandstone and a 1 Mhz transducer. The frequency at the peak energy was 850kHz.

(4) Hydrostatic pressure of 1MPa on a dry rock sample of 2.5mm by 60mm using a 1.5 Mhz transducer. The peak energy was at a frequency of 1300kHz.

The numerical model was validated with the above four experimental multi-frequency data of 300khz, 500khz, 850khz and 1300khz and they were in good agreement within an acceptable experimental error (Figure 8.6). This shows the applicability of the KG model for dispersion in this sandstone over the MHz frequency band.

8.8.1 Appropriateness of the KG Model

None of the dispersion models given in the literature was developed specifically for rocks as has been highlighted in the review. However application of any of the model to a particular problem at hand would depend on the nature of the rocks and the extent to which losses due to intrinsic attenuation and scattering has to be taken into consideration. This research uses the KG model. As stated by Anno (1992) a change of the dependant variable in the acoustic variable-density wave equation reveal it to be essentially the simpler Klien Gordon equation used in this study. Anno further said that the Klien Gordon operator is dispersive exhibiting in the acoustic context a dispersion coefficient related to the density gradient. These gradients enter the into a dispersion relation and phase and group velocity expressions derived by Fourier analyses on the Klein Gordon operator

However, researchers from different background may argue about it applicability to specific geo-science problems. To avoid this complications all the other six dispersion models reviewed in the literature have been coded in the NSD computer program for users to decide on the type of dispersion model applicable to the type of work at hand. One other possible source of error between the model and the experiments may be due to the techniques used to measure the arrival times. Our measurements of velocity were based on the pulse transmission technique by Birch, 1960. This is the standard for laboratory acoustic velocity measurements. Generally, the elastic-wave velocities are determined by picking the time of a certain feature of a propagating pulse, such as the first amplitude maximum. However, as shown in our modeling results, attenuation and dispersion contribute to changing the shape of a propagating wave, making determination of a physically meaningful velocity problematic. As a consequence, the velocities so determined are not necessarily representative of the material's intrinsic wave phase and group velocities and the associated quality factors. Wave velocities determined from the time at which the pulse was first detected (signal velocity) differ from the predominant group and phase velocities. At best, the onset wave velocity arguably provides a lower bound for the high-frequency limit of the phase velocity in a material where wave velocity increases with frequency. This may impact on our laboratory and model results. Further research is needed to investigate whether the observed arrival times versus the actual propagation time are in good agreement, especially in a highly dispersive medium.

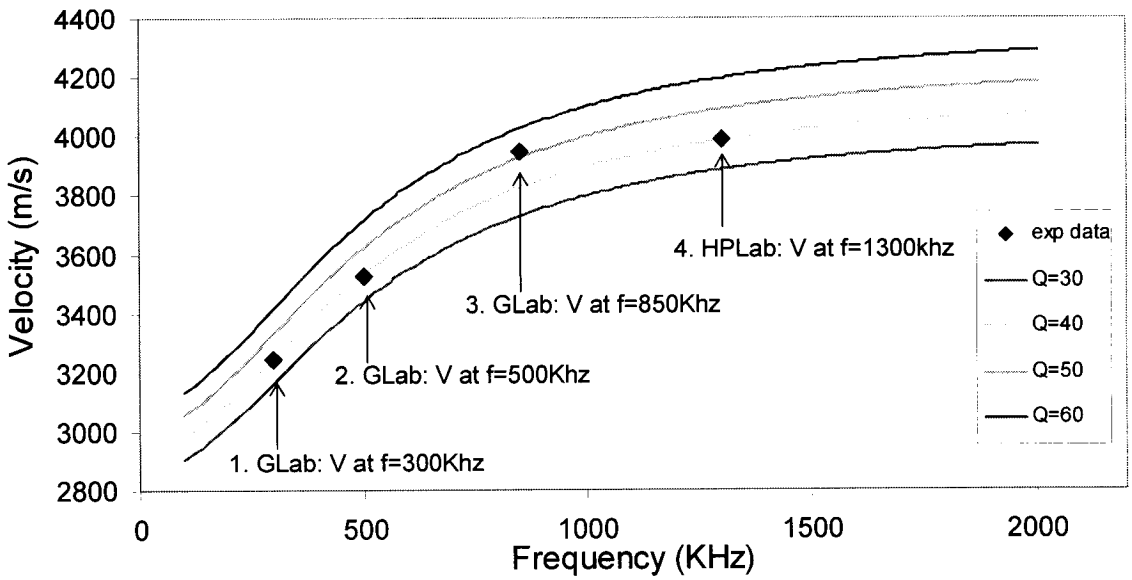

Figure 9.10: The measured velocities for the quartz sandstone using at 4 different dominant frequencies.

9.20 Other application of the dispersion model

As has been indicated above, imaging at high effective stress with attenuation, instead of velocity, offers more advantages in terms of sensitivity and response of stress to attenuation. However, measurement of attenuation is more difficult and uses many assumptions that give inaccurate value of Q. With the focus being on velocity data, there has been less attenuation data collected in the field. The potential for high-resolution attenuation imaging is evident in the laboratory under a controlled environment. However, there are many difficulties for direct measurements of attenuation in the field.

Of late, attenuation and velocity dispersion measurements in the field are growing rapidly with room for more advancement. One of the challenges is the frequency independence assumption when using the spectral ratios techniques. The insitu method of spectral ratios in estimating Q is based on the spectral ratios of signals recorded at two different stations of the same event. This ignores dispersion effect between the two stations, which can be in a high order of magnitude. The above developed model can be used to estimate Q by quantifying the attenuation effect due to dispersion, between these two stations, before the spectral ratio method is applied. Further research is needed to investigate this possibility.

9.21 Calibration, experimental errors and accuracy.

9.21.1 Velocity measurement

One possible source of error between the model and the experiments may be due to the techniques used to measure the arrival times. Our measurements of velocity were based on the pulse transmission technique by Birch 1960. This is the standard for laboratory acoustic velocity measurements. Generally, the elastic-wave velocities are determined by picking the time of a certain feature of a propagating pulse, such as the first amplitude maximum. However, as shown in our modeling results, attenuation and dispersion contribute to changing the shape of a propagating wave, making determination of a

physically meaningful velocity problematic. As a consequence, the velocities so determined are not necessarily representative of the material's intrinsic wave phase and group velocities and the associated quality factors. Wave velocities determined from the time at which the pulse was first detected (signal velocity) differ from the predominant group and phase velocities. At best, the onset wave velocity arguably provides a lower bound for the high-frequency limit of the phase velocity in a material where wave velocity increases with frequency. This may impact on our laboratory and model results. Further research is needed to investigate whether the observed arrival times versus the actual propagation time are in good agreement, especially in a highly dispersive medium.

9.21.2 Attenuation measurement and calculation

Measuring and calculating Q in the laboratory rely on the spectral ratio techniques originally proposed and introduced by Tosköz et al., 1979. This method utilizes the spectral amplitudes recorded by propagating a waveform through the sample and again through a non-attenuating reference sample with the same dimensions as the sample. This technique assumes frequency independence of Q so that, Q does not change over the frequency range of interest. This implies that there is no source of intrinsic energy dissipation such as friction or viscosity (attenuation) catered for in the spectral ratio model. Laboratory experiments on natural reservoir rocks (Frempong and Butt, 2004) have shown that different dispersion and attenuation mechanisms in the rocks caused by

intrinsic anelasticity and scattering, cause changes in velocities and attenuation which impact on the Q estimates. The accuracy of measuring Q across the frequency spectrum therefore depends on the dispersion characteristics of the waves and the nature of the rocks that disperse the waves. Thus alternative ways should be found for laboratory and field Q measurements, calculation methods, quantification of errors made using spectral ratio techniques and possible correction of spectral ratio derived Q.

9.22 The limitation of NSD model

The observed dispersion in the NSD is in the high frequency range (KHz to MHz). The dispersion model can not be applied directly to dispersion model in the Hz frequency range. Some authors have agued that the observed dispersion of the lower frequency range (Hz) is negligible in the field application (Tatham and McCormack, 1991). However the specific frequency limit where the observed dispersion appears to be negligible has not been specifically quantified. The changes in dispersion in the NSD model developed above can be extrapolated to lower frequency ranges if it is assumed that the change in dispersion with frequency is linear. Question arises about the validity of extrapolating velocity and attenuations measurements on rocks from these high frequency bad down into seismic frequency region. Again, the experimental multi-frequency data collected in the laboratory were in the upper frequency range (350KH to 1.5Mh) and therefore dispersion in the (Hz) frequency range has not been validated.

9.23 Recommendation and further studies

The research reveals many areas in reservoir engineering that needs to be studied further for thorough understanding and to validate some of the experimental methods and calculation techniques in acoustic imaging. Some of these areas have already been explained. The summary below gives areas that need further research:

(1) The need to investigate whether the observed arrival times versus the actual propagation time in a visco-elastic material are in good agreement, especially in a highly dispersive medium.

(2) The need to find alternative ways for laboratory and field measurements of Q, calculation methods, quantification of errors, and be used to validate the traditional spectral ratio technique, which assumes frequency independence.

(3) It is also recommended that similar research on scaling that uses wavelet transform instead of Fourier transform be undertaken to analyze the dispersion characteristics. The two results (from Fourier and Wavelet Transform) can then be compared with the laboratory results and uses the model of earth attenuation.

(4) Velocity is insensitive to changes in pressure at high pressures. This occurs at a depth of approximately 4km and beyond. Imaging with velocity beyond this point is very limited and presents challenges. New ways have to be explored for determining pore pressures changes in reservoirs.

9.24 Conclusions

The objectives of the project were to (i) investigate the factors that contribute to velocity dispersion across the frequency bands, and (ii) to develop practical scaling models and methodology that take into account intrinsic energy dissipation. This was accomplished through the development of a Numerical Spectral Discretization model (numerical discretization in Fourier domain) . The model uses spectral ratio techniques to break multi-frequency non linear waves into individual components. Frequency analyses shows that the problem of scaling is due to the different dispersion and attenuation mechanisms in the rocks caused by intrinsic anelasticity of the rock material, scattering, and diffraction. These mechanisms are responsible for the velocity disparities across the different frequency waves throughout the spectrum. The accuracy of measuring velocity across the frequency spectrum therefore depends on the dispersion characteristics of the waves and the nature of the rocks (modulus, density, saturation, etc) that disperse the waves. When normal dispersion occurs, the high frequency waves tend to travel faster than low frequency waves. Again the high frequency wave attenuate faster (travel at a

shorter distance) than the low frequency waves. The spectral discretization technique adopted in this research was able to decompose these traveling waves into the frequency domain. Thus, different frequency components were analyzed and accurate velocity differences quantified for a particular frequency. The model that was developed for the multi-frequency velocity analysis scales the velocities across the various frequency bands.

8APPENDIX 1: CONVERSION TABLES

A: Pressure Conversion tables

To convert	Into	Multiply by
atmosphere	bar	1.01295
atmosphere	dynes/cm^2	1.01295 x 10^6
atmosphere	in. Hg	29.9213
atmosphere	in. water	406.86
atmosphere	kg/cm^2	1.03325
atmosphere	mbar	1012.95
atmosphere	mtorr or micron Hg	7.6 x 10^5
atmosphere	Pa or N/m^2	1.01295 x 10^5
atmosphere	PSI or lb/in^2	14.696
atmosphere	torr or mm Hg	760
bar	atmosphere	0.9872
bar	dynes/cm^2	1 x 10^6
bar	in. Hg	29.54
bar	in. water	401.65
bar	kg/cm^2	1.02
bar	mbar	1000
bar	mtorr or micron Hg	7.5028 x 10^5
bar	Pa or N/m^2	1 x 105
bar	psi or lb/in^2	14.508
bar	torr or mm Hg	750.2838
dynes/cm^2	atmosphere	9.872 x 10^-7
dynes/cm^2	bar	1 x 10^-6
dynes/cm^2	in. Hg	2.954 x 10^-5
dynes/cm^2	in. water	4.0165 x 10^-4
dynes/cm^2	kg/cm^2	1.0200 x 10^-6
dynes/cm^2	mbar	1 x 10^-3
dynes/cm^2	mtorr or micron Hg	0.75028
dynes/cm^2	Pa or N/m^2	0.1
dynes/cm^2	psi or lb/in^2	1.4508 x 10^-5
dynes/cm^2	torr or mm Hg	7.5028 x 10^-4
in. Hg	atmosphere	3.342 x 10^-2
in. Hg	bar	3.385 x 10^-2
in. Hg	dynes/cm^2	3.385 x 10^4
in. Hg	in. water	13.598
in. Hg	kg/cm^2	3.4532 x 10^-2
in. Hg	mbar	33.85
in. Hg	mtorr or micron Hg	2.54 x 10^4
in. Hg	Pa or N/m^2	3385
in. Hg	psi or lb/in^2	0.4912
in. Hg	torr or mm Hg	25.4
in. water	atmosphere	2.458 x 10^-3
in. water	bar	2.489 x 10^-3
in. water	dynes/cm^2	2.489 x 10^-3
in. water	kg/cm^2	2.5396 x 10^-3
in. water	in. Hg	7.354 x 10^-2
in. water	mbar	2.489
in. water	mtorr or micron Hg	1.868 x 10^-3
in. water	Pa or N/m^2	248.9
in. water	psi or lb/in^2	3.612 x 10^-2
in. water	torr or mm Hg	1.868
kg/cm^2	atmosphere	0.9678
kg/cm^2	bar	0.9804
kg/cm^2	dynes/cm^2	9.804 x 10^5
kg/cm^2	in. Hg	28.958
kg/cm^2	in. water	393.76

To convert	Into	Multiply by
kg/cm^2	mbar	9.804 x 10^2
kg/cm^2	mtorr or micron Hg	7.3554 x 10^5
kg/cm^2	Pa or N/m^2	9.804 x 10^4
kg/cm^2	psi or lb/in^2	14.223
kg/cm^2	torr or mm Hg	7.3554 x 10^2
mbar	atmosphere	9.872 x 10^-4
mbar	bar	0.001
mbar	dynes/cm^2	1000
mbar	kg/cm^2	1.0200 x 10^-3
mbar	in. Hg	2.954 x 10^-2
mbar	in. water	0.4018
mbar	mtorr or micron Hg	7.5028 x 10^2
mbar	Pa or N/m^2	100
mbar	psi or lb/in^2	1.450 x 10^-2
mbar	torr or mm Hg	0.75028
mtorr or micron Hg	atmosphere	1.316 x 10^-6
mtorr or micron Hg	bar	1.3328 x 10^-6
mtorr or micron Hg	dynes/cm^2	1.3328
mtorr or micron Hg	kg/cm^2	1.3595 x 10^-6
mtorr or micron Hg	in. Hg	3.937 x 10^-5
mtorr or micron Hg	in. water	5.353 x 10^-4
mtorr or micron Hg	mbar	1.3328 x 10^-3
mtorr or micron Hg	Pa or N/m^2	0.13328
mtorr or micron Hg	psi or lb/in^2	1.934 x 10^-5
mtorr or micron Hg	torr or mm Hg	1 x 10^-3
Pa or N/m^2	atmosphere	9.869 x 10^-6
Pa or N/m^2	bar	1 x 10^-5
Pa or N/m^2	dynes/cm^2	10
Pa or N/m^2	kg/cm^2	1.020 x 10^-5
Pa or N/m^2	in. Hg	2.954 x 10^-4
Pa or N/m^2	in. water	4.018 x 10^-3
Pa or N/m^2	mbar	0.01
Pa or N/m^2	mtorr or micron Hg	7.5028
Pa or N/m^2	psi or lb/in^2	1.4508 x 10^-4
Pa or N/m^2	torr or mm Hg	7.5028 x 10^-3
psi or lb/in^2	atmosphere	0.06805
psi or lb/in^2	bar	0.06893
psi or lb/in^2	dynes/cm^2	6.8927 x 10^4
psi or lb/in^2	kg/cm^2	7.0309 x 10^-2
psi or lb/in^2	in. Hg	2.036
psi or lb/in^2	in. water	27.68
psi or lb/in^2	mbar	68.97
psi or lb/in^2	mtorr or micron Hg	5.171 x 10^4
psi or lb/in^2	Pa or N/m^2	6.8927 x 10^3
psi or lb/in^2	torr or mm Hg	51.71
torr or mm Hg	atmosphere	1.3158 x 10^-3
torr or mm Hg	bar	1.3328 x 10^-3
torr or mm Hg	dynes/cm^2	1.3328 x 10^-3
torr or mm Hg	kg/cm^2	1.3595 x 10^-3
torr or mm Hg	in. Hg	3.937 x 10^-2
torr or mm Hg	in. water	0.5353
torr or mm Hg	mbar	1.3328
torr or mm Hg	mtorr or micron Hg	1000
torr or mm Hg	Pa or N/m^2	133.28
torr or mm Hg	psi or lb/in^2	1.934 x 10^-2

B: Diffraction loss tables

Dimensionless distance (S)	A	B	Diffraction Loss	Diffraction Phase shift (rad)	Diffraction Attenuation (dB)
0.0	0.99675	0.03725	0.99745	0.03735	0.02221
0.2	0.89305	0.10881	0.89965	0.12124	0.91849
0.4	0.87209	0.15411	0.88560	0.17491	1.05523
0.6	0.81333	0.17044	0.83100	0.20657	1.60801
0.8	0.81433	0.19413	0.83715	0.23403	1.54395
1.0	0.77899	0.24387	0.81627	0.30339	1.76328
1.2	0.72890	0.25557	0.77240	0.33724	2.24312
1.4	0.70518	0.24706	0.74721	0.33699	2.53118
1.6	0.70436	0.24745	0.74656	0.33784	2.53871
1.8	0.70924	0.26480	0.75706	0.35733	2.41738
2.0	0.70839	0.29445	0.76714	0.39393	2.30247
2.2	0.69791	0.32916	0.77164	0.44070	2.25173
2.4	0.67836	0.36336	0.76955	0.49176	2.27528
2.6	0.65197	0.39383	0.76168	0.54340	2.36451
2.8	0.62120	0.41913	0.74937	0.59355	2.50609
3.0	0.58814	0.43897	0.73390	0.64117	2.68730
3.2	0.55439	0.45367	0.71635	0.68581	2.89749
3.4	0.52102	0.46382	0.69757	0.72738	3.12830
3.6	0.48877	0.47012	0.67817	0.76595	3.37328
3.8	0.45806	0.47321	0.65860	0.80167	3.62757
4.0	0.42913	0.47372	0.63918	0.83474	3.88747
4.2	0.40206	0.47214	0.62014	0.86539	4.15024
4.4	0.37687	0.46893	0.60160	0.89382	4.41380
4.6	0.35350	0.46445	0.58367	0.92022	4.67663
4.8	0.33187	0.45899	0.56640	0.94478	4.93758
5.0	0.31186	0.45280	0.54981	0.96766	5.19582

APPENDIX 2: ROCK SAMPLE DESCRIPTIONS

Geological classification of the rock samples used is important for interpretation of elastic wave propagation under varying pore pressure and effective stress conditions in the laboratory. Parameters such as mineralogy, grain size, and fabric are key factors when relating rock strength and stiffness to the nature of elastic wave propagation. These parameters are presented for the two types of natural rock samples used in the simulated production experiments. Inter-granular strength, cementation and pore structure have influences on wave velocity and attenuation as described in the literature review and discussion for each experiment. This section provides a more comprehensive geological reference for the natural sandstone samples used in the experiments.

The Glass Sand Unit

The Glass Sand Unit samples were taken from the abandoned Falls Brook Quarry on June 27th, 2003 near Windsor, Nova Scotia (Figure A1). This quarry was the first stop on The Society for Organic Petrology Annual Meeting Field Trip on the 29th and 30th of June 1998. This field trip specifically examined classic organic deposits of the Cumberland and Minas Basins of Nova Scotia and the geological information presented is taken in part from the Open File Report ME 1998-5 (Calder et al., 1998). Paul Frempong and Adam Donald gathered the rock samples with the help of Dr. Bob Ryan, Manager of Resource Evaluation Geological Services Division at the Nova Scotia Department of Natural Resources.

During the early 1930's in the Depression, the Glass Sand was quarried as a material for glass manufacturing, hence the name Glass Sand. This sandstone package is very consistent and may be traced for more than 30 km along strike. This interval is equivalent to the sandstone reservoir in the Mc Cully gas field of Sussex New Brunswick in what is called the Albert Formation. There have been long-producing oil and gas fields in the

Sussex area from this formation, giving reason to study this formation as it occurs as an over-pressured gas reservoir rock less than 100 km to the north.

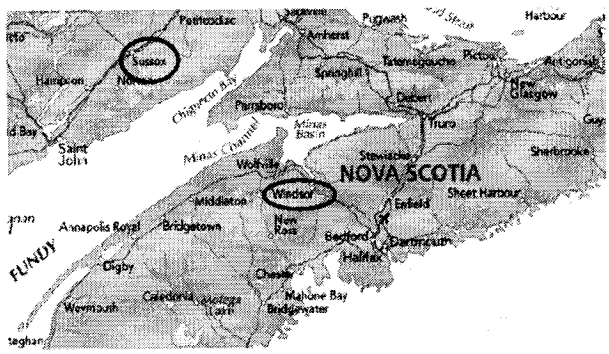

Figure A1: Map of the Minas Basin, the Falls Brook Quarry near Windsor outlined in red and the Sussex Gas Field outlined in blue.

Mineralogy and Grain Size

The Glass Sand unit is primarily comprised of quartz (>90%) with minor kaolinite (<5%), traces of pyrite and rock fragments (<1%). The evidence of pyrite is noticeable from the outcrop where oxidation of the iron may be seen (Figure A2). The outcrop samples appear to be fine grained (100-150 μm), uniform grain size, light brown in colour.

Figure A2: Close up picture of the Glass Sand outcrop

Photomicrographs of a typical sample are shown in Figures A3. The rock is well sorted and grain shape ranges from angular to sub-angular. Table A1 also shows the mineralogical and petrophysical properties.

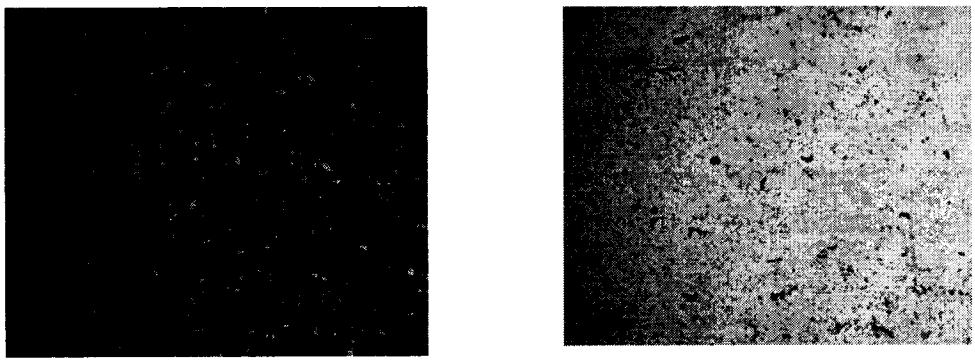

(a) Under cross polarized lens (XPL) (b)Under plane polarized lens (PPL)

Figure A3: Photomicrograph of natural sandstone

Table A1: Material properties

Mineralogy		**Petrophysics**	
Quartz	>90%	Porosity	15%
Kaolinite	<5%	Permeability	5-10mD
Prrite	<1%	Grain Size	100-150μm
Rock Fragment	<1%	Bulk Density	2.225g/cc

APPENDIX 3: SYNTHETIC SANDSTONE (ARTIFICIAL SANDSTONE) MANUFACTURE AND PROPERTIES

The sandstone from the field (Glass sandstone described earlier in Appendix 2) was supplemented with synthetic sandstone. This is to get a weakly-consolidated sandstones which are difficult to get from the field because of coring problems. Moreover, in the experimental studies, the use of consistent samples is preferable, increasing the likelihood that the results obtained would be reproducible in future or ongoing research and to use to validate the results from the natural rocks. For samples extracted from the quarries, a quick spatial change of physical and mechanical properties are common. This inconsistency usually introduces difficulties in the interpretation of the results. Therefore, it was decided to depend on both synthetic sandstone and natural samples that can closely represent sandstone formations therefore facilitating the control of important parameters and for validation.

Material Composition

The synthetic sandstone consists of sand, Portland cement, and water. The material composition contained a weight ratio of 0.11 for cement/sand, and 1.25 for water/cement. The grain size distribution of the sand used in sample making grain size distributions of the silica sand grains ranged between 100 to 1000 m as shown in Table A2 and Figure A3.

Table A2: Grain sizes of synthetic sand

US Sieve number/Size	Microns /diameter (mm)	Mass retained	Mass Passing	Percent finer by weight
20	0.84	0	1716.1	100.00
30	0.59	11.3	1704.8	99.34
40	0.42	367.3	1337.5	77.94
50	0.297	697.4	640.1	37.30
60	0.25	165.5	474.6	27.66
80	0.177	262.7	211.9	12.35
100	0.149	173.7	38.2	2.23
above 100		38.2	0.00	0.00
SUM		1716.1		
total mass			1716.1	

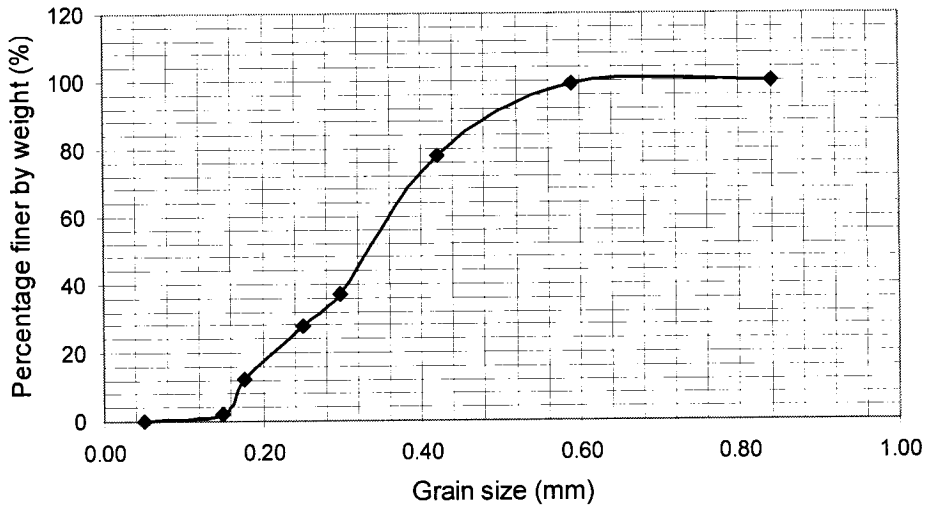

Figure A3: Grain size distributions of the sand used in synthetic samples

Qualitative description of the sand

Coefficient of curvature {Cc} is given by: D302(D10*D60)

Coefficient of uniformity {Cu} is given by:D60/D10

Where, D10, D60 and D30 are the diameter of the sand at 10, 60 and 30 percent point on the % finer verses size graph. From the graph, D10=0.170, D30=0.267, D60=0.360, Cc=1.16, Cu= 2.12 Based on these values the silica sand can be described as: clean sand, medium drained, It is not well graded because Cu less than 6 and Cc is about 1. It has much fines (it is a finer sand) and may exhibit some form of plasticity. The proportion of sand water and cement for the 3 different recipe used is given in table A3.

Table A3: Sample recipe

	Recipe 1(A)	Recipe 2(B)	Recipe 3(C)
Sand (% by weight)	79.55	82.55	76.55
Cement (% by weight)	9.09	6.09	12.09
Water (% by weight)	11.36	11.36	11.36
Total	100	100	100

Sample preparations

All samples were prepared by ASTM standards. Dry ingredients were mixed and water added and mixed to form the mortar paste. It was then caste in a cylindrical molds, Cylindrical, D/L ratio is ½, Leave them for 24 hours, Remove them from the mold, Keep them in water for 3 days to avoid cracks formation

Manufacturing Process

Sand, cement, and water are mixed into slurry, and then slightly pre-compacted when packed by a spatula into a mould and vibrated by gentle hits. To prevent the formation of distinct layers, the top of each layer was ploughed.

Casting of small solid samples was carried out in a cylindrical mould made of Playtex material. The internal diameter of the mould was 54 mm and the height was approximately 110 mm. Casting of HCS was performed in an aluminium mould with an 125 mm inside diameter, and a central rod which created the hole in the centre. After each casting (both small and large samples), the sample remained in the mould for 3 days. It was then taken out of the mould and put in water for 18 days at ambient temperature. After this, the sample was put in an oven set to 50oC. All of the samples were ground at both ends. For the HCS, epoxy was applied in order to make a stiff smooth cap at each end. The samples were kept dry in the oven and saturated before the start of each experiment.

Stringent quality control was implemented during the casting to obtain uniform material properties in each sample, as well as from one sample to another. The process of sample making was consistent for all samples in order to make sure that they would provide reproducible results.

Material Properties

The synthetic sandstone was described for both physical and mechanical properties. For the mechanical description, Unconfined Compressive Strength (UCS), was considered. UCS is a conventional strength indicator. Tables A4, A5 and A6 give the ultrasonic, geomechanics and petrophysical properties of the sandstone.

Table A4: Ultrasonic

	Ultrasonics					
Sample	V_p(m/s)	V_s(m/s)	$E_{dynamic}$ (GPa)	$\nu_{dynamic}$	G_d (GPa)	K_d (GPa)
Synthetic-2 (B)	1874.00	1288.00	5.3770	0.0523	2.5548	2.0019
Synthetic-1 (A)	2290.00	1540.00	8.1477	0.0872	3.7471	3.2895
Synthetic-3 (C)	2922.00	1952.00	14.0449	0.0970	6.4013	5.8089
Quartz Sandstone	2868.00	1975.00	18.4954	0.0490	8.8154	6.8356

Table A5: Geomechanics

	Geomechanics					
Sample	UCS (MPa)	E_{static} (GPa)	ν_{static}	G_s (GPa)	K_s (GPa)	ρ (g/cm^3)
Synthetic-2 (B)	1.6000	0.2158	0.3300	0.0811	0.0637	1.5400
Synthetic-1 (A)	4.3600	0.6949	0.3600	0.2555	0.3475	1.5800
Synthetic-3 (C)	6.7500	0.7355	0.4100	0.2608	0.3678	1.6800
Quartz Sandstone	100.0000	5.4000	0.3000	2.0769	4.5000	2.2600

Table A6: Petrophysics

		Petrophysics	
Sample	Geological Description	Permeability k (mD)	Porosity f (%)
Synthetic-2 (B)	Silica Sand, Portland Cement, Water, S/W/C: 83/6/11	**	40
Synthetic-1 (A)	Silica Sand, Portland Cement, Water, S/W/C: 80/9/19	255	36
Synthetic-3 (C)	Silica Sand, Portland Cement, Water, S/W/C: 77/12/11	36	34
Glass Sandstone	Fined grained, consistent, trace pyrite, minor kaolinite	3.9	15

APPENDIX 4: EQUIPMENT DESIGN

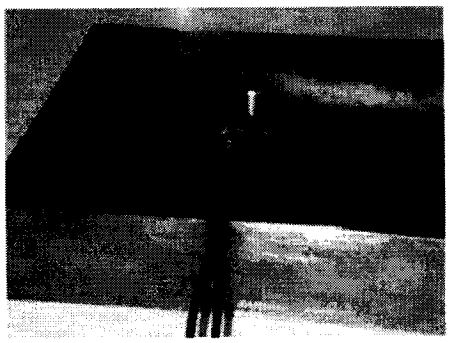

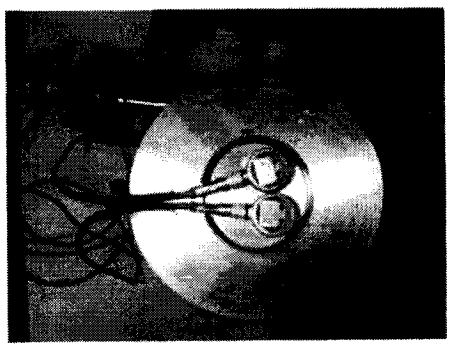

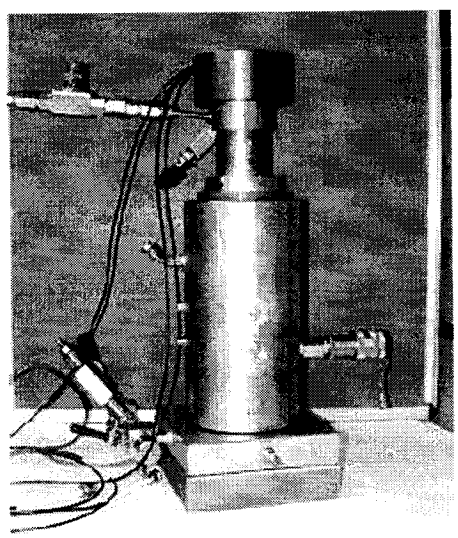

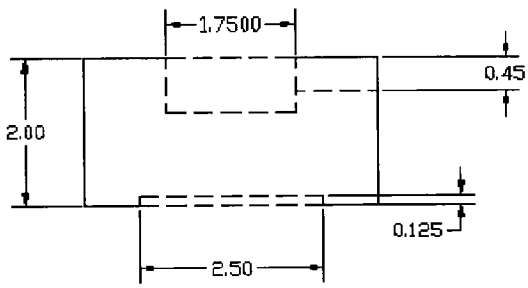

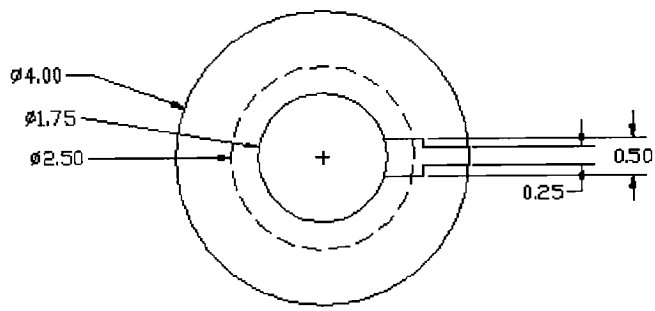

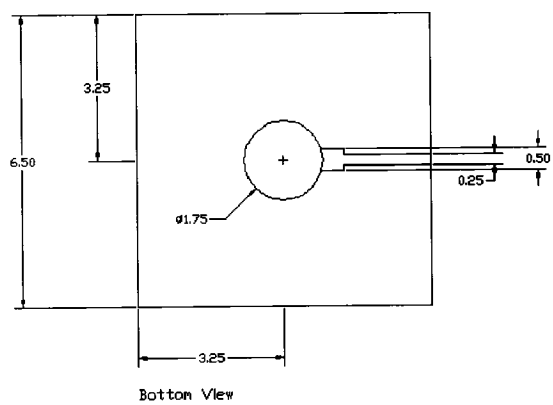

Figure A4: Equipment design

Design parameters

a. 4140 HR steel
b. Top platen 2" thick, with gradations marked to measure angles•
c. Bottom platen 1.5" thick
d. Reflection coefficient less than 1% between platens and triaxial cell•
e. Machining by D. Adams
f. 1 MHz central frequency
g. –P&S transducers
h 17.8 mm diameter,
i. 15.3 mm height
j. Ceramic face
k. Epoxy used for attaching inside the cavity

APPENDIX 5: CLASSES OF ANISOTROPY

The non zero components of the more symmetric anisotropy classes commonly used in modeling rock properties are given below.

1. Isotropic with two independent constant

$$\begin{bmatrix} c_{11} & c_{12} & c_{12} & 0 & 0 & 0 \\ c_{12} & c_{11} & c_{12} & 0 & 0 & 0 \\ c_{12} & c_{12} & c_{11} & 0 & 0 & 0 \\ 0 & 0 & 0 & c_{44} & 0 & 0 \\ 0 & 0 & 0 & 0 & c_{44} & 0 \\ 0 & 0 & 0 & 0 & 0 & c_{44} \end{bmatrix} \quad c_{12} = c_{11} - 2c_{44}$$

The relations between the elements c and Lame's constant λ and μ of isotropic lenera elasticity are

$C_{11} = \lambda + 2\mu$

$C_{12} = \lambda$

$C_{44} = \mu$

2. Cubic with three independent constants

$$\begin{bmatrix} c_{11} & c_{12} & c_{12} & 0 & 0 & 0 \\ c_{12} & c_{11} & c_{12} & 0 & 0 & 0 \\ c_{12} & c_{12} & c_{11} & 0 & 0 & 0 \\ 0 & 0 & 0 & c_{44} & 0 & 0 \\ 0 & 0 & 0 & 0 & c_{44} & 0 \\ 0 & 0 & 0 & 0 & 0 & c_{44} \end{bmatrix}$$

3. Hexagonal or transversely isotropic with five independent constants

$$\begin{bmatrix} c_{11} & c_{12} & c_{13} & 0 & 0 & 0 \\ c_{12} & c_{11} & c_{13} & 0 & 0 & 0 \\ c_{13} & c_{13} & c_{33} & 0 & 0 & 0 \\ 0 & 0 & 0 & c_{44} & 0 & 0 \\ 0 & 0 & 0 & 0 & c_{44} & 0 \\ 0 & 0 & 0 & 0 & 0 & c_{66} \end{bmatrix}$$

c66 =½(c11-c12)

4. Orthorhombic with 9 independent constants

$$\begin{bmatrix} c_{11} & c_{12} & c_{13} & 0 & 0 & 0 \\ c_{12} & c_{22} & c_{23} & 0 & 0 & 0 \\ c_{13} & c_{23} & c_{33} & 0 & 0 & 0 \\ 0 & 0 & 0 & c_{44} & 0 & 0 \\ 0 & 0 & 0 & 0 & c_{55} & 0 \\ 0 & 0 & 0 & 0 & 0 & c_{66} \end{bmatrix}$$

For isotropic symmetry, the phase velocity of wave propagation is given by

$$V_P = \sqrt{\frac{c_{11}}{\rho}} = \sqrt{\frac{\lambda + 2\mu}{\rho}}$$

$$V_S = \sqrt{\frac{c_{44}}{\rho}} = \sqrt{\frac{\mu}{\rho}}$$

c11 =λ+2μ

c12= λ

c44=μ

APPENDIX 6: SCALING MODELS

A Effective Medium Theory

For a wave propagating in a stratified media in the long wavelength limit, the stratified medium behaves as a homogenous effective medium with velocity given by the effective medium as:

$$V_{ENT} = (\frac{M_{EMT}}{\rho_{ave}})^{\frac{1}{2}}$$

The effective modulus M_{EMT} is from Backus average.

$$M_{EMT} = [\sum_k \frac{f_k}{M_K}]^{-1}$$

$$\frac{1}{\rho_{ave} V_{EMT}^{\ 2}} = \sum_k \frac{f_k}{\rho_k V_K^{\ 2}}$$

$$\rho_{ave} = \sum_k f_k \rho_k$$

where f_k ρ_k M_k and V_k are the Volume fractions, densities, Moduli and velocities of each constituent layer

B Ray theory

In the short wave length limit or ray theory limit the velocity is given by a harmonic average

$$\frac{1}{V_{RT}} = \sum_k \frac{f_k}{V_k}$$

The ray theory involves averaging slowness whereas effective medium theory involves averaging slowness squared. The result is that V_{RT} is always faster than V_{EMT}

C. Backus average

Backus showed that in the long wavelength limit, a stratified medium composed of layers of transversely isotropic materials (each with its symmetry axis normal to the strata) is also effectively isotropic. By far the most accepted laboratory-field scaling acoustic imaging model with practical application and value is the Backus averaging and filtering. Backus showed that in the long wavelength limit, ($\lambda/a>>1$) a stratified medium composed of layers of transversely isotropic materials (each with its symmetry axis normal to the strata) is also effectively isotropic with effective stiffness given by the matrix in Figure A5b, as opposed to matrix in Figure A5a, for a non scaled model. These matrices give the elastic stiffness tensor or modulus of elasticity of a transversely isotropic medium with the symmetry axis and all the other orientation. The relationship between this tensor and the tensor that Backus averaging uses is given in figure A5a and A5b. The values in the tensor matrix are basically the modulus of the formation and are based on the crystalline nature of the material involved This tensor controls the velocity in each of the foliated medium which according to Backus is considered one medium called effective medium. It is used to model a finely stratified medium as a single homogeneous medium. (i.e. deals with finely layered media)

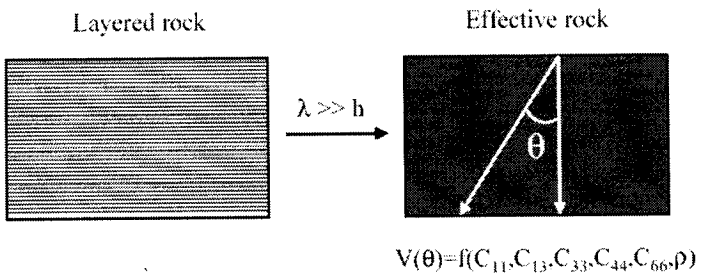

$$\begin{pmatrix} a & b & f & 0 & 0 & 0 \\ b & a & f & 0 & 0 & 0 \\ f & f & c & 0 & 0 & 0 \\ 0 & 0 & 0 & d & 0 & 0 \\ 0 & 0 & 0 & 0 & d & 0 \\ 0 & 0 & 0 & 0 & 0 & m \end{pmatrix} \Rightarrow \begin{pmatrix} A & B & F & 0 & 0 & 0 \\ B & A & F & 0 & 0 & 0 \\ F & F & C & 0 & 0 & 0 \\ 0 & 0 & 0 & D & 0 & 0 \\ 0 & 0 & 0 & 0 & D & 0 \\ 0 & 0 & 0 & 0 & 0 & M \end{pmatrix}$$

Figure A5a: Original matrix

Figure A5b: scaled matrix

$$A = \left\langle a - f^2 c^{-1} \right\rangle + \left\langle c^{-1} \right\rangle^{-1} \left\langle f c^{-1} \right\rangle^2$$

$$B = \left\langle B - f^2 c^{-1} \right\rangle + \left\langle c^{-1} \right\rangle^{-1} \left\langle f c^{-1} \right\rangle^2$$

$$C = \left\langle c^{-1} \right\rangle^{-1}$$

$$F = \left\langle c^{-1} \right\rangle^{-1} \left\langle f c^{-1} \right\rangle$$

$$D = \left\langle d^{-1} \right\rangle^{-1}$$

$$D = \langle m \rangle$$

$a = c = \lambda + 2\mu$
$b = f = \lambda$
$d = m = \mu$

$\langle \, . \, \rangle$ averages weighted by their volumetric proportions

$$A = \left\langle \frac{4\mu(\lambda+\mu)}{\lambda+\mu} \right\rangle + \left\langle \frac{1}{\lambda+2\mu} \right\rangle^{-1} \left\langle \frac{\lambda}{\lambda+2\mu} \right\rangle^{2}$$

$$B = \left\langle \frac{2\mu\lambda}{\lambda+2\mu} \right\rangle + \left\langle \frac{1}{\lambda+2\mu} \right\rangle^{-1} \left\langle \frac{\lambda}{\lambda+2\mu} \right\rangle^{2}$$

$$C = \left\langle \frac{1}{\lambda+2\mu} \right\rangle^{-1}$$

$$F = \left\langle \frac{1}{\lambda+2\mu} \right\rangle^{-1} \left\langle \frac{\lambda}{\lambda+2\mu} \right\rangle$$

$$D = \left\langle \frac{1}{\mu} \right\rangle^{-1}$$

$$M = \langle \mu \rangle$$

In terms of P and S waves, the effective medium in isotropic media of every thing layer is:

$$a = \rho V_P{}^2$$
$$d = \rho V_S{}^2$$
$$a = \rho(V_P{}^2 - V_S{}^2)$$

$$A = \left\langle 4\rho V_S{}^2 [1 - \frac{V_S{}^2}{V_P{}^2}] \right\rangle + \left\langle 1 - 2\frac{V_S{}^2}{V_P{}^2} \right\rangle^2 \left\langle (\rho V_P{}^2)^{-1} \right\rangle^{-1}$$

$$B = \left\langle 2\rho V_S{}^2 [1 - \frac{V_S{}^2}{V_P{}^2}] \right\rangle + \left\langle 1 - 2\frac{V_S{}^2}{V_P{}^2} \right\rangle^2 \left\langle (\rho V_P{}^2)^{-1} \right\rangle^{-1}$$

$$C = \left\langle (\rho V_P{}^2)^{-1} \right\rangle^{-1}$$

$$F = \left\langle 1 - 2\frac{V_S{}^2}{V_P{}^2} \right\rangle^2 \left\langle (\rho V_P{}^2)^{-1} \right\rangle^{-1}$$

$$D = \left\langle (\rho V_P{}^2)^{-1} \right\rangle^{-1}$$

$$M = \left\langle \rho V_S{}^2 \right\rangle$$

Horizontally and vertically propagating waves

$$V_{SH,h} = \sqrt{\frac{M}{\rho}}$$

$$V_{SH,v} = V_{SH,h} = V_{SV,v} = \sqrt{\frac{D}{\rho}}$$

Horizontally and vertically polarized waves

$$V_{P,h} = \sqrt{\frac{A}{\rho}}$$

$$V_{P,v} = \sqrt{\frac{C}{\rho}}$$

Thus the general expressions for velocity are:

$$V_S = \sqrt{\frac{\mu}{\rho}} \qquad V_P = \sqrt{\frac{K + \frac{4}{3}\mu}{\rho}}$$

Using this Backus averaging methodology, one would be able to quantify:

- vertically propagating P waves,
- horizontally propagating P waves,
- horizontally propagation, horizontally polarized P waves,
- horizontally propagating vertically polarized S waves
- vertically propagating horizontally polarized S waves
- Vertically propagating vertically polarized S waves and in fact velocity in any direction and orientation.

This is a classic method and has been working fairly well and very applicable. However it has got some shortcomings and limitations, which are explained in the next section.

APPENDIX 7: DERIVATION OF THE WAVE EQUATION

The physics that describes the general wave equation in three dimensions is given by:

$$\frac{\partial^2 u}{\partial x^2}(x,t) + \frac{\partial^2 u}{\partial y^2}(x,t) + \frac{\partial^2 u}{\partial z^2}(x,t) = \frac{1}{C^2}\frac{\partial^2 u}{\partial t^2}(x,t) \qquad (1)$$

Where $u(x,t)$ is the vibration amplitude describing the to and fro microscopic particle movements in the medium, t is the time of wave energy travel and x y and z are the distances along the three directions in the medium that the wave energy travels. The essential feature of the wave motion is the transmission of energy without the transmission of matter. This basic wave equation is a linear differential equation which means, for example, that the amplitude of say two of such waves interacting is simply the sum of the waves. This also means that a behavior of a wave can be analyzed by breaking up the wave into components and this is the basis of Fourier transform. The Fourier transform breaks up a wave into sinusoidal components and is useful for analyzing the wave equation.

But the linear nature of the wave (equation 1) is a very simplistic view of the real world situation. In the derivation of this wave equation many assumptions were made to make it simple and linear so that it can be solved in easy terms. In order to see the assumptions made, the wave equation above is derived below from first principles.

1.1 Derivation of the fundamental wave equation

The wave equation is derived from two basic fundamental laws (1) Conservation of energy and (2) Newton second law of motion (law of momentum). The one-dimensional form of the wave equation can be derived from considering a flexible string, stretched between two points P an Q on x-axis as below (Figure A6 a and b).

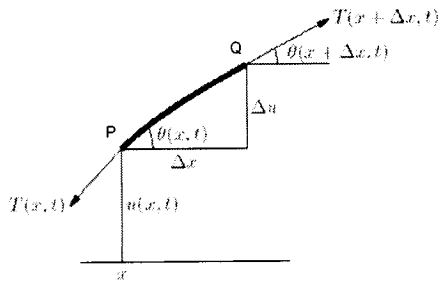

Figure A6a: Stretched string used in deriving the wave equation

The diagram above (figure 1) shows a string stretched by two tensions and it is allowed to vibrate freely producing a wave along the x axis. The notations in the diagram are:

$u(x, t)$ = vertical displacement of the string from the x axis at position x and time t

$\theta(x, t)$ = angle between the string and a horizontal line at position x and time t

$T(x, t)$ = tension in the string at position x and time t

$\rho(x)$ = mass density of the string at position x

The forces acting on the tiny element of string PQ are;

(a) The tension pulling to the right, which has magnitude $T(x+\Delta x, t)$ and acts at an angle $\theta(x+\Delta x, t)$ above horizontal

(b) The tension pulling to the left, which has magnitude, $T(x, t)$ and acts at an angle $\theta(x, t)$, below the horizontal. To derive the wave equation from this string, four basic simplifying assumptions are made:

1.2 Four basic assumptions made in the derivation of the wave equation

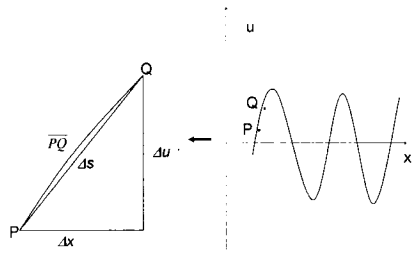

Figure A6b: Stretched string used in deriving the wave equation (details)

(A) Assumption 1

The density of the material through which the wave travels (in this case, the string), ρ, is constant so that the mass of the string between two points say P and Q is simply ρ times the length of the material (string) between P and Q, Thus mass of material (m) is:

m = $\overline{PQ}$ * ρ

(B) Assumption 2

The displacement, $u(x,t)$, and its derivatives are assumed small so that these geometric approximations can be made:

a. $\overline{PQ} \approx \Delta s$

b. $\Delta s \approx \Delta x$

c. $\frac{\Delta u}{\Delta x} \approx \frac{\partial u}{\partial x}$

d. $(\frac{\partial u}{\partial x})^2 \approx 0$

(e) The mass of the portion of the spring is therefore $\rho \Delta s$

but, $\Delta s = \sqrt{(\Delta x)^2 + (\Delta u)^2} = \Delta x \sqrt{(\frac{\Delta u}{\Delta x})^2} \approx \Delta x \sqrt{1 + (\frac{\partial u}{\partial x})^2}$

Thus mass = $\rho \Delta s \approx \rho \Delta x$

(C) Assumption 3

All external forces including gravitational force and frictional forces are neglected. Thus when the wave is moving, the only force acting on this portion of the string are the tensions, $T(x,t)$ at P and $T(x+\Delta x,t)$ at Q.

(D) Assumption 4

The motion of a particle in the medium is purely vertical. There is no horizontal motion of any portion of the string or the medium

1.3 Derivation of the wave equation with these assumptions

Now considering the forces acting on the typical string portion shown in Figure 1, Tension acts tangential to the string and the gradient of the tangent is, the slope of u(x,t) or simply du/dt . Resolving the forces into their horizontal and vertical components, would give:

(a) Horizontal Forces: At P, the tension force is $T_1Cos\theta_1$ and it acts to the left, whereas at Q the force is $T_2Cos\theta_2$, acting to the right. Since there is no horizontal motion, these forces must balance and so

$T_1Cos\theta_1 = T_2Cos\theta_2 = T = \text{constant}$ (2)

(b) Vertical Forces: From the figure (figure 1) it is clear that the vertical force at Q is $T_2Sin\theta_2$ *and at P is* $-T_1Sin\theta_1$.

Using these two forces and considering Newton second law of motion, (The rate of change of momentum is proportional to the applied force and it takes place in the direction of the force) then,

Mass * Acceleration = Force acting on the body. So that

$$\rho\Delta x\frac{\partial^2 u}{\partial t^2} = T_2 Sin\theta_2 - T_1 Sin\theta_1 \tag{3}$$

Divide by T and substitute the horizontal forces (equation 2), it implies that

$$\frac{\rho\Delta x}{T}\frac{\partial^2 u}{\partial t^2} = \frac{T_2 Sin\theta_2}{T_2 Cos\theta_2} - \frac{T_1 Sin\theta_1}{T_1 Cos\theta_1} = \tan\theta_2 - \tan\theta_1 \tag{4}$$

But $\tan\theta_2$ is the gradient of the tangent of *u(x,t) at* $x=x+\Delta x$ and this is just

$$\left(\frac{\partial u}{\partial x}\right)_{x+\Delta x} \tag{5}$$

In similar manner $\tan\theta_1$ is the gradient of the tangent of *u(x,t)* at x and is given by:

$$\left(\frac{\partial u}{\partial x}\right)_{x} \tag{6}$$

Substitute equation 5 and 6 into equation 4 gives

$$\frac{\rho}{T}\frac{\partial^2 u}{\partial t^2} = \frac{1}{\Delta x}\left[\left(\frac{\partial u}{\partial x}\right)_{x+\Delta x} - \left(\frac{\partial u}{\partial x}\right)_{x}\right] \tag{7}$$

Using the definition of derivative, and taking limits as Δx goes to zero, implies that

$$\Delta x \xrightarrow{\lim} 0\left\{\frac{f(x+\Delta x)-f(x)}{\Delta x}\right\}$$

$$\frac{\rho}{T}\frac{\partial^2 u}{\partial t^2} = \frac{\partial^2 u}{\partial x^2} \tag{8}$$

Therefore

$$\frac{\partial^2 u}{\partial x^2} = \frac{1}{c^2}\frac{\partial^2 u}{\partial t^2} \tag{9}$$

where, $c=T/\rho$ the tension divided by the density, is the wave speed.

Equation 9 is one dimensional wave equation and it is a linear equation made possible because of the four assumptions listed above in its derivation. It is normally called the equation of vibrating string. It propagates along a particular axis with a constant speed c independent of direction.

APPENDIX 8: FINITE DIFFERENCE MODELING

Introduction to numerical modeling and its application to the wave equation using finite difference methods

1. Chaos

A state of extreme confusion and disorder

2 The real world situation

In the real world of science, there is nothing like chaos, randomness, noise, disorder etc. Rather, scale effect has blurred understanding in the orderly manner of processes of natural phenomenon. Every phenomenon is orderly structured and could be described by some sort of relationship between two or more changing variables, for example:
Heat flow in a metal bar
Wave motion in a rock medium
Diffusion of gas in a another gas
Movement of a butterfly in air

3. Simple relationships

Variable x relates directly to variable y

$$y = x \qquad y = 2x \qquad y = 5x^2 \qquad y = y^{-1/2}x^2$$

The rate at which y and x are changing relates with original variables x and y

$$\frac{dy}{dx} = yx \qquad \frac{dy}{dt} = y\frac{dx}{dt}$$

4 Complex relationships

The mathematics of these phenomenon can generally be described with the ordinary differential equations of the variables consisting of the the phenomenon

$$\frac{\partial^2 u}{\partial x^2}(x,t)+\frac{Kr}{\rho C}=K\frac{\partial u}{\partial t}(x,t) \qquad \text{Heat equation}$$

$$\frac{\partial u}{\partial t}(x,t)-\frac{\partial^2 u}{\partial x^2}(x,t)=0 \qquad \text{Diffusion equation}$$

$$\frac{\partial^2 u}{\partial x^2}+\frac{\partial^2 u}{\partial y^2}+\frac{\partial^2 u}{\partial z^2}=\frac{1}{C^2}\frac{\partial^2 u}{\partial t^2} \qquad \text{Wave equation}$$

5 Simple theories exist to solve these simple phenomenon

The first-order (integrating factor)
The integral transforms such as the Laplace transform
The second-order (Sturm-Liouville theory)
These techniques are called analytical solutions of the phenomenon

6 Numerical models

While there are many general techniques for analytically solving classes of ODEs, the only practical solution technique for complicated equations is to use numerical methods when all else fails (which it frequently does)--numerical methods such as finite differences becomes the only practical way to solve the problem.

7 What are numerical methods?

Numerical methods are approximation techniques therefore no better than analytical models. So, if one can solve an equation analytically there is really no advantage in going through numerical methods.

8 What is numerical model

It is a technique where methods are found to break down the original problem into smaller pieces (discretization) and approximate it with the solution of the broken pieces Therefore numerical model is a discretization and approximation technique to solve a complex mathematical equation

9. Implementation techniques

Two implementation techniques are involved in numerical modeling
Discretization techniques (these are physical division of the problem)
Approximation techniques (mathematical procedures to bring the solution of the broken pieces together ie. averaging)

10. Spatial Discretization methods and techniques

Finite element methods
Finite difference methods
Boundary element methods
Finite volume methods
Spectral methods
Mesh free method

11. Approximation techniques

Euler's methods
Taylor's methods
Runge Kutta Formula
Heuns methods
Adams Bashforth methods

Adam Moulton methods

Extrapolation methods

Mid point methods

Trapezium methods

Simpson methods

Galerkin Methods

Colocation methods

12 Finite Difference methods

This is a method where differentiation or differential equation is replaced by a finite difference

$$\frac{\partial u}{\partial x}(x_i, t_j) \approx \frac{u(x_i, t_j + k) - u(x_i, t_j)}{k}$$

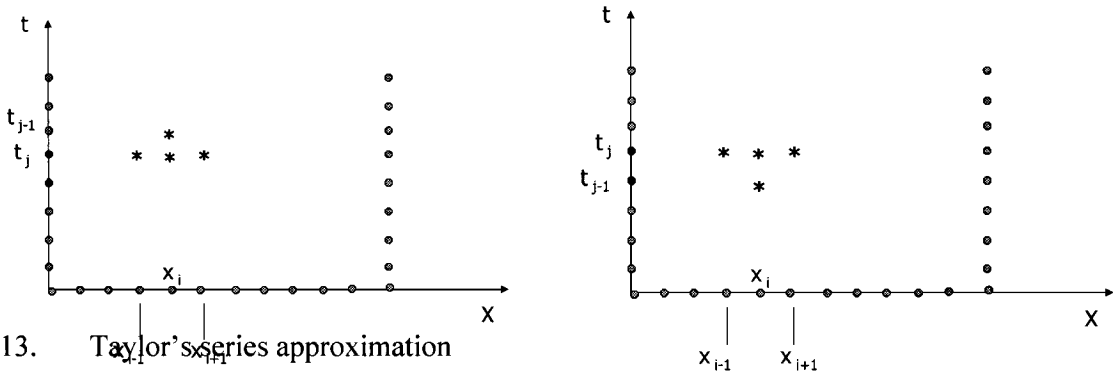

13. Taylor's series approximation

Taylor's expansion is used to express the partial derivative algebraic expansion say f(a) using backward or forward difference

$$f(a+h) = f(a) + \frac{f'(a)h}{1!} + \frac{f''(a)h^2}{2!} + \frac{f'''(a)h^3}{3!} + \frac{f''''(a)h^4}{4!} + \ldots\ldots$$

For example

$$\frac{\partial^2 u}{\partial t^2}(x_i, t_j) \approx \frac{u(x_i, t_{j+1}) - 2u(x_i, t_j) + u(x_i, t_{j-1})}{k^2} - \frac{k^2}{12}\frac{\partial^4 u}{\partial t^4}(x_i, \mu_j)$$

$$\frac{\partial u}{\partial x}(x_i, t_j) \approx \frac{u(x_i, t_j + k) - u(x_i, t_j)}{k} - \frac{k}{2}\frac{\partial^2 u}{\partial t^2}(x_i, \mu_j)$$

14. Implicit versus explicit conditions

Direct computation of dependant variable from known quantities (explicit)

Dependent variables are defined by coupled sets of equations, and either a matrix or iterative technique is needed to obtain the solution (implicit)

15. Numerical stability and accuracy

Whether explicit or implicit has to do with two considerations

numerical stability

numerical accuracy

Numerical stability is the behavior of the solution as the time-step dt is increased.

If the solution remains well behaved for arbitrarily large values of the time step, the method is said to be unconditionally stable. This situation never occurs with explicit methods, which are always conditionally stable

16. Boundary and initial conditions

A set of mathematical conditions to be satisfied, in the solution of a differential equation, at the edges or physical boundaries. The nature of these conditions usually is determined by the physical nature of the problem or the physical conditions at the boundaries of a system

17. Standard mathematical models of physical phenomenon in numerical analysis

Most of the standard mathematical models describing most physical phenomenon have already been established
hyperbolic models ie. Laplace equation
parabolic model/ equation
elliptical models ie. poisson equation

18. From physical phenomenon to mathematical description

$$\frac{\partial^2 u}{\partial x^2}+\frac{\partial^2 u}{\partial y^2}+\frac{\partial^2 u}{\partial z^2}=\frac{1}{C^2}\frac{\partial^2 u}{\partial t^2}$$

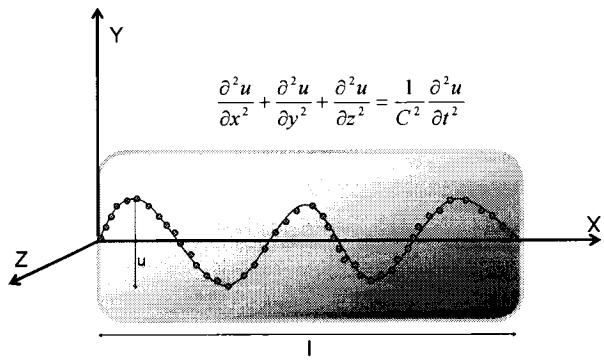

19. One dimensional case

$$\frac{\partial^2 u}{\partial t^2}(x,t) = C^2 \frac{\partial^2 u}{\partial x^2}(x,t)$$

Boundary and initial conditions are

$$u(0,t) = 0 \qquad u(l,t) = 0 \qquad \text{for} \qquad t > 0$$

$$u(x,t) = f(x) \qquad \frac{\partial u}{\partial t}(x,0) = g(x) \qquad \text{for} \qquad 0 \le x \le l$$

$$m > 0 \qquad h = \frac{l}{m} \qquad \text{Time step = k where } k > 0$$

$$(x_i, t_j) \qquad x_i = ih \qquad t_i = jk$$

From Taylor's expansion

$$\frac{\partial^2 u}{\partial x^2}(x_i,t_j) = \frac{u(x_{i+1},t_j) - 2u(x_i,t_j) + u(x_{i-1},t_j)}{h^2}$$

$$\frac{\partial^2 u}{\partial t^2}(x_i,t_j) = \frac{u(x_i,t_{j+1}) - 2u(x_i,t_j) + u(x_i,t_{j-1})}{k^2}$$

By substitution into the wave equation implies that,

$$\frac{u(x_i,t_{j+1}) - 2u(x_i,t_j) + u(x_i,t_{j-1})}{k^2} - \alpha^2 \frac{u(x_{i+1},t_j) - 2u(x_i,t_j) + u(x_{i-1},t_j)}{h^2} = 0$$

This leads to the difference equation by neglecting the error term

$$\frac{w_{i,j+1} - 2w_{ij} + w_{i,j-1}}{k^2} - \alpha^2 \frac{w_{i+1,j} - 2w_{ij} + w_{i-1,j}}{h^2} = 0$$

With $\lambda = \alpha k/h$ we can solve for $W_{i,j+k}$ the most advance time step approximation, to obtain:

$$w_{i,j+1} = 2(1-\lambda^2)w_{ij} + \lambda^2 (w_{i+1,j} + w_{i-1,j}) - w_{i,j-1}$$

Writing these set of equations in matrix form give:

The equation holds for i = 1, 2, 3, ...(m-1) and j = 1, 2, 3, ...

The boundary conditions give $w_{oj} = w_{mj} = 0$

For each j = 1, 2, 3, ...

And the initial conditions implies that $w_{io} = f(x_i)$

For each I = 1, 2, 3 ....m-1

$$\begin{bmatrix} w_{1,j+1} \\ w_{2,j+1} \\ . \\ . \\ w_{m-1,j+1} \end{bmatrix} = \begin{bmatrix} 2(1-\lambda^2) & \lambda^2 & 0 & . & 0 \\ \lambda^2 & 2(1-\lambda^2) & \lambda^2 & & \\ 0 & & & & 0 \\ . & & & & \lambda^2 \\ 0 & & 0 & \lambda^2 & 2(1-\lambda^2) \end{bmatrix} * \begin{bmatrix} w_{1,j} \\ w_{2,j} \\ . \\ . \\ w_{m-1,j} \end{bmatrix} - \begin{bmatrix} w_{1,j-1} \\ w_{2,j-1} \\ . \\ . \\ w_{m-1,j-1} \end{bmatrix}$$

The matrix is then coded in a small fortran/matlab/excel macro/Maple/Visual Basic etc. for values of wi

For the program, matlab was used and following initialized parameters were employed m=10, Bound = 2, h =0.1, k = 0.05,

$\lambda = 1$ $\quad u(x,t) = Sin\pi x Cos 2\pi x$

20. Results of the finite difference modelling

Xi	wi , 20
0.0	0.0000000000000
0.1	0.3090169944000
0.2	0.5877852523000
0.3	0.8090169944000
0.4	0.9510565163000
0.5	1.0000000000000
0.6	0.9510565163000
0.7	0.8090169944000
0.8	0.5877852523000
0.9	0.3090169944000
1.0	0.0000000000000
1.1	-0.3090169944000
1.2	-0.5877852523000
1.3	-0.8090169944000
1.4	-0.9510565163000
1.5	-1.0000000000000
1.6	-0.9510565163000
1.7	-0.8090169944000
1.8	-0.5877852523000
1.9	-0.3090169944000
2.0	0.0000000000000

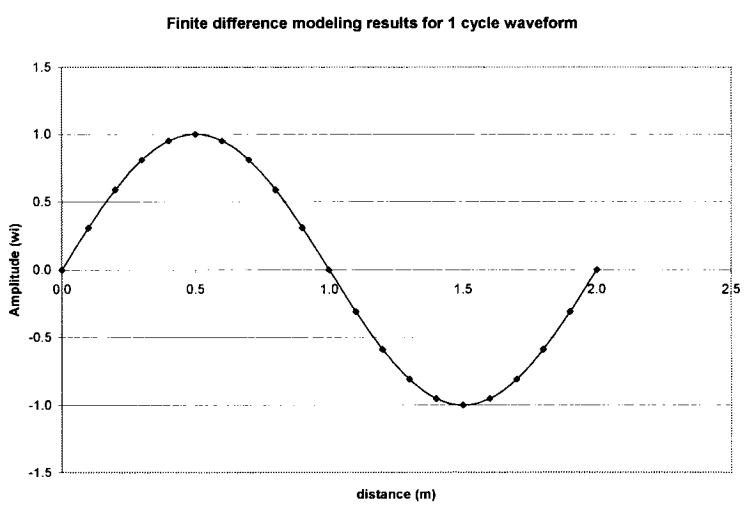

21. The summary gives steps involved in numerical modelling

STEP 1: Physics of the problem

Define the science or mathematics that describes the phenomena under study.

Most physical phenomena of interest have their physics adequately described in the form of partial differential equations: wave, diffusion, mass balance, conduction etc.

They are called the governing equations

STEP 2: Discretization methods

Decide on discretization methods

Finite element, finite difference etc.

In our case we choose finite difference method

STEP 3 :Approximation methods
Decide on approximation techniques
ie. Simpson methods, Galerkin, Taylor's
In our case we choose Taylor's series approximation

STEP 4: Boundary and initial conditions
Set your boundary and initial conditions
Set your time step/distance step

STEP 5: Solve governing equations
Solve the governing equation either by:
-explicit or
-implicit technique

STEP 6: Code the resulting equation
Coding is usually by iteration techniques /method
Coding could be done in any program of interest or even in excel

22. Conclusions

Numerical techniques are approximation methods therefore are better than analytical technique
Therefore numerical solutions has to be always checked and verified by either analytical solutions, if available, or experimental solutions
Issues like error, convergence, stability, accuracy etc. have to be critically analyzed.

APPENDIX 9: SPECTRAL RATIO TECHNIQUES

The spectral ratio method is the most widely used and accepted technique when testing jacketed rock samples in triaxial stress machines (Johnston et al., 1980). This processing technique is used for the experiments presented in this thesis. Advantages of this method are as follows; it is robust, it compensates for changes in acoustic amplitudes and no corrections are needed for sample geometry (Butt, 2001). A standard sample is used as a reference such as aluminum that has very little attenuation (Q ~ 15000). The waveforms acquired through the rock sample are compared to the waveform acquired through the aluminum standard. The general equation of a seismic wave is:

$$A_1(f) = A_0(f)(G(x))\exp(-\frac{\pi f x}{cQ})$$

Where, A_1 (f) is the amplitude at frequency f, A_0 (f) is the initial amplitude at frequency f, G (x) is the geometric spreading factor, x is sample length, c is the phase wave velocity and Q is the quality factor specifically related to the attenuation or energy loss of the initial acoustic wave. This expression may be applied to both waves through the rock sample and aluminum standards respectively. By taking the ratio of the aluminum waveform to the rock waveform, using the above general equation for each, the resultant relationship is as follows:

$$In(\frac{A_{AL}(f)}{A_{ROCK}(f)}) = \left\{\frac{\pi x}{c_{ROCK}Q_{ROCK}} - \frac{\pi x}{c_{AL}Q_{AL}}\right\}f + In(\frac{G_{AL}(x)}{G_{ROCK}(x)})$$

Knowing that Q_{AL} is very high, the second term approaches zero, and the equation takes the form of y = mx + b, where:

$$m = \frac{\pi x}{c_{ROCK}Q_{ROCK}}$$

The quality factor Q may be calculated over a frequency band directly from the slope of the linear portion of the spectral ratio. The linear portion may vary depending on the strength and petrophysical properties of the medium.

APPENDIX 10: CALCULATION OF DIFFRACTION LOSS

William gave the exact expression of equation 1 as a uniformly sensitive receiver in an infinite uniform isotropic media (without adsorption) as:

$$P = \rho c v_0 e^{ikz} - \frac{4\rho c v_0}{\pi} \int_0^{\pi/2} \exp[-ik(z^2 + 4a^2\cos^2\theta)^{1/2}]\sin^2\theta d\theta \quad (2)$$

Where, k is the wave number ($k=2\pi/\lambda$), λ the wavelength, z is the distance between transducers and v_0 the amplitude of the initial vibration on the transmitting transducer. The plane wave term (from equation 2) is given by:

$$P_0 = \rho c v_0 \exp[i(\omega t - kz)] \quad (3)$$

The diffraction loss which is the ratio of the spatially averaged acoustic pressure received at the receiving transducer front face from the transmitter P (equation 2), to a plane wave with the same initial pressure emanating from the full infinite plane of the transmitter front face P_0 (Equation 3) is mathematically given by:

$$\left|\frac{P}{P_0}\right| = (X^2 + Y^2)^{1/2} \quad (4)$$

Where,

$$X = 1 - A\frac{4}{\pi}\cos kz - B\frac{4}{\pi}\sin kz \quad (5)$$

$$Y = B\frac{4}{\pi}\cos kz - A\frac{4}{\pi}\sin kz \quad (6)$$

$$A = \int_0^{\pi/2} \cos[k(z^2 + 4a^2\cos^2\theta)^{1/2}] * \sin^2\theta d\theta \quad (7)$$

$$B = \int_0^{\pi/2} \sin[k(z^2 + 4a^2\cos^2\theta)^{1/2}] * \sin^2\theta d\theta \quad (8)$$

These equations are sufficient to estimate the diffraction corrections. However general form of energy adsorption can be deduces taking into consideration the intrinsic adsorption so that when the intrinsic adsorption is equal to zero then we retrieve the diffraction loss.

APPENDIX 11: COMPUTER PROGRAMS

A Finite difference code to solve the wave equation

```
% This MATLAB code was written by Paul Frempong
% It is used to calculate the numerical value of the wave equation
% It allows you to define the amplitude only. Other variable are fixed
% I want to define functions so that I can use them in the program
function y=f(x)

% I tried to let the computer prompt me in a form of a tool bar/icon to
% put in the Amplitude of the wave but I could not make it very nice nice
prompt  = {'Enter the amplitude of wave:'};
title   = 'INPUT FOR NUMERICAL MODEL BY PAUL FREMPONG';
lines= 1;
% I put in a default value so that it would always appear at the command promt window
def  = {'50'};
%This code is to be able to resize and move the command prompt tool bar icon
AddOpts.Resize='on';
  AddOpts.WindowStyle='normal';
  AddOpts.Interpreter='tex';
  answer=inputdlg(prompt,title,lines,def,AddOpts);
  % The computer reads in the Amplitude and assigns it a value Am
 Am=STR2DOUBLE(answer{1,1});

%It would test the input Amplitude value and if it is bigger than 200 it would stop the
program
% I have not been able to implement this, so I echo off the code. I would make another
attempt next time
```

```
%If
%Am>200
%prompt = {'Maximum Amplitude should be 100'}
 %end

% I defined all the variables and constants, and those that are to hold matrice
% distance = l, any interger value m interger =50, time step size k=0.01, distance step size h = l/m,
% wavelength lambda =Lam, N is the number of iteration for the accuracy needed, alpha is the inverse
% velocity squared .

l=10; alpha=2; m=50; N=100; h=1/m; k=0.01; A=[m-1, m-1, 0]; w0=[m-1; 0]; w1=[m-1; 0];
w2=[m-1; 0]; u=[m-1; 0];

% I evaluate the wave funtion for w0 from 1 to m-1
for i=1:m-1
   w0(i)=Am*sin(4*pi*(i*h));
end

% Assuming the wavelength is constant lamda(Lam, then I estimate the wave length
Lam=alpha*k/h;

% % I evaluate the wave function for w1 from 1 to m-1
for i =1:m-1
   w1(i)=(1-Lam^2)*Am*sin((4*pi*(i*h))+Am*sin(4*pi*(i+1)*h)+Am*sin(4*pi*(i-1)*h)*Lam^2/2+ k*(i*h));
 end
% I fill in the matrix A with the coefficient of the unique lamda values A(1,1) and A(1,2),
```

```
A(1,1)=2*(1-Lam^2);
A(1,2)=Lam^2;
% I fill in the matrix A with the coefficient of the lamda values,
 % note that some repeat themselves
for i=2:m-2
   A(1,i-1)=2*(1-Lam^2);
   A(1,i+1)=2*(1-Lam^2);
   A(i,i)=2*(1-Lam^2);
end
% I also fill in the matrix A with the coefficient of the unique lamda values,
% of m-1, m-2 combinations
A(m-1,m-2)=Lam^2;
A(m-1,m-1)=2*(1-Lam^2);

% I calculate the final answer w1 of each pass through the loop by matrix multiplication
A
% with a vector w1 and get all the individual elements in the matrix w1

 for i=1:N-1
  u=A*w1;
  w2=u-w0;
  w0=w1;
  w1=w2;
end

% These are then the final elements to lot with time element from 0 to m-1
   f1=w1
   t=1.0:1.0:m-1;
 % I want to save the numerical values of the results in the c drive
 % for future/further analyses and I call it NumRes.txt, a text file
```

```
save c:\NumRes.txt w1 /ascii

% Plot the graph of thr results
clf
plot(t,f1,'r*-')
xlabel('Time, ms')
ylabel('Amplitude, mV')
Title('Results of Finite Elements Model')
grid

% This is a great attempt but it took me so many days to accomplish
```

B. Stacking program for acoustic data processing

```
title  = 'Input for data processing';
lines= 1;
def    = {'test1','1','50'};
AddOpts.Resize='on';
  AddOpts.WindowStyle='normal';
  AddOpts.Interpreter='tex';
  answer=inputdlg(prompt,title,lines,def,AddOpts);

fname=answer{1,1};
fnumber=answer{2,1};
nsample=str2num(answer{3,1});
f1=[fname '_'];
```

```
f1=[f1 fnumber];
f1=[f1 '_'];f3='.txt';
i=0;
B=0;
while i<nsample
i=i+1;
f2=num2str(i);
f4=[f1,f2];
f=[f4,f3];
A = dlmread(f,',');
B=B+A;
end
f=[f1 'stk'];
f=[f f3];
dlmwrite(f,B,',');
```

C Diffraction loss program for modeling diffraction loss in rocks

% input, n	= number of iteration for Simpson Quadrature
Pie, pi	= 3.142
Input Velocity, V	= 6000000mm/s
Central frequency of sensor, f	= 1000000Hz
Wavelength, lamda, λ	= 6mm
Wave number, k	= 2pi/λ =1.04719755
Radius of transducer, a	= 12.5mm
'ka' Value, 'ka'	= 1, 5, ..100
Dimensionless distance, S	= 0:0.01:20
Actual distance between transducers, z	= S/λa^2

Changing frequency would change λ and therefore S and 'ka' values. Changing these parameters would change the distance and produce the Loss curve with distance at a fixed frequency. Changing the frequency would also change the 'ka' curve and produce the loss curve with frequency and fixed distance.

Parameter definitions

```
u=0; v=pi/2; ii=0; iii=0; n=100; pi= 3.142; a=12.5; lamda=6.0000; k=2*pi/lamda;
ka=k*a;
for S=0:0.01:20
 z=S/(lamda/a^2);
Tsimp=(sin(k*(z^2+4*a^2*(cos(u)^2))^0.5)*(sin(u)^2))+(sin(k*(z^2+4*a^2*(cos(v)^2))
^0.5)*(sin(v)^2));
h = (v-u) / n;
Tsum4 = 0.0;
for i = 1:2:(n-1)
x = u + i*h;
Tsum4 = Tsum4 + (sin(k*(z^2+4*a^2*(cos(x)^2))^0.5)*(sin(x)^2));
end
Tsum2 = 0.0;
for i = 2:2:(n-2)
x = a + i*h;
Tsum2 = Tsum2 + (sin(k*(z^2+4*a^2*(cos(x)^2))^0.5)*(sin(x)^2));
end
Tsimp = (h/3.0)*(Tsimp + 4*Tsum4 + 2*Tsum2);
D1=Tsimp;
simp=(cos(k*(z^2+4*a^2*(cos(u)^2))^0.5)*(sin(u)^2))+(cos(k*(z^2+4*a^2*(cos(v)^2))^
0.5)*(sin(v)^2));
h = (v-u) / n;
sum4 = 0.0;
for i = 1:2:(n-1)
x = u + i*h;
```

```
sum4 = sum4 + (cos(k*(z^2+4*g^2*(cos(x)^2))^0.5)*(sin(x)^2));
end
sum2 = 0.0;
for i = 2:2:(n-2)
x = a + i*h;
sum2 = sum2 + (cos(k*(z^2+4*a^2*(cos(x)^2))^0.5)*(sin(x)^2));
end
simp = (h/3.0)*(simp + 4*sum4 + 2*sum2);
C1=simp;
---------------------------------------------------
3 CALCULATION OF B
B1= D1*(4/pi)*cos(k*z)-C1*(4/pi)*sin(k*z);
 ---------------------------------------------------
CALCULATION OF A
A1=1-C1*(4/pi)*cos(k*z)-D1*(4/pi)*sin(k*z);
 ---------------------------------------------------
iii=iii+1;
ii=ii+1;
test(ii)=A1;
exam(iii)=B1;
end
test=test';
exam=exam';
save C:\LOSSA test /ascii
save C:\LOSSB exam /ascii
Plot the graph of the results
 t=0:0.01:20;
  t=1:501;
 clf
 plot(t,test,'r-')
```

```
xlabel('Dimensionless Dist. S')
ylabel('|P/Po|')
Title('Results of Diffraction Loss for K=13.09')
Grid
```

D. NSD Program for dispersion of waves and scaling

```
% PROGRAM:  Numerical Fourier Discretization
% PAUL FREMPONG    11 JANUARY 2005

% The above models are implemented in the MATLAB program below:
% This program uses the (inverse) fast Fourier transform to compute the solutions of 6
% different dispersive equations with the same initial data u(x,0). The three equations are:
%       ω = √ (k^2-1)          Current model
%       ω = √ (k^2+1)          Klein-Gordon
%       ω = k^3                Korteweg-de Vries
%       ω = sin (k)*k^2        Benjamin-Ono
%       ω = k^2                Schroedinger
%       ω = k / (1+k^2)        Regularized Long Wave
%
%  The initial data for each is
%
%       u(x,0) = 50exp(-((x**2)/24))*exp(2ix)
%
%  In the transform variable the initial data is
%
%      u(k,0) = 50exp(-6*(k-2)**2)*sqrt(24*pi)
%
```

```
%  The data is sampled on the interval  k in [0,K]. K is set to 100.
%  The number of sample points is N (set to 4096), so delk = 100/4096 = 0.016.
%  The result is displayed on the interval x in [-pi/delk, pi/delk]
%  intervals delx = 2*pi/K.
%
%  The values of u(x,t) go into the vector u
%  The values of u(x,0) go into the vector u0
%  The values of u(x,0) translated to the right with speed
%  equal to the group velocity at k = 2 go into the vector v.
%  The latter can be used to compare how the wave is being
%  deformed by the dispersion process.
%  The values of the group velocities for all k goes to Vg
%  The values of the group velocities for all k goes to Vp
%
%  There are seven supporting mfiles:
%      0. Initial.m          For initial data and boundary conditions
%      1. CSModel.m:         Dispersion relation for the current model
%      2.KGModel.m:          Dispersion relation for the Klien Gordon model
%      3.KdVModel.m:         Dispersion relation for the Korteweg-de Vries model
%      4.BOModel.m:          Dispersion relation for the Benjamin-Ono model
%      5.SModel.m:           Dispersion relation for the Schroedinger model
%      6.RLWModel.m:         Dispersion relation for the Regularized Long Wave model

disp(' ')
disp(' There are six choices of dispersion relations ')
disp(' Enter 1 for the Current Scaling Model')
disp(' Enter 2 for the Klein-Gordon equation ')
disp(' Enter 3 for the Korteweg-deVries equation ')
disp(' Enter 4 for the Benjamin-Ono equation  ')
disp(' Enter 5 for the Schroedinger equation ')
```

```
disp(' Enter 6 for the Regularized Long Wave equation ')
m = input('Enter the choice of dispersion relation   ')

t = input('Enter the time t at which you wish to view the solution   ')

%  Note that, in theory, the time can be anywhere between zero and infinity but care must
% be taken not to enter a time when the wave has already lost energy and does not exist
% in the medium. This can be deduced from the attenuation coefficient and the Initial
% amplitude given in  the initial condition

K = 100;                          % Maximum wavenumber considered
N = 4096;                         % Maximum sampling points considered
delk = K/N;                        % Descritization interval of the wavenumber
k = 0:delk:K - delk;               % k from zero incrementing by delk to K
delx = 2*pi/K;                    % equivalenth descritization in terms of length x
x = -N*pi/K: delx : N*pi/K -delx;  % from –ve value incrementing to positive values.
% This is because of the ifft that produce both
% negative and positive values
W = Initial(k);

if m == 1

ww = exp(-i.*CSModel(k).*t).*W    %  The wave in Fourier domain at time t and with
% dispersive relation substituting w for k

z = exp(-i*k*t*2/sqrt(2)).*W;          % A vector v which is the original wave u0
% translated by the quantity t*omega'(2)
 elseif m ==2
   ww = exp(-i.*KGModel(k).*t).*W;
   z = exp(-i.*2/sqrt(5)*k.*t).*W;
```

```
elseif m=3
  ww = exp(-i.*KdVModel(k).*t).*W;
  z = exp(-i*12*k*t).*W;
elseif m=4
  ww = exp(-i.*BOModel(k).*t).*W;
  z = exp(-i*(1.973)*k*t).*W;
elseif  m=5
  ww = exp(-i.*SModel(k).*t).*W;
  z = exp(-i*4*k*t).*W;
else
ww = exp(-i.*RLWModel(k).*t).*W;
  z = exp(-i*(26/25)*k*t).*W;
end
  uu = real(ifft(ww));
  u = (N*delk/(2*pi))*[uu((N/2)+1:N),uu(1:N/2)];
  uu0 = real(ifft(w));
  u0 = (N*delk/(2*pi))*[uu0((N/2)+1:N), uu0(1:N/2)];

  vv = real(ifft(z));
  v = (N*delk/(2*pi))*[vv((N/2)+1:N),vv(1:N/2)];
% save C:\MATLAB6p1\Christmas2004\fresult.txt v /ascii
c=w/k      %Phase velocity ( c) calculations
%    Group velocity (g) calculations
if m == 1
        g= k*(k^2-1)^(-0.5)
elseif  m=2
        g=k*(k^2+1)^(-0.5)
elseif  m=3
        g=3k^2
elseif  m=4
```

```
        g=2k
elseif m=5
        g=(2*k*sin(k))+(k^(2)*cos(k))
else
g= (1/(1+k^2))*(((2*k^2)/(1+k^2))+1)
 %      Transposition of data
   transu0=u0';
   transx=x';
   transv=v';
   transu=u';
   transc=c';
   transg=g';
   transw=w';
   transk=k';
%      Save all dats in ASCII for further analyses
  save C:\MATLAB6p1\Christmas2004\u0result.txt transu0 /ascii /tabs
  save C:\MATLAB6p1\Christmas2004\xresult.txt transx /ascii /tabs
  save C:\MATLAB6p1\Christmas2004\uresult.txt transu /ascii /tabs
  save C:\MATLAB6p1\Christmas2004\vresult.txt transv /ascii /tabs
  save C:\MATLAB6p1\Christmas2004\cresult.txt transc /ascii /tabs
  save C:\MATLAB6p1\Christmas2004\gresult.txt transg /ascii /tabs
 save C:\MATLAB6p1\Christmas2004\wresult.txt transw /ascii /tabs
 save C:\MATLAB6p1\Christmas2004\kresult.txt transk /ascii /tabs

% Plot them in MATLAB, view and analyse.
plot(x,u0,x,u,'g')
plot(k,w)
plot(k,c)
plot(x,u0)
plot(x,v)
```

```
plot(x,u)
plot(x,u,x,v)
plot(x,u0,x,u,'g')
plot(k,g)
axis([0 250 -1 1])
 plot (x,u0,x,u,'g')

%       SUPPORTING FILES: These files should be in different files nad placed in the same directory as the main file

% File 1. Initial pulse
function y = Initial(k)
  y = 50*exp(-6*(k-2).^2)*sqrt(24*pi);

% File 2. Current Scaling Model
function w = CSModel(k)
w = sqrt( k.^2 -1);

%  File 3. Klein-Gordon Model
function w=KGModel(k)
w = sqrt( k.^2 + 1);

%  File 4. Korteweg-deVries  Model
function w = KdVModel(k)
    w =  k.^3;

% File 5. Benjamin Ono Model
function w = BOModel(k)
ω = sin (k)*k^2;
```

```
% File   6. Schroedinger model
function w=SModel(k)
   w = k.^2;

% File 7. Regularized Long Wave model
function w = RLWModel(k)
    w = k / (1+k^2)
END
```

E Excel macro for stacking

```
Sub macro2()
'
' FFTMacro Macro
' Macro recorded 10/29/2003 by Paul Frempong
'
' Keyboard Shortcut: Ctrl+Shift+S
'
   With ActiveSheet.QueryTables.Add(Connection:= _
     "TEXT;C:\Fall          Experiment\GC3_Desktop_5Dec2003\Pwaves\test2_1_1.txt",
Destination:=Range _
     ("A1"))
     .Name = "test2_1_1"
     .FieldNames = True
     .RowNumbers = False
     .FillAdjacentFormulas = False
     .PreserveFormatting = True
     .RefreshOnFileOpen = False
```

```
        .RefreshStyle = xlInsertDeleteCells
        .SavePassword = False
        .SaveData = True
        .AdjustColumnWidth = True
        .RefreshPeriod = 0
        .TextFilePromptOnRefresh = False
        .TextFilePlatform = 437
        .TextFileStartRow = 1
        .TextFileParseType = xlDelimited
        .TextFileTextQualifier = xlTextQualifierDoubleQuote
        .TextFileConsecutiveDelimiter = False
        .TextFileTabDelimiter = True
        .TextFileSemicolonDelimiter = False
        .TextFileCommaDelimiter = False
        .TextFileSpaceDelimiter = False
        .TextFileColumnDataTypes = Array(1)
        .TextFileTrailingMinusNumbers = True
        .Refresh BackgroundQuery:=False
    End With
    Range("B1").Select

    With ActiveSheet.QueryTables.Add(Connection:= _
        "TEXT;C:\Fall          Experiment\GC3_Desktop_5Dec2003\Pwaves\test2_1_2.txt",
Destination:=Range _
        ("B1"))
        .Name = "test2_1_2"
        .FieldNames = True
        .RowNumbers = False
        .FillAdjacentFormulas = False
        .PreserveFormatting = True
```

```
    .RefreshOnFileOpen = False
    .RefreshStyle = xlInsertDeleteCells
    .SavePassword = False
    .SaveData = True
    .AdjustColumnWidth = True
    .RefreshPeriod = 0
    .TextFilePromptOnRefresh = False
    .TextFilePlatform = 437
    .TextFileStartRow = 1
    .TextFileParseType = xlDelimited
    .TextFileTextQualifier = xlTextQualifierDoubleQuote
    .TextFileConsecutiveDelimiter = False
    .TextFileTabDelimiter = True
    .TextFileSemicolonDelimiter = False
    .TextFileCommaDelimiter = False
    .TextFileSpaceDelimiter = False
    .TextFileColumnDataTypes = Array(1)
    .TextFileTrailingMinusNumbers = True
    .Refresh BackgroundQuery:=False
End With
```

APPENDIX 12: SELECTED PUBLICATIONS

1. Butt, S., Frempong, P. K., Mukherjee, C. and Upshall, J., (2005), Experimental measurement of the ultrasonic velocity, attenuation and permeability characteristics of outburst prone sandstone, Journal of Applied Geophysics, (accepted, February 2005, Manuscript No: APPGEO770)

2 Roy, D., Butt, S.D. and Frempong, P.K., (2004), Geostatistical resource estimation for the Poura narrow-vein gold deposit, Canadian Institute of Mining Bulletin, Vol. 97, No. 1077, p 47 -50

3. Frempong, P. K., (1999), The development of a robust sampling strategy and protocol in underground gold mines. J. of Australasian Institute of Mining and Metallurgy, 304(2), p15-22

4. Frempong, P. K. and Clark I., (1996), An indicator-based geostatistical assessment of the global vermiculite reserves at Palabora Mining Company. South African Institute of Mining and Metallurgy, Surface Mining '96, Johannesburg, SAIMM, pp. 1-12

5. Frempong, P. K., Butt, S. and Islam, R., (2003), Linking acoustic and mechanical properties of materials with particular reference to reservoir rocks: A critical literature review, Annual conference of Canadian society for Civil Engineers, Moncton, NB, Canada

6. Frempong, P. Butt S., (2005), Scaling multi frequency acoustic data: a case of normal dispersive medium, Procedings, Rainbow in the Earth – 2nd International Workshop 2005, Lawrence Berkeley National Laboratory, Berkeley, California, August 17-18, 2005

7. Frempong, P. Butt S., Donald, A. (2005), Frequency dependent spectral ratio technique for Q estimate, Procedings, Rainbow in the Earth – 2nd International Workshop 2005, Lawrence Berkeley National Laboratory, Berkeley, California, August 17-18, 2005

8. Donald, A., Frempong, P. K., Butt, S. and Nouri, A., (2003), Laboratory acoustic measurements of the attenuation factor Q in petroleum reservoirs during simulated pore pressure prediction, Annual conference of Canadian society for Civil Engineers, Moncton, NB, Canada

9. Nouri, A., Donald, A., Frempong, P. K., Butt, S., Vaziri, H. and Islam, R., (2003), Using acoustic measurements in evaluating pore collapse occurrence and associated sand production, Annual conference of Canadian society for Civil Engineers, Moncton, NB, Canada

10. Belhaj, H.A., Ryan, R.J., Butt, S.D., Frempong, P., Donald, A. and Islam, M.R., (2004), A New Coupled Fluid Flow/Stress Model for Porous Media Behavior: Numerical Modeling and Experimental Investigation, SPE International Petroleum Conference, Puebla, Mexico, SPE 90265

11. Frempong, P. K., Donald, A. and Butt, S., (2004), The effect of injection and depletion cycles on ultrasonic velocity and quality factor in glass sandstone, Geophysics, (in press) paper no. GEO 2004 0096-R1

12. Donald, J. A., Frempong, P. K., Butt, S. D., (2004), Characterizing volumetric failure in weak sandstone reservoirs using P-wave quality factor, velocity and acoustic emissions, Geophysics, (in press), paper no., GEO-2004-0077

13. Frempong, P. K., and Butt, S., (2004), Modeling of diffraction loss and phase shift angels in a low adsorption media: example of a quartz sandstone, Geophysics, (in press) paper no: GEO 2004 0114

14. Frempong, P. K., and Butt, S., (2005), Laboratory experiments and numerical modeling to study the effect of diffraction on acoustic velocity and quality factor of rock materials, Journal of the Acoustical Society of America, submitted paper No: (05-02012)

15. Frempong, P. K. and Butt, S., (2005), Non destructive techniques to determine the effective stress coefficient of porous sandstone Canadian Journal of Petroleum Technology, CJPT, (submitted)

16. Frempong, P.K. Butt, S. and Islam, R., (2004), Construction of general acousto-mechanical model in reservoir rocks: a review, Journal of Applied Geophysics, (in press), Manuscript No: APPGEO 689

17. Frempong, P. K., (2003), Seeing the unseen: imaging beneath the surface, First innovation colloquium of Energy Environment and Communication, April 28-29 2003, Halifax, NS, Canada.

18. Frempong, P. K., (2002), Handling outliers for resource estimation in gold deposits, Mining Matters for Novas Scotia, Opportunities for economic development, November 13 2002, D. R. MacDonald edited, No. ME20002-2 p 8-10

19. Frempong, P.K. Butt, S. and Islam, R., (2004), Numerical Fourier discretization (NFD) modeling of non linear wave in a dispersive medium, J. of Mathematical geology, submitted.

REFERENCE

Imhof, M., G., (2003), Scale dependence of reflection and transmission coefficients, Geophysics Vol. 68, No.. 1, p. 322–336

Marion, D., Mukerji, T., and Mavko, G., (1994), Scale effects on velocity dispersion:Fromray to effectivemediumtheories in stratified media: Geophysics, 59, p. 1613–1619.

Mukerji, T., Mavko, G., Mujica, D., and Lucet, N., (1995), Scale dependent seismic velocity in heterogeneous media: Geophysics, Vol. 60, p. 1222–1233.

Parra, J. O., Hackert, C. L, Ababou, R., Sablik, M. J., (1999) Dispersion and attenuation of acoustic waves in randomly heterogeneous media Journal of Applied Geophysics, Vol. 42, p. 99–115

Backus, G.E., (1962). Long-wave elastic anisotropy produced by horizontal layering. Journal of Geophysical Research, Vol. 67, p. 4427–4440.

Prasad, M., Manghnani, M. H., (1997), Effects of pore and differential pressures on compressional wave velocity and quality factor on Berea and Michigan sandstones, Vol. Geophysics, 62, 1163-1176.

Carcione, J. M., Hellev, H., B., (2002), Rock physics of geopressure and prediction of abnormal pore fluid pressures using seismic data
CSEG Recorder, 2002 p. 8 to 32

Dvorkin, J. and Walls, J. 2000, Detecting overpressure from seismic velocity calibrated to log and core measurements, 32nd Annual Offshore technology conference, Paper OTC 11912.

Christoffel, E. W. (1877) Annali di matematica pura, ed. Applicata Ser II 8: 193

Imhof, M., G., (2003), Scale dependence of reflection and transmission coefficients, Geophysics Vol. 68, No.. 1, p. 322–336

Marion, D., Mukerji, T., and Mavko, G., (1994), Scale effects on velocity dispersion:Fromray to effectivemediumtheories in stratified media: Geophysics, 59, p. 1613–1619.

Mukerji, T., Mavko, G., Mujica, D., and Lucet, N., (1995), Scale dependent seismic velocity in heterogeneous media: Geophysics, Vol. 60, p. 1222–1233.

Parra, J. O., Hackert, C. L, Ababou, R., Sablik, M. J., (1999) Dispersion and attenuation of acoustic waves in randomly heterogeneous media Journal of Applied Geophysics, Vol. 42, p. 99–115

Backus, G.E., (1962). Long-wave elastic anisotropy produced by horizontal layering. Journal of Geophysical Research, Vol. 67, p. 4427–4440.

Prasad, M., Manghnani, M. H., (1997), Effects of pore and differential pressures on compressional wave velocity and quality factor on Berea and Michigan sandstones, Vol. Geophysics, 62, 1163-1176.

Carcione, J. M., Hellev, H., B., (2002), Rock physics of geopressure and prediction of abnormal pore fluid pressures using seismic data
CSEG Recorder, 2002 p. 8 to 32

Dvorkin, J. and Walls, J. 2000, Detecting overpressure from seismic velocity calibrated to log and core measurements, 32nd Annual Offshore technology conference, Paper OTC 11912.

Christoffel, E. W. (1877) *Annali di matematica pura*, ed. Applicata Ser II 8: 193

Landro, M., and Kvam., O, (2002), Pore Pressure Estimation-What can we Learn from 4D?, CSEG Recorder, Vol. 27, pp. 83-87.

Carcione J. M. and Hellev, H. B. (2002), Rock physics of geopressure and prediction of abnormal pore fluid pressures using seismic data, CSEG Recorder September, 2002, page 8 to 32

Carcione J. M and Tinivella, U., 2001, The seismic response to overpressure: a modelling study based on laboratory, well and seismic data , Geophysical Prospecting, 2001, 49, 523±539

Christoffel, E. W. (1877) *Annali di matematica pura*, ed. Applicata Ser II 8: 193

Miranda, M., Aleotti, L., Abramo, F., Poletto, F., Craglietto, A., Persoglia, S., and Rocca, F., 1996, Impact of the seismic "while drilling" technique on exploration wells: First Break, **14**, 55–68.

Ziolkowski A and Bokhorst K. (1993), Determination of signature of a dynamic source using source scaling, Part 2 Experiment Vol. 58 no 8, 1183-1194

Islam M. R. (1996), Emerging technologies in enhanced oil recovery, Energy sources, 21: 97-111

Islam M. R. (2001), Emerging technologies insubsurfsce monitoring of petroleum reservoir, Petroleum Res J. 13:33-46

Ziolkowski, A., Underhill, J. R., and Johnston, R.G. K., 1998,Wavelets, well ties, and the search for subtle stratigraphic traps: Geophysics, 63, 297–313.

Bowers, G.L., 1995, Pore pressure estimation from velocity data: Accounting for porepressure mechanisms besides undercompaction, SPE Drilling and Completion, June, 89-95.

Eaton, B.A., (1985), The equation for geopressure prediction from well logs, SPE 5544.

Hottman, C.E. and Johnson, R.K., (1965), Estimation of formation pressures from logderived shale properties, JPT, June 717-722.

Sayers, C.M., Johnson, G.M. and Denyer, G., (2000), Predrill Pore Pressure Prediction Using Seismic Data, IADC/SPE Drilling Conference 59122.

Briers, J.M. (2004, April 20) Rockies Seen as Lonely Bright Spot for US Natural Gas, Dow Jones Newswires. Retrieved April 26, 2004, from http://www.slb.com/news/story.cfm?storyID=616409

Winkler, K. W. (1986), Estimates of velocity dispersion between seismic and ultrasonic frequencies Geophysics, Vol. 51, No. I (January 1986); p. 183-189,

Miranda, M., Aleotti, L., Abramo, F., Poletto, F., Craglietto, A., Persoglia, S., and Rocca, F., (1996), Impact of the seismic "while drilling" technique on exploration wells: First Break, **14**, 55–68.

Calder, J.H., Boehner, R.C., Brown, D.E., Gibling, M.R., Mukhopadhyay, P.K., Ryan, R.J. and Skilliter, D.M., (1998), Classic Carboniferous Sections of the Minas and Cumberland Basins in Nova Scotia, The Society for Organic Petrology Annual Meeting Field Trip, 29-30 July 1998. Open File Report ME 1998-5, Nova Scotia Natural Resources.

Keck, E.B., (1999), THE CITY ROCKS! Explore the Hidden World of Building Stone, Retrieved April 13th, 2004, from http://homepage.mac.com/bandpck/cityrocks/intro.html

McHone, J.G., (2000), Non-plume magmatism and rifting during the opening of the central Atlantic Ocean. Tectonophysics, 316 (3-4), 287-296.